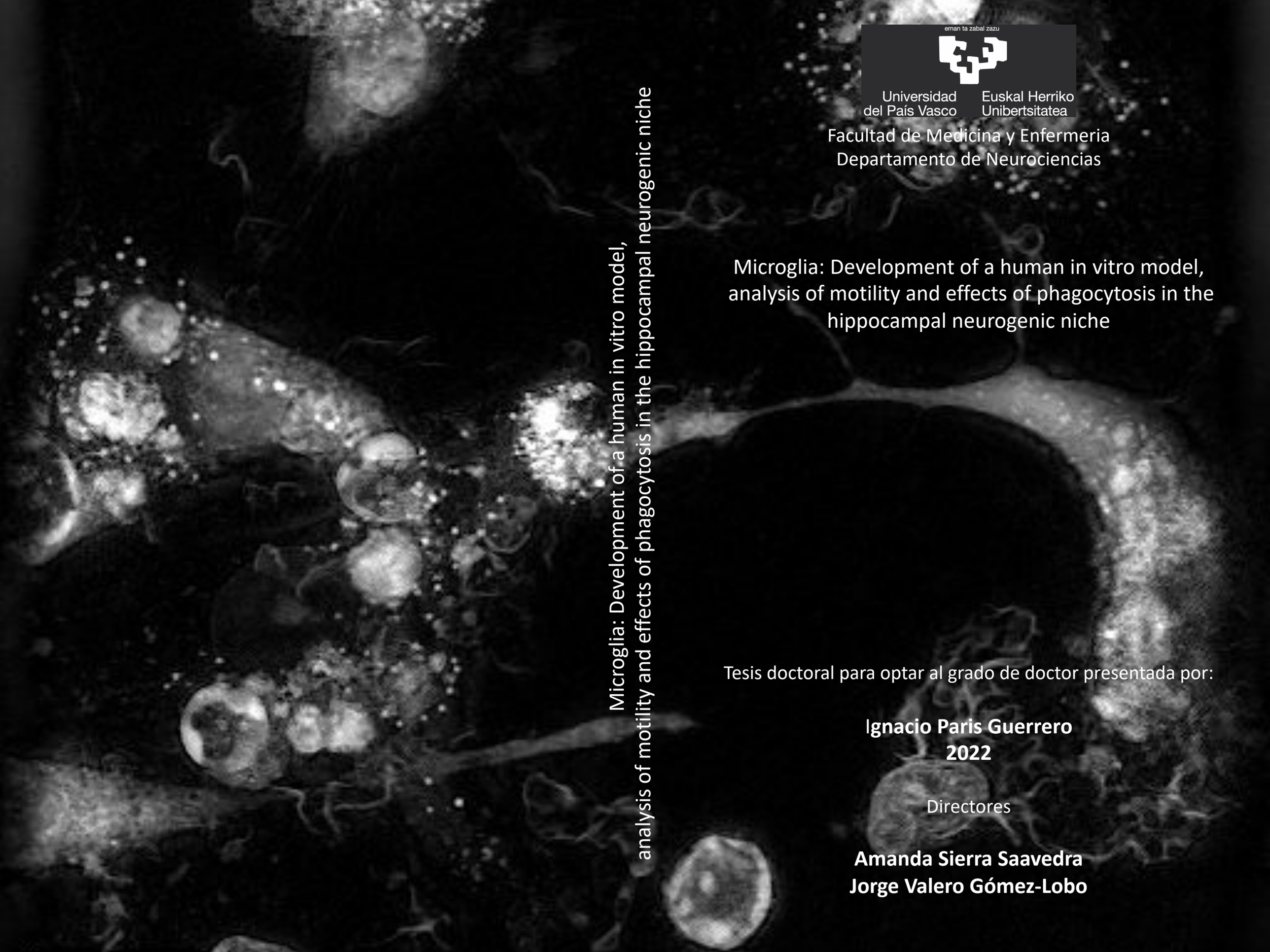

Microglia: Development of a human in vitro model, analysis of motility and effects of phagocytosis in the hippocampal neurogenic niche

eman ta zabal zazu

Universidad del País Vasco
Euskal Herriko Unibertsitatea

Facultad de Medicina y Enfermeria
Departamento de Neurociencias

Microglia: Development of a human in vitro model, analysis of motility and effects of phagocytosis in the hippocampal neurogenic niche

Tesis doctoral para optar al grado de doctor presentada por:

Ignacio Paris Guerrero

2022

Directores

Amanda Sierra Saavedra
Jorge Valero Gómez-Lobo

(cc)2022 IGNACIO PARIS GUERRERO (cc by-nc-sa 4.0)

Agradecimientos

A mis directores de tesis:

A Amanda Sierra por acogerme en su laboratorio, por todas las oportunidades de aprendizaje y de proyección profesional que nos ofrece a todos los miembros de su grupo, pero sobre todo gracias por los brownies.

A Jorge Valero por su paciencia, su humor, introducirme al maravilloso mundo de las macros de ImageJ y por llevarme a Coimbra a ser su ayudante en los cursos de análisis de imagen.

A mi familia:

Antonio y Mª Angeles, todo vuestro esfuerzo y sacrificio me han traído hasta aquí, nada puede expresar el orgullo que siento por ser vuestro hijo.

A mi hermana Judith, si hay algo que me condujo al campo de la neurociencia eres tú.

A mis abuelas Mª Pilar y Pudenciana, gracias por vuestro cariño incondicional

A mis abuelos Antonio y Felix, aunque ya no estéis entre nosotros yo os llevo conmigo

A mis compas del laboratorio Sierra

A Oihane, Sol, Irune, Victor y Virginia, la primera oleada del grupo Sierra, gracias por los buenos momentos que hemos compartido y por los que aún nos quedan. Gracias por la confianza que habéis depositado en mí y el cariño con el que me habéis tratado.

A Mar, Noelia y Marta, os deseo todo lo mejor en lo que os queda de doctorado y espero que coincidamos en el futuro (aunque sea en congresos!). Gracias por alegrarme muchas mañanas.

A los miembros del grupo Encinas por todos los buenos momentos en congresos, cenas que se convierten en fiesta y mañanas de intentos de surf.

A mis compañeros de Salamanca

A Miguel, mi bomboncito, y a Diego, compartir el piso de la Rua con vosotros fue, con diferencia, el mejor año que pasé en Salamanca, desde entonces cada uno hemos seguido rumbos distintos, volviendo a compartir piso con miguel durante la época del doctorado fue lo mejor que me podría haber pasado, e ir de vacaciones con vosotros y hacer y recibir visitas me llena de felicidad. Sois mi familia.

A Sara y Marta, os quiero.

A Michy, Clara, Agata y Amanda.

To my colleagues from Basel: Markus, Simon and Marvin, thank you for having me in your lab and for all the fun times.

To Jessica, thanks for being by my side and for your support. I love you.

A quien esté leyendo esto en este momento: Gracias

1. Introduction
1.1. Introduction
1.2. Theoretical framework and methods
1.2.1. Introduction to microglia
1.2.1.1. Ontogeny
1.2.1.2. Developmental origin of microglia
1.2.1.3. Transcriptional control of microglial lineage
1.2.1.3.1. Transcription factors
1.2.1.3.2. Environmental cues
1.2.1.4. Development of in vitro models
1.2.2. Microglial functions
1.2.2.1. Inflammation
1.2.2.1.1. Pro-inflammatory
1.2.2.1.2. Anti-inflammatory
1.2.2.1.3. Microglial states
1.2.2.2. Motility
1.2.2.2.1. Signaling mechanisms
1.2.2.2.2. Methods to quantify motility
1.2.2.3. Phagocytosis
1.2.2.3.1. Types of cargo
1.2.2.3.2. Types of signals
1.2.2.4. Adult Neurogenic niches
1.2.2.4.1. Microglial in adult neurogenic niches
1.2.2.4.2. Phagocytosis in adult neurogenic niches
1.3. Hypothesis and objectives
1.4. Summary
1.5. Bibliography
2. Conclusions
3. Published articles

1. Introduction

1.1. Introduction

In this PhD Thesis, I will discuss several topics related to microglia, the resident macrophages of the brain parenchyma. They are derived from yolk sack primitive macrophages that colonize the brain early during embryonic development. Microglia contribute to the correct development and functioning of the central nervous system with their multiple functions, including their role as phagocytes clearing the brain parenchyma from apoptotic cells and protein aggregates. Microglia are also involved in most neurological and neurodegenerative diseases, especially since genome-wide association studies have found that many microglia-specific genes are significant risk factors for neurodegenerative diseases. In this PhD Thesis, I will specifically discuss two aspects of microglial physiology. First, I will focus on the development of human models of microglia and their importance in the use of microglia as a therapeutic target in neurodegenerative diseases. Finally, I will discuss microglial process motility and phagocytosis, two essential functions of homeostatic microglia that can become compromised in pathology. In this introduction, I will first provide a brief overview of the three main topics and, in the next section, I will provide a wider theoretical framework.

(i) Human models of microglia:

Interest in microglia as a therapeutic target for human diseases has been growing for quite some time. Most in vitro studies use murine primary microglia or immortalized cell lines, which have proved useful in studying the basic mechanisms of microglia. However, it has become increasingly apparent that these models have to be refined to be more representative of human microglial physiology, since immortalized cell lines and primary cultures have transcriptional differences with freshly isolated human microglia (Melief et al., 2016; Timmerman et al, 2018; Geirsdottir et al., 2019). Fresh human microglia would be very useful to create in vitro models but is nearly impossible to obtain, relying on cells isolated from recently deceased patients or biopsies. Thus, these microglia obtained from post mortem samples or patient biopsies can have patterns of expression that do not resemble what can be found on homeostatic microglia (Mizee *et al.*, 2017). The scarcity of human microglia sources and variability of gene expression that can be found in these samples make them non-ideal for the study of microglia in vitro, especially for large scale experiments. Therefore, an alternative source of human microglia is needed.

A novel alternative to the culture of human microglia is the differentiation of induced pluripotent stem cells (iPSCs) to microglia in vitro (Abud *et al.*, 2017; Haenseler *et al.*, 2017; McQuade *et al.*,

2018). During my secondment at Roche in Basel, I focused on generating microglia-like cells from human iPSCs in vitro, using a previously described method to obtain primitive macrophages (Gutbier *et al.*, 2020). I optimized culture conditions to find those that displayed a classic microglial branched morphology and gene expression characteristic of microglia. After determining the best conditions, these cells were further characterized using transcriptomic analysis and phenotypic characterization (intracellular calcium variations and migration in response to different stimuli, mitochondrial metabolism, and phagocytosis of beta amyloid coated nanoparticles). These results were published in (Reich *et al.*, 2021).

(ii) Microglial process motility:

Microglial process motility is crucial for the correct functioning of microglia. Microglia are constantly surveilling the brain parenchyma to respond to any disturbances (Nimmerjahn et al., 2005). Microglial process motility has been traditionally analyzed using very time consuming, non-standardized methods that rely on 2D projections of 3D images obtained by two-photon microscopy. However, microglial processes move in all three dimensions of the brain parenchyma, and thus use of 2D projections can lead to measurement errors.

To address this issue, I developed a series of macros that provide a standardized, free to use, semi-automated and robust method for analyzing microglial process motility in 3D using the open-access software ImageJ. I used this method to demonstrate that analyzing microglial process motility in 3D instead of 2D projections yields significantly different results; and that our semi-automated method can obtain more reliable data faster and with reduced experimenter bias than manual analysis. Results obtained from this project can be found in (Abiega *et al.*, 2016), where microglial process motility was analyzed in the context of a model of murine mesial temporal lobe epilepsy; and in (Paris *et al.*, 2018), where I described and validated the full set of macros and used them to assess process motility in a model of systemic inflammation.

(iii) Microglial phagocytosis:

Phagocytosis of apoptotic cells is a key function of the professional phagocytes of the brain parenchyma: microglia. In the adult brain in physiological conditions, this function is particularly important in the neurogenic niches, where newborn cells constantly undergo apoptosis (Sierra *et al.*, 2010). These apoptotic cells must be cleared rapidly by microglia to maintain homeostasis in the neurogenic niches. However, we hypothesize that microglia's role in the neurogenic niches is not only limited to clearing apoptotic cells but that phagocytic microglia have an active role in the regulation of the neurogenic cascade.

In order to evaluate that hypothesis, I used several strains of mice that lacked the expression of receptors involved in microglial phagocytosis(MerTK, Axl, and P2Y12).

MerTK and Axl are, along with Tyro3, part of the TAM receptor family (Lemke and C. V. Rothlin, 2008). These are receptor tyrosine kinases that bind to Gas6 for the recognition of apoptotic cells for their engulfment. Gas6 is an adapter protein that binds to phosphatidylserine (PS) exposed by apoptotic cells to facilitate their recognition by TAM receptors. The depletion of these receptors has been previously reported to be detrimental for the clearance of apoptotic cells by macrophages and dendritic cells (Seitz *et al.*, 2007).

P2Y12 is a metabotropic purinergic receptor crucial for microglial environmental surveillance through the sensing of the find me signals ATP/ADP. This receptor has been previously shown to be crucial for the motility of microglia, which is an important step in phagocytosis (Haynes *et al.*, 2006).

I confirmed that microglial phagocytosis of apoptotic cells was reduced in these models and used them to evaluate the role of phagocytosis on neurogenesis. To asses neurogenesis, I used a combination of immunofluorescence for markers of the different cell types of the neurogenic cascade and tracked the fate of newborn cells using Bromodeoxyuridine (BrdU), which integrates into the DNA of proliferating cells. Mice injected with BrdU were studied at different time points. This allowed us to evaluate differences in proliferation, survival, and ultimate differentiation into neurons between controls and mice where phagocytosis is impaired, thus revealing that deficient phagocytosis leads to a reduced yield in the neurogenic cascade. These results were published in (Diaz-Aparicio *et al.*, 2020)

In the next section (Theoretical framework and methods), I will provide a general introduction to microglia and their role in maintaining homeostasis in the brain and delve deeper into aspects related to the three topics covered in this PhD Thesis

1.2. Theoretical framework and methods

1.2.1. Introduction to microglia

Microglia are the main resident innate immune cells of the central nervous system (CNS) parenchyma. They are therefore in charge of orchestrating immune responses in the brain together with border associated macrophages (BAMs) located in the meninges, perivascular space, and choroid plexus. Microglia were first distinguished from other glial populations by Pío del Río Hortega in 1919 (Sierra et al., 2019). Microglia are distributed across the entire CNS with little to no contact with other microglia and constantly surveil the entire brain parenchyma to sense any disturbances (Nimmerjahn et al., 2005). Nowadays, they are considered one of the main therapeutic targets for treating neurodegenerative and neurological diseases. First, microglia uniquely express many genes that have been identified in genome wide association studies (Cruchaga *et al.*, 2013; Efthymiou and Goate, 2017; Wightman *et al.*, 2021). And second, they are the main cell type in control of the release of proinflammatory cytokines, a major characteristic of these diseases (Smith *et al.*, 2012).

In the following sections, I will describe various aspects of microglia, starting with its ontogeny, which was debated since their discovery until their origin was confirmed to be mesodermal, specifically from the yolk sac (Ginhoux et al., 2010). Understanding the ontogeny of microglia has been crucial for developing protocols for the differentiation of iPSC to microglia *in vitro*, which is a very important advancement in the use of microglia as a therapeutic target.

Next, I will summarize the functions that microglia have *in vivo*. Specifically, I will focus on the response to environmental cues, process motility, and phagocytosis. These functions are very tightly related and crucial to maintaining homeostasis in the brain (Sierra *et al.*, 2010; Paolicelli *et al.*, 2011; Ueno *et al.*, 2013).

Finally, I will introduce adult neurogenesis and the adult neurogenic niches since microglia is tasked with constantly phagocytosing apoptotic cells from these niches to maintain tissue homeostasis (Sierra et al., 2010; Cunningham et al., 2013). I will also explore the consequences of microglial phagocytosis on these niches and how microglia released factors can influence the neurogenic cascade.

1.2.1.1. Ontogeny

Microglia are now known to arise from primitive macrophage progenitors that originate from the yolk sack at embryonic day 7.5 in the mouse(Ginhoux *et al.*, 2010) and at around estimated gestational day 19 in humans (Tavian and Péault, 2005). However, determining the embryonic origin of microglia proved challenging because hematopoiesis occurs in two major sites during embryonic development, the yolk sac and the fetal liver (Tavian and Péault, 2005; Orkin and Zon, 2008). In this section, I will first summarize how hematopoiesis changes locations at different stages of embryonic development until the onset of definitive hematopoiesis in the bone marrow. Next, I will focus on the presence of microglial progenitors in the CNS during development. Finally, I will explore how bone marrow derived cells can contribute to the microglial population perinatally and in adulthood.

1.2.1.2. Developmental origin of microglia

Hematopoiesis, from the Greek *haima* (blood) and *poiēsis* (to produce something), refers to the production of blood cells, including macrophages. Primitive hematopoiesis initiates at around embryonic day 7 in the yolk sac, when erythrocytes and primitive macrophages are produced (Moore and Metcalf, 1970; Palis *et al.*, 1999; Bertrand *et al.*, 2005). These primitive macrophages skip a monocytic intermediate stage, as opposed to adult macrophages (Takahashi, Yamamura, and Naito, 1989). Once the circulatory system is established around embryonic days 8.5 to 10, they colonize the embryo and differentiate to fetal macrophages (McGrath *et al.*, 2003). After embryonic day 8.5, the generation of hematopoietic progenitors also occurs inside the embryo proper around the aorta, gonads, and mesonephros (Godin *et al.*, 1993; Medvinsky *et al.*, 1993). The hematopoietic stem cells generated in these areas colonize the fetal liver together with yolk sac generated hematopoietic progenitors at around embryonic day 10.5 (Kumaravelu *et al.*, 2002) (Figure 1). The fetal liver then generates the definitive hematopoietic progenitors that will settle in the bone marrow and will proceed to generate all adult hematopoietic lineages: erythroid, lymphoid, and myeloid lineages. Erythrocytes and megakaryocytes belong to the erythroid lineage; B and T cells belong to the lymphoid lineage; and neutrophils, basophils, eosinophils, mast cells, dendritic cells, and monocytes belong to the myeloid lineage. Human embryonic hematopoiesis follows a similar dynamic. It begins in the yolk sack around estimated gestational day 19 and continues in the fetal liver at 4-5 weeks of estimated gestational age, before being finally established in the bone marrow at around 10.5 weeks of estimated gestational age (Tavian and Péault, 2005). To summarize, the generation of blood cells and resident macrophages begins in the yolk sac in both rodents and humans. It then relocates to the aorta, gonads, and mesonephros. Finally, it moves to the fetal liver, where the progenitors

for definitive hematopoiesis will be generated. Finally, these progenitors will settle to form the bone marrow to give rise to erythroid, lymphoid, and myeloid cells (Figure 2).

However, microglia and other tissue macrophages do not derive from the bone marrow as initially thought. Therefore, they are not technically considered myeloid cells, even though they share with monocytes and other macrophages many lineage markers such as CD11b, CD45, IBA-1, CX3CR1 (Grassivaro *et al.*, 2020), among others; and similar functions, such as scanning the environment for pathogens, the release of different factors in response to injury, phagocytosis, etc (Andersson *et al.*, 2000; Davalos *et al.*, 2005; Pollard, 2009; Waisman *et al.*, 2015; Grassivaro *et al.*, 2020). The first reports of the presence of microglia in the mouse brain date back to 1990, when Ashwell found them in the fetal cerebellum at embryonic day 11 (Ashwell, 1990). Soon after that, microglial precursors were observed in the neuroepithelium at embryonic day 8.5, suggesting that this could be the earliest stage at which seeding of microglial precursors occurs (Alliot *et al.*, 1991). After the establishment of blood circulation, these microglia precursor cells were found to colonize the embryo using autoradiography of a radioactively labeled nucleotide that integrates into DNA ([3H]-thymidine) (Takahashi and Naito, 1993). Since, at that stage, only yolk sack hematopoiesis occurred, Alliot proposed that these microglial progenitors must originate from the yolk sack. This group then documented the presence of microglial progenitors both in the yolk sack and the brain at around embryonic day 9 (Alliot, et al, 1999). This was later confirmed when cells expressing macrophage and microglial markers (Alliot et al., 1999; Chan et al., 2007; Ginhoux et al., 2010; Mizutani et al., 2012) were observed in the brain rudiment during embryonic development. A similar timeline was also observed in humans. Amoeboid microglial cells entered the ventricular lumen at 4-5 weeks of gestation (Rezaie *et al.*, 2005; Monier *et al.*, 2007). Simultaneously, cells with ramified morphology could be detected in the yolk sack (Janossy *et al.*, 1986). These reports finally shed light on the developmental origin of microglia, demonstrating its yolk sac origin **(Figure 1).**

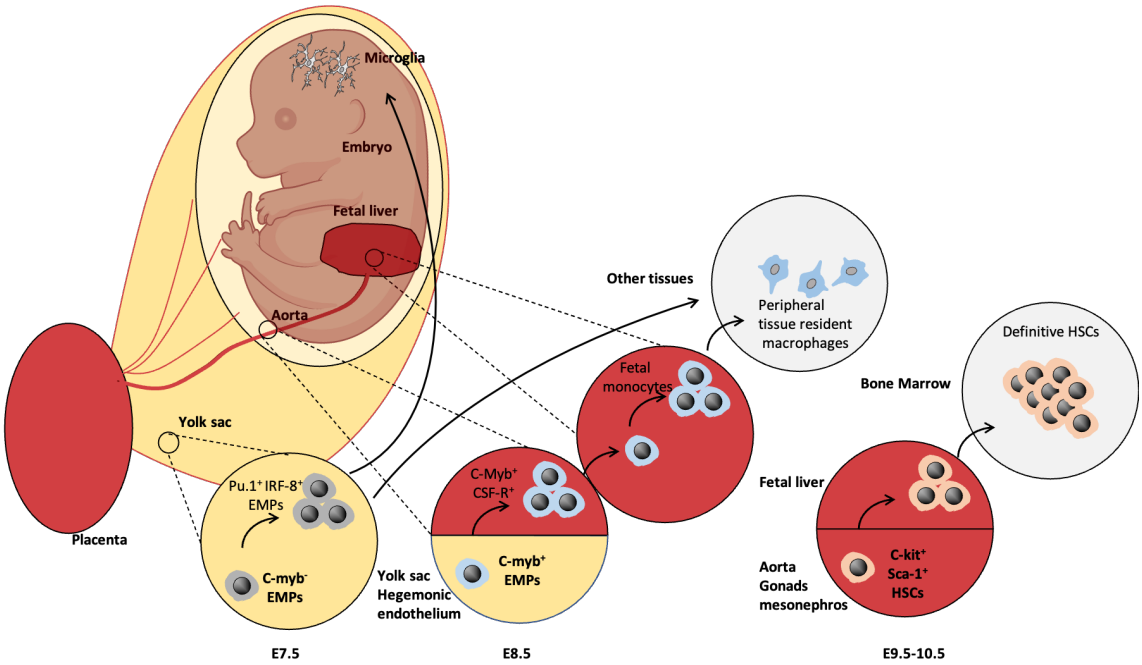

Figure 1. Embryonic origin of microglia and other hematopoietic populations: cartoon depicting the generation of different cell lineages at different time points and their colonization of several structures in the embryo to differentiate into microglia, peripheral tissue macrophages, and hematopoietic stem cells.

After the initial seeding of progenitors, the microglial population rapidly increases in number in the brain after birth (Alliot, et al, 1999; Tambuyzer, et al, 2009). This led many researchers to propose, based on previous literature, that there might be an influx of peripheral monocytes that would contribute to the microglial population. Early studies in the 70s used [3H]-thymidine to label blood cells and track their ingress in the brain parenchyma. In these early experiments, 5 days old rats were injected with [3H]-thymidine, and their brains were analyzed at different time points to track the newly generated cells. The radioactively labelled cells could be found as ameboid cells in the postnatal corpus callosum shortly after [3H]-thymidine administration and, a week later, labelled microglia were found. At the time, these ameboid cells were thought to be blood-derived based on their different morphology compared to ramified microglia, leading to the incorrect conclusion that microglia derived from circulating cells (Imamoto and Leblond, 1978). This was later followed by the use of a model where the expression of Pu.1 is abolished, resulting in a lack of embryonic microglia. Pu.1 is a transcription factor central to the regulation of hematopoiesis. These Pu.1 KO mice were transplanted with wild type bone marrow at birth, which led peripheral macrophages to colonize the brain parenchyma. Once in the brain parenchyma, these peripheral macrophages would differentiate into microglia (Beers *et al.*, 2006). However, the transformation of peripherally generated cells into microglia is now recognized to occur only under either extreme circumstances, such as when the blood brain

barrier (BBB) is compromised (Larochelle *et al.*, 2016), or to be very infrequent, limited in terms of contribution to the total population, and restricted to specific CNS regions (Ling et al., 1980). Further research using intra utero fluorescent labeling of fetal liver hematopoietic precursors has also shown that there is a transient population of fetal liver generated monocytes that can invade the brain parenchyma. These fetal liver generated monocytes are rapidly depleted by apoptosis and do not contribute to the final microglial population (Askew et al., 2017). Therefore, this strongly suggests that microglia originate solely from the yolk sac during embryonic development. Therefore, microglial origin during embryonic development can be traced to erythromyeloid progenitors that arise in the yolk sac with no significant contribution from the fetal liver.

Further studies focused on the long-term maintenance of the microglial population in the adult brain. In order to do so, the influx of bone marrow derived cells in the CNS, and their possible differentiation to microglia for the long-term maintenance of the microglial population was checked. Using [3H]-thymidine incorporation in adult mice, it was found that circulating monocytes could be recruited into the brain parenchyma through the BBB and differentiate into microglia. However, they also reported that resident microglia were also proliferating (Lawson, et al1992), suggesting that both mechanisms could contribute to the maintenance of the microglial population. Similar studies followed using bone marrow transplantation, and it was found that donor cells could be found to differentiate into microglia within the brain of adult mice (Eglitis and Mezey, 1997; Mezey *et al.*, 2000; Simard and Rivest, 2004). However, these studies conflicted with previous data showing little or no contribution to the microglial population in the adult brain from transplanted bone marrow (Matsumoto and Fujiwara, 1987; Lassmann *et al.*, 1993; Priller *et al.*, 2001). Recent studies also show that the engraftment of blood derived macrophages in the CNS results from the opening of the BBB following irradiation for the transplantation of bone marrow (Larochelle *et al.*, 2016). This was further confirmed by the use of parabiosis (fusing the circulatory system of animals), which showed that, when the BBB is undisturbed, no infiltration and engraftment of blood derived cells occurs (Ajami *et al.*, 2007). More recent studies show that the resident population of microglia is only exceptionally supplemented by cells of peripheral origin, such as after CNS lesions (Vallières and Sawchenko, 2003) and in pathological conditions (Zhang et al., 2018). Therefore, we currently consider microglia to be a self-sustaining population with an estimated turnover of 96 days (Askew, et al., 2017; Huang et al., 2018).

1.2.1.3. Transcriptional control of microglial lineage

The unique origin of microglia and their development in the CNS environment confers them a unique transcriptomic profile, distinctly different from other tissue resident macrophages and circulating monocytes. While they express general macrophage markers such as Ionized calcium binding adaptor molecule 1 (IBA1), cluster of differentiation receptors (CD68, CD45, CD11b), C-X3-C Motif Chemokine Receptor 1 (CX3CR1), and high affinity immunoglobulin epsilon receptor subunit gamma (FCGR1A), microglia also specifically express the purinergic receptor P2Y12 and transmembrane protein 119 (TMEM119). In order to acquire their unique transcriptomic signature, they rely on the following transcription factors and environmental signals **(Figure 2)**:

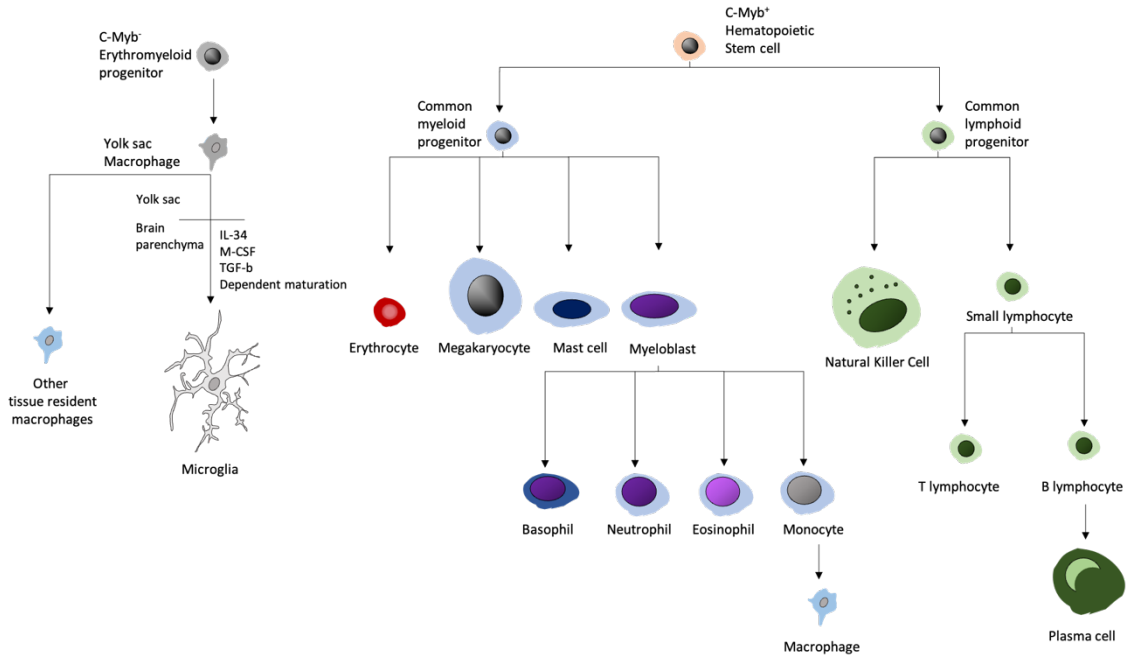

Figure 2. Hematopoietic lineages: cartoon depicting the generation of different hematopoietic populations. In grey, the origin of microglia and other peripheral tissue resident macrophages from C-Myb⁻ erythromyeloid progenitors. In blue, generation of the different myeloid lineages from a common myeloid progenitor. In red, erythropoiesis, or generation of red blood cells. In green, generation of the different lymphoid populations from a common lymphoid progenitor.

1.2.1.3.1. Transcription factors:

Pu.1 is a transcription factor central to regulating hematopoiesis (Kastner and Chan, 2008). Pu.1 determines in a dose-dependent manner the fate that hematopoietic progenitors will follow and their commitment to lymphoid, erythroid, and macrophage lineages (Mak *et al.*, 2011). Pu.1 is highly expressed in mononuclear phagocytes and controls macrophage differentiation and function through the control of expression of CD11b, the receptors for macrophage colony-stimulating factor (M-CSF), and

granulocyte macrophage colony-stimulating factor (GM-CSF), as well as many transcription regulators such as early growth response 1/2 (Egr 1/2) and NGFI-A binding protein 2 (Nab-2) (Laslo *et al.*, 2006), which are crucial for macrophage differentiation. In Pu.1 KO mutants macrophages, microglia and osteoclasts are absent (McKercher *et al.*, 1996).

Irf8 is a transcription factor that works together with Pu.1, driving the differentiation of myeloid progenitors to mononuclear phagocytes while also suppressing the differentiation of these precursors to neutrophils (Tamura, Kurotaki and Koizumi, 2015). Irf8 is primarily expressed in common myeloid progenitors and granulocyte-monocyte progenitors and is highly expressed in the mononuclear phagocyte and dendritic cell lineage (Tamura, Kurotaki and Koizumi, 2015). Abolishing the expression of Irf8 in mice leads to an accumulation of monocyte progenitors that cannot differentiate into the different monocyte/macrophage populations. Lack of Irf8 expression, however, does not completely impede colonization of the CNS by microglia (Horiuchi *et al.*, 2012; Kierdorf *et al.*, 2013). However, lack of Irf8 leads to a decreased expression of the canonical microglial marker IBA1, transcriptional changes in other genes related to microglial function (such as fractalkine receptors and other surface receptors that allow microglia to interact with their environment), changes in morphology and motility (Horiuchi *et al.*, 2012; Minten *et al.*, 2012; Masuda *et al.*, 2014).

Myb is a transcription factor necessary for the generation of hematopoietic stem cells but not for yolk sac hematopoiesis (Schulz et al., 2012). A lack of Myb during embryogenesis results in embryos that develop normally until day 13. However, it leads to a lack of hematopoiesis and death of the embryo by day 15, suggesting that yolk sac hematopoiesis is intact although hematopoiesis in all subsequent locations is abolished (Mucenski *et al.*, 1991). On day 15, however, the populations of cells generated by the yolk sac are still present, including microglia, showing that these cells are generated independently of Myb.

1.2.1.3.2. Environmental cues:

M-CSF is a specific ligand of the colony-stimulating factor-1 receptor (CSF-1R). Signaling through this receptor is required for the development and differentiation of microglia (Ginhoux *et al.*, 2010). M-CSF can change microglial morphology (Lee et al., 1994) and

increase their proliferation and phagocytosis of amyloid beta (Imai and Kohsaka, 2002; Smith *et al.*, 2013). CSF-1R signaling has also been described to be necessary for adult microglial survival, as its antagonists PLX3397 and PLX5622 are currently used as a tool to deplete microglia (Elmore *et al.*, 2014; Dagher *et al.*, 2015). On the other hand, engagement of CSF-1R by M-CSF increases microglial proliferation (Smith et al., 2013).

IL-34 is the only other known ligand for the CSF-1R. It has a similar structure to M-CSF, is present in all vertebrates, and shows high conservation among species (Lin *et al.*, 2008; Garceau *et al.*, 2010). Similar to M-CSF, it activates several signaling pathways that regulate major cellular functions, including proliferation, differentiation, survival, metabolism, and cytokine/chemokine expression, in addition to cellular adhesion and migration (Elmore *et al.*, 2014; Masteller and Wong, 2014; Wu *et al.*, 2018). IL-34 contributes to the development and maintenance of microglia in the brain (Baghdadi *et al.*, 2018). Similar to M-CSF, these effects can be blocked by the antagonists PLX 3397 or PLX5622, leading to microglia depletion.

TGF-β is a family of cytokines that play a role in many cell functions including proliferation, differentiation, migration and metabolism (Morikawa, Derynck and Miyazono, 2016). The lack of TGF-β dependent maturation in mice that do not express TGF-β or its corresponding receptor in microglia results in an increased pro-inflammatory phenotype (Brionne *et al.*, 2003; Zöller *et al.*, 2018). A lack of the TGF-β receptor in microglia has also been shown to produce severe brain abnormalities resulting in spastic motor deficits in mice (Arnold *et al.*, 2019). TGF-β has also been shown to be necessary for the acquisition of a canonical microglial signature both in primary microglia and *in vivo* (Butovsky *et al.*, 2014).

To summarize, microglial precursors develop through Pu.1 and Irf8-dependent pathways (Kierdorf *et al.*, 2013) but in a Myb independent manner, which differentiates them from other mononuclear phagocytes (Hoeffel *et al.*, 2015). Microglial precursors migrate to the CNS after the formation of the embryonic circulatory system, and the blood circulation is established until the BBB formation (McGrath *et al.*, 2003). The settlement of microglia in the brain parenchyma occurs as the CNS undergoes rapid proliferation and expands during development. Microglia progenitors receive environmental cues that trigger their differentiation into microglia (Easley-Neal et al., 2019; Spittau et al., 2020). This maturation process is highly

dependent on CSF1R engagement by IL-34, which is crucial for the migration of the microglial precursors to the neural tube and for the survival of microglia in the CNS, and TGF-β signaling, which controls microglial transcriptional maturation (Spittau et al., 2020).

1.2.1.4. Development of in vitro models

In vitro models of microglia have been used to understand the basic cellular and molecular mechanisms that govern the behavior of these cells. Since microglia is a key target in the treatment of neurodegenerative diseases, these models are of utmost importance in the search for therapies that target microglia. In this section, I will focus on how the development of in vitro models of microglia has progressed to this day.

The first *in vitro* model of microglia was developed in the mid-80s using microglia isolated from early post-natal rat brains (Giulian and Baker, 1986). The development of this model allowed researchers to perform functional studies that were not possible *in vivo*; for example, these experiments showed that microglia were key players in the pathological production and release of cytokines and chemokines (Hetier *et al.*, 1988; Sawada *et al.*, 1989).

The next major development was the immortalization of murine microglia using retroviruses (Blasi *et al.*, 1990). This resulted in the creation of the BV-2 cell line, which is used in many in vitro studies nowadays. Since then, many more immortalized cell lines of microglia were created relying on viral transduction of oncogenes from mice, rat, macaque, and human samples, such as N9, HAPI, HMO6, or SV40, respectively. These cell lines all expressed microglial cell markers and showed functional characteristics that resemble *in vivo* microglia to some extent. They upregulate reactive oxygen and nitrogen oxide species (ROS and RNOS) production and proinflammatory gene expression following stimulation with bacterial lipopolysaccharides (LPS) and are capable of phagocytosing(Timmerman et al., 2018). However, it has become evident that immortalized and primary microglia significantly differ from microglia *in vivo* in terms of their transcriptomic profile and many functional aspects, such as cytokine expression, response to inflammatory stimuli, etc (Butovsky *et al.*, 2014; Melief *et al.*, 2016).

The evolving understanding of microglial ontogeny summarized in the section above has allowed the development of several methods for the production of human stem cell derived microglia-like cells (Muffat *et al.*, 2016; Abud *et al.*, 2017; Douvaras *et al.*, 2017; Haenseler *et al.*, 2017; Pandya *et al.*, 2017). These methods can be either employed with embryonic stem cells (ESCs),

obtained from the inner cell mass of the blastocyst, or with iPSCs reprogrammed from somatic cells using the protocol defined by (Takahashi and Yamanaka, 2006). These methods aim to generate embryonic macrophage precursors that recapitulate the yolk sac ontogeny. Next, I will provide a summary of the protocols mentioned above **(Figure 3)**.

Protocol 1: Muffat et al

Human pluripotent stem cells are treated with collagenase IV, followed by trituration and plating in clumps on low adhesion plates to form embryoid bodies. The same medium is used from day 0 of the differentiation and contains the growth factors M-CSF and IL-34. Stage specific cues for the step wise differentiation to embryonic intermediates are not provided. However, the authors showed that the embryoid bodies form cystic structures from which round vacuolated cells that expressed PU.1 and IBA1 originate. They refer to these cells as microglial precursors. One month after plating these precursors, they start expressing the canonical microglial markers P2Y12 and TMEM119 in addition to IBA1 and CD45. These cells were also co-cultured with neural precursor cells, which made microglia acquire a ramified morphology and shift their transcriptional profile closer to primary microglia.

Protocol 2: Pandya et al

This protocol follows a two-step paradigm. First, iPSCs are maintained in pluripotency media at a low oxygen concentration for two days. Afterward, they are differentiated using a commercially available differentiation medium (STEMdiff) under hypoxic conditions for 15 days. For the first 4 days, the medium is supplemented with the growth factors bone morphogenetic protein 4 (BMP4), stem cell factor (SCF), vascular endothelial growth factor (VEGF), and activin A. After day 4, VEGF and activin A are replaced by IL-3, IL-6, Flt3 ligand, and Granulocyte colony-stimulating factor (G-CSF). On day 15, some cells can be found in the supernatant. These cells are then harvested and plated with human astrocytes and medium supplemented with FBS 10%, IL-3, M-CSF, and GM-CSF for 2 weeks. After the coculture period, these cells start expressing CD11b, CX3CR1, and IBA1. Transcriptional analysis of these cells showed similarities to human fetal microglia but also dendritic cells and macrophages, and the ratio of cells obtained from each iPSC is relatively low (0.8-3 times) when comparing it to the other protocols that are described here.

Protocol 3: Abud et al

In this protocol, iPSCs are differentiated using sequential exposure to stage-specific growth factors to mimic the extracellular signals during embryonic development. During the first 2 days

of differentiation, the medium is supplemented with fibroblast growth factor 2 (FGF2), BMP4, and activin A. From day 2 to day 4, BMP4 and activin A are replaced by VEGF. After day 4, thrombopoietin (TPO), SCF, IL-3, and IL-6 are added alongside FGF2 and VEGF. On day 10, cells start to appear in the supernatant. These cells are then sorted by fluorophore activated cell sorting (FACS) to obtain CD43+ cells. These CD43+ progenitors are then transferred to Matrigel coated plates and cultivated for 28 days under a chemically defined microglia differentiation medium containing M-CSF, IL-34, and TGF-β. During the last 3 days of differentiation, the medium is supplemented with CD200 and CX3CL1. Transcriptomic analysis of these cells shows them clustering with fetal and adult primary microglia and proximity to hematopoietic progenitors at day 10 of the differentiation protocol. Undifferentiated iPSCs, peripheral blood dendritic cells, and monocytes clustered away from microglia obtained with this protocol. The yield of microglia like cells is as high as 30–40 times the starting number of iPSCs, and the purity reaches almost 100%, although the protocol requires FACS to enrich for hematopoietic progenitors.

Protocol 4: Douvaras et al

Here, differentiation of iPSC colonies is induced in commercial media (mTeSR/StemPro) through exposure to stage-specific growth factors to mimic the extracellular signals during embryonic development. During the first 4 days of differentiation, the medium is supplemented with BMP4. On day 4, BMP4 is replaced by FGF2, VEGF, and SCF. From day 6, the medium is supplemented with TPO, Flt3 ligand, IL-3, and M-CSF alongside SCF. After day 14, the medium contains Flt3 ligand, M-CSF, and GM-CSF. From day 25, microglial precursors appear in the supernatant and can be harvested and enriched by FACS or magnetic bead separation (MACS). These precursors can be harvested weekly for up to 1 month. The sorted cells are then transferred to coverslips and cultivated for another 20 days in a chemically defined microglia differentiation medium containing GM-CSF and IL-34. The resulting microglia like cells express canonical microglia markers IBA1, CD11b, CD11c, CX3CR1, P2Y12, and TMEM119. Transcriptomic analysis showed clustering of microglia like cells and primary microglia and their segregation from different types of macrophages.

Protocol 5: Haenseler et al

This protocol uses chemically defined media (mTeSR1) for the culture of iPSCs. Once confluent, these iPSCs are transferred to Aggrewell plates at a concentration of 4 million cells per well and spun down for the formation of embryoid bodies. During the first 4 days, embryoid bodies are cultivated in a commercial mTeSR1 medium supplemented with BMP4, VEGF-A, and SCF. On day

4, embryoid bodies are transferred to flasks and cultivated with the commercially available medium X-VIVO15 supplemented with IL-3 and M-CSF. During 3 weeks, embryoid bodies start developing adherent and cystic structures similar to the ones described by Muffat et al. After 3 weeks, microglial precursors appear in the supernatant and can be harvested for further differentiation in mono- or co- culture. These precursors can be harvested weekly for up to 2 months. These microglial precursors differentiate in medium supplemented with GM-CSF and IL-34. The differentiated microglia display a ramified morphology and the canonical microglial markers CD11b, IBA1, CX3CR1, and P2Y12. Transcriptomic analysis shows these mono- and co-cultured cells clustering with fetal microglia and segregation from peripheral blood derived monocytes. Recently, an optimized version of this protocol has been described (Gutbier *et al.*, 2020). The protocol has been optimized for large scale culture by using an extra step of accumulation of embryonic macrophage precursors, thus, improving the yield from the original protocol.

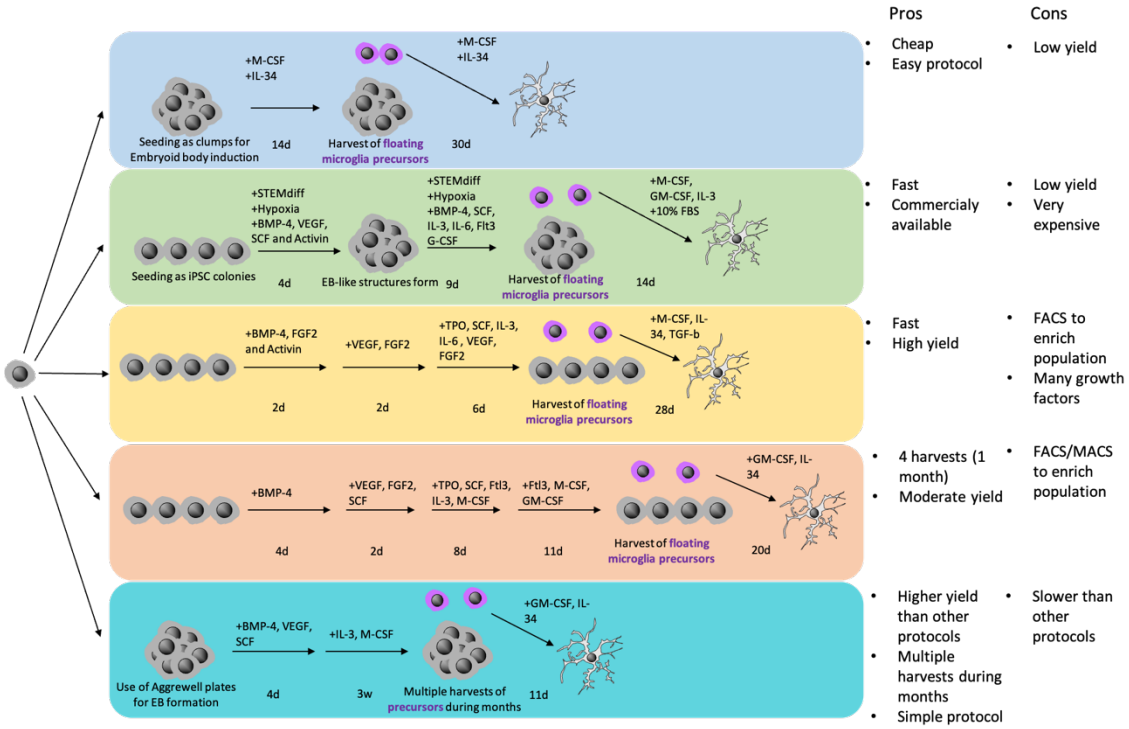

Figure 3. Methods to differentiate microglia from iPSCs: cartoon summarizing the critical steps and components needed for differentiating iPSCs to microglia according to the protocols discussed in this section with a list of pros and cons.

In this thesis, I have focused on building upon the protocol described by Haenseler (Haenseler *et al.*, 2017) and optimized by Gutbier (Gutbier *et al.*, 2020). This protocol was chosen due to the higher yields, simplicity, and scalability that it provides. The optimized protocol by Gutbier also allows the accumulation of microglial progenitors in bioreactors without detrimental effects

on their viability. I built upon these protocols to develop an in vitro model of monoculture microglia from iPSC that resembled adult microglia. This will provide a humanized model to study potential targeting strategies involving microglia in disease and the mechanisms that govern human microglial physiology.

1.2.2. Microglial functions

Microglia, as the main resident immune cells of the brain parenchyma, have to be able to respond rapidly to any disturbances in the environment. In order to do so, they rely on three canonical macrophage main functions: inflammation, motility, and phagocytosis, which will be further explored in the next sections of this PhD Thesis.

1.2.2.1. Inflammation

Microglia are in charge of orchestrating the brain inflammatory response. Inflammation is a mechanism of the innate immune system to protect the organism against harmful stimuli and initiate tissue repair (Lucas, Rothwell, and Gibson, 2006). This process can be triggered by the presence of pathogens and other stimuli. In the CNS, this process is usually triggered by injury, protein aggregates, and environmental toxins (Block and Hong, 2005). When faced with these challenges, microglia respond by releasing a wide variety of factors such as cytokines (pro- and anti- inflammatory), proteins of the complement system, reactive oxygen and nitrogen species, chemokines, prostaglandins, leukotrienes, and trophic factors (Nayak, Roth and McGavern, 2014). Inflammation has been shown to contribute to tissue damage and has been reported in all neurodegenerative diseases (Alzheimer's, Parkinson's, multiple sclerosis, stroke, and epilepsy) (Amor *et al.*, 2010; Vezzani *et al.*, 2011). Different studies have shown the contribution that pro-inflammatory cytokines have to neurodegenerative diseases and how they aggravate the disease progression (Rocha *et al.*, 2012; Zheng, Zhou and Wang, 2016). In this next section, I will explain the classic pro- and anti- inflammatory cytokines and the current understanding of microglial states.

1.2.2.1.1. Pro-inflammatory cytokines

Harmful stimuli are recognized by microglia through pattern recognizing receptors, such as toll like receptors (TLR), nucleotide binding oligomerization domain (nod)-like receptors (NLR), and triggering receptors expressed in myeloid cells (TREM), among others. The activation of these receptors leads to the production of pro-inflammatory cytokines such as interleukin 1 β (IL-1β), interleukin 6 (IL-6), interferon gamma (IFN-γ),

and tumor necrosis factor α (TNF-α) (Vezzani *et al.*, 2011). These cytokines can act in an endocrine, paracrine or autocrine manner and trigger a wide array of responses, from the promotion of infiltration of other immune cells to enhancing the release of other cytokines and chemokines or a pyrogenic response coupled to the release of prostaglandins (Duque and Descoteaux, 2014).

Although the acute pro-inflammatory response is necessary for the protective role of microglia by promoting microglial phagocytosis of protein aggregates (DiCarlo, 2001; Herber *et al.*, 2004), chronic inflammation leads to an impairment of phagocytosis of these aggregates (Mawuenyega *et al.*, 2010; Rangaraju *et al.*, 2018). Phagocytosis of apoptotic cells during acute and chronic inflammation *in vivo*, via LPS or an omega-3 fatty acid deficient diet administration, respectively, has been shown to remain coupled to apoptosis (Abiega *et al.*, 2016). This means that even though there is an increase in the number of apoptotic cells, microglia are able to cope with this increase by increasing the number of apoptotic cells engulfed per microglial cell. Therefore, pro-inflammatory cytokines modulate microglial activity and their response to different stimuli.

1.2.2.1.2. Anti-inflammatory cytokines

Anti-inflammatory cytokines are key for the control of the process of inflammation and the resolution of the inflammatory process (Opal and DePalo, 2000) to prevent the detrimental effects of chronic inflammation (Vezzani, Friedman and Dingledine, 2013). Apart from being an important factor in the development an acquisition of their molecular signature, TGF-β is also an important anti-inflammatory cytokine that induces a protective response in pathological conditions in the brain (Ruocco *et al.*, 1999). TGF-β, along with interleukin 1 and 10 (IL-1 and IL-10), have been shown to decrease antigen presentation by microglia and reduce the release of pro-inflammatory cytokines, chemokines, and RNOS (Aloisi *et al.*, 1999; O'Keefe, Nguyen and Benveniste, 1999).

1.2.2.1.3. Microglial states

Until recently, the states of microglia were classified using the classic terms previously used for macrophages M1 (or pro-inflammatory) and M2 (anti-inflammatory) (Cherry, Olschowka and O'Banion, 2014). This classification was used interchangeably with "activated" (equivalent to M1) or "resting" (equivalent to M2). These terms, however,

have become obsolete since they fail to summarize the diversity of microglial responses (Ransohoff, 2016), which are characterized by distinct molecular signatures (Butovsky *et al.*, 2014; Keren-Shaul *et al.*, 2017; Hammond *et al.*, 2019). These distinct transcriptional states have been described with the onset of single cell transcriptomics and may correspond to context-specific functions. The use of single cell technologies has led to an ever-growing list of microglial states defined by the different clusters observed in these experiments. However, there is a caveat to this approach: the functional properties of many of these clusters remain uncharacterized, and, many times, the relations and differences between the different clusters generated by computational methods are obscured by the very large sets of data and their complex processing. Among the different states displayed by microglia, the disease-associated microglia (DAM) signature has gained attention for its relevance in Alzheimer's disease and will be explored in more detail in the next section. In this thesis, I will focus on the DAM signature since the *in vitro* model I developed has a high expression of TREM-2, which is crucial for acquiring this signature.

1.2.2.1.4. DAM signature

Microglia have been shown to exhibit a distinctly different transcriptomic profile in Alzheimer's disease. More specifically, microglia near amyloid plaques show a marked decrease in homeostatic gene expression (P2Y12, CX3CR1, TMEM119) and an increase in the expression of genes that have been identified as risk factors for Alzheimer's disease (APOE, TREM-2) (Keren-Shaul *et al.*, 2017). The population of microglia that shows this transcriptomic profile was named disease-associated microglia (DAM microglia). This signature shows wide effects on the expression of genes involved in metabolism, motility, and phagocytosis. This signature was originally associated with Alzheimer's disease, but it has been observed in other conditions such as ageing, frontotemporal dementia, and amyotrophic lateral sclerosis (Butovsky and Weiner, 2018). Importantly, TREM2 activity is crucial for the transition of microglia to the DAM state and the clustering of microglia around plaques, and the seeding of amyloid (Parhizkar *et al.*, 2019). Whether this signature is protective or detrimental in the context of disease is still debated and is of key relevance when approaching a treatment for these disorders.

1.2.2.2. Motility

Microglia, and other professional phagocytes (Paterson and Lämmermann, 2022), constantly survey the brain parenchyma by extension and retraction of their highly ramified processes at a speed of about 1.5 µm/min (Nimmerjahn, Kirchhoff and Helmchen, 2005). Microglia continuously extend and retract their processes while maintaining a static cell body. This process requires cytoskeletal rearrangements (Capani et al., 2001), which are triggered by a variety of chemoattractant molecules (Andreasson *et al.*, 2016) acting on a wide repertoire of sensing receptors expressed by microglia (Kettenmann *et al.*, 2011) **(Figure 4).** This mechanism is crucial for microglia to be able to sense and respond rapidly to changes in their environment.

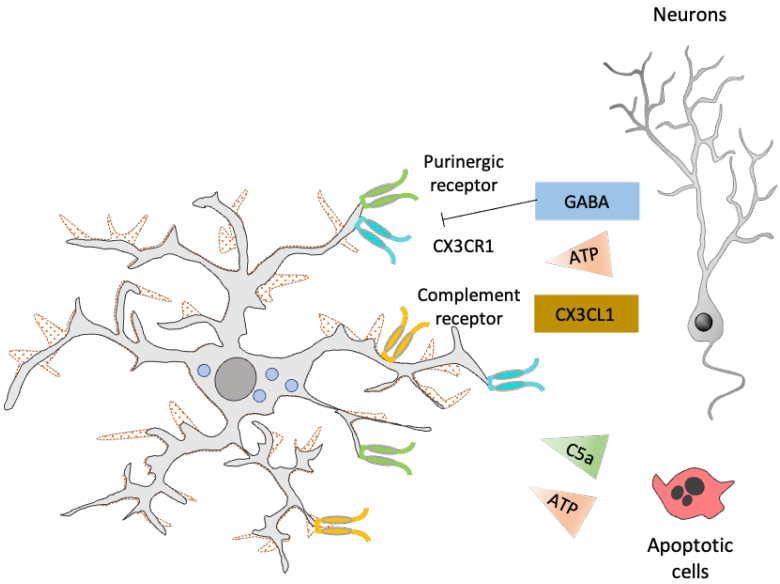

Figure 4. Microglial motility: cartoon depicting the different molecules that can affect microglial motility, together with their sources and the microglial receptors through which they exert their function.

1.2.2.2.1. Signaling mechanisms

<u>Purinergic receptor mediated:</u>

Nucleotides such as adenosine triphosphate (ATP), adenosine diphosphate (ADP), uridine triphosphate (UTP), and uridine diphosphate (UDP) can be released by neurons and astrocytes into the brain parenchyma. These nucleotides can serve both as neurotransmitters in physiological conditions (Burnstock, 2006) and as damage signals from apoptotic cells (Chen, Zhao and Liu, 2014). The gradient generated by the liberation of these nucleotides guides microglial motility through the activation of microglial purinergic receptors (Davalos *et al.*, 2005). Depending on the stimulus, these receptors can be divided into two families: those activated by adenosine (P1 receptors) or by ATP/ADP and UTP/UDP nucleotides (P2 receptors). P2 receptors can also be divided in two subgroups, ionotropic (P2X) and metabotropic (P2Y). The P2Y receptors

are G protein-coupled receptors that mediate microglial motility through K^+ currents and a Ca^{2+}, phospholipase C, and phosphatidylinositol 3 kinase dependent phosphorylation of the secondary messenger Akt (Wu *et al.*, 2007; Wu, Vadakkan and Zhuo, 2007; Madry and Attwell, 2015).

The ADP/ATP receptor P2Y12 is regarded as a microglial-specific protein and has been suggested as a marker of homeostatic microglia (Keren-Shaul *et al.*, 2017). This receptor has been reported to regulate directed motility (Haynes *et al.*, 2006). In addition to affecting motility, many more roles of purinergic signaling are being uncovered. Purinergic signaling has been shown to be critical for the microglia/neuron somatic junction, where microglia contact the soma of neurons to provide support (Cserép *et al.*, 2020). Purinergic signaling has also been shown to be involved in microglia/synaptic patrolling and the modulation of synaptic plasticity (Sipe *et al.*, 2016). Purinergic signaling in microglia has also been shown to contribute to the regulation of cerebral blood flow and neurovascular coupling (Bisht *et al.*, 2021; Császár *et al.*, 2022).

<u>Neurotransmitter mediated</u>:

The main neurotransmitters in the brain, glutamate and gamma-aminobutyric acid (GABA), have been reported to be involved in microglial motility. Experiments performed in retinal explants showed that GABA application decreases motility, and bicuculine (a GABA receptor antagonist) leads to an increase in size and basal velocity of microglial processes (Fontainhas *et al.*, 2011). This group also showed that agonists and antagonists of ionotropic glutamate receptors affect the size and motility of microglial processes. However, it has been reported that microglia do not express ionotropic glutamate receptors (Fontainhas *et al.*, 2011; Eyo *et al.*, 2014). The neurotransmitter norepinephrine has been shown to modulate microglial motility i*n vitro*, in acute slices (Gyoneva and Traynelis, 2013), and *in vivo* (Stowell *et al.*, 2019). This suggests that neurotransmitters can exert a direct activity on microglia in the case of norepinephrine or through an increased release of ATP or other chemotactic compounds due to increased circuit activity.

<u>Fractalkine (CX3CL1)</u>:

Fractalkine is predominantly expressed in neurons in the CNS, and the fractalkine receptor (CX3CR1) is expressed in microglia (Harrison *et al.*, 1998). CX3CL1 can be

cleaved by several proteases to generate a soluble fragment (Garton et al., 2001; Hundhausen et al., 2003; Clark, Yip and Malcangio, 2009), and it can signal in both its membrane-bound and soluble form. The chemotactic activity of CX3CL1 on microglia was first described *in vitro* (Maciejewski-Lenoir *et al.*, 1999). It has been shown that microglia lacking CX3CR1 expression injected in mice brains are not able to migrate into the brain parenchyma when compared to microglia expressing one copy of CX3CR1 (Cardona *et al.*, 2006). It was later described that CX3CR1 knock-out leads to decreased microglial basal motility and migration in retinal explants (Liang *et al.*, 2009).

In addition to the effects of fractalkine on motility, it has also been shown to modulate microglial metabolism (Lauro *et al.*, 2019) and the production of RNOS after an inflammatory challenge (Inoue *et al.*, 2021).

1.2.2.2.2. Measurement of microglial motility

The measurement of microglial motility *in vivo* requires the use of fluorophores, either intrinsic expression by microglia or the administration of fluorophore conjugated lectins (such as tomato lectin) and the use of various imaging modalities such as: multi-photon laser-scanning, lightsheet or confocal microscopy to obtain time-lapse images from brain slices or the brains of living animals. This process generates large files containing 4 dimensionally coded images (XYZ+T) which can be challenging to analyze. The challenges we face when analyzing these sets of images are technical artifacts that must be corrected, such as 3D drift due to animal movements during the experimental procedure, bleaching of the fluorophore during the acquisition procedure, and background signals. The next challenge is the analysis of the images themselves since there are no standardized methods for the analysis of motility in 3D. Most publications have relied on 2D image projections for the analysis of process length (Davalos *et al.*, 2005; Nimmerjahn, Kirchhoff and Helmchen, 2005), tip position (Kondo, Kohsaka and Okabe, 2011; Batti *et al.*, 2016; Fourgeaud *et al.*, 2016), and the area occupied by microglial processes or microglia (Davalos *et al.*, 2005; Fontainhas *et al.*, 2011). However, the use of 2D projections can lead to errors in the measurement of motility due to the three-dimensional nature of microglial motility. Therefore, in this PhD Thesis, we developed a method to measure microglial motility in 3D in a semi-automated manner to provide tools that can help standardize and compare experimental data from different sources.

1.2.2.3. Phagocytosis

Microglia are the professional phagocytes of the brain. Phagocytosis is a sequential process in which several signaling mechanisms govern the activity of microglia. First, microglia have to find the structures to be phagocytosed through directed motility governed by find me signals. Second, microglia have to recognize the structures to be phagocytosed by direct contact in a receptor specific manner for the engulfment of these structures to take place. This second step is governed by eat me signals (Gardai *et al.*, 2006; Peter, Wesselborg and Lauber, 2010). Lastly, these structures will be internalized, forming a phagosome that will fuse with lysosomes for the degradation of its cargo (Park *et al.*, 2011). This process protects the brain against pathogens such as viruses, bacteria, fungi, and parasites (Mariani and Kielian, 2009). However, due to the BBB, which is a physical barrier protecting the CNS, these are rarely the targets of phagocytosis. In the CNS, the most common phagocytic cargo are misfolded proteins (such as amyloid beta), cell debris (such as myelin and axonal debris), and apoptotic cells

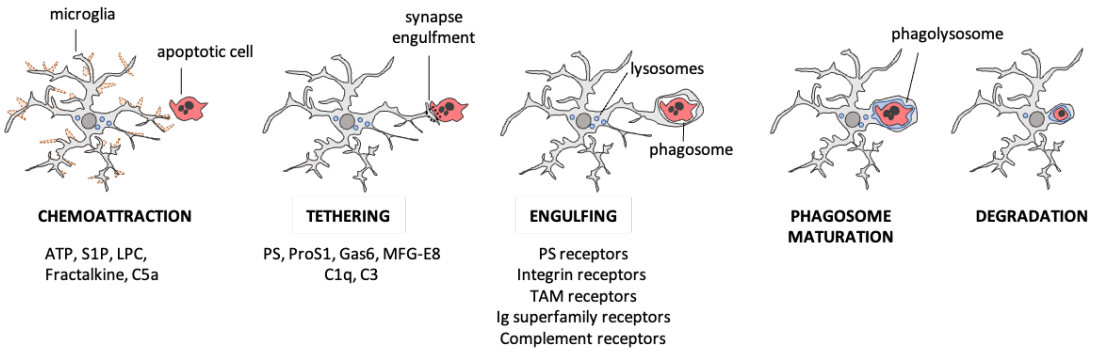

Figure 5. Microglial phagocytosis: cartoon depicting the different stages of microglial phagocytosis of apoptotic cells together with a list of molecules and receptors that are key for the proper functioning of these mechanisms. Modified from (Sierra *et al.*, 2013).

1.2.2.3.1. Types of cargo

Synapses: during development, more synapses are formed than necessary, and microglia are thought to play a role in the selective pruning of synapses (Katz and Shatz, 1996; Hua and Smith, 2004). Synaptic pruning has been suggested to be regulated by the fractalkine (Paolicelli *et al.,* 2011) and complement (Schafer *et al.,* 2012) systems and also the MERTK phagocytic pathways (Chung *et al.,* 2013).

Myelin: myelin debris clearance by microglia is very important for the correct myelination of axons after damage to the myelin sheath (Napoli and Neumann, 2010). It has been shown that clearance of myelin debris and remyelination is severely

impaired (Lampron *et al.*, 2015; Cignarella *et al.*, 2020) in mice lacking CX3CR1 or Triggering receptor expressed in myeloid cells 2 (TREM2) expression.

Amyloid beta: amyloid beta plaque accumulation is the defining criterion for Alzheimer's disease diagnosis, and it has been hypothesized to be the driving force behind disease progression. Microglia have been shown to associate with amyloid plaques in a TREM2 dependent manner. It has been shown that TREM2 deletion leads to plaque accumulation and prevents microglial from migrating to enclose amyloid beta plaques (Ulrich *et al.*, 2014; Yuan *et al.*, 2016).

Apoptotic cells: apoptotic cells expose PS on their membrane surface, which can be recognized by a wide array of receptors such as BAI1, TIM4, and stabilins, or it can be indirectly detected by bridging molecules such as ProS1 and Gas6 that bind to PS to facilitate the recognition of apoptotic cells by microglia for the initiation of TAM receptor mediated phagocytosis (Zhao et al., 2018).

In this PhD Thesis, I will focus on the phagocytosis of apoptotic cells. Apoptosis, or programmed cell death, is the mechanism by which cells that are damaged or are no longer needed die in an orderly manner. Apoptosis occurs through the activation of a caspase cascade. This activation can occur through different mechanisms, but it converges with the activation of caspases 3, 6, and 7, which will result in the cleavage of many different targets and ultimately in the morphological and biochemical changes associated with apoptosis (Maciejewski-Lenoir *et al.*, 1999; Li and Yuan, 2008; Brentnall *et al.*, 2013). These changes include cell shrinkage, nuclear condensation (pyknosis), and fragmentation (karyorrhexis)(Zheng *et al.*, 1998; Ziegler and Groscurth, 2004).

Apoptosis is a very important developmental process. During CNS development, there is extensive apoptosis of both neural and glial cells. Apoptosis has been shown to take place during neural tube closure, and defects in apoptosis have been shown to affect this process in chick (Weil, Jacobson and Raff, 1997), mice (Massa *et al.*, 2009), and human development (Liu *et al.*, 2018; Spellicy *et al.*, 2018; Zhou *et al.*, 2018). Furthermore, apoptosis of cells in signaling centers, such as FGF-8 expressing cells in the rostral anterior neural ridge, has been suggested to be very important for the correct development of the CNS (Nonomura *et al.*, 2013). These apoptotic cells have to be phagocytosed by microglia to maintain homeostasis and prevent inflammatory reactions (Arandjelovic and Ravichandran, 2015). Microglia have been shown to colonize

proliferative zones in rodents and macaques, where they phagocytose apoptotic neural progenitor cells (Cunningham, Martínez-Cerdeño and Noctor, 2013). When phagocytosis is blocked in models lacking phagocytosis receptors such as TREM2, MerTK, and Axl, apoptotic cells accumulate during development (Takahashi, Rochford and Neumann, 2005; Fourgeaud *et al.*, 2016). Microglia are not only limited to phagocytose apoptotic neural cells, as they also phagocytose apoptotic retinal ganglion cells in the embryonic retina shortly after birth (Anderson *et al.*, 2019), and oligodendrocytes within the corpus callosum (Li *et al.*, 2019; Nemes-Baran, White and DeSilva, 2020). Apoptosis also continues to take place in the adult brain in adult neurogenic sites such as the hippocampal dentate gyrus, where the majority of newborn cells undergo apoptosis before integrating into the circuitry (Sierra *et al.*, 2010).

The timely and effective phagocytosis of apoptotic cells by phagocytes is key in preventing the spillover of toxic intracellular compounds since cells undergoing apoptosis maintain the integrity of their plasma membrane up to an advanced stage (Coleman et al., 2001; Sebbagh et al., 2001). As previously mentioned, phagocytosis of apoptotic cells is a sequential process governed by different signals. First, microglia will find the cargo to be phagocytosed through find me signals. Next, microglia will recognize this cargo through eat me signals. Finally, microglia will degrade the cargo. Different types of find me and eat me signals exist and will be further explored in the next section (Figure 5).

1.2.2.3.2. Types of signals

Find me:

Purinergic signaling: nucleotides such as ATP/UTP are released during apoptosis (Elliott *et al.*, 2009). These nucleotides have been shown to exert a strong chemotactic response in microglia *in vivo* (Davalos *et al.*, 2005). The role of purinergic signaling was explored in more detail in the motility section (2.2.1.1).

Sphingosine-1-Phosphate (S1P): S1P is a chemoattractant molecule that has been shown to be produced after the induction of apoptosis (Gude *et al.*, 2008). Microglia have been shown to express all receptors for S1P (S1P1-5), and S1P signaling has been shown to affect microglial morphology *in vivo* (Langeslag and Kress, 2020).

Lysophosphatidylcholine (LPC): LPC is produced by calcium-independent phospholipase A2 after cleavage by caspases during apoptosis (Lauber *et al.*, 2003). This study also showed the chemotactic activity of LPC in vitro. In more recent studies,

injection of LPC in vivo has been shown to lead to an accumulation of microglia around the injection site (Xu *et al.*, 2016; Plastini, Desu and Brambilla, 2020), although LPC at high concentrations can promote apoptosis, which can lead to the release of other chemotactic factors.

Fractalkine (CX3CL1): fractalkine is a well know chemotactic factor released during apoptosis in a caspase dependent manner (Sokolowski *et al.*, 2014). CX3CR1 is the specific receptor for CX3CL1, and it is exclusively expressed in microglia in the brain. The role of fractalkine was explored in further detail in the motility section (2.2.1.1) of this thesis.

Complement system: the complement system is a central part of the innate immune response. It comprises plasma proteins mainly synthesized by the liver and locally in the brain. These proteins can exert a wide variety of functions: the complement proteins C1q and C3 can opsonize pathogens and structures to be phagocytosed, and the complement protein C5a has been shown to be an important chemoattractant molecule (Nolte et al., 1996).

Eat me:

Phosphatidylserine (PS): PS is a phospholipid that becomes exposed on the cell membrane of apoptotic cells (Fadok *et al.*, 1998) for their identification by macrophages either through PS receptors or with the aid of bridging molecules and other supplementary receptors.

Protein S (ProS1) and Gas6: ProS1 and Gas6 are soluble TAM receptor ligands that bind to PS and act as bridging molecules to recognize and engulf apoptotic cells (Lemke and C. v. Rothlin, 2008). MerTK, one of the TAM receptors, is exclusively expressed in microglia in the CNS (Fourgeaud *et al.*, 2016).

Milk fat globule-EGF factor 8 (MFG-E8): MFG-E8 is another soluble factor that binds to PS exposed by apoptotic cells. MFG-E8 bound to PS can then be recognized by integrin receptors in microglia for the phagocytosis of apoptotic cells (Fuller and van Eldik, 2008).

Complement system: C1q and C3 opsonins opsonize structures to be phagocytosed. Opsonized structures can be then recognized by microglia through complement receptor 3 (CR3). C3 has been shown to be involved in synaptic pruning (Schafer *et al.*, 2012) and clearance of myelin debris (Vargas et al., 2010), and amyloid beta (Czirr *et al.*, 2017).

After the find me and eat me process, microglia have to degrade the phagocytosed structure. In order to do so, the phagosome goes through a maturation process in which they fuse with lysosomes to form phagolysosomes (Desjardins *et al.*, 1994). Recently, it has been described that phagosomes are first shrunk in a glucose 6-phosphate transporter (Slc37a2) dependent manner and fuse to a newly described organelle called gastrosome, a process that has been shown to be important for the maintenance of microglial motility and phagocytic function (Villani *et al.*, 2019). Phagolysosomes contain many proteins, such as cathepsins and N-acetyl-beta-glucosaminidase, that degrade the target with the aid of proton pumps that will acidify the lumen of the phagolysosome allowing the activation of these enzymes (Geisow and Evans, 1984; Liu *et al.*, 2008).

The subcellular localization of the phagolysosome when degradation occurs has also been debated. It has been shown in live imaging experiments that phagosomes are transported to the cell soma (Nimmerjahn et al., 2005). It has also been shown in other phagocytes that phagosomes have to be transported to the perinuclear region for their fusion with lysosomes to form phagolysosomes (Marion *et al.*, 2011; Li *et al.*, 2016; Keller, Berghoff and Kress, 2017). This suggests that the cytoskeleton might play a role in the transportation and maturation of phagosomes during the degradation process.

All these different signals and mechanisms are points where microglial phagocytosis can be regulated to affect phagocytic efficiency. Next, I will discuss the functional implications of apoptotic cell phagocytosis in physiological conditions.

1.2.3. Microglial phagocytosis in neurogenic niches

Apoptotic cells are not only produced during development, they can also be found in physiology during the entire lifespan in the neurogenic niches of the brain. In the adult, brain neurogenesis is limited to two regions: the subventricular zone (SVZ), which generates neuronal progenitors that will migrate through the rostral migratory stream to the olfactory bulb (OB), where they will integrate as neurons (Alvarez-Buylla and García-Verdugo, 2002); and the subgranular zone

(SGZ) of the hippocampus, in which newborn cells integrate into the granular cell layer of the dentate gyrus (DG) (Kempermann *et al.*, 2004). In physiological conditions, a large proportion of the SGZ newborn cells will undergo apoptosis (Sierra *et al.*, 2010). Similarly, many newly generated cells in the SVZ undergo apoptosis and are cleared by microglia in a MerTK dependent manner (Fourgeaud *et al.*, 2016). The dynamics of proliferation and apoptotic cell generation in the SGZ are conserved throughout adulthood (Beccari *et al.*, 2017): 40-60% of these newly generated cells undergo apoptosis during a primary critical period from day 2 to 4, followed by a smaller proportion of newly generated cells undergoing apoptosis in the secondary critical periods from day 4 to 10 and days 10 to 30. This constitutive generation of apoptotic cells has proven to be very useful to characterize the baseline phagocytic activity of microglia and its efficiency, with 90% of all newborn apoptotic cells being engulfed by microglia and cleared from the parenchyma in under 1.5h (Sierra *et al.*, 2010). In this PhD thesis, I will focus on the consequences that the lack of phagocytosis has on the adult neurogenic niche of the SGZ. In the next section, I will first describe the cellular composition of the adult neurogenic niches, then I will focus on the role of microglia in the elimination of the apoptotic cells that are generated in the neurogenic niches, and lastly on the effects that microglia can exert in the neural progenitor pool.

1.2.3.1. Adult hippocampal neurogenic niche

Neurogenesis occurs primarily in two areas of the adult brain (the SVZ and the SGZ) in various species including humans (Eriksson *et al.*, 1998; Ming and Song, 2011; Spalding *et al.*, 2013; Hevner, 2016). However, there is currently conflicting literature regarding the persistence of neurogenesis in humans during aging, with reports stating that it persists until late age (Boldrini *et al.*, 2018) and reports that claim that it is absent after childhood (Sorrells *et al.*, 2018). Importantly, in the context of Alzheimer's disease and other neurodegenerative diseases, it has been shown that although adult hippocampal neurogenesis persists, it results in the generation of neurons that show anatomical and functional differences (Teixeira *et al.*, 2018; J. Terreros-Roncal *et al.*, 2021). In the SVZ, neuroblasts are generated in the anterior part of the SVZ and migrate through the rostral migratory stream to the OB, where they differentiate into interneurons (Whitman and Greer, 2007). In the murine hippocampus, where my PhD Thesis focuses, neurogenesis has been shown to occur throughout the entire life of an organism. These newly generated neurons originate from neural stem cells called radial neuroprogenitors (rNPCs). rNPCs are a population of multipotent cells capable of generating neurons and astrocytes. rNPCs have a radial process that extends through the granule cell layer and express nestin, glial fibrillary acidic protein (GFAP), and Sox2 (Kempermann *et al.*, 2004). The behaviour

of rNPCs is still a matter of debate. It is currently debated if they can self-renew to maintain the rNPC pool during the entire life of the organism (Bonaguidi *et al.*, 2011) if they don't have that capability and this pool gets reduced during aging (Encinas *et al.*, 2011; Martín-Suárez *et al.*, 2019) or if there are subsets of rNPCs that can return to a resting state (Urbán *et al.*, 2016; Harris *et al.*, 2021). Regardless of their fate, rNPCs generate amplifying neural progenitor cells (ANPs) that have a bipolar morphology and express Tbr2 and doublecortin (DCX). They undergo rapid symmetrical proliferation to generate neuroblasts and a copy of themselves. These neuroblasts migrate to the GCL of the DG, where they will mature and integrate into the circuitry (Sun *et al.*, 2015).

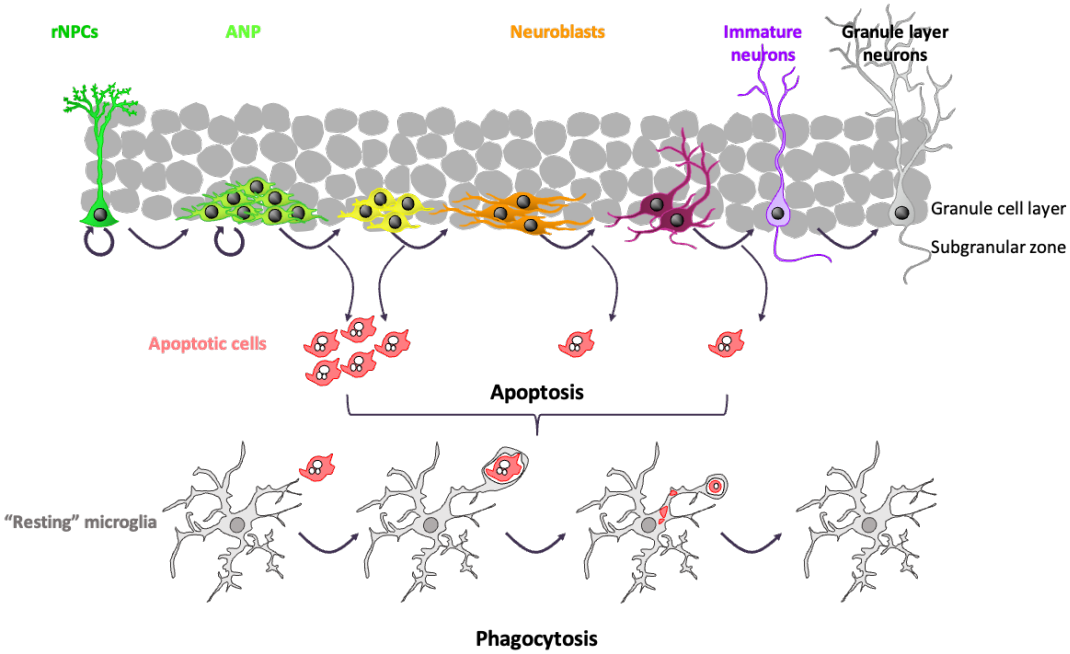

Figure 6. Microglia in the neurogenic niche of the SGZ: cartoon depicting the different cellular populations of the adult neurogenic niche of the SGZ of the hippocampus. The generation of apoptotic cells from newborn cells and their elimination by microglia through phagocytosis is also depicted here. Modified from (Encinas and Sierra, 2012).

Adult hippocampal neurogenesis has been shown to be involved in learning and memory (Deng, Aimone, and Gage, 2010), spatial and object recognition (Jessberger *et al.*, 2009), fear conditioning and synaptic plasticity (Saxe *et al.*, 2006), and pattern separation (Sahay *et al.*, 2011; Toda *et al.*, 2019). Importantly, adult hippocampal neurogenesis dramatically decreases in patients suffering from neurodegenerative diseases such as Alzheimer's, frontotemporal dementia, Parkinson's disease, etc., when compared to healthy individuals (Moreno-Jiménez *et al.*, 2019; J Terreros-Roncal *et al.*, 2021). Thus, it is important to understand the relationship between neurogenesis and microglia since neurogenesis has been shown to be negatively

affected in patients of these diseases, and microglia is one of the key players in neurodegenerative diseases.

1.2.3.2. Microglia in adult neurogenesis

There is growing evidence that microglia can affect neurogenesis through various mechanisms: first, through direct interactions with neurons, microglia have been proposed to engulf synaptic spines, physically modulate synaptic activity, and affect the growth of both axons and synaptic spines. Second, through the release of various factors, it has been proposed that microglia can influence the proliferation, survival, differentiation, and integration of newly generated neurons into the hippocampal circuitry. (Rodríguez-Iglesias, Sierra and Valero, 2019).

Microglia released factors have been shown to have an effect on the migration and differentiation of NPCs in vitro. (Aarum *et al.*, 2003) and the proliferation of neural progenitors in vitro (Aarum et al., 2003). Such microglia-released factors that can influence neurogenesis include neuronal growth factor (NGF) and transforming growth factor β (TGF-β), which have been shown to be produced by phagocytic microglia in vitro (de Simone et al., 2003), along with insulin growth factor-1 (IGF-1) and tumor necrosis factor α (TNF-α) (Butovsky *et al.*, 2006), among others. Proliferation of NPCs in vivo has been shown to be affected in an IL-1β dependent manner by modulating microglial activity through CX3CR1 (Bachstetter *et al.*, 2011). Microglia have also been shown to modulate neurogenesis in a TGF-β dependent manner (Battista *et al.*, 2006; Wachs *et al.*, 2006; de Lucia *et al.*, 2016). When challenged by a pro-inflammatory stimulus such as bacterial lipopolysaccharide (LPS), microglia have been shown to have a detrimental effect on neurogenesis (Ekdahl et al., 2003; Monje, Toda, and Palmer, 2003). All these data taken together suggest that microglia released factors, some of which are induced after phagocytosis, play a role in the regulation of adult neurogenesis. However, most of these experiments were performed in vitro, and there are only a few reports on microglia's effects on neurogenesis in vivo. The PhD thesis of Irune Diaz-Aparicio, 2019, already shows that microglial phagocytosis triggers a transcriptional switch in microglia, which results in an upregulation of, among others, neurogenesis related genes **(Figure 7)**. We also show that conditioned media from phagocytic microglia have an effect on the growth and differentiation of neurospheres *in vitro*. Therefore, in this PhD thesis, I will focus on how a blockade of microglial phagocytosis affects neurogenesis in the adult hippocampal neurogenic niche.

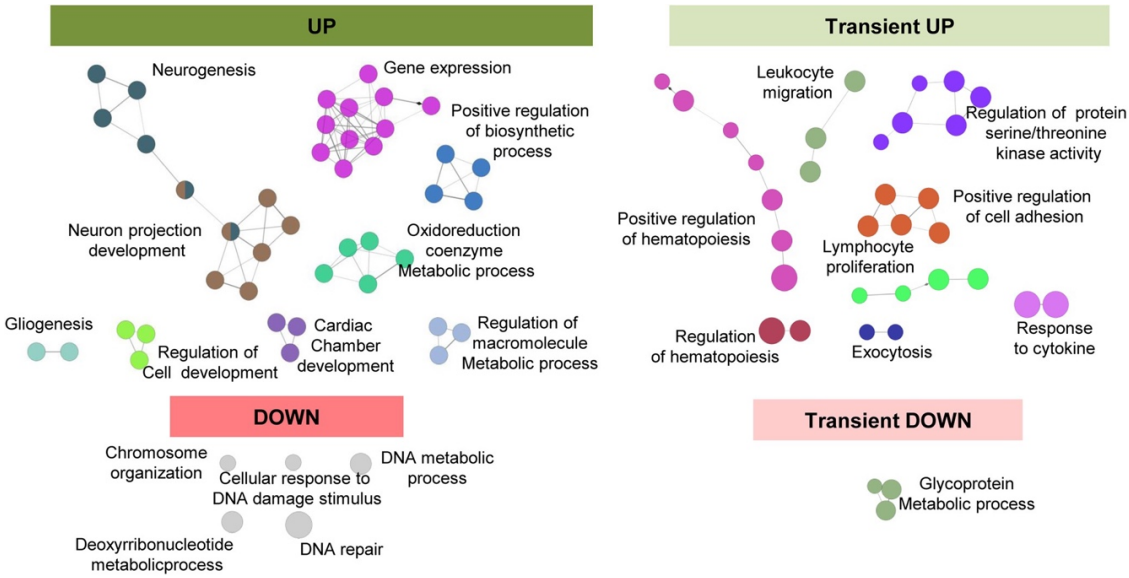

Figure 7. Functions significantly changed in phagocytic microglia: chart showing the interactions between the functions that are significantly changed in microglia after a phagocytic challenge in vitro. Each color depicts a different biological function, and the size of each node depicts enrichment. Taken from (Diaz-Aparicio *et al.*, 2020). Note the upregulation of "Neurogenesis" and "Neuron projection development" genes in phagocytic microglia.

1.3. Hypothesis and objectives

Each of the articles that comprise this thesis responds to a hypothesis regarding the behavior and nature of microglia

Hypothesis 1. Microglia-like cells can be obtained in monoculture from iPSCs mimicking developmental cues.

Objectives:

- Optimize a culture protocol to obtain monoculture microglia
- Characterize human iPSC derived microglia-like cells

This hypothesis and objectives are tackled in (Reich *et al.*, 2021).

Hypothesis 2. The automated measurement of microglial motility in 3D gives more robust and precise data than the manual analysis of 2D projections

Objectives:

- Develop a set of macros to analyze microglial process motility
- Demonstrate that data obtained with our macros are more robust than manually obtained data: Compare 3D vs 2D and Automated vs Manual

This hypothesis and objectives are tackled in (Paris *et al.*, 2018).

Hypothesis 3. Microglial phagocytosis impairment in the neurogenic niche has effects on adult neurogenesis

Objectives:

- Analyze phagocytosis impairment in MerTK and P2Y12 KO mice
- Analyze the effects that it has on proliferation and survival in the neurogenic niche

This hypothesis and objectives are tackled in (Diaz-Aparicio *et al.*, 2020).

1.4. Summary

In this PhD Thesis, we have tackled three major aspects and the development of tools to study microglial physiology. First, we generated a human model of monoculture microglia and its characterization. Secondly, we generated a method for the automated and unbiased measurement of microglial motility. Finally, we have shown that a blockade of microglial phagocytosis has a detrimental effect on the adult neurogenic niche of the hippocampus.

In Reich and Paris, et al 2021, we describe the optimization of a protocol to generate iPSC derived microglia in monoculture and the characterization of these cells. We build upon the protocol previously described by (Gutbier *et al.*, 2020), in which myeloid progenitors can be obtained on a large scale and differentiated to microglia-like cells for 14 additional days. The method we describe differs from other previously published mono- and co-culture methods on the expression level of TREM2 by microglia, which is higher in our method. The functional impact of increased TREM2 levels was tackled by comparing wild type with isogenic TREM2 KO cells in functional assays and gene expression analysis. We show that these monoculture microglia express the canonical microglial markers P2Y12 and CX3CR1; they are able to phagocytose apoptotic cells, amyloid beta coated beads, and yeast particles; and show Ca^{2+} activity after stimulation with ATP, ADP, and C5a. This model is particularly useful for mechanistic studies in Alzheimer's disease due to their expression of TREM2, which is particularly relevant in the context of this pathology.

In Paris, et al 2017, We describe a set of tools that allow the automatic analysis of microglial process motility in 3D. An earlier version of these tools was previously used to demonstrate reduced microglial process motility in a model of murine mesial temporal lobe epilepsy (Abiega *et al.*, 2016). The data obtained with this tool was validated by comparing it with data obtained by manually measuring process motility in 3D. In order to calculate process motility, we used the measurement of process length and tip position at every time point. The results obtained showed that ProMoIJ was faster and less sensitive to experimenter bias than manual analysis. The data obtained from this automated analysis was also compared with motility data obtained from 2D projections (maximum projection) of the same set of images that were used for the 3D analysis. This was done because the most commonly used methods of process motility rely on 2D projections to simplify and expedite the analysis. Furthermore, these analyses are often non-comparable, given that they can often rely on different parameters. In addition, we found that data obtained from 2D projections significantly underestimates microglial process motility.

Furthermore, we can obtain very valuable biologically relevant data, such as tip position and process length at every time point, which allows us to calculate its velocity and directionality towards or away from a lesion.

Furthermore, we analyzed the effects that systemic inflammation has on microglial process motility using ProMoIJ. Previous studies showed very different results after administration of LPS, reporting either no changes or increased process motility. Our analysis determined that there was a small reduction in process motility, likely to be missed when using manual 2D analysis. Inflammation is known to be exacerbated in neurodegenerative diseases, and further experiments to explore the relationship between microglial process motility and these diseases would be necessary to determine if this could be a potential therapeutic target.

In summary, we have created and shared with the community a set of tools for the semi-automated analysis of microglial process motility with high reproducibility and reduced experimenter bias. We have also shown that microglial process motility is reduced during inflammation.

In Diaz-Aparicio, et al 2020, we explored the role that microglial phagocytosis of apoptotic cells has on the adult neurogenic niche of the subgranular zone of the hippocampus. In order to do so, we relied on both constitutive and inducible KO of different receptors that have been previously reported to be involved in phagocytosis. We further explored the transcriptional changes that microglia undergo after the phagocytosis of apoptotic cells *in vitro* and the effects that their secretome exerts on neural progenitor cells.

Using constitutive KOs for P2Y12 and MerTK/Axl, previously shown to be involved in the find-me and eat-me stages of phagocytosis, we show that they exhibit a decreased phagocytic index. This disruption in phagocytosis leads to a decrease in neurogenesis. However, it is important to remark that these receptors regulate various features of microglial physiology and that a chronic accumulation of apoptotic cells could also affect the neurogenic cascade itself. Therefore, we also used an inducible KO model for MerTK, in which MerTK expression was abolished after tamoxifen injection. The acute effects of the lack of expression of this receptor led to an even greater decrease in microglial phagocytosis and a transient increase in proliferation in the neurogenic niche. This effect was, however, reversed when analyzing the yield of the early proliferative cells at a later time point. Considering all these findings, we hypothesize that

microglia is part of a regulatory feedback loop that maintains homeostasis in the adult neurogenic niche to preserve the rNSCs population and avoid their early exhaustion.

In order to further explore the role that microglia have on neurogenesis, we used our model of in vitro phagocytosis and performed a transcriptomic analysis. This analysis revealed that phagocytosis of apoptotic cells induced a modulatory phenotype in microglia that was related to their secretome. The main ones being genes that encode secreted proteins such as VGF, VEGF, and FGF2, which had already been described to play a role in the regulation of neurogenesis by microglia. Additionally, other secreted factors may contribute to the regulation of neurogenesis, such as the horizontal transmission of mRNA from microglia to the cells of the neurogenic niche, metabolites, and extracellular vesicles. To follow up on this, we harvested the media of this phagocytic microglia and administered it to NPC cultures and in vivo using osmotic pumps. The administration of this secretome resulted in a decrease in neurogenesis both in-vivo and in-vitro.

To summarize, blocking microglial phagocytosis leads to deregulation in adult neurogenesis in which there is an early increase in proliferation that is not translated to higher integration of these newborn cells as mature granule cell layer neurons (a decrease in survival of these newborn cells). The release of factors by phagocytic microglia and their effect on neurogenesis should be considered when designing therapies for neurodegenerative diseases since adult hippocampal neurogenesis is known to be affected by both neurodegenerative diseases and, as shown in this project, impaired microglial phagocytosis.

1.5. Bibliography

Aarum, J. *et al.* (2003) 'Migration and differentiation of neural precursor cells can be directed by microglia', *Proceedings of the National Academy of Sciences*, 100(26), pp. 15983–15988. Available at: https://doi.org/10.1073/pnas.2237050100.

Abiega, O. *et al.* (2016) 'Neuronal Hyperactivity Disturbs ATP Microgradients, Impairs Microglial Motility, and Reduces Phagocytic Receptor Expression Triggering Apoptosis/Microglial Phagocytosis Uncoupling', *PLoS Biology*, 14(5). Available at: https://doi.org/10.1371/journal.pbio.1002466.

Abud, E.M. *et al.* (2017) 'iPSC-Derived Human Microglia-like Cells to Study Neurological Diseases', *Neuron*, 94(2), pp. 278-293.e9. Available at: https://doi.org/10.1016/j.neuron.2017.03.042.

Ajami, B. *et al.* (2007) 'Local self-renewal can sustain CNS microglia maintenance and function throughout adult life', *Nature Neuroscience*, 10(12), pp. 1538–1543. Available at: https://doi.org/10.1038/nn2014.

Alliot, F. *et al.* (1991) 'Microglial progenitors with a high proliferative potential in the embryonic and adult mouse brain', *Proceedings of the National Academy of Sciences of the United States of America*, 88(4), pp. 1541–1545. Available at: https://doi.org/10.1073/pnas.88.4.1541.

Alliot, F., Godin, I. and Pessac, B. (1999) 'Microglia derive from progenitors, originating from the yolk sac, and which proliferate in the brain', *Developmental Brain Research*, 117(2), pp. 145–152. Available at: https://doi.org/10.1016/S0165-3806(99)00113-3.

Aloisi, F. *et al.* (1999) 'Opposite effects of interferon-γ and prostaglandin E2 on tumor necrosis factor and interleukin-10 production in microglia: A regulatory loop controlling microglia pro- and anti-inflammatory activities', *Journal of Neuroscience Research*, 56(6), pp. 571–580. Available at: https://doi.org/10.1002/(SICI)1097-4547(19990615)56:6<571::AID-JNR3>3.0.CO;2-P.

Alvarez-Buylla, A. and García-Verdugo, J.M. (2002) 'Neurogenesis in Adult Subventricular Zone', *The Journal of Neuroscience*, 22(3), pp. 629–634. Available at: https://doi.org/10.1523/JNEUROSCI.22-03-00629.2002.

Amor, S. *et al.* (2010) 'Inflammation in neurodegenerative diseases', *Immunology*, pp. 154–169. Available at: https://doi.org/10.1111/j.1365-2567.2009.03225.x.

Anderson, S.R. *et al.* (2019) 'Complement targets newborn retinal ganglion cells for phagocytic elimination by microglia', *Journal of Neuroscience*, 39(11), pp. 2025–2040. Available at: https://doi.org/10.1523/JNEUROSCI.1854-18.2018.

Andersson, U. *et al.* (2000) 'High Mobility Group 1 Protein (Hmg-1) Stimulates Proinflammatory Cytokine Synthesis in Human Monocytes', *Journal of Experimental Medicine*, 192(4), pp. 565–570. Available at: https://doi.org/10.1084/jem.192.4.565.

Andreasson, K.I. *et al.* (2016) 'Targeting innate immunity for neurodegenerative disorders of the central nervous system', *Journal of Neurochemistry*. Blackwell Publishing Ltd, pp. 653–693. Available at: https://doi.org/10.1111/jnc.13667.

Arandjelovic, S. and Ravichandran, K.S. (2015) 'Phagocytosis of apoptotic cells in homeostasis', *Nature Immunology*. Nature Publishing Group, pp. 907–917. Available at: https://doi.org/10.1038/ni.3253.

Arnold, T.D. *et al.* (2019) 'Impaired αVβ8 and TGFβ signaling lead to microglial dysmaturation and neuromotor dysfunction', *Journal of Experimental Medicine*, 216(4), pp. 900–915. Available at: https://doi.org/10.1084/jem.20181290.

Ashwell, K. (1990) 'Microglia and cell death in the developing mouse cerebellum', *Developmental Brain Research*, 55(2), pp. 219–230. Available at: https://doi.org/10.1016/0165-3806(90)90203-B.

Askew, K., Li, K., Olmos-Alonso, A., Garcia-Moreno, F., Liang, Y., Richardson, P., Tipton, T., Chapman, Mark A, *et al.* (2017) 'Coupled Proliferation and Apoptosis Maintain the Rapid Turnover of Microglia in the Adult Brain', *Cell reports*, 18(2), pp. 391–405. Available at: https://doi.org/10.1016/j.celrep.2016.12.041.

Askew, K., Li, K., Olmos-Alonso, A., Garcia-Moreno, F., Liang, Y., Richardson, P., Tipton, T., Chapman, Mark A., *et al.* (2017) 'Coupled Proliferation and Apoptosis Maintain the Rapid Turnover of Microglia in the Adult Brain', *Cell Reports*, 18(2), pp. 391–405. Available at: https://doi.org/10.1016/j.celrep.2016.12.041.

Bachstetter, A.D. *et al.* (2011) 'Fractalkine and CX 3CR1 regulate hippocampal neurogenesis in adult and aged rats', *Neurobiology of Aging*, 32(11), pp. 2030–2044. Available at: https://doi.org/10.1016/j.neurobiolaging.2009.11.022.

Baghdadi, M. *et al.* (2018) 'Interleukin-34, a comprehensive review', *Journal of Leukocyte Biology*. John Wiley and Sons Inc., pp. 931–951. Available at: https://doi.org/10.1002/JLB.MR1117-457R.

Batti, L. *et al.* (2016) 'TMEM16F Regulates Spinal Microglial Function in Neuropathic Pain States', *Cell Reports*, 15(12), pp. 2608–2615. Available at: https://doi.org/10.1016/j.celrep.2016.05.039.

Battista, D. *et al.* (2006) 'Neurogenic niche modulation by activated microglia: transforming growth factor β increases neurogenesis in the adult dentate gyrus', *European Journal of Neuroscience*, 23(1), pp. 83–93. Available at: https://doi.org/https://doi.org/10.1111/j.1460-9568.2005.04539.x.

Beccari, S. *et al.* (2017) 'A simulation model of neuroprogenitor proliferation dynamics predicts age-related loss of hippocampal neurogenesis but not astrogenesis', *Scientific Reports*, 7(1). Available at: https://doi.org/10.1038/s41598-017-16466-3.

Beers, D.R. *et al.* (2006) 'Wild-type microglia extend survival in PU.1 knockout mice with familial amyotrophic lateral sclerosis', *Proceedings of the National Academy of Sciences of the*

United States of America, 103(43), pp. 16021–16026. Available at: https://doi.org/10.1073/pnas.0607423103.

Bertrand, J.Y. *et al.* (2005) 'Three pathways to mature macrophages in the early mouse yolk sac', *Blood*, 106(9), pp. 3004–3011. Available at: https://doi.org/10.1182/blood-2005-02-0461.

Bisht, K. *et al.* (2021) 'Capillary-associated microglia regulate vascular structure and function through PANX1-P2RY12 coupling in mice', *Nature Communications*, 12(1). Available at: https://doi.org/10.1038/s41467-021-25590-8.

Blasi, E. *et al.* (1990) 'Immortalization of murine microglial cells by a v-raf / v-myc carrying retrovirus', *Journal of Neuroimmunology*, 27(2–3), pp. 229–237. Available at: https://doi.org/10.1016/0165-5728(90)90073-V.

Block, M.L. and Hong, J.-S. (2005) 'Microglia and inflammation-mediated neurodegeneration: Multiple triggers with a common mechanism', *Progress in Neurobiology*, 76(2), pp. 77–98. Available at: https://doi.org/https://doi.org/10.1016/j.pneurobio.2005.06.004.

Boldrini, M. *et al.* (2018) 'Human Hippocampal Neurogenesis Persists throughout Aging', *Cell Stem Cell*, 22(4), pp. 589-599.e5. Available at: https://doi.org/10.1016/j.stem.2018.03.015.

Brentnall, M. *et al.* (2013) 'Caspase-9, caspase-3 and caspase-7 have distinct roles during intrinsic apoptosis', *BMC Cell Biology*, 14(1). Available at: https://doi.org/10.1186/1471-2121-14-32.

Brionne, T.C. *et al.* (2003) 'Loss of TGF-β1 Leads to Increased Neuronal Cell Death and Microgliosis in Mouse Brain', *Neuron*, 40(6), pp. 1133–1145. Available at: https://doi.org/10.1016/S0896-6273(03)00766-9.

Burnstock, G. (2006) 'Historical review: ATP as a neurotransmitter', *Trends in Pharmacological Sciences*, 27(3), pp. 166–176. Available at: https://doi.org/10.1016/j.tips.2006.01.005.

Butovsky, O. *et al.* (2006) 'Microglia activated by IL-4 or IFN-γ differentially induce neurogenesis and oligodendrogenesis from adult stem/progenitor cells', *Molecular and Cellular Neuroscience*, 31(1), pp. 149–160. Available at: https://doi.org/https://doi.org/10.1016/j.mcn.2005.10.006.

Butovsky, O. *et al.* (2014) 'Identification of a unique TGF-β-dependent molecular and functional signature in microglia', *Nature Neuroscience*, 17(1), pp. 131–143. Available at: https://doi.org/10.1038/nn.3599.

Butovsky, O. and Weiner, H.L. (2018) 'Microglial signatures and their role in health and disease', *Nature Reviews Neuroscience*. Nature Publishing Group, pp. 622–635. Available at: https://doi.org/10.1038/s41583-018-0057-5.

Capani, F., Ellisman, M.H. and Martone, M.E. (2001) 'Filamentous actin is concentrated in specific subpopulations of neuronal and glial structures in rat central nervous system', *Brain Research*, 923(1), pp. 1–11. Available at: https://doi.org/https://doi.org/10.1016/S0006-8993(01)03189-4.

Cardona, A.E. *et al.* (2006) 'Control of microglial neurotoxicity by the fractalkine receptor', *Nature Neuroscience*, 9(7), pp. 917–924. Available at: https://doi.org/10.1038/nn1715.

Chan, W.Y., Kohsaka, S. and Rezaie, P. (2007) 'The origin and cell lineage of microglia-New concepts', *Brain Research Reviews*, 53(2), pp. 344–354. Available at: https://doi.org/10.1016/j.brainresrev.2006.11.002.

Chen, J., Zhao, Y. and Liu, Y. (2014) 'The role of nucleotides and purinergic signaling in apoptotic cell clearance - implications for chronic inflammatory diseases', *Frontiers in Immunology*, 5(DEC). Available at: https://doi.org/10.3389/fimmu.2014.00656.

Cherry, J.D., Olschowka, J.A. and O'Banion, M.K. (2014) 'Neuroinflammation and M2 microglia: The good, the bad, and the inflamed', *Journal of Neuroinflammation*. BioMed Central Ltd. Available at: https://doi.org/10.1186/1742-2094-11-98.

Cignarella, F. *et al.* (2020) 'TREM2 activation on microglia promotes myelin debris clearance and remyelination in a model of multiple sclerosis', *Acta Neuropathologica*, 140(4), pp. 513–534. Available at: https://doi.org/10.1007/s00401-020-02193-z.

Clark, A.K., Yip, P.K. and Malcangio, M. (2009) 'The liberation of fractalkine in the dorsal horn requires microglial cathepsin S', *Journal of Neuroscience*, 29(21), pp. 6945–6954. Available at: https://doi.org/10.1523/JNEUROSCI.0828-09.2009.

Cruchaga, C. *et al.* (2013) 'GWAS of cerebrospinal fluid tau levels identifies risk variants for alzheimer's disease', *Neuron*, 78(2), pp. 256–268. Available at: https://doi.org/10.1016/j.neuron.2013.02.026.

Császár, E. *et al.* (2022) 'Microglia modulate blood flow, neurovascular coupling, and hypoperfusion via purinergic actions', *Journal of Experimental Medicine*, 219(3). Available at: https://doi.org/10.1084/jem.20211071.

Cserép, C. *et al.* (2020) 'Microglia monitor and protect neuronal function through specialized somatic purinergic junctions', *Science*, 367(6477), pp. 528–537. Available at: https://doi.org/10.1126/science.aax6752.

Cunningham, C.L., Martínez-Cerdeño, V. and Noctor, S.C. (2013) 'Microglia regulate the number of neural precursor cells in the developing cerebral cortex', *Journal of Neuroscience*, 33(10), pp. 4216–4233. Available at: https://doi.org/10.1523/JNEUROSCI.3441-12.2013.

Czirr, E. *et al.* (2017) 'Microglial complement receptor 3 regulates brain Aβ levels through secreted proteolytic activity', *Journal of Experimental Medicine*, 214(4), pp. 1081–1092. Available at: https://doi.org/10.1084/jem.20162011.

Dagher, N.N. *et al.* (2015) 'Colony-stimulating factor 1 receptor inhibition prevents microglial plaque association and improves cognition in 3xTg-AD mice', *Journal of Neuroinflammation*, 12(1). Available at: https://doi.org/10.1186/s12974-015-0366-9.

Davalos, D. *et al.* (2005) 'ATP mediates rapid microglial response to local brain injury in vivo', *Nature Neuroscience*, 8(6), pp. 752–758. Available at: https://doi.org/10.1038/nn1472.

Deng, W., Aimone, J.B. and Gage, F.H. (2010) 'New neurons and new memories: How does adult hippocampal neurogenesis affect learning and memory?', *Nature Reviews Neuroscience*, pp. 339–350. Available at: https://doi.org/10.1038/nrn2822.

Desjardins, M. *et al.* (1994) 'Biogenesis of phagolysosomes proceeds through a sequential series of interactions with the endocytic apparatus', *Journal of Cell Biology*, 124(5), pp. 677–688. Available at: https://doi.org/10.1083/jcb.124.5.677.

Diaz-Aparicio, I. *et al.* (2020) 'Microglia actively remodel adult hippocampal neurogenesis through the phagocytosis secretome', *Journal of Neuroscience*, 40(7), pp. 1453–1482. Available at: https://doi.org/10.1523/JNEUROSCI.0993-19.2019.

DiCarlo, G. (2001) 'Intrahippocampal LPS injections reduce AÎ² load in APP+PS1 transgenic mice', *Neurobiology of Aging*, 22(6), pp. 1007–1012. Available at: https://doi.org/10.1016/S0197-4580(01)00292-5.

Douvaras, P. *et al.* (2017) 'Directed Differentiation of Human Pluripotent Stem Cells to Microglia', *Stem Cell Reports*, 8(6), pp. 1516–1524. Available at: https://doi.org/10.1016/j.stemcr.2017.04.023.

Duque, G.A. and Descoteaux, A. (2014) 'Macrophage cytokines: Involvement in immunity and infectious diseases', *Frontiers in Immunology*. Frontiers Media S.A. Available at: https://doi.org/10.3389/fimmu.2014.00491.

Easley-Neal, C. *et al.* (2019) 'CSF1R Ligands IL-34 and CSF1 Are Differentially Required for Microglia Development and Maintenance in White and Gray Matter Brain Regions', *Frontiers in Immunology*, 10. Available at: https://doi.org/10.3389/fimmu.2019.02199.

Efthymiou, A.G. and Goate, A.M. (2017) 'Late onset Alzheimer's disease genetics implicates microglial pathways in disease risk', *Molecular Neurodegeneration*. BioMed Central Ltd. Available at: https://doi.org/10.1186/s13024-017-0184-x.

Eglitis, M.A. and Mezey, É. (1997) 'Hematopoietic cells differentiate into both microglia and macroglia in the brains of adult mice', *Proceedings of the National Academy of Sciences of the United States of America*, 94(8), pp. 4080–4085. Available at: https://doi.org/10.1073/pnas.94.8.4080.

Ekdahl, C.T. *et al.* (2003) 'Inflammation is detrimental for neurogenesis in adult brain', *Proceedings of the National Academy of Sciences*, 100(23), pp. 13632–13637. Available at: https://doi.org/10.1073/pnas.2234031100.

Elliott, M.R. *et al.* (2009) 'Nucleotides released by apoptotic cells act as a find-me signal to promote phagocytic clearance', *Nature*, 461(7261), pp. 282–286. Available at: https://doi.org/10.1038/nature08296.

Elmore, M.R.P. *et al.* (2014) 'Colony-stimulating factor 1 receptor signaling is necessary for microglia viability, unmasking a microglia progenitor cell in the adult brain', *Neuron*, 82(2), pp. 380–397. Available at: https://doi.org/10.1016/j.neuron.2014.02.040.

Encinas, J.M. *et al.* (2011) 'Division-coupled astrocytic differentiation and age-related depletion of neural stem cells in the adult hippocampus', *Cell Stem Cell*, 8(5), pp. 566–579. Available at: https://doi.org/10.1016/j.stem.2011.03.010.

Encinas, J.M. and Sierra, A. (2012) 'Neural stem cell deforestation as the main force driving the age-related decline in adult hippocampal neurogenesis', *Behavioural Brain Research*, 227(2), pp. 433–439. Available at: https://doi.org/https://doi.org/10.1016/j.bbr.2011.10.010.

Eriksson, P.S. *et al.* (1998) 'Neurogenesis in the adult human hippocampus', *Nature Medicine*, 4(11), pp. 1313–1317. Available at: https://doi.org/10.1038/3305.

Eyo, U.B. *et al.* (2014) 'Neuronal hyperactivity recruits microglial processes via neuronal NMDA receptors and microglial P2Y12 receptors after status epilepticus', *Journal of Neuroscience*, 34(32), pp. 10528–10540. Available at: https://doi.org/10.1523/JNEUROSCI.0416-14.2014.

Fadok, V.A. *et al.* (1998) 'The role of phosphatidylserine in recognition of apoptotic cells by phagocytes', *Cell Death & Differentiation*, 5(7), pp. 551–562. Available at: https://doi.org/10.1038/sj.cdd.4400404.

Fontainhas, A.M. *et al.* (2011) 'Microglial morphology and dynamic behavior is regulated by ionotropic glutamatergic and GABAergic neurotransmission', *PLoS ONE*, 6(1). Available at: https://doi.org/10.1371/journal.pone.0015973.

Fourgeaud, L. *et al.* (2016) 'TAM receptors regulate multiple features of microglial physiology', *Nature*, 532(7598), pp. 240–244. Available at: https://doi.org/10.1038/nature17630.

Fuller, A.D. and van Eldik, L.J. (2008) 'MFG-E8 regulates microglial phagocytosis of apoptotic neurons', *Journal of Neuroimmune Pharmacology*, 3(4), pp. 246–256. Available at: https://doi.org/10.1007/s11481-008-9118-2.

Garceau, V. *et al.* (2010) ' Pivotal Advance: Avian colony-stimulating factor 1 (CSF-1), interleukin-34 (IL-34), and CSF-1 receptor genes and gene products ', *Journal of Leukocyte Biology*, 87(5), pp. 753–764. Available at: https://doi.org/10.1189/jlb.0909624.

Gardai, S.J. *et al.* (2006) 'Recognition ligands on apoptotic cells: a perspective', *Journal of Leukocyte Biology*, 79(5), pp. 896–903. Available at: https://doi.org/10.1189/jlb.1005550.

Garton, K.J. *et al.* (2001) 'Tumor Necrosis Factor-α-converting Enzyme (ADAM17) Mediates the Cleavage and Shedding of Fractalkine (CX3CL1)', *Journal of Biological Chemistry*, 276(41), pp. 37993–38001. Available at: https://doi.org/10.1074/jbc.m106434200.

Geirsdottir, L. *et al.* (2019) 'Cross-Species Single-Cell Analysis Reveals Divergence of the Primate Microglia Program', *Cell*, 179(7), pp. 1609-1622.e16. Available at: https://doi.org/10.1016/j.cell.2019.11.010.

Geisow, M.J. and Evans, W.H. (1984) 'pH in the endosome: Measurements during pinocytosis and receptor-mediated endocytosis', *Experimental Cell Research*, 150(1), pp. 36–46. Available at: https://doi.org/https://doi.org/10.1016/0014-4827(84)90699-2.

Ginhoux, F. *et al.* (2010) 'Fate mapping analysis reveals that adult microglia derive from primitive macrophages.', *Science*, 330(6005), pp. 841–5. Available at: https://doi.org/10.1126/science.1194637.

Giulian, D. and Baker, T.J. (1986) 'Characterization of ameboid microglia isolated from developing mammalian brain', *Journal of Neuroscience*, 6(8), pp. 2163–2178. Available at: https://doi.org/10.1523/jneurosci.06-08-02163.1986.

Godin, I.E. *et al.* (1993) 'Para-aortic splanchnopleura from early mouse embryos contains B1a cell progenitors', *Nature*, 364(6432), pp. 67–70. Available at: https://doi.org/10.1038/364067a0.

Grassivaro, F. *et al.* (2020) 'Convergence between microglia and peripheral macrophages phenotype during development and neuroinflammation', *Journal of Neuroscience*, 40(4), pp. 784–795. Available at: https://doi.org/10.1523/JNEUROSCI.1523-19.2019.

Gude, D.R. *et al.* (2008) 'Apoptosis induces expression of sphingosine kinase 1 to release sphingosine-1-phosphate as a "come-and-get-me" signal', *The FASEB Journal*, 22(8), pp. 2629–2638. Available at: https://doi.org/10.1096/fj.08-107169.

Gutbier, S. *et al.* (2020) 'Large-scale production of human IPSC-derived macrophages for drug screening', *International Journal of Molecular Sciences*, 21(13), pp. 1–23. Available at: https://doi.org/10.3390/ijms21134808.

Gyoneva, S. and Traynelis, S.F. (2013) 'Norepinephrine modulates the motility of resting and activated microglia via different adrenergic receptors', *Journal of Biological Chemistry*, 288(21), pp. 15291–15302. Available at: https://doi.org/10.1074/jbc.M113.458901.

Haenseler, W. *et al.* (2017) 'A Highly Efficient Human Pluripotent Stem Cell Microglia Model Displays a Neuronal-Co-culture-Specific Expression Profile and Inflammatory Response', *Stem Cell Reports*, 8(6), pp. 1727–1742. Available at: https://doi.org/10.1016/j.stemcr.2017.05.017.

Hammond, T.R. *et al.* (2019) 'Single-Cell RNA Sequencing of Microglia throughout the Mouse Lifespan and in the Injured Brain Reveals Complex Cell-State Changes', *Immunity*, 50(1), pp. 253-271.e6. Available at: https://doi.org/10.1016/j.immuni.2018.11.004.

Harris, L. *et al.* (2021) 'Coordinated changes in cellular behavior ensure the lifelong maintenance of the hippocampal stem cell population', *Cell stem cell*. 2021/02/12, 28(5), pp. 863-876.e6. Available at: https://doi.org/10.1016/j.stem.2021.01.003.

Harrison, J.K. *et al.* (1998) *Role for neuronally derived fractalkine in mediating interactions between neurons and CX3CR1-expressing microglia*. Available at: www.pnas.org.

Haynes, S.E. *et al.* (2006) 'The P2Y12 receptor regulates microglial activation by extracellular nucleotides', *Nature Neuroscience*, 9(12), pp. 1512–1519. Available at: https://doi.org/10.1038/nn1805.

Herber, D.L. *et al.* (2004) 'Time-dependent reduction in Aβ levels after intracranial LPS administration in APP transgenic mice', *Experimental Neurology*, 190(1), pp. 245–253. Available at: https://doi.org/https://doi.org/10.1016/j.expneurol.2004.07.007.

Hetier, E. *et al.* (1988) *Brain Macrophages Synthesize Interleukin-1 and Interleukin-1 mRNAs In Vitro*, *Journal of Neuroscience Research*.

Hevner, R.F. (2016) 'Evolution of the mammalian dentate gyrus', *Journal of Comparative Neurology*, 524(3), pp. 578–594. Available at: https://doi.org/https://doi.org/10.1002/cne.23851.

Hoeffel, G. *et al.* (2015) 'C-Myb(+) erythro-myeloid progenitor-derived fetal monocytes give rise to adult tissue-resident macrophages.', *Immunity*, 42(4), pp. 665–78. Available at: https://doi.org/10.1016/j.immuni.2015.03.011.

Horiuchi, M. *et al.* (2012) 'Interferon regulatory factor 8/interferon consensus sequence binding protein is a critical transcription factor for the physiological phenotype of microglia', *Journal of Neuroinflammation*, 9, pp. 1–14. Available at: https://doi.org/10.1186/1742-2094-9-227.

Huang, Y. *et al.* (2018) 'Repopulated microglia are solely derived from the proliferation of residual microglia after acute depletion', *Nature Neuroscience*, 21(4), pp. 530–540. Available at: https://doi.org/10.1038/s41593-018-0090-8.

Hundhausen, C. *et al.* (2003) 'The disintegrin-like metalloproteinase ADAM10 is involved in constitutive cleavage of CX3CL1 (fractalkine) and regulates CX3CL1-mediated cell-cell adhesion', *Blood*, 102(4), pp. 1186–1195. Available at: https://doi.org/10.1182/blood-2002-12-3775.

Imai, Y. and Kohsaka, S. (2002) 'Intracellular signaling in M-CSF-induced microglia activation: Role of Iba1', *GLIA*, pp. 164–174. Available at: https://doi.org/10.1002/glia.10149.

Inoue, K. *et al.* (2021) 'Modulation of inflammatory responses by fractalkine signaling in microglia', *PLoS ONE*, 16(5 May). Available at: https://doi.org/10.1371/journal.pone.0252118.

Janossy, G. *et al.* (1986) 'Separate ontogeny of two macrophage-like accessory cell populations in the human fetus.', *The journal of immunology : official journal of the American Association of Immunologists.* Baltimore, U.S.A. : Williams & Wilkins, pp. 4354–4361.

Jessberger, S. *et al.* (2009) 'Dentate gyrus-specific knockdown of adult neurogenesis impairs spatial and object recognition memory in adult rats', *Learning and Memory*, 16(2), pp. 147–154. Available at: https://doi.org/10.1101/lm.1172609.

Kastner, P. and Chan, S. (2008) 'PU.1: A crucial and versatile player in hematopoiesis and leukemia', *International Journal of Biochemistry and Cell Biology*, pp. 22–27. Available at: https://doi.org/10.1016/j.biocel.2007.01.026.

Keller, S., Berghoff, K. and Kress, H. (2017) 'Phagosomal transport depends strongly on phagosome size', *Scientific Reports*, 7(1). Available at: https://doi.org/10.1038/s41598-017-17183-7.

Kempermann, G. *et al.* (2004) 'Milestones of neuronal development in the adult hippocampus', *Trends in Neurosciences*, 27(8), pp. 447–452. Available at: https://doi.org/10.1016/j.tins.2004.05.013.

Keren-Shaul, H. *et al.* (2017) 'A Unique Microglia Type Associated with Restricting Development of Alzheimer's Disease', *Cell*, 169(7), pp. 1276-1290.e17. Available at: https://doi.org/10.1016/j.cell.2017.05.018.

Kettenmann, H. *et al.* (2011) 'Physiology of Microglia', *Physiological Reviews*, 91(2), pp. 461–553. Available at: https://doi.org/10.1152/physrev.00011.2010.

Kierdorf, K. *et al.* (2013) 'Microglia emerge from erythromyeloid precursors via Pu.1-and Irf8-dependent pathways', *Nature Neuroscience*, 16(3), pp. 273–280. Available at: https://doi.org/10.1038/nn.3318.

Kondo, S., Kohsaka, S. and Okabe, S. (2011) 'Long-term changes of spine dynamics and microglia after transient peripheral immune response triggered by LPS in vivo', *Molecular Brain*, 4(1). Available at: https://doi.org/10.1186/1756-6606-4-27.

Kumaravelu, P. *et al.* (2002) 'Quantitative developmental anatomy of definite haematopoietic stem cells/long-term repopulating units (HSC/RUs): Role of the aorta-gonad-mesonephros (AGM) region and the yolk sac in colonisation of the mouse embryonic liver', *Development*, 129(21), pp. 4891–4899. Available at: https://doi.org/10.1242/dev.129.21.4891.

Lampron, A. *et al.* (2015) 'Inefficient clearance of myelin debris by microglia impairs remyelinating processes', *Journal of Experimental Medicine*, 212(4), pp. 481–495. Available at: https://doi.org/10.1084/jem.20141656.

Langeslag, M. and Kress, M. (2020) 'The ceramide-S1P pathway as a druggable target to alleviate peripheral neuropathic pain', *Expert Opinion on Therapeutic Targets*. Taylor and Francis Ltd., pp. 869–884. Available at: https://doi.org/10.1080/14728222.2020.1787989.

Larochelle, A. *et al.* (2016) 'Bone marrow-derived macrophages and the CNS: An update on the use of experimental chimeric mouse models and bone marrow transplantation in neurological disorders', *Biochimica et Biophysica Acta - Molecular Basis of Disease*, 1862(3), pp. 310–322. Available at: https://doi.org/10.1016/j.bbadis.2015.09.017.

Laslo, P. *et al.* (2006) 'Multilineage Transcriptional Priming and Determination of Alternate Hematopoietic Cell Fates', *Cell*, 126(4), pp. 755–766. Available at: https://doi.org/10.1016/j.cell.2006.06.052.

Lassmann, H. *et al.* (1993) 'Bone marrow derived elements and resident microglia in brain inflammation', *Glia*, 7(1), pp. 19–24. Available at: https://doi.org/10.1002/glia.440070106.

Lauber, K. *et al.* (2003) 'Apoptotic Cells Induce Migration of Phagocytes via Caspase-3-Mediated Release of a Lipid Attraction Signal', *Cell*, 113(6), pp. 717–730. Available at: https://doi.org/https://doi.org/10.1016/S0092-8674(03)00422-7.

Lauro, C. *et al.* (2019) 'Fractalkine Modulates Microglia Metabolism in Brain Ischemia', *Frontiers in Cellular Neuroscience*, 13. Available at: https://doi.org/10.3389/fncel.2019.00414.

Lawson, L.J., Perry, V.H. and Gordon, S. (1992) 'Turnover of resident microglia in the normal adult mouse brain', *Neuroscience*, 48(2), pp. 405–415. Available at: https://doi.org/10.1016/0306-4522(92)90500-2.

Lemke, G. and Rothlin, C. V. (2008) 'Immunobiology of the TAM receptors', *Nature Reviews Immunology*, 8(5), pp. 327–336. Available at: https://doi.org/10.1038/nri2303.

Lemke, G. and Rothlin, C. v. (2008) 'Immunobiology of the TAM receptors', *Nature Reviews Immunology*, pp. 327–336. Available at: https://doi.org/10.1038/nri2303.

Li, J. and Yuan, J. (2008) 'Caspases in apoptosis and beyond', *Oncogene*, pp. 6194–6206. Available at: https://doi.org/10.1038/onc.2008.297.

Li, Q. *et al.* (2019) 'Developmental Heterogeneity of Microglia and Brain Myeloid Cells Revealed by Deep Single-Cell RNA Sequencing', *Neuron*, 101(2), pp. 207-223.e10. Available at: https://doi.org/10.1016/j.neuron.2018.12.006.

Li, X. *et al.* (2016) 'A molecular mechanism to regulate lysosome motility for lysosome positioning and tubulation', *Nature Cell Biology*, 18(4), pp. 404–417. Available at: https://doi.org/10.1038/ncb3324.

Liang, K.J. *et al.* (2009) 'Regulation of dynamic behavior of retinal microglia by CX3CR1 signaling', *Investigative Ophthalmology and Visual Science*, 50(9), pp. 4444–4451. Available at: https://doi.org/10.1167/iovs.08-3357.

Lin, H. *et al.* (2008) 'Discovery of a Cytokine and Its Receptor by Functional Screening of the Extracellular Proteome', *Science*, 320(5877), pp. 807–811. Available at: https://doi.org/10.1126/science.1154370.

Ling, E.A., Penney, D. and Leblond, C.P. (1980) 'Use of carbon labeling to demonstrate the role of blood monocytes as precursors of the "ameboid cells" present in the corpus callosum of postnatal rats', *Journal of Comparative Neurology*, 193(3), pp. 631–657. Available at: https://doi.org/10.1002/cne.901930304.

Liu, J. *et al.* (2008) 'Restoration of lysosomal pH in RPE cells from cultured human and ABCA4 -/- mice: Pharmacologic approaches and functional recovery', *Investigative Ophthalmology and Visual Science*, 49(2), pp. 772–780. Available at: https://doi.org/10.1167/iovs.07-0675.

Liu, X.Z. *et al.* (2018) 'Genetic screening and functional analysis of CASP9 mutations in a Chinese cohort with neural tube defects', *CNS Neuroscience and Therapeutics*, 24(5), pp. 394–403. Available at: https://doi.org/10.1111/cns.12797.

Lucas, S.M., Rothwell, N.J. and Gibson, R.M. (2006) 'The role of inflammation in CNS injury and disease', *British Journal of Pharmacology*. Available at: https://doi.org/10.1038/sj.bjp.0706400.

de Lucia, C. *et al.* (2016) 'Microglia regulate hippocampal neurogenesis during chronic neurodegeneration', *Brain, Behavior, and Immunity*, 55, pp. 179–190. Available at: https://doi.org/10.1016/j.bbi.2015.11.001.

Maciejewski-Lenoir, D. *et al.* (1999) 'Characterization of Fractalkine in Rat Brain Cells: Migratory and Activation Signals for CX3CR-1-Expressing Microglia', *The Journal of Immunology*, 163(3), pp. 1628–1635. Available at: https://www.jimmunol.org/content/163/3/1628.

Madry, C. and Attwell, D. (2015) 'Receptors, ion channels, and signaling mechanisms underlying Microglial dynamics', *Journal of Biological Chemistry*. American Society for Biochemistry and Molecular Biology Inc., pp. 12443–12450. Available at: https://doi.org/10.1074/jbc.R115.637157.

Mak, K.S. *et al.* (2011) 'PU.1 and haematopoietic cell fate: Dosage matters', *International Journal of Cell Biology*, 2011. Available at: https://doi.org/10.1155/2011/808524.

Mariani, M.M. and Kielian, T. (2009) 'Microglia in infectious diseases of the central nervous system', *Journal of neuroimmune pharmacology : the official journal of the Society on NeuroImmune Pharmacology*. 2009/09/02, 4(4), pp. 448–461. Available at: https://doi.org/10.1007/s11481-009-9170-6.

Marion, S. *et al.* (2011) 'Ezrin Promotes Actin Assembly at the Phagosome Membrane and Regulates Phago-Lysosomal Fusion', *Traffic*, 12(4), pp. 421–437. Available at: https://doi.org/10.1111/j.1600-0854.2011.01158.x.

Martín-Suárez, S. *et al.* (2019) 'Phenotypical and functional heterogeneity of neural stem cells in the aged hippocampus', *Aging Cell*, 18(4). Available at: https://doi.org/10.1111/acel.12958.

Massa, V. *et al.* (2009) 'Apoptosis is not required for mammalian neural tube closure', *Proceedings of the National Academy of Sciences*, 106(20), pp. 8233–8238. Available at: https://doi.org/10.1073/pnas.0900333106.

Masteller, E.L. and Wong, B.R. (2014) 'Targeting IL-34 in chronic inflammation', *Drug Discovery Today*. Elsevier Ltd, pp. 1212–1216. Available at: https://doi.org/10.1016/j.drudis.2014.05.016.

Masuda, T. *et al.* (2014) 'IRF8 is a transcriptional determinant for microglial motility', *Purinergic Signalling*, 10(3), pp. 515–521. Available at: https://doi.org/10.1007/s11302-014-9413-8.

Matsumoto, Y. and Fujiwara, M. (1987) 'Absence of donor-type major histocompatibility complex class I antigen-bearing microglia in the rat central nervous system of radiation bone marrow chimeras', *Journal of Neuroimmunology*, 17(1), pp. 71–82. Available at: https://doi.org/10.1016/0165-5728(87)90032-4.

Mawuenyega, K.G. *et al.* (2010) 'Decreased Clearance of CNS β-Amyloid in Alzheimer's Disease', *Science*, 330(6012), pp. 1774–1774. Available at: https://doi.org/10.1126/science.1197623.

McGrath, K.E. *et al.* (2003) 'Circulation is established in a stepwise pattern in the mammalian embryo', *Blood*, 101(5), pp. 1669–1676. Available at: https://doi.org/10.1182/blood-2002-08-2531.

McKercher, S.R. *et al.* (1996) 'Targeted disruption of the PU.1 gene results in multiple hematopoietic abnormalities', *EMBO Journal*, 15(20), pp. 5647–5658. Available at: https://doi.org/10.1002/j.1460-2075.1996.tb00949.x.

McQuade, A. *et al.* (2018) 'Development and validation of a simplified method to generate human microglia from pluripotent stem cells', *Molecular Neurodegeneration*, 13(1). Available at: https://doi.org/10.1186/s13024-018-0297-x.

Medvinsky, A.L. *et al.* (1993) 'An early pre-liver intraembryonic source of CFU-S in the developing mouse', *Nature*, 364(6432), pp. 64–67. Available at: https://doi.org/10.1038/364064a0.

Melief, J. *et al.* (2016) 'Characterizing primary human microglia: A comparative study with myeloid subsets and culture models', *GLIA*, 64(11), pp. 1857–1868. Available at: https://doi.org/10.1002/glia.23023.

Mezey, E. *et al.* (2000) 'Turning blood into brain: Cells bearing neuronal antigens generated in vivo from bone marrow', *Science*, 290(5497), pp. 1779–1782. Available at: https://doi.org/10.1126/science.290.5497.1779.

Ming, G. li and Song, H. (2011) 'Adult Neurogenesis in the Mammalian Brain: Significant Answers and Significant Questions', *Neuron*, pp. 687–702. Available at: https://doi.org/10.1016/j.neuron.2011.05.001.

Minten, C. *et al.* (2012) 'IFN regulatory factor 8 is a key constitutive determinant of the morphological and molecular properties of microglia in the CNS.', *PloS one*, 7(11). Available at: https://doi.org/10.1371/journal.pone.0049851.

Mizee, M.R. *et al.* (2017) 'Isolation of primary microglia from the human post-mortem brain: effects of ante- and post-mortem variables', *Acta neuropathologica communications*, 5(1), p. 16. Available at: https://doi.org/10.1186/s40478-017-0418-8.

Mizutani, M. *et al.* (2012) 'The Fractalkine Receptor but Not CCR2 Is Present on Microglia from Embryonic Development throughout Adulthood', *The Journal of Immunology*, 188(1), pp. 29–36. Available at: https://doi.org/10.4049/jimmunol.1100421.

Monier, A. *et al.* (2007) 'Entry and distribution of microglial cells in human embryonic and fetal cerebral cortex', *Journal of Neuropathology and Experimental Neurology*, 66(5), pp. 372–382. Available at: https://doi.org/10.1097/nen.0b013e3180517b46.

Monje, M.L., Toda, H. and Palmer, T.D. (2003) 'Inflammatory Blockade Restores Adult Hippocampal Neurogenesis', *Science*, 302(5651), pp. 1760–1765. Available at: https://doi.org/10.1126/science.1088417.

Moore, M.A.S. and Metcalf, D. (1970) 'Ontogeny of the Haemopoietic System: Yolk Sac Origin of In Vivo and In Vitro Colony Forming Cells in the Developing Mouse Embryo', *British Journal of Haematology*, 18(3), pp. 279–296. Available at: https://doi.org/10.1111/j.1365-2141.1970.tb01443.x.

Moreno-Jiménez, E.P. *et al.* (2019) 'Adult hippocampal neurogenesis is abundant in neurologically healthy subjects and drops sharply in patients with Alzheimer's disease', *Nature Medicine*, 25(4), pp. 554–560. Available at: https://doi.org/10.1038/s41591-019-0375-9.

Morikawa, M., Derynck, R. and Miyazono, K. (2016) 'TGF-β and the TGF-β Family: Context-Dependent Roles in Cell and Tissue Physiology.', *Cold Spring Harbor perspectives in biology*, 8(5). Available at: https://doi.org/10.1101/cshperspect.a021873.

Mucenski, M.L. *et al.* (1991) *A Functional c-myb Gene Is Required for Normal Murine Fetal Hepatic Hematopoiesis*, *Cell*.

Muffat, J. *et al.* (2016) 'Efficient derivation of microglia-like cells from human pluripotent stem cells', *Nature Medicine*, 22(11), pp. 1358–1367. Available at: https://doi.org/10.1038/nm.4189.

Napoli, I. and Neumann, H. (2010) 'Protective effects of microglia in multiple sclerosis', *Experimental Neurology*, 225(1), pp. 24–28. Available at: https://doi.org/https://doi.org/10.1016/j.expneurol.2009.04.024.

Nayak, D., Roth, T.L. and McGavern, D.B. (2014) 'Microglia development and function', *Annual Review of Immunology*. Annual Reviews Inc., pp. 367–402. Available at: https://doi.org/10.1146/annurev-immunol-032713-120240.

Nemes-Baran, A.D., White, D.R. and DeSilva, T.M. (2020) 'Fractalkine-Dependent Microglial Pruning of Viable Oligodendrocyte Progenitor Cells Regulates Myelination', *Cell Reports*, 32(7). Available at: https://doi.org/10.1016/j.celrep.2020.108047.

Nimmerjahn, A., Kirchhoff, F. and Helmchen, F. (2005) 'Resting Microglial Cells Are Highly Dynamic Surveillants of Brain Parenchyma in Vivo', *Science*, 308(5726), pp. 1314–1318. Available at: https://doi.org/10.1126/science.1110647.

Nolte, C. *et al.* (1996) *COMPLEMENT 5a CONTROLS MOTILITY OF MURINE MICROGLIAL CELLS IN VITRO VIA ACTIVATION OF AN INHIBITORY G-PROTEIN AND THE REARRANGEMENT OF THE ACTIN CYTOSKELETON*.

Nonomura, K. *et al.* (2013) 'Local apoptosis modulates early mammalian brain development through the elimination of morphogen-producing cells', *Developmental Cell*, 27(6), pp. 621–634. Available at: https://doi.org/10.1016/j.devcel.2013.11.015.

O'Keefe, G.M., Nguyen, V.T. and Benveniste, E.N. (1999) 'Class II transactivator and class II MHC gene expression in microglia: modulation by the cytokines TGF-beta, IL-4, IL-13 and IL-

10.', *European journal of immunology*, 29(4), pp. 1275–85. Available at: https://doi.org/10.1002/(SICI)1521-4141(199904)29:04<1275::AID-IMMU1275>3.0.CO;2-T.

Opal, S.M. and DePalo, V.A. (2000) 'Anti-Inflammatory Cytokines', *Chest*, 117(4), pp. 1162–1172. Available at: https://doi.org/https://doi.org/10.1378/chest.117.4.1162.

Orkin, S.H. and Zon, L.I. (2008) 'Hematopoiesis: An Evolving Paradigm for Stem Cell Biology', *Cell*, 132(4), pp. 631–644. Available at: https://doi.org/10.1016/j.cell.2008.01.025.

Palis, J. *et al.* (1999) 'Development of erythroid and myeloid progenitors in the yolk sac and embryo proper of the mouse', *Development*, 126(22), pp. 5073–5084. Available at: https://doi.org/10.1242/dev.126.22.5073.

Pandya, H. *et al.* (2017) 'Differentiation of human and murine induced pluripotent stem cells to microglia-like cells', *Nature Neuroscience*, 20(5), pp. 753–759. Available at: https://doi.org/10.1038/nn.4534.

Paolicelli, R.C. *et al.* (2011) 'Synaptic pruning by microglia is necessary for normal brain development', *Science*, 333(6048), pp. 1456–1458. Available at: https://doi.org/10.1126/science.1202529.

Parhizkar, S. *et al.* (2019) 'Loss of TREM2 function increases amyloid seeding but reduces plaque-associated ApoE', *Nature Neuroscience*, 22(2), pp. 191–204. Available at: https://doi.org/10.1038/s41593-018-0296-9.

Paris, I. *et al.* (2018) 'ProMoIJ: A new tool for automatic three-dimensional analysis of microglial process motility', *Glia*, 66(4), pp. 828–845. Available at: https://doi.org/10.1002/glia.23287.

Park, D. *et al.* (2011) 'Continued clearance of apoptotic cells critically depends on the phagocyte Ucp2 protein', *Nature*, 477(7363), pp. 220–224. Available at: https://doi.org/10.1038/nature10340.

Paterson, N. and Lämmermann, T. (2022) 'Macrophage network dynamics depend on haptokinesis for optimal local surveillance', *eLife*, 11. Available at: https://doi.org/10.7554/elife.75354.

Peter, C., Wesselborg, S. and Lauber, K. (2010) 'Molecular Suicide Notes: Last Call from Apoptosing Cells', *Journal of Molecular Cell Biology*, 2(2), pp. 78–80. Available at: https://doi.org/10.1093/jmcb/mjp045.

Plastini, M.J., Desu, H.L. and Brambilla, R. (2020) 'Dynamic Responses of Microglia in Animal Models of Multiple Sclerosis', *Frontiers in Cellular Neuroscience*. Frontiers Media S.A. Available at: https://doi.org/10.3389/fncel.2020.00269.

Pollard, J.W. (2009) 'Trophic macrophages in development and disease', *Nature Reviews Immunology*, pp. 259–270. Available at: https://doi.org/10.1038/nri2528.

Priller, J. *et al.* (2001) 'Targeting gene-modified hematopoietic cells to the central nervous system: Use of green fluorescent protein uncovers microglial engraftment', *Nature Medicine*, 7(12), pp. 1356–1361. Available at: https://doi.org/10.1038/nm1201-1356.

Rangaraju, S. *et al.* (2018) 'Differential phagocytic properties of CD45low microglia and CD45high brain mononuclear phagocytes-activation and age-related effects', *Frontiers in Immunology*, 9(MAR). Available at: https://doi.org/10.3389/fimmu.2018.00405.

Ransohoff, R.M. (2016) 'A polarizing question: Do M1 and M2 microglia exist', *Nature Neuroscience*. Nature Publishing Group, pp. 987–991. Available at: https://doi.org/10.1038/nn.4338.

Reich, M. *et al.* (2021) 'Alzheimer's Risk Gene TREM2 Determines Functional Properties of New Type of Human iPSC-Derived Microglia', *Frontiers in Immunology*, 11(February), pp. 1–15. Available at: https://doi.org/10.3389/fimmu.2020.617860.

Rezaie, P. *et al.* (2005) 'Microglia in the cerebral wall of the human telencephalon at second trimester', *Cerebral Cortex*, 15(7), pp. 938–949. Available at: https://doi.org/10.1093/cercor/bhh194.

Rocha, N.P. *et al.* (2012) 'Peripheral blood mono-nuclear cells derived from Alzheimer's disease patients show elevated baseline levels of secreted cytokines but resist stimulation with β-amyloid peptide', *Molecular and Cellular Neuroscience*, 49(1), pp. 77–84. Available at: https://doi.org/10.1016/j.mcn.2011.09.005.

Rodríguez-Iglesias, N., Sierra, A. and Valero, J. (2019) 'Rewiring of memory circuits: Connecting adult newborn neurons with the help of microglia', *Frontiers in Cell and Developmental Biology*. Frontiers Media S.A. Available at: https://doi.org/10.3389/fcell.2019.00024.

Ruocco, A. *et al.* (1999) 'A Transforming Growth Factor-β Antagonist Unmasks the Neuroprotective Role of This Endogenous Cytokine in Excitotoxic and Ischemic Brain Injury', *Journal of Cerebral Blood Flow & Metabolism*, 19(12), pp. 1345–1353. Available at: https://doi.org/10.1097/00004647-199912000-00008.

Sahay, A. *et al.* (2011) 'Increasing adult hippocampal neurogenesis is sufficient to improve pattern separation', *Nature*, 472(7344), pp. 466–470. Available at: https://doi.org/10.1038/nature09817.

Sawada, M. *et al.* (1989) *Production of tumor necrosis factor-alpha by microglia and astrocytes in culture*, *Brain Re~'earch*.

Saxe, M.D. *et al.* (2006) 'Ablation of hippocampal neurogenesis impairs contextual fear conditioning and synaptic plasticity in the dentate gyrus', *Proceedings of the National Academy of Sciences*, 103(46), pp. 17501–17506. Available at: https://doi.org/10.1073/pnas.0607207103.

Schafer, D.P. *et al.* (2012) 'Microglia Sculpt Postnatal Neural Circuits in an Activity and Complement-Dependent Manner', *Neuron*, 74(4), pp. 691–705. Available at: https://doi.org/10.1016/j.neuron.2012.03.026.

Schulz, C. *et al.* (2012) 'A lineage of myeloid cells independent of myb and hematopoietic stem cells', *Science*, 335(6077), pp. 86–90. Available at: https://doi.org/10.1126/science.1219179.

Seitz, H.M. *et al.* (2007) 'Macrophages and Dendritic Cells Use Different Axl/Mertk/Tyro3 Receptors in Clearance of Apoptotic Cells', *The Journal of Immunology*, 178(9), pp. 5635–5642. Available at: https://doi.org/10.4049/jimmunol.178.9.5635.

Sierra, A. *et al.* (2010) 'Microglia shape adult hippocampal neurogenesis through apoptosis-coupled phagocytosis', *Cell Stem Cell*, 7(4), pp. 483–495. Available at: https://doi.org/10.1016/j.stem.2010.08.014.

Sierra, A. *et al.* (2013) 'Janus-faced microglia: Beneficial and detrimental consequences of microglial phagocytosis', *Frontiers in Cellular Neuroscience* [Preprint]. Available at: https://doi.org/10.3389/fncel.2013.00006.

Sierra, A., Paolicelli, R.C. and Kettenmann, H. (2019) 'Cien Años de Microglía: Milestones in a Century of Microglial Research', *Trends in Neurosciences*. Elsevier Ltd, pp. 778–792. Available at: https://doi.org/10.1016/j.tins.2019.09.004.

Simard, A.R. and Rivest, S. (2004) 'Bone marrow stem cells have the ability to populate the entire central nervous system into fully differentiated parenchymal microglia', *The FASEB Journal*, 18(9), pp. 998–1000. Available at: https://doi.org/10.1096/fj.04-1517fje.

de Simone, R. *et al.* (2003) 'Apoptotic PC12 Cells Exposing Phosphatidylserine Promote the Production of Anti-Inflammatory and Neuroprotective Molecules by Microglial Cells', *Journal of Neuropathology & Experimental Neurology*, 62(2), pp. 208–216. Available at: https://doi.org/10.1093/jnen/62.2.208.

Sipe, G.O. *et al.* (2016) 'Microglial P2Y12 is necessary for synaptic plasticity in mouse visual cortex', *Nature Communications*, 7. Available at: https://doi.org/10.1038/ncomms10905.

Smith, A.M. *et al.* (2013) 'M-CSF increases proliferation and phagocytosis while modulating receptor and transcription factor expression in adult human microglia', *Journal of Neuroinflammation*, 10, pp. 1–15. Available at: https://doi.org/10.1186/1742-2094-10-85.

Smith, J.A. *et al.* (2012) 'Role of pro-inflammatory cytokines released from microglia in neurodegenerative diseases', *Brain Research Bulletin*, 87(1), pp. 10–20. Available at: https://doi.org/https://doi.org/10.1016/j.brainresbull.2011.10.004.

Sokolowski, J.D. *et al.* (2014) 'Fractalkine is a "find-me" signal released by neurons undergoing ethanol-induced apoptosis', *Frontiers in Cellular Neuroscience*, 8(November). Available at: https://doi.org/10.3389/fncel.2014.00360.

Sorrells, S.F. *et al.* (2018) 'Human hippocampal neurogenesis drops sharply in children to undetectable levels in adults', *Nature*, 555(7696), pp. 377–381. Available at: https://doi.org/10.1038/nature25975.

Spalding, K.L. *et al.* (2013) 'XDynamics of hippocampal neurogenesis in adult humans', *Cell*, 153(6), p. 1219. Available at: https://doi.org/10.1016/j.cell.2013.05.002.

Spellicy, C.J. *et al.* (2018) 'Key apoptotic genes APAF1 and CASP9 implicated in recurrent folate-resistant neural tube defects', *European Journal of Human Genetics*, 26(3), pp. 420–427. Available at: https://doi.org/10.1038/s41431-017-0025-y.

Spittau, B., Dokalis, N. and Prinz, M. (2020) 'The Role of TGFβ Signaling in Microglia Maturation and Activation', *Trends in Immunology*, 41(9), pp. 836–848. Available at: https://doi.org/10.1016/j.it.2020.07.003.

Stowell, R.D. *et al.* (2019) 'Noradrenergic signaling in the wakeful state inhibits microglial surveillance and synaptic plasticity in the mouse visual cortex', *Nature Neuroscience*, 22(11), pp. 1782–1792. Available at: https://doi.org/10.1038/s41593-019-0514-0.

Sun, G.J. *et al.* (2015) 'Tangential migration of neuronal precursors of glutamatergic neurons in the adult mammalian brain', *Proceedings of the National Academy of Sciences of the United States of America*, 112(30), pp. 9484–9489. Available at: https://doi.org/10.1073/pnas.1508545112.

Takahashi, K. and Naito, M. (1993) 'Development, differentiation, and proliferation of macrophages in the rat yolk sac', *Tissue and Cell*, 25(3), pp. 351–362. Available at: https://doi.org/10.1016/0040-8166(93)90077-X.

Takahashi, K., Rochford, C.D.P. and Neumann, H. (2005) 'Clearance of apoptotic neurons without inflammation by microglial triggering receptor expressed on myeloid cells-2', *Journal of Experimental Medicine*, 201(4), pp. 647–657. Available at: https://doi.org/10.1084/jem.20041611.

Takahashi, K. and Yamanaka, S. (2006) 'Induction of Pluripotent Stem Cells from Mouse Embryonic and Adult Fibroblast Cultures by Defined Factors', *Cell*, 126(4), pp. 663–676. Available at: https://doi.org/10.1016/j.cell.2006.07.024.

Tambuyzer, B.R., Ponsaerts, P. and Nouwen, E.J. (2009) 'Microglia: gatekeepers of central nervous system immunology', *Journal of Leukocyte Biology*, 85(3), pp. 352–370. Available at: https://doi.org/10.1189/jlb.0608385.

Tamura, T., Kurotaki, D. and Koizumi, S. ichi (2015) 'Regulation of myelopoiesis by the transcription factor IRF8', *International Journal of Hematology*. Springer-Verlag Tokyo, pp. 342–351. Available at: https://doi.org/10.1007/s12185-015-1761-9.

Tavian, M. and Péault, B. (2005) 'Embryonic development of the human hematopoietic system', *International Journal of Developmental Biology*, 49(2-3 SPEC. ISS.), pp. 243–250. Available at: https://doi.org/10.1387/ijdb.041957mt.

Teixeira, C.M. *et al.* (2018) 'Untold New Beginnings: Adult Hippocampal Neurogenesis and Alzheimer's Disease', *Journal of Alzheimer's Disease*. IOS Press, pp. S497–S505. Available at: https://doi.org/10.3233/JAD-179918.

Terreros-Roncal, J. *et al.* (2021) 'Impact of neurodegenerative diseases on human adult hippocampal neurogenesis', *Science*, 374(6571), pp. 1106–1113. Available at: https://doi.org/10.1126/science.abl5163.

Terreros-Roncal, J *et al.* (2021) 'Impact of neurodegenerative diseases on human adult hippocampal neurogenesis', *Science*, 374(6571), pp. 1106–1113. Available at: https://doi.org/10.1126/science.abl5163.

Timmerman, R., Burm, S.M. and Bajramovic, J.J. (2018) 'An overview of in vitro methods to study microglia', *Frontiers in Cellular Neuroscience*. Frontiers Media S.A. Available at: https://doi.org/10.3389/fncel.2018.00242.

Toda, T. *et al.* (2019) 'The role of adult hippocampal neurogenesis in brain health and disease', *Molecular Psychiatry*. Nature Publishing Group, pp. 67–87. Available at: https://doi.org/10.1038/s41380-018-0036-2.

Ueno, M. *et al.* (2013) 'Layer V cortical neurons require microglial support for survival during postnatal development.', *Nature neuroscience*, 16(5), pp. 543–551. Available at: https://doi.org/10.1038/nn.3358.

Ulrich, J.D. *et al.* (2014) 'Altered microglial response to Aβ plaques in APPPS1-21 mice heterozygous for TREM2', *Molecular Neurodegeneration*, 9(1), pp. 1–9. Available at: https://doi.org/10.1186/1750-1326-9-20.

Urbán, N. *et al.* (2016) 'Return to Quiescence of mouse neural stem cells by degradation of a proactivation protein', *Science*, 353(6296), pp. 292–295. Available at: https://doi.org/10.1126/science.aaf4802.

Vallières, L. and Sawchenko, P.E. (2003) 'Bone marrow-derived cells that populate the adult mouse brain preserve their hematopoietic identity', *Journal of Neuroscience*, 23(12), pp. 5197–5207. Available at: https://doi.org/10.1523/jneurosci.23-12-05197.2003.

Vargas, M.E. *et al.* (2010) 'Endogenous antibodies promote rapid myelin clearance and effective axon regeneration after nerve injury', *Proceedings of the National Academy of Sciences of the United States of America*, 107(26), pp. 11993–11998. Available at: https://doi.org/10.1073/pnas.1001948107.

Vezzani, A. *et al.* (2011) 'The role of inflammation in epilepsy', *Nature Reviews Neurology*, pp. 31–40. Available at: https://doi.org/10.1038/nrneurol.2010.178.

Vezzani, A., Friedman, A. and Dingledine, R.J. (2013) 'The role of inflammation in epileptogenesis', *Neuropharmacology*, pp. 16–24. Available at: https://doi.org/10.1016/j.neuropharm.2012.04.004.

Villani, A. *et al.* (2019) 'Clearance by Microglia Depends on Packaging of Phagosomes into a Unique Cellular Compartment', *Developmental Cell*, 49(1), pp. 77-88.e7. Available at: https://doi.org/10.1016/j.devcel.2019.02.014.

Wachs, F.-P. *et al.* (2006) 'Transforming Growth Factor-β1 Is a Negative Modulator of Adult Neurogenesis', *Journal of Neuropathology and Experimental Neurology*, 65(4), pp. 358–370. Available at: https://doi.org/10.1097/01.jnen.0000218444.53405.f0.

Waisman, A. *et al.* (2015) 'Homeostasis of Microglia in the Adult Brain: Review of Novel Microglia Depletion Systems', *Trends in Immunology*, 36(10), pp. 625–636. Available at: https://doi.org/https://doi.org/10.1016/j.it.2015.08.005.

Weil, M., Jacobson, M.D. and Raff, M.C. (1997) 'Is programmed cell death required for neural tube closure?', *Current Biology*, 7, pp. 281–284.

Whitman, M.C. and Greer, C.A. (2007) 'Adult-generated neurons exhibit diverse developmental fates', *Developmental Neurobiology*, 67(8), pp. 1079–1093. Available at: https://doi.org/https://doi.org/10.1002/dneu.20389.

Wightman, D.P. *et al.* (2021) 'A genome-wide association study with 1,126,563 individuals identifies new risk loci for Alzheimer's disease', *Nature Genetics*, 53(9), pp. 1276–1282. Available at: https://doi.org/10.1038/s41588-021-00921-z.

Wu, J. *et al.* (2007) 'Purinergic receptor-stimulated IP3-mediated Ca2+ release enhances neuroprotection by increasing astrocyte mitochondrial metabolism during aging', *Journal of Neuroscience*, 27(24), pp. 6510–6520. Available at: https://doi.org/10.1523/JNEUROSCI.1256-07.2007.

Wu, L.J., Vadakkan, K.I. and Zhuo, M. (2007) 'ATP-induced chemotaxis of microglial processes requires P2Y receptor-activated initiation of outward potassium currents', *GLIA*, 55(8), pp. 810–821. Available at: https://doi.org/10.1002/glia.20500.

Wu, S. *et al.* (2018) 'Il34-Csf1r Pathway Regulates the Migration and Colonization of Microglial Precursors', *Developmental Cell*, 46(5), pp. 552-563.e4. Available at: https://doi.org/10.1016/j.devcel.2018.08.005.

Xu, J. *et al.* (2016) 'Microglia Colonization of Developing Zebrafish Midbrain Is Promoted by Apoptotic Neuron and Lysophosphatidylcholine', *Developmental Cell*, 38(2), pp. 214–222. Available at: https://doi.org/10.1016/j.devcel.2016.06.018.

Yuan, P. *et al.* (2016) 'TREM2 Haplodeficiency in Mice and Humans Impairs the Microglia Barrier Function Leading to Decreased Amyloid Compaction and Severe Axonal Dystrophy', *Neuron*, 90(4), pp. 724–739. Available at: https://doi.org/10.1016/j.neuron.2016.05.003.

Zhang, C. *et al.* (2018) 'Invasion of peripheral immune cells into brain parenchyma after cardiac arrest and resuscitation', *Aging and Disease*, 9(3), pp. 412–425. Available at: https://doi.org/10.14336/AD.2017.0926.

Zhao, Y. *et al.* (2018) 'TREM2 Is a Receptor for β-Amyloid that Mediates Microglial Function', *Neuron*, 97(5), pp. 1023-1031.e7. Available at: https://doi.org/10.1016/j.neuron.2018.01.031.

Zheng, C., Zhou, X.W. and Wang, J.Z. (2016) 'The dual roles of cytokines in Alzheimer's disease: Update on interleukins, TNF-α, TGF-β and IFN-γ', *Translational Neurodegeneration*. BioMed Central Ltd. Available at: https://doi.org/10.1186/s40035-016-0054-4.

Zheng, T.S. *et al.* (1998) *Caspase-3 controls both cytoplasmic and nuclear events associated with Fas-mediated apoptosis in vivo*, *Cell Biology*. Available at: www.pnas.org.

Zhou, X. *et al.* (2018) 'Rare mutations inapoptosis related genes APAF1, CASP9, and CASP3 contribute to human neural tube defects', *Cell Death and Disease*. Nature Publishing Group. Available at: https://doi.org/10.1038/s41419-017-0096-2.

Ziegler, U. and Groscurth, P. (2004) 'Morphological features of cell death', *News in Physiological Sciences*, pp. 124–128. Available at: https://doi.org/10.1152/nips.01519.2004.

Zöller, T. *et al.* (2018) 'Silencing of TGFβ signalling in microglia results in impaired homeostasis', *Nature Communications*, 9(1), pp. 1–13. Available at: https://doi.org/10.1038/s41467-018-06224-y.

2. Conclusions

In Reich and Paris, et al 2021,

- we optimize a protocol to generate iPSC derived microglia in monoculture and characterize these cells.
- The cells obtained using this method differs from other previously described methods on the expression level of TREM2 by microglia, which is higher in our method. The functional characteristics and gene expression of these cells were compaired to isogenic TREM2KO.
- We show that these monoculture microglia express the canonical microglial markers P2Y12 and CX3CR1; they are able to phagocytose apoptotic cells, amyloid beta coated beads, and yeast particles; and show Ca^{2+} activity after stimulation with ATP, ADP, and C5a.
- This model is particularly useful for mechanistic studies in Alzheimer's disease due to their expression of TREM2, which is particularly relevant in the context of this pathology.

In Paris, et al 2017,

- We describe a set of tools that allow the automatic analysis of microglial process motility in 3D.
- The results obtained showed that ProMoIJ was faster and less sensitive to experimenter bias than manual analysis.
- We found that data obtained from 2D projections significantly underestimates microglial process motility.
- We can obtain very valuable biologically relevant data, such as tip position and process length at every time point, which allows us to calculate its velocity and directionality towards or away from a lesion.
- In systemic inflammation our analysis determined that there was a small reduction in process motility, likely to be missed when using manual 2D analysis.

In Diaz-Aparicio, et al 2020,

- Constitutive KOs for P2Y12 and MerTK/Axl exhibit a decreased phagocytic index.
- Constitutive disruption in phagocytosis leads to a decrease in neurogenesis.
- An inducible KO model for MerTK displays an even greater decrease in microglial phagocytosis.

- An acute decrease in phagocytosis leads to a transient increase in proliferation in the neurogenic niche. At a later time point this acute increase in proliferation was reverted when analyzing the yield of these proliferating cells.
- We hypothesize that microglia is part of a regulatory feedback loop that maintains homeostasis in the adult neurogenic niche to preserve the rNSCs population and avoid their early exhaustion.
- Analyzing gene expression in phagocytic microglia *in vitro* revealed that phagocytosis of apoptotic cells induced a modulatory phenotype in microglia that was related to their secretome. The main ones being genes that encode secreted proteins such as VGF, VEGF, and FGF2.
- The administration of media from phagocytic microglia to NPC cultures and *in vivo* using osmotic pumps resulted in a decrease in neurogenesis in both models.

3. Published articles

- Alzheimer's Risk Gene TREM2 Determines Functional Properties of New Type of Human iPSC-Derived Microglia
  Frontiers in immunology
  Published: 03 February 2021
  DOI: 10.3389/fimmu.2020.617860
- ProMoIJ: A new tool for automatic three-dimensional analysis of microglial process motility
  Glia
  Published: 30 December 2017
  DOI: 10.1002/glia.23287
- Microglia Actively Remodel Adult Hippocampal Neurogenesis through the Phagocytosis Secretome
  The Journal of Neuroscience
  Published: 12 February 2020
  DOI: https://doi.org/10.1523/JNEUROSCI.0993-19.2019

frontiers in Immunology

ORIGINAL RESEARCH
published: 03 February 2021
doi: 10.3389/fimmu.2020.617860

Alzheimer's Risk Gene TREM2 Determines Functional Properties of New Type of Human iPSC-Derived Microglia

Marvin Reich[1,2†‡], Iñaki Paris[1,3‡], Martin Ebeling[4], Nadine Dahm[5], Christophe Schweitzer[1], Dieter Reinhardt[1], Roland Schmucki[4], Megana Prasad[4], Fabian Köchl[4], Marcel Leist[2], Sally A. Cowley[6], Jitao David Zhang[4], Christoph Patsch[5†], Simon Gutbier[5] and Markus Britschgi[1*]*

[1] Roche Pharma Research and Early Development, Neuroscience and Rare Diseases Discovery and Translational Area, Roche Innovation Center Basel, F. Hoffmann-La Roche Ltd, Basel, Switzerland, [2] In Vitro Toxicology and Biomedicine, Department inaugurated by the Doerenkamp-Zbinden Foundation, University of Konstanz, Konstanz, Germany, [3] Achucarro Basque Center for Neuroscience, Science Park of the UPV/EHU, Leioa, Spain, [4] Roche Pharma Research and Early Development, Pharmaceutical Sciences, Roche Innovation Center Basel, F. Hoffmann-La Roche Ltd, Basel, Switzerland, [5] Roche Pharma Research and Early Development, Therapeutic Modalities, Roche Innovation Center Basel, F. Hoffmann-La Roche Ltd, Basel, Switzerland, [6] James Martin Stem Cell Facility, Sir William Dunn School of Pathology, University of Oxford, Oxford, United Kingdom

Microglia are key in the homeostatic well-being of the brain and microglial dysfunction has been implicated in neurodegenerative disorders such as Alzheimer's disease (AD). Due to the many limitations to study microglia *in situ* or isolated for large scale drug discovery applications, there is a high need to develop robust and scalable human cellular models of microglia with reliable translatability to the disease. Here, we describe the generation of microglia-like cells from human induced pluripotent stem cells (iPSC) with distinct phenotypes for mechanistic studies in AD. We started out from an established differentiation protocol to generate primitive macrophage precursors mimicking the yolk sac ontogeny of microglia. Subsequently, we tested 36 differentiation conditions for the cells in monoculture where we exposed them to various combinations of media, morphogens, and extracellular matrices. The optimized protocol generated robustly ramified cells expressing key microglial markers. Bulk mRNA sequencing expression profiles revealed that compared to cells obtained in co-culture with neurons, microglia-like cells derived from a monoculture condition upregulate mRNA levels for Triggering Receptor Expressed On Myeloid Cells 2 (TREM2), which is reminiscent to the previously described disease-associated microglia. TREM2 is a risk gene for AD and an important regulator of microglia. The regulatory function of TREM2 in these cells was confirmed by comparing wild type with isogenic TREM2 knock-out iPSC microglia. The TREM2-deficient cells presented with stronger increase in free cytosolic calcium upon stimulation with ATP and ADP, as well as stronger migration towards complement C5a, compared to TREM2 expressing cells. The functional differences were associated with

OPEN ACCESS

Edited by:
Rosa Chiara Paolicelli,
University of Lausanne, Switzerland

Reviewed by:
Jessica Elaine Young,
University of Washington,
United States
Susanne Krasemann,
University Medical Center Hamburg-Eppendorf, Germany

***Correspondence:**
Simon Gutbier
simon.gutbier@roche.com
Markus Britschgi
markus.britschgi@roche.com

†Present address:
Marvin Reich,
Chair of Metabolic Biochemistry, Biomedical Center (BMC), Faculty of Medicine, Ludwig-Maximilians-Universität München,
Munich, Germany
Christoph Patsch,
BlueRock Therapeutics, New York, NY, United States

‡These authors share first authorship

Specialty section:
This article was submitted to Multiple Sclerosis and Neuroimmunology, a section of the journal Frontiers in Immunology

Received: 15 October 2020
Accepted: 29 December 2020
Published: 03 February 2021

Citation:
Reich M, Paris I, Ebeling M, Dahm N, Schweitzer C, Reinhardt D, Schmucki R, Prasad M, Köchl F, Leist M, Cowley SA, Zhang JD, Patsch C, Gutbier S and Britschgi M (2021) Alzheimer's Risk Gene TREM2 Determines Functional Properties of New Type of Human iPSC-Derived Microglia. Front. Immunol. 11:617860. doi: 10.3389/fimmu.2020.617860

gene expression modulation of key regulators of microglia. In conclusion, we have established and validated a work stream to generate functional human iPSC-derived microglia-like cells by applying a directed and neuronal co-culture independent differentiation towards functional phenotypes in the context of AD. These cells can now be applied to study AD-related disease settings and to perform compound screening and testing for drug discovery.

Keywords: iPSC (induced pluripotent stem cell), microglia, cell culture protocols, drug development, TREM2 (triggering receptor expressed on myeloid cells), Alzheimer's disease (AD)

INTRODUCTION

Microglia play a key role in the well-being of the brain by fulfilling various functions in development, homeostasis and the first-line immune defense (1–7). Alzheimer's disease (AD) is a devastating age-related neurodegenerative disorder where microglia have been implicated for over a century in the pathogenesis based on neuropathological findings and by mimicking microglia dysfunction in preclinical models (8). More recently, genome wide association studies substantiated the long-time proposed active implication of microglia within initiation and progression of AD and other neurodegenerative diseases of the central nervous system (9, 10). Together, this strongly supports the rationale for developing therapies that pharmacologically modulate microglia.

In order to facilitate investigating the biology of microglia and to make them available for drug screening assays, cellular models had to be established. Until recently, *in vitro* studies with microglia have been limited to either employing primary rodent cells or cell lines (e.g. BV2) (11). Due to the stress implicated during their isolation process and the loss of tissue context, primary cells rapidly alter their previous *in situ* microglial properties (12, 13), and batch-to-batch variations as well as impurities are known hurdles of this approach. Moreover, generation of primary cells requires either euthanizing large numbers of animals or accessing difficult to obtain highly characterized human brain samples with short postmortem delay. Both approaches result in only a small number of cells, which in turn limits the throughput for compound screening campaigns or larger biological studies (14, 15). In contrast, due to their proliferative nature, cell lines do not have limitations in cell numbers, can be of human origin and are therefore often used in screening setups (16). However, due to their immortalization or neoplastic-origin, cell lines show strong discrepancies compared to the desired *in vivo* characteristics (17, 18).

With the arrival of human induced pluripotent stem cell (iPSC) technology (19, 20), and with the evolving understanding of microglial origin (21–23), several methods were reported for the generation of iPSC-derived microglia-like cells (24–26), hereafter called iPSC microglia. These protocols commonly aim to resemble the yolk sac ontogeny for the generation of primitive macrophage progenitors. Current reports indicate that iPSC microglia seem to be superior to primary cells or cell lines with regard to expressing key microglial marker genes (25). Importantly, unlike primary cells, iPSC microglia or their macrophage precursors can be generated robustly and in a controlled manner in scalable amounts (25, 27). This makes iPSC microglia ideal for drug screening and for extensively studying biological mechanisms under conditions resembling better the physiological state of microglia. Additionally, iPSC based models provide the opportunity to study the effect of disease associated genes with isogenic mutations or knockout pairs.

Despite the advances in developing cell culture models, *in vitro* microglia often lack important properties such as modulating the expression of a fully functional repertoire of various surface receptors, which microglia require to interact with their environment (28). For instance, microglia are the major cell type in the brain to express Triggering Receptor Expressed On Myeloid Cells 2 (TREM2). Signaling through this receptor modulates crucial microglia functions such as phagocytosis, proliferation, survival, and lipid metabolism in homeostatic, inflammatory or neurodegenerative conditions [extensively reviewed in (29, 30)]. Mutations in TREM2 are associated with an increased risk to develop various neurodegenerative disorders including AD (9, 10, 31–36). In the context of amyloid plaques, a neuropathological hallmark of AD, TREM2 was found in preclinical experiments to be essential for the metabolic fitness and transition of homeostatic to disease-associated microglia (DAM) (37, 38). Although the function and role of TREM2 in AD pathogenesis remains unclear, it became a key target for potential therapeutic intervention (39–41).

Some TREM2 loss-of-function-related phenotypes in the context of AD were recently described by others in iPSC-derived microglia (42–45). While the literature about iPSC microglia is growing, more descriptions are needed to compare different approaches that generate robust and scalable human cellular models of microglia. Such cellular models of microglia will hopefully become soon more translatable to microglia in the brain thereby establishing themselves as valuable tools to study disease mechanisms and to perform compound screens for drug development *in vitro*.

Here, we present the optimization of a protocol to generate iPSC microglia in a monoculture condition and explored whether these cells can serve as a model to study microglia function and gene expression in the context of TREM2 modulation. Building on our previously published large scale differentiation protocol of myeloid progenitors from iPSC (27), we have extended the differentiation of these myeloid progenitors for additional 14 days to microglia-like-cells. As a major distinction from previously published co-culture methods, we observed in iPSC microglia from monoculture an increased TREM2 mRNA expression. The regulatory function of

TREM2 in these cells was confirmed by comparing wild type with isogenic TREM2 knock-out iPSC microglia. The overall approach resulted in a work stream to generate human iPSC microglia by a directed and neuronal co-culture independent differentiation resulting in distinct phenotypes for mechanistic studies in AD. Our iPSC microglia protocol can now be applied to scale up the production of these cells, study certain AD-related disease settings, and perform compound screening and mechanistic experiments in drug development.

MATERIALS AND METHOD

iPSC Culture

All work with human iPSC and the derived cell types was performed under the respective Swiss legislation, ethical guidelines, and approval. All media compositions are summarized in **Table S1**. We recently reported an improved and highly scalable variant of the method published by van Wilgenburg et al. (27, 46) for the differentiation of iPSC to primitive macrophages. In brief, for iPSC maintenance culture dishes (Corning) were coated with 12.5 µg/ml rhLaminin-521 (BioLamina). Human iPSC were seeded and cultured in mTesR1 media (StemCell Technologies) at 37°C with 5% CO_2 and media was changed daily. Cells were passaged at 90% confluency, media was removed, cells were washed 1x with PBS and detached with Accutase™ (Innovative Cell Technologies) for 2 to 5 min at 37° C. After removal of Accutase™ by centrifugation cells were either used for maintenance or start of differentiation. The cell lines used in this study, Bioneer WT (BIONi010-C) and Bioneer C17 (BIONi010-C17/TREM2 KO) were obtained from Bioneer. Cells were quality controlled by STR profiling, SNP phenotyping and karyotyping after banking. To avoid genetic drift and variations sub-culturing was limited to an absolute minimum.

Differentiation of iPSC to Primitive Macrophages

Embryoid Body (EB) Generation

This step was performed as previously described (27). Briefly, to obtain uniform EBs, iPSCs were seeded into AggreWell 800 (StemCell Technologies) plates. Two ml mTesR1, supplemented with 10 µM ROCK inhibitor (Y27632, StemCell Technologies) and containing a single cell suspension of $4*10^6$ iPSCs were added to each AggreWell and centrifuged for 3 min at 100xg to assure an even and fast distribution of the iPSC into the AggreWells. The next day, mesoderm and subsequent hemogenic endothelium induction was started by exchange of 75% of the mTeSR1 media with mTeSR1 media supplemented with 50 ng/ml rhBMP4 (biotechne), 50 ng/ml rhVEGF (biotechne), and 20 ng/ml rhSCF (biotechne), and repeated the following 2 days.

Plating of EBs and Continued Maturation Along the Myeloid Lineage

On day 4 of differentiation, EBs were harvested and transferred to factory media, consisting of X-VIVO 15 media (Lonza) supplemented with 2 mM GlutaMAX (Thermo Fisher Scientific), 10 U/ml Penicillin/Streptomycin (Thermo Fisher Scientific), 50 µg/ml Mercaptoethanol (Thermo Fisher Scientific), 100 ng/ml rhM-CSF (Miltenyi Biotech), and 25 ng/ml rhIL3 (Miltenyi Biotech). EBs were plated at a density of 1 EB/cm^2 in growth factor reduced matrigel (Corning) precoated cell culture vessels and myeloid factories were matured as described previously (25).

Macrophage Progenitor Harvesting

Macrophage progenitors were collected from the supernatant by centrifugation (4 min, 300xg) and were either matured into co-culture or monoculture microglia-like cells (**Figure 1A**).

Differentiation of iPSC Into Microglia-Like Cells in Co-Culture

Induced pluripotent stem cells were differentiated to neurons using a protocol that was previously published (47). Neurons were quickly thawed at 37°C and seeded at a density of 200,000 cells/cm^2 in neuronal differentiation media [consisting of 1:1 Advanced DMEM/F12 media (with GlutaMAX I) (Thermo Fisher Scientific) and Neurobasal media (Thermo Fisher Scientific) + 1% B27 supplement without vitamin A (Thermo Fisher Scientific), 1% N2 supplement (Thermo Fisher Scientific), 50 µg/ml Beta-Mercaptoethanol (Thermo Fisher Scientific), 10 U/ml Penicillin-Streptomycin (Thermo Fisher Scientific), 20 ng/ml rhBDNF (PeproTech), 10 ng/ml rhGDNF (PeproTech), 100 µM Aa2-P (Sigma Aldrich), 500 µM cAMP (BIOLOG Life Science), and 1 µg/ml murine laminin (Roche), supplemented with 10 µM ROCKi (Y27632, StemCell Technologies) for seeding]. After a 100% media change one day after seeding, 50% of the media was changed twice a week. After 14 days, macrophage precursor cells were added at a density of 160,000 cells/cm^2. Therefore, the media was replaced with a macrophage precursor cell suspension in N2 media [Advanced DMEM/F12 + 1% N2 supplement, 10 U/ml Penicillin-Streptomycin, 2 mM Glutamax, 50 µg/ml β-ME, 100 ng/ml rhIL34 (Miltenyi Biotech), and 10 ng/ml rhGM-CSF (biotechne)]. Half of the media was changed twice a week for two additional weeks.

Differentiation of iPSC to Microglia-Like Cells in Monoculture

Initially, different variations of coating and media were tested (indicated in figure legends). For the final protocol flasks and plates were coated with fibronectin. Fibronectin (Corning, 10 µg/ml in $PBS^{-/-}$) was added and incubated for 3 h at RT, before washing three times with water. Macrophage precursors were seeded in RPMI media [RPMI 1640 media (Thermo Fisher Scientific) + 10 U/ml P/S supplemented with 100 ng/ml rhIL34, 25 ng/ml rhM-CSF, and 50 ng/ml rhTGF-β1 (PeproTech) at a density of 160,000 cells/cm^2]. Half the media was changed twice a week for 14 days. On day 14, cells were replated by collecting cells from the supernatant and detaching adherent cells with Accutase™. These cells were replated into fibronectin pre-coated assay plates and cultured for at least two additional days prior to the assays.

Magnetic-Activated Cell Sorting (MACS)

For the separation of co-cultured iPSC-derived microglia-like cells from neurons and astrocytes, immunomagnetic separation

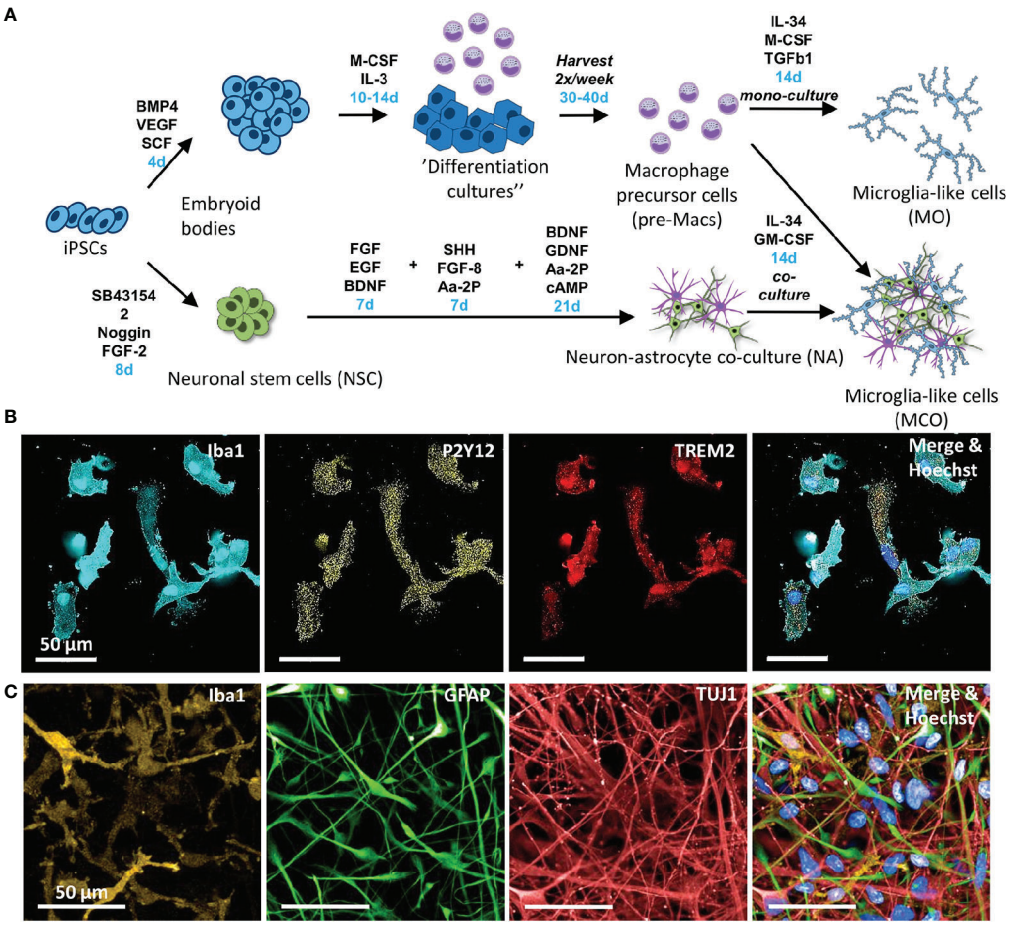

FIGURE 1 | Approaches employed to differentiate human iPSC towards microglia-like cells. **(A)** Schematic diagram of the protocols to generate different microglia-like cells from human iPSC. Relevant growth factors and durations (blue) of differentiation steps are indicated. The upper part depicts the differentiation of iPSCs into "myeloid factories" that produce macrophage precursor cells (pre-Macs) (27). For the generation of monocultured iPSC-derived microglia, pre-Macs were differentiated in the presence of IL-34, M-CSF, and TGF-β1. The lower part depicts the differentiation steps from iPSCs to neural stem cells and further to neurons. For the generation of neural co-culture-derived microglia, pre-Macs were seeded on top of the neuron/astrocyte cultures. **(B)** Representative images of immunostaining of iPSC microglia after 24 days differentiation in monoculture. Monoculture-derived microglia-like cells stain positive for Iba1 (cyan), P2Y12 (yellow), and TREM2 (red). Cellular nuclei were labeled with Hoechst 33342 (blue). **(C)** Immunostaining of microglia-like cells, neurons and astrocytes after 14 days differentiation in co-culture. Representative images are shown from three biological replicates. Microglia-like cells are detected by Iba1 (orange), astrocytes by GFAP (green), and neurons by TuJ1 (red), respectively. Cellular nuclei were labeled with Hoechst 33342 (blue).

was applied. Cells were detached after 14 days in co-culture by incubation with accutase at 37°C for 45 min. After centrifugation at 300xg for 5 min, the cells were resuspended in N2 media containing 100 U/ml DNaseI (Roche) and incubated at RT for 10 min to minimize the amount of free-floating DNA and cell aggregates. Then, the cell suspension was filtered through a 70 µm cell strainer (Greiner). Magnetic labeling and magnetic separation using the autoMACSpro (Miltenyi Biotec) was performed using anti-CD45 MicroBeads (Miltenyi Biotech), following the CD45 MicroBeads separation manual, provided by Miltenyi Biotech. Higher specificity of antigen-binding was achieved by the addition of 12.5 µg/ml Fc Block (BD Biosciences) during incubation with the MicroBeads. Microglia-like cells were obtained in the positive selection.

Quantitative Real-Time PCR

Cells were lysed and the RNA purified using the High Pure RNA Isolation Kit from Roche following the provided protocol. Macrophage precursor cell aggregates were lysed directly after the harvest, microglia-like cells, derived using the monoculture protocol were lysed directly in the cell culture plate. Co-cultured microglia-like cells were lysed directly after MACS.

For a one-step reverse transcription and PCR, the AgPath-ID One-Step RT-PCR kit (Thermo Fisher) was used. It contains an enzyme mix of reverse transcriptase and DNA polymerase. The reaction mixture was prepared according to the manufacturers descriptions and reverse transcription as well as PCR performed in LightCycler 480 384-well plates in a LightCycler 480 II (Roche) (reverse transcription for 10 min at 45°C, reverse

transcriptase inactivation and initial denaturation for 10 min at 95°C, 50 cycles of 15 s denaturation at 95°C and 60 s annealing at 60°C). PPIA was used as a housekeeping gene and was detected simultaneously with the gene of interest using two different dyes (VIC for PPIA, FAM for the gene of interest). Specificity of the readout was ensured using no-enzyme and no-primer controls. A detailed list of the primers used can be found in **Table S2**.

RNAseq and Data Analysis

Characterization by Bulk RNA Sequencing

Induced pluripotent stem cell derived macrophage progenitors, co- and monoculture microglia were generated as described above. Co-cultured microglia were purified as described above. All cultures were started at five different days to obtain five independent replicates for the RNAseq experiment. Cells were lysed and the RNA purified as described above. RNA purity was assessed using the Agilent 2100 Bioanalyzer. Strand-specific mRNA-seq libraries were generated from 1 µg total RNA using the TruSeq Stranded mRNA library prep kit (Illumina) according to manufacturer's instructions. Briefly, mRNA was purified from total RNA by polyA capture, fragmented and subjected to first-strand cDNA synthesis. The second-strand synthesis was performed incorporating dUTP instead of dTTP to ensure strand-specificity. Barcoded DNA adapters were ligated to both ends of the double-stranded cDNA and subjected to PCR amplification. The resulting libraries were checked on an AATI Fragment Analyzer, quantified with Qubit and pooled. The resulting library pool was diluted for cluster generation on the cBot2 and finally sequenced on the Illumina HiSeq 4000 platform.

RNAseq Analysis

Base calling was performed with BCL to FASTQ file converter bcl2fastq v2.17.1.14 from Illumina (https://support.illumina.com/downloads.html). In order to estimate gene expression levels, paired-end RNASeq reads were mapped to the human genome (build hg38) with STAR aligner version 2.5.2a using default mapping parameters (48). Aligned reads were quality checked with FastQC and MultiQC version 1.7 (49, 50). Numbers of mapped reads for all RefSeq transcript variants of a gene (counts) were combined into a single value by using SAMTOOLS software (51) and normalized as rpkms (number of mapped reads per kilobase transcript per million sequenced reads (52),. RNA-seq data have been deposited in Gene Expression Omnibus (GEO accession number GSE159108).

Principal Component Analysis and Heatmaps

Principal component analysis (PCA) of the gene expression profiles was generated using ClustVis (53). Each dot in the PCA plot is a biological replicate. Heatmaps were generated using ClustVis and default settings (53).

Generation of MA Plots

To visualize changes in gene expression between different conditions MA plots were generated. The MA plots are based on gene expression levels measured in $\log_2$(RPKM), the logarithm to the base of two of the reads per kilobase of transcript per million reads sequenced. The x axis shows, for every gene, the average expression value between the two conditions that were compared. On the y axis, the difference between the two expression levels for every gene is depicted. Each gene is represented by a single dot. Some strongly affected genes were highlighted in yellow, with gene names specified.

Microglia Expression Modules

Microglia expression modules were derived from the publication of Friedman et al. (54) and complemented by two modules (DAM signatures TREM2 dependent and TREM2 independent) derived from the publication of Keeren shaul et al. (38). Gene list for expression modules can be found in **Table S3**. Differences between two groups in these expression modules were visualized in a Radar plot using python.

Gene Ontology Analysis

A gene ontology analysis was performed that used the differentially expressed genes that showed at least four RPKM difference between WT and TREM2 KO. The GO terms were condensed using the GO slim immune response tool from dice tools (55).

Immunofluorescence Staining

Cells were fixed by replacing the medium with 4% PFA (Thermo Fisher Scientific, in PBS) followed by incubation at RT for 15 min. After washing three times using PBS, the cells were permeabilized by incubation in 0.1% PBS-T [0.1% Triton-X-100 (Sigma Aldrich) in PBS] for 15 min at RT. Following another washing step, non-specific binding sites were blocked by incubation in SuperBlock (Thermo Fisher Scientific) for 60 min at RT. The primary antibody was added in SuperBlock and incubated overnight at 4°C. Iba1, TREM2 and P2Y12 were added together, as well as Iba1, TuJ1, and GFAP. For the no-primary antibody controls, only SuperBlock was added. Following three washing steps, the cells were incubated with the three respective secondary antibodies (donkey anti-goat AF555, donkey anti-mouse AF647 and donkey anti-rabbit AF488, in SuperBlock) for 90 min at RT in the dark and unbound antibodies removed in two washing steps. Nuclei were counterstained with Hoechst33342 (Invitrogen, in SuperBlock) in the dark at RT, followed by two washing steps. The cells were kept in PBS and images acquired using the 63x objective of an OperaPhenix (Perkin Elmer). Images were processed and analyzed using the built-in Harmony software. The no-primary antibody control was used for background correction. A complete list of the antibodies used can be found in **Table S4**.

Mitochondrial Respiration Assay

The assay was performed using the Seahorse XF Cell Mito Stress Test kit (Agilent). Cells were differentiated as described above (14 days monoculture microglia like) and, in a Seahorse XF96

cell culture microplate, 50,000 cells (480,000 cells/cm^2) were seeded two days prior to the experiment. On the day of the experiment, the medium was replaced with 180 µl media for the mitochondrial respiration stress test (base medium + 2 mM L-glutamine (Thermo Fisher Scientific), 1 mM sodium pyruvate (Thermo Fisher Scientific), and 0.45% glucose (Sigma Aldrich), pH 7.4). Prior to the experiment, the cell culture microplate was incubated for 1 h at 37 ˚C in a non-CO_2 incubator. The assay was performed using a Seahorse XFe 96 Analyzer and compounds (prepared according to the assay manual) were injected sequentially (1 µM oligomycin, 2 µM FCCP, and 500 mM rotenone/antimycin A) and the oxygen consumption rate (OCR) measured three times before treatment and after every injection. Data was processed and analyzed using the Seahorse Wave software. For normalization, cells were fixed with 4% PFA at 37°C for 15 min and nuclei stained with Hoechst 33342 for 15 min, before washing twice with PBS. The Operetta CLS high-content screening system (Perkin Elmer) was used for imaging nuclei counted and the ratio between cell types calculated.

Transwell Migration Assay

Cells were differentiated as described above (14 days monoculture microglia like), detached from the dishes with accutase and plated at a density of 8,000 cells per well in a 96-well IncuCyte ClearView cell migration plate (Essen BioScience). In the lower compartment, either recombinant human complement C5a (biotechne, 1 ng/ml) or solvent control were added as chemoattractant, which generates by natural diffusion a gradient of the chemoattractant. Plates were incubated in an IncuCyte S3 (Essen BioScience) and images acquired using the 10x objective every 4 h for upper and lower well. Migration was assessed for 72 h and quantified using the Incucyte software Migration Analysis tool.

Determination of Free Intracellular Ca^{2+}

Cells were differentiated as described above (14 days monoculture microglia like) and 8,000 cells were plated per well of a 384 well plate. For calcium measurements, cells were incubated with the FLIPR calcium 6 imaging dye (Molecular Devices) following the manufacturer's instructions. Briefly, dye was dissolved in 10 ml of assay buffer 1 and 20 µl per well were added to the cells. Cells were incubated for 2 h with the dye. Increase in cytosolic calcium in response to ATP (Thermo Fisher Scientific), ADP (Sigma Aldrich), as well as C5a was assessed using the Hamamatsu FDSS7000 detection system. Background signal (average of 10 pictures prior to addition of stimuli) was subtracted from the measured maximum following stimulation. RFU values were assessed per well.

Phagocytosis Assay

Cells were differentiated as described above (14 days monoculture microglia like) and 40,000 cells were plated per well of a 96 well plate (Falcon 353219). For the phagocytosis assay, cells were incubated with Abeta coated, pHrodo labeled beads. To obtain these beads Amidine Latex Beads (A37322/Thermo Fisher Scientific) were washed once with PBS, pelleted by centrifugation (16,000 g/5 min) and incubated at 37°C overnight in PBS containing 1 mg/ml Aβ42 (AnaSpec). After incubation with Aβ42 beads were pelleted, washed with PBS and re-suspended PBS containing 0.2 mg/ml pHrodo™ Red, succinimidyl ester (pHrodo™ Red, SE/Thermo Fisher Scientific). Beads and pHrodo were incubated for 1 h at room temperature. After the incubation, beads were washed with PBS and re-suspended in PBS. Phagocytosis of beads was monitored using Incucyte S3 acquiring brightfield and red fluorescence images. Cells were recognized using the Incucyte software adherent cell-by-cell classification tool.

Statistics

Unless otherwise mentioned, all data values are expressed as means ± standard deviation (SD). Unless otherwise indicated, experiments were performed at least three times (i.e., using three different cell preparations), with at least three technical replicates per condition. Statistical methods for analyzing the various data sets are indicated directly in the figure legends, data were analyzed using Graphpad Prism software.

RESULTS

For the generation of iPSC microglia many protocols still mostly rely on co-culturing microglia with neurons, astrocytes or neurons and astrocytes to mimic the brain environment (25, 26, 56). However, for drug screening purposes, e.g., with functional cellular assays, pure cultures of monolayer cells are highly desirable. One key aspect is to achieve proper microglia morphology *in vitro* in order to establish their functional phenotype as well (8).

In our hands, using the media condition that was closest to the previously published approach to generate iPSC microglia in monoculture (25), the cells showed only little ramifications (**Figure S1** N2, IL34, GM-CSF, Fibronectin). To increase ramification and marker gene expression of iPSC monoculture microglia, we began to screen existing protocols and tested six different media conditions (either N2 or RPMI media supplemented with either IL34+GM-CSF, IL34+M-CSF+TGF-β1 or IL34+M-CSF+TGF-β+CD200+CX3CL1) in combination with six different matrix coatings (Tissue culture treated only, Poly-D-lysine, CollagenI, Gelatin, Fibronectin, or Laminin) (**Figure S1A**). Conditions, where cells displayed ramifications, were chosen for follow up qPCR analysis (**Figure S1B**). Strongest differences between the different cultures were observed for key regulatory receptors of microglia such as fractalkine receptor CX3CR1, ADP chemoreceptor P2Y12, receptor tyrosine kinase AXL and lipoprotein lipase LPL mRNA expression. Based on the morphology and only minor differences upon CD200 and CX3CL1 addition for the last three days of differentiation, we chose for further analysis the condition of RPMI supplemented with IL-34, M-CSF and TGF-β1 on fibronectin coating (**Figure S1A** and **Figure 1A** for timeline). Under this condition, we confirmed the expression of P2Y12 on protein level by immunocytochemistry as well (**Figure 1B**). The iPSC microglia from monoculture displayed a similar morphology as the co-culture iPSC microglia (**Figure 1C**) suggesting that the fibronectin matrix resembles aspects of the matrix found in co-cultures.

To benchmark the microglia monoculture model towards iPSC microglia in co-culture with iPSC-derived neurons, we performed magnetic-activated cell sorting to remove the neurons and compared the microglia based on their bulk RNA-seq profile. A principal component analysis (PCA) demonstrated a sufficient cellular differentiation of the mono- and co-culture derived microglia with their common macrophage precursor (pre-Macs) (**Figure 2A**). Similarly, gene expression profiling between mono- versus co-cultured microglia revealed a higher expression of ENPP2, FOSB,CCL13, F13A1, IL1B, CD74 in microglia co-cultured with iPSC-derived neurons, whereas monocultured microglia expressed higher levels of ID1, LINC01235, MRC2, FABP4, TIMP3, APOE, and SPP1 (**Figure 2B**). Together, this confirms that the mono- and co-culture conditions induce two different microglia subsets.

Microglia are highly plastic cells that can change their morphological and functional phenotype as a reaction to different stimuli (8). Such stimuli can derive from environmental alterations in the brain due to aging and neurodegeneration. In support of this, comprehensive RNA-seq analyses of microglia isolated from human and mouse brain in an AD or other neurodegenerative disease context indicate an association between gene transcription pattern and a specific activation state of microglia. Recently, different transcription patterns were proposed to categorize microglia into different subsets (38, 54, 57, 58). In that context the

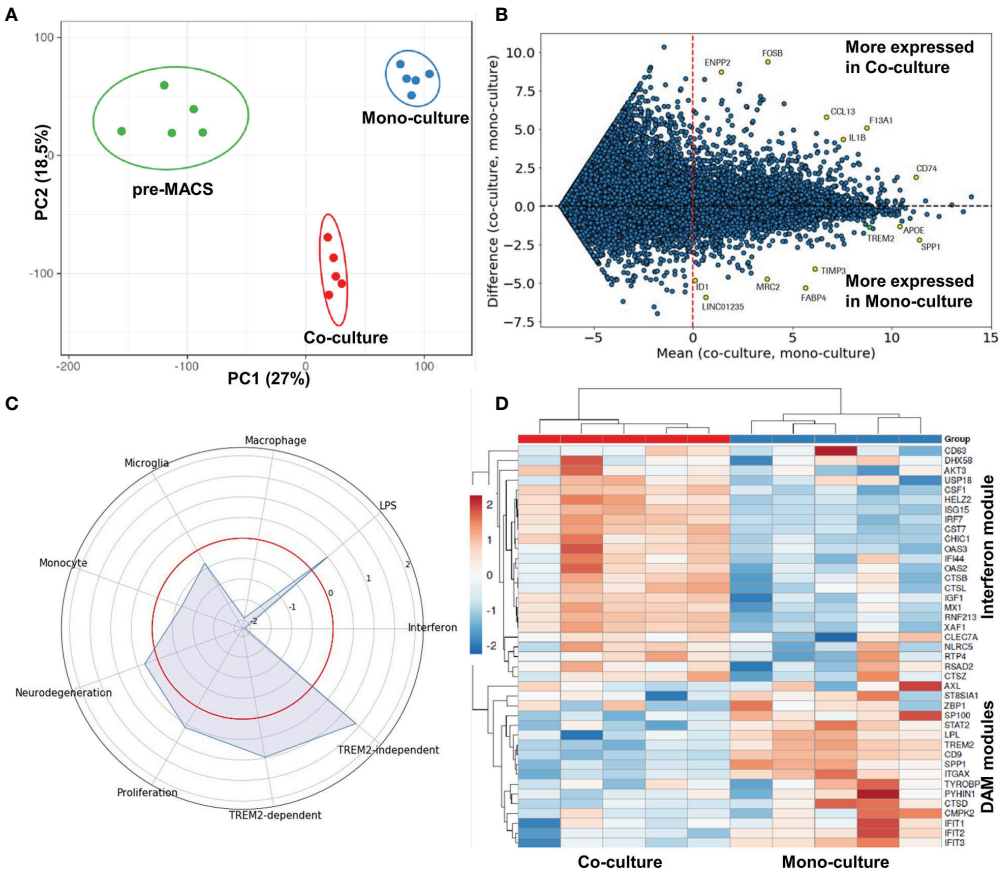

FIGURE 2 | Comparison of gene expression profiles in mono- and co-culture-derived microglia. **(A)** Principal component analysis of complete expression profiles of macrophage precursors (pre-MACS), mono- and co-cultured microglia-like cells. The lack of any intersection between the ellipses (95% confidence interval) indicates a clear statistically significant separation between the gene patterns of the different cell types. **(B)** MA plot to visualize gene expression differences between mono- and co-culture-derived microglia-like cells. The MA plot is based on gene expression levels measured in $\log_2$(rpkm), the logarithm to the base of two of the reads per kilobase of transcript per million reads sequenced. The x-axis shows, for every gene, the average expression value between the two conditions, on the y-axis is, for every gene, the difference between the two expression levels. Some strongly affected genes are highlighted in yellow, with gene names specified. **(C)** Radar plot to visualize changes in gene expression in microglial modules. The red circle indicates the reference level as detected in co-cultured microglia. Peaks outside the red circle indicate higher expression in monoculture microglia and modules closer to the center indicate higher expression in microglia generated in co-culture with neurons. **(D)** Heatmap of the genes belonging to the DAM or interferon module in co- and monoculture derived microglia. Expression values were standardized and depicted on a z-scale with red indicating high and blue low expression, respectively. The five red and five blue boxes on top of the heatmap indicate the two different culture conditions, respectively, and that each culture condition was performed in five independent experiments. The downregulation of the "interferon" module and the upregulation of "DAM" modules is consistent between different experiments as indicated by the similar gene expression patterns between different biological replicates. This confirms the robustness of our new protocol.

upregulation of APOE and SPP1 as observed in our monoculture condition is part of a DAM signature (38). This indicates that in contrast to the co-culture condition, our monoculture condition provides stimuli that drive iPSC microglia towards a more disease associated expression pattern.

In order to explore the transcriptional pattern of the monoculture microglia further and to gain more insight into the different stimuli that possibly induced the transcriptional phenotype, we defined nine different modules of microglia states based on published data sets (See **Table S3** for the names of the genes and of the different modules) (38, 54). We then mapped the differences in gene expression profiles of the two culture conditions towards these modules (**Figure 2C**). Our mono- and co-culture iPSC microglia were similar in the "microglia" module validating the chosen differentiation conditions to generate microglia. The most prominent differences were observed for "macrophage" and "interferon" modules, which were lower expressed in the monocultured iPSC microglia. The reduced "interferon" signature is most likely attributed to the change from GM-CSF supplementation in co-culture to M-CSF supplementation in monoculture (59). The lower "macrophage" signature combined with the also slightly reduced "monocyte" module indicates an even stronger differentiation away from the peripheral myeloid cells than the co-cultured microglia. Furthermore, we observed upregulation of "TREM2-dependent" and "TREM2-independent" modules suggesting a more DAM-like phenotype for iPSC microglia in monoculture compared with microglia from co-culture. The downregulation of the "interferon" module and the upregulation of "DAM" modules is consistent between different experiments as indicated by the similar gene expression patterns between different biological replicates (**Figure 2D**).

At this point, we wanted to complement the DAM-like gene expression pattern of our monoculture iPSC microglia with functional data. Given the implication of TREM2 in the DAM-like expression pattern and the association of TREM2 with AD we focused on modulating this gene. To that end, we employed the isogenic TREM2 knock-out (KO) of the same iPSC line and differentiated the two cell lines in parallel in the same monoculture condition. As before, we first made sure there is an effect of TREM2 KO on a gene expression level. The PCA revealed a minor but clear separation in RNAseq-based gene expression between iPSC-derived microglia and their isogenic KO form (**Figure 3A**). The majority of differentially regulated genes were downregulated in the KO compared to the cells having functional TREM2 (**Figure 3B**). This included DAM-signature associated genes and became evident in the module analysis as well (**Figure 3C**). The iPSC-derived microglia lacking TREM2 also displayed an upregulation of the interferon, proliferation and macrophage module, while the monocyte and neurodegeneration module were downregulated. Confirming the genotype, TREM2 independent DAM signature stayed unaffected by the loss of TREM2. The upregulation of the "interferon" module and the downregulation of "DAM" modules in the TREM2 KO microglia compared with wild type cells is consistent and robust between different experiments as indicated by the similar gene expression patterns between different biological replicates (**Figure 3D**). A gene ontology (GO) term analysis revealed that in iPSC-derived microglia lacking TREM2 "myeloid cell homeostasis", "myeloid cell development", and "myeloid progenitor cell differentiation", and GO terms related to cell adhesion, motility, and migration as well as lipid metabolism and mitochondrial organization were enriched (**Figure S2**, red boxes). Together, this indicates that the transcriptional phenotypes of the TREM2 KO and wild type iPSC microglia are sufficiently different from each other in order to expect functional differences as well.

To confirm some of the GO term associated functions and to explore feasibility of functional assays with microglia from our monoculture condition, we subsequently tested iPSC-derived microglia for their mitochondrial activity, cellular calcium responses and migratory capacity. First, we used Seahorse extracellular flux analysis to assess mitochondrial respiration. TREM2 KO microglia displayed a significantly lower basal mitochondrial respiration (**Figure 4A, B**), spare respiratory capacity (**Figure 4C**), and less ATP production (**Figure 4D**), while there was no significant difference detected in the proton leak (**Figure 4E**) when compared to isogenic wild type iPSC microglia, indicating reduced use of the respiratory chain for ATP production.

Microglia continuously monitor their environment and can react to damage signals (e.g., ADP/ATP released by dying neurons, local activation of complement pathways in the aging brain and in neurodegeneration), i.e., by directed migration to the damage site (60). Many of the microglial receptors rely on changes of free intracellular calcium levels to mediate the internal signal transmission and integration. For instance, chemoattractants and damage-associated molecules signal through GPCR receptors thereby increasing intracellular calcium levels. To check for this functionality, we stimulated the cells with different concentrations of the typical chemoattractants and damage signals ADP, ATP and complement factor C5a (**Figures 5A–C**) and monitored the related intracellular calcium changes. The anaphylatoxin C5a is a well-described chemoattractant for innate immune cells that can be employed in cell culture (27). In an *in vivo* setting light induced microglial migration in the retina has been reported to be C5aR dependent (61) and in context of AD recent reports suggest a role of C5a in the regulation of microglial inflammatory response (62). ATP and its metabolites are also well-described chemoattractants for microglia through their plethora of receptors (63–65) Confirming the GO term result, TREM2 KO cells reacted already at lower concentrations and with a higher maximum to all three stimuli than their isogenic wild type iPSC microglia. This indicates a potentially more rapid signal integration in the TREM2 KO versus the wild type microglia. This is supported by a slightly elevated baseline migratory phenotype, and much more by the robust almost doubling of the migration speed of TREM2 KO versus wild type microglia upon stimulation by C5a (**Figure 5D**).

Phagocytosis and in particular uptake of Aβ—a major component of senile plaques in the AD brain—is a prominent function of microglia, which according to preclinical *in vitro* and *in vivo* models is reduced by TREM2 loss of function (39, 66–68). In line with literature, we observed a strongly diminished uptake

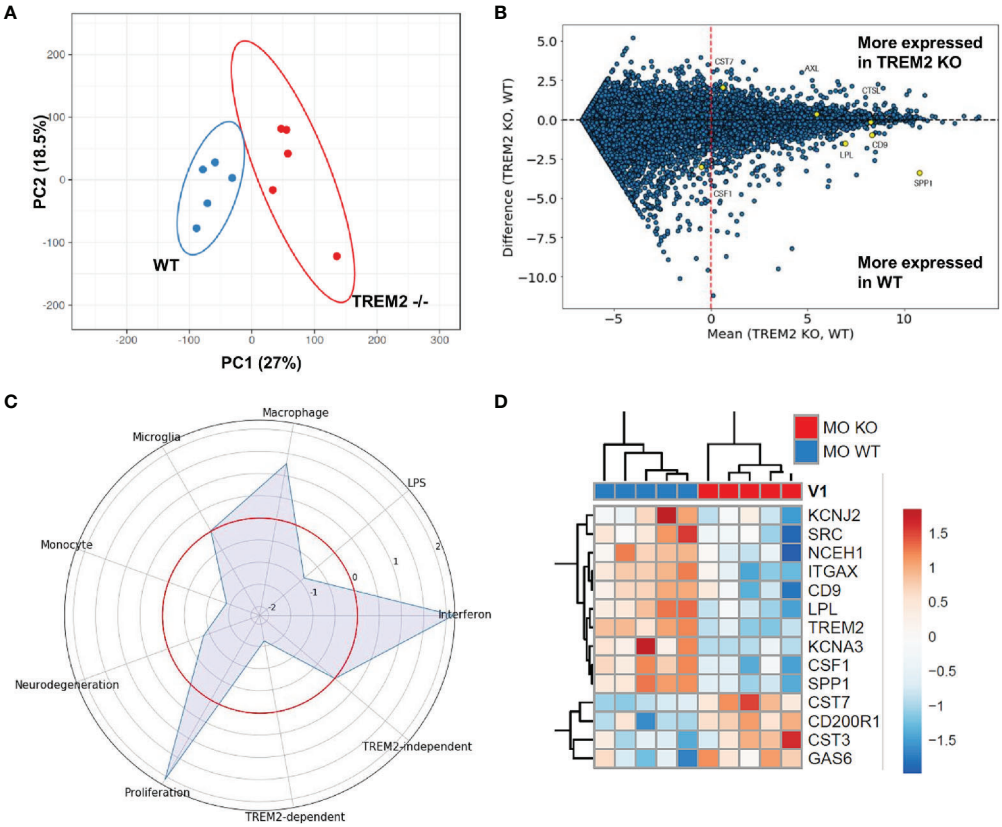

FIGURE 3 | Differences in gene expression in wild type and TREM2 KO monoculture-derived iPSC microglia. **(A)** Principal component analysis of complete expression profile of monoculture derived microglia-like cells generated from wild type (WT) and TREM2 knockout (KO) iPSC lines. The lack of intersection between the ellipses (95% confidence interval) indicate a statistically significant separation between the gene patterns of the two cell types while the fact that the ellipses seem to touch each other indicate only a minimal separation in the PCA. **(B)** MA plot to visualize gene expression differences between WT and TREM2 KO monoculture iPSC microglia. The MA plot is based on gene expression levels measured in $\log_2$(rpkm), the logarithm to the base of two of the reads per kilobase of transcript per million reads sequenced. The x-axis shows, for every gene, the average expression value between the two conditions, on the y-axis is, for every gene, the difference between the two expression levels. Genes highlighted in yellow are part of the TREM2-dependent DAM signature genes according to Keren-Shaul et al. (38). **(C)** Radar plot to visualize changes in gene expression in microglial modules. The red circle indicates the reference level as detected in WT iPSC microglia. Peaks outside the red circle indicate higher expression in TREM2 KO microglia and modules closer to the center indicate higher expression in microglia generated from the WT iPSC line. **(D)** Heatmap of the genes belonging to the DAM module in WT and KO monoculture microglia. Expression values were standardized and depicted as z-scores with red indicating high and blue low expression, respectively. The five red and five blue boxes on top of the heatmap indicate the two different cell types, respectively, and that each cell type was analyzed in five independent experiments. The gene expression patterns for each cell type appear consistent between different experiments. This confirms the robustness of our new protocol for WT and TREM2 KO iPSC microglia.

of Aβ-coated beads by the TREM2 KO compared with the wild type microglia (**Figures 5E, F**) confirming a critical role of TREM2 in regulation of microglial phagocytosis. Together, these functional data confirm the DAM-like phenotype of our iPSC microglia; a phenotype which can be reversed by knocking out TREM2.

In conclusion, the overall results of our different approaches to generate iPSC microglia combined with gene expression and functional phenotypes confirm the feasibility to employ monoculture conditions to generate microglia-like cells, which express relevant functional gene sets including the key surface receptor TREM2. The ability to ablate specific genes such as TREM2 to reverse their DAM-like phenotype make these iPSC microglia a valuable tool for studying biological mechanisms relevant for AD and to perform compound screening and testing for drug discovery.

DISCUSSION

Studying microglia in humans and ultimately finding and testing novel therapeutic approaches targeting these cells remains a huge challenge. This is attributed to the heterogeneity of phenotypes microglia can acquire. For instance, proliferation, migration, phagocytosis, neurotrophic signaling, factor release for the

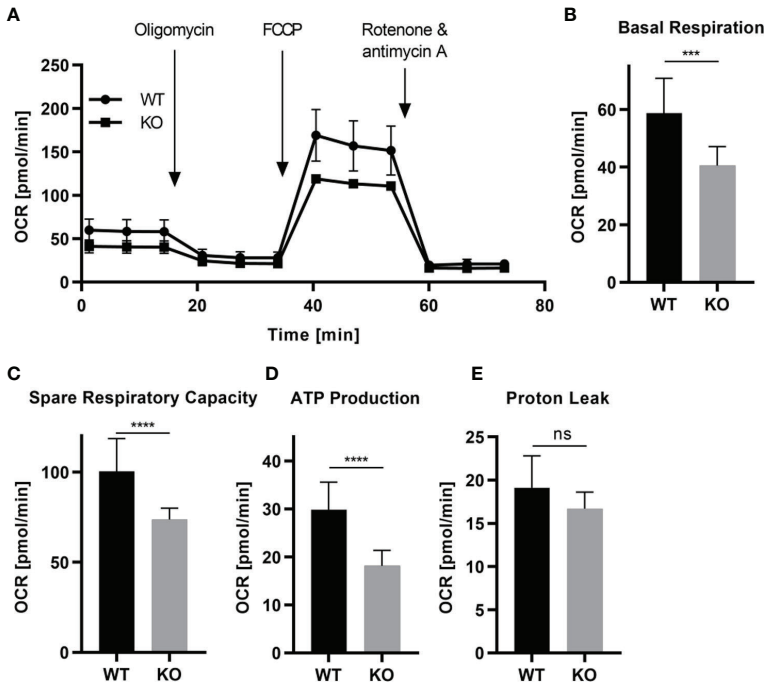

FIGURE 4 | Differential mitochondrial respiratory activity in TREM2 KO versus wild type iPSC microglia. WT and TREM2 KO monoculture iPSC microglia-like cells were re-plated after 14 days of differentiation into fibronectin pre-coated seahorse assay plates **(A–E)**. **(A)** The baseline oxygen consumption rate (OCR) of WT and TREM2 KO cells was assessed, followed by the sequential injection of different indicated mitochondrial electron transport chain complex inhibitors (oligomycin and a combination of rotenone and antimycin A) and the mitochondrial uncoupler carbonyl cyanide-4-(trifluoromethoxy)phenylhydrazone (FCCP). OCR was measured three times initially and after each injection. **(B)** The basal respiration was calculated by subtracting the OCR of non-mitochondrial respiration (OCR after rotenone/antimycin A injection) from the baseline OCR. **(C)** The spare respiratory capacity results from the subtraction of the basal respiration from the maximal respiration [(OCR after FCCP injection) – (non-mitochondrial respiration)]. **(D)** ATP production is the OCR of the basal respiration with the proton leak subtracted. **(E)** The proton leak is the remaining OCR after injection with oligomycin without non-mitochondrial respiration. n=3; Data shown as mean with standard deviation. Statistical analysis was performed using t-test. (ns, $p \geq 0.05$; ***$p \leq 0.001$; ****$p \leq 0.0001$).

modulation of immune function and blood-brain barrier integrity contribute to their high degree of plasticity (1–7, 69). This allows them to react to various cues and to switch between the phenotypes rapidly (8). Moreover, microglia are reported to have different regional abundance and activity states during aging, brain activity and neurodegenerative processes (58, 70–72). In addition, accessing microglia in the human brain is in the majority of cases only possible in postmortem tissue (73).

To overcome the need to study microglia in or isolated from humans, the field investigates rodent microglia *in situ* or as primary cells *in vitro* as a surrogate (38, 74, 75). Apart from the need to use large numbers of animals in order to isolate sufficient quantities of microglia, there are also many technical caveats when using rodent microglia; for instance batch-to-batch variations caused by the isolation process and a rapid switch of their previous gene expression pattern and phenotype (12, 13). Additionally, there are concerns about phenotypes induced by in-breeding, different mouse strains with different immune backgrounds and the often-limited translatability between mice and humans. This inter species translatability is of general concern for all animal models but especially for various receptors and ligands related to innate immunity and particularly microglia (74, 76).

Besides rodent models, microglia like cells have also been derived from human peripheral monocytes (77). These cells have been shown to resemble microglia specific gene signatures and functional properties. However, due to the difference in hematopoietic origin, these cells rather resemble infiltrating monocytes than brain resident microglia (77).

The iPSC technology together with the evolving understanding of microglial origin in mice and humans (21–23) allow now the robust generation of human iPSC-derived microglia-like cells (24–26, 78) in large amounts (25, 27).This provides the opportunity to employ human iPSC microglia for large-scale drug screening and for extensively studying biological mechanisms under more physiological and translational conditions. Additionally, iPSC based models provide the opportunity to study the effect of disease associated genes with isogenic mutation or knockout pairs (42, 43, 45). All of these protocols aim to follow the course of embryonic development and to recapitulate this *in vitro* as far as possible (24–27, 79). For the first part, the generation of myeloid progenitors *via*

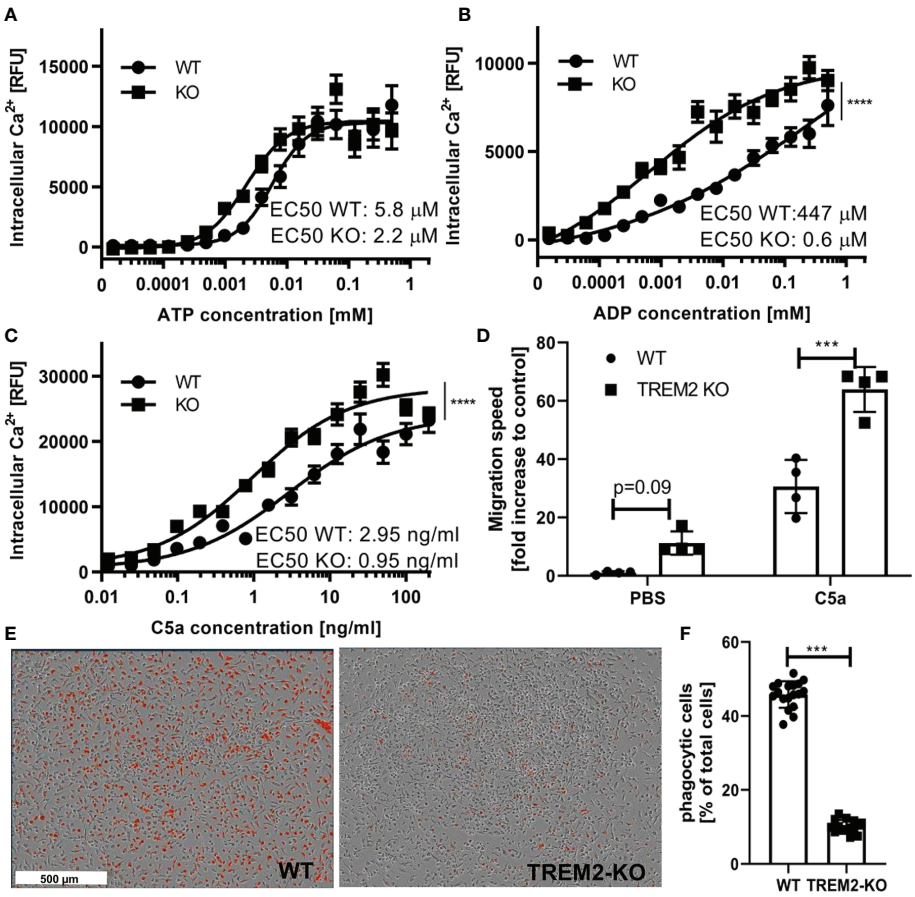

FIGURE 5 | Functional differences in TREM2 KO versus wild type iPSC microglia. **(A–C)** Intracellular calcium kinetics following different stimuli. **(A)** Intracellular calcium levels upon stimulation with different concentrations of ATP. Maximum measured fluorescence is indicated as relative fluorescence units (RFU), which are baseline corrected (n = 3). Data shown as mean with standard error of the mean. Statistical analysis of two data sets was performed using a two-way ANOVA. **(B)** Intracellular calcium levels upon treatment with different concentrations of ADP. Maximum measured fluorescence is indicated as relative fluorescence units (RFU), which are baseline corrected (n = 3). Data shown as mean with standard error of the mean Statistical analysis of two data sets was performed using a two-way ANOVA(****$p < 0.0001$). **(C)** Intracellular calcium levels upon treatment of different concentrations of complement component 5a (C5a). Maximum measured fluorescence is indicated as relative fluorescence units (RFU), which are baseline corrected (n = 3). Data shown as mean with standard error of the mean. Statistical analysis of two data sets was performed using a two-way ANOVA (****$p < 0.0001$). **(D)** Migration speed of WT and TREM2 KO monoculture microglia in presence or absence of 1 ng/ml C5a as chemoattractant in the bottom compartment. Migration speed was calculated from the increase in iPSC microglia occupied area over time in the bottom compartment of the transwell and expressed relative to untreated WT control. Statistical analysis was performed using t-test for PBS and complement C5a condition, respectively (***$p < 0.001$). **(E)** Representative images of WT and TREM2 KO iPSC microglia incubated for 2 h with pH-rodo labeled Aß-coated beads. **(F)** Quantification of pHrodo positive microglia after 2 h incubation with pHrodo labeled Aß-coated beads. n = 3; Data shown as mean with standard deviation. Statistical analysis was performed using t-test (***$p < 0.001$).

transcription factor MYB-independent primitive myelopoiesis, most protocols are broadly similar. However, the challenge for microglia generation as well as for the maintenance of primary microglia lies in the simulation of the correct neuronal microenvironment that determines the final differentiation and is essential for the maintenance of the phenotype (12). Several approaches exist for the *in vitro* simulation of this tissue niche, most of which are based on co-culture approaches with either neurons (25), astrocytes (42) or both. Other approaches use chemokines, morphogens and metabolites to differentiate the microglia-like cells in monoculture (17, 80)

Recently, we demonstrated the scalability of a protocol for the generation of myeloid precursors and primitive macrophages (27). The protocol is based on a publication by van Wilgenburg et al. (46) and cells generated with this differentiation protocol have already been used previously to obtain microglia like cells in co-cultures (2 and 3D) as well as in monoculture (25, 81). However, further optimization of the monoculture protocol seemed desirable. In our study, we aimed for such a reductionist approach of monoculture microglia and compared them on the morphological and gene expression level to the more elaborate co-culture model. Our observations on the

transcriptional as well as on the phenotypic level correlate with the results reported from others (24, 25, 78)and extend these. The constitution of growth factors in our finally chosen microglia differentiation media is similar to the one published by McQuade and colleagues (78). Even though the two protocols differ in mesoderm induction and pre-Mac generation, resulting cells showed similar transcriptional and morphological profiles. However, a key advantage of the protocol shown here is the long lifetime of the myeloid factories, which allows continuous pre-Mac supply over a production period of 60–80 days (27).

We observed on the transcriptional level that monoculture-derived iPSC microglia showed an increase in genes related to the so-called DAM signature compared with neuronal co-culture derived microglia (**Figure 2**). The cell surface receptor TREM2 is part of the DAM signature (37, 38). It is an important molecule for microglia to interact with their environment and mutations in the gene for TREM2 are associated with neurodegenerative disorders including AD (9, 10, 31–36). Due to the importance of TREM2 for microglia and in drug discovery attempts for AD in general, we focused the characterization of our human iPSC microglia on TREM2 related functions and chose a TREM2 KO isogenic pair to further challenge the suitability of our monoculture model in cellular assays. First, we compared the isogenic controls on the transcriptional level and identified differences in genes associated with mitochondrial organization, cell motility and migration. Indeed, we could confirm differences in mitochondrial respiration by the Seahorse assay. Furthermore, we observed different responses in free intracellular calcium following exposure to well-established microglia chemoattractants, and pronounced differences in the migration towards one of these attractants (complement C5a) (**Figures 5A–D**), which is in line with observations by others (82). Furthermore, we demonstrated that the monocultured iPSC microglia are also suitable for phagocytosis assays (**Figures 5E, F**) and confirmed here observations published by others (39, 66–68). TREM2 signals *via* DAP12 and phosphorylation of SYK resulting in phosphorylation of the downstream kinases PI3K, PLCy and ERK (42, 67). These pathways have already been linked to alterations in cell proliferation, survival, metabolism, motility, and phagocytosis (42, 82–84). TREM2 KO has been shown to restore a homeostatic phenotype in AD and SOD models *in vivo* (82, 84). However, our observation that TREM2 KO cells show an increase in proliferative signatures and in motility was rather unexpected. One possible explanation could be that DAP12 may be stronger involved in the integration of other signaling cascades upon TREM2 loss. For the complete understanding of the pathway, we plan to explore the effect of loss of downstream targets on the cellular phenotypes in future studies.

Overall, our monoculture microglia model performed robustly in the applied functional cellular assays, pointing to its suitability to study cellular effects of TREM2 modulation. In a next step, our iPSC microglia model could be applied for cellular screening and profiling of various microglia modulatory pathways in the context of AD or other neurological diseases. Additionally, the established protocol to generate iPSC microglia now forms the basis to expand the single cell type culture with other cell types in order to generate multicellular spheroids and organoids. However, such complex cell models also come with greatly increased cultivation time, limited throughput and reduced number of available readouts (85) and more optimization will be required.

In this study, we have not addressed the suitability of the monoculture microglia system to investigate the effects of other disease-associated mutations or to model aspects of other diseases. However, the transcriptional data set in combination with the microglial module analysis provides a good basis to judge suitability of this model for other purposes. Using this as a starting point, one could test a variety of stimuli and see how they affect the expression in the different modules. Once we know what drives the differentiation of iPSC microglia towards a desired phenotype could enable the development of a toolbox for modeling key aspects of different microglial subtypes in monoculture.

In conclusion, the combined results of our experiments demonstrate that human iPSC microglia can be produced robustly in monoculture and our data confirm that these cells can be used in various microglia-relevant functional assays. Additionally, genetic ablation of TREM2 leads to the expected phenotypes validating these cells as a valuable tool for studying microglia-related biological mechanisms and to perform compound screening and testing for drug discovery.

DATA AVAILABILITY STATEMENT

The datasets presented in this study can be found in online repositories. The names of the repository and accession number can be found here: https://www.ncbi.nlm.nih.gov/geo/, GSE159108.

AUTHOR CONTRIBUTIONS

MB and SG conceived, designed, and supervised the study and SC and ME provided critical scientific input. MR, IP, ND, DR, and CS performed the cellular experiments. FK, MP, RS, and ME did the RNAseq analysis and evaluated the data. SG drafted the article and co-wrote the paper with MB. CP, SC, ML, MR, ME, and JZ revised the article critically. ML academically supervised MR's master's thesis, which is part of this manuscript. All authors contributed to the article and approved the submitted version.

FUNDING

SG was supported by the Roche Postdoctoral Fellowship (RPF) program and IP by the Roche Internships for Scientific Exchange (RiSE) program.

ACKNOWLEDGMENTS

We thank Dr. A. Sierra for academic mentorship of IP and critical feedback on the manuscript. We thank K. Dernick for support with imaging.

SUPPLEMENTARY MATERIAL

The Supplementary Material for this article can be found online at: https://www.frontiersin.org/articles/10.3389/fimmu.2020.617860/full#supplementary-material

REFERENCES

1. Ousman SS, Kubes P. Immune surveillance in the central nervous system. *Nat Neurosci* (2012) 15:1096–101. doi: 10.1038/nn.3161
2. Paolicelli RC, Bolasco G, Pagani F, Maggi L, Scianni M, Panzanelli P, et al. Synaptic Pruning by Microglia Is Necessary for Normal Brain Development. *Science* (2011) 333:1456–8. doi: 10.1126/science.1202529
3. Parkhurst CN, Yang G, Ninan I, Savas JN, Yates JR,3, Lafaille JJ, et al. Microglia promote learning-dependent synapse formation through brain-derived neurotrophic factor. *Cell* (2013) 155(7):1596–609. doi: 10.1016/j.cell.2013.11.030
4. Schafer DP, Lehrman EK, Kautzman AG, Koyama R, Mardinly AR, Yamasaki R, et al. Microglia sculpt postnatal neural circuits in an activity and complement-dependent manner. *Neuron* (2012) 74:691–705. doi: 10.1016/j.neuron.2012.03.026
5. Shigemoto-Mogami Y, Hoshikawa K, Goldman JE, Sekino Y, Sato K. Microglia Enhance Neurogenesis and Oligodendrogenesis in the Early Postnatal Subventricular Zone. *J Neurosci* (2014) 34:2231–43. doi: 10.1523/JNEUROSCI.1619-13.2014
6. Sierra A, Encinas JM, Deudero JJ, Chancey JH, Enikolopov G, Overstreet-Wadiche LS, et al. Microglia shape adult hippocampal neurogenesis through apoptosis-coupled phagocytosis. *Cell Stem Cell* (2010) 7:483–95. doi: 10.1016/j.stem.2010.08.014
7. Zhou L-J, Peng J, Xu Y-N, Zeng W-J, Zhang J, Wei X, et al. Microglia Are Indispensable for Synaptic Plasticity in the Spinal Dorsal Horn and Chronic Pain. *Cell Rep* (2019) 27:3844–3859.e6. doi: 10.1016/j.celrep.2019.05.087
8. Sierra A, Paolicelli RC, Kettenmann H. Cien Anos de Microglia: Milestones in a Century of Microglial Research. *Trends Neurosci* (2019) 42:778–92. doi: 10.1016/j.tins.2019.09.004
9. Kunkle BW, Grenier-Boley B, Sims R, Bis JC, Damotte V, Naj AC, et al. Genetic meta-analysis of diagnosed Alzheimer's disease identifies new risk loci and implicates Aβ, tau, immunity and lipid processing. *Nat Genet* (2019) 51:414–30. doi: 10.1038/s41588-019-0358-2
10. Lambert J-C, Ibrahim-Verbaas CA, Harold D, Naj AC, Sims R, Bellenguez C, et al. Meta-analysis of 74,046 individuals identifies 11 new susceptibility loci for Alzheimer's disease. *Nat Genet* (2013) 45:1452–8. doi: 10.1038/ng.2802
11. Henn A, Lund S, Hedtjarn M, Schrattenholz A, Porzgen P, Leist M. The suitability of BV2 cells as alternative model system for primary microglia cultures or for animal experiments examining brain inflammation. *ALTEX* (2009) 26:83–94. doi: 10.14573/altex.2009.2.83
12. Bohlen CJ, Bennett FC, Tucker AF, Collins HY, Mulinyawe SB, Barres BA. Diverse Requirements for Microglial Survival, Specification, and Function Revealed by Defined-Medium Cultures. (2017) 94(4):759–73. doi: 10.1016/j.neuron.2017.04.043
13. Lund S, Christensen KV, Hedtjarn M, Mortensen AL, Hagberg H, Falsig J, et al. The dynamics of the LPS triggered inflammatory response of murine microglia under different culture and in vivo conditions. *J Neuroimmunol* (2006) 180:71–87. doi: 10.1016/j.jneuroim.2006.07.007
14. Mizee MR, Miedema SSM, van der Poel M, Schuurman AKG, van Strien ME, Melief J, et al. Isolation of primary microglia from the human post-mortem brain: effects of ante- and post-mortem variables. *Acta Neuropathologica Commun* (2017) 5:16. doi: 10.1186/s40478-017-0418-8
15. Olah M, Raj D, Brouwer N, De Haas AH, Eggen BJL, Den Dunnen WFA, et al. An optimized protocol for the acute isolation of human microglia from autopsy brain samples. *Glia* (2012) 60:96–111. doi: 10.1002/glia.21251
16. Timmerman R, Burm SM, Bajramovic JJ. An Overview of in vitro Methods to Study Microglia. *Front Cell Neurosci* (2018) 12:242. doi: 10.3389/fncel.2018.00242
17. Butovsky O, Jedrychowski MP, Moore CS, Cialic R, Lanser AJ, Gabriely G, et al. Identification of a unique TGF-β–dependent molecular and functional signature in microglia. *Nat Neurosci* (2014) 17:131–43. doi: 10.1038/nn.3599
18. Melief J, Sneeboer MAM, Litjens M, Ormel PR, Palmen SJMC, Huitinga I, et al. Characterizing primary human microglia: A comparative study with myeloid subsets and culture models. *Glia* (2016) 64:1857–68. doi: 10.1002/glia.23023
19. Takahashi K, Tanabe K, Ohnuki M, Narita M, Ichisaka T, Tomoda K, et al. Induction of Pluripotent Stem Cells from Adult Human Fibroblasts by Defined Factors. *Cell* (2007) 131:861–72. doi: 10.1016/j.cell.2007.11.019
20. Takahashi K, Yamanaka S. Induction of Pluripotent Stem Cells from Mouse Embryonic and Adult Fibroblast Cultures by Defined Factors. *Cell* (2006) 126:663–76. doi: 10.1016/j.cell.2006.07.024
21. Ginhoux F, Greter M, Leboeuf M, Nandi S, See P, Gokhan S, et al. Fate Mapping Analysis Reveals That Adult Microglia Derive from Primitive Macrophages. *Science* (2010) 330:841–5. doi: 10.1126/science.1194637
22. Gomez Perdiguero E, Klapproth K, Schulz C, Busch K, Azzoni E, Crozet L, et al. Tissue-resident macrophages originate from yolk-sac-derived erythro-myeloid progenitors. *Nature* (2015) 518:547–51. doi: 10.1038/nature13989
23. Kierdorf K, Erny D, Goldmann T, Sander V, Schulz C, Perdiguero EG, et al. Microglia emerge from erythromyeloid precursors via Pu.1- and Irf8-dependent pathways. *Nat Neurosci* (2013) 16:273–80. doi: 10.1038/nn.3318
24. Abud EM, Ramirez RN, Martinez ES, Healy LM, Nguyen CHH, Newman SA, et al. iPSC-Derived Human Microglia-like Cells to Study Neurological Diseases. *Neuron* (2017) 94:278–293.e9. doi: 10.1016/j.neuron.2017.03.042
25. Haenseler W, Sansom SN, Buchrieser J, Newey SE, Moore CS, Nicholls FJ, et al. A Highly Efficient Human Pluripotent Stem Cell Microglia Model Displays a Neuronal-Co-culture-Specific Expression Profile and Inflammatory Response. *Stem Cell Rep* (2017) 8:1727–42. doi: 10.1016/j.stemcr.2017.05.017
26. Pandya H, Shen MJ, Ichikawa DM, Sedlock AB, Choi Y, Johnson KR, et al. Differentiation of human and murine induced pluripotent stem cells to microglia-like cells. *Nat Neurosci* (2017) 20:753–9. doi: 10.1038/nn.4534
27. Gutbier S, Wanke F, Dahm N, Rummelin A, Zimmermann S, Christensen K, et al. Large-Scale Production of Human iPSC-Derived Macrophages for Drug Screening. *Int J Mol Sci* (2020) 21:4808. doi: 10.3390/ijms21134808
28. Lucin KM, Wyss-Coray T. Immune activation in brain aging and neurodegeneration: too much or too little? *Neuron* (2009) 64:110–22. doi: 10.1016/j.neuron.2009.08.039
29. Jay TR, von Saucken VE, Landreth GE. TREM2 in Neurodegenerative Diseases. *Mol Neurodegeneration* (2017) 12:56. doi: 10.1186/s13024-017-0197-5
30. Ulland TK, Colonna M. TREM2 - a key player in microglial biology and Alzheimer disease. *Nat Rev Neurol* (2018) 14:667–75. doi: 10.1038/s41582-018-0072-1
31. Colonna M, Wang Y. TREM2 variants: new keys to decipher Alzheimer disease pathogenesis. *Nat Rev Neurosci* (2016) 17:201–7. doi: 10.1038/nrn.2016.7
32. Guerreiro R, Wojtas A, Bras J, Carrasquillo M, Rogaeva E, Majounie E, et al. TREM2 variants in Alzheimer's disease. *New Engl J Med* (2013) 368:117–27. doi: 10.1056/NEJMoa1211851
33. Jonsson T, Stefansson H, Steinberg S, Jonsdottir I, Jonsson PV, Snaedal J, et al. Variant of TREM2 associated with the risk of Alzheimer's disease. *New Engl J Med* (2013) 368:107–16. doi: 10.1056/NEJMoa1211103
34. Kleinberger G, Brendel M, Mracsko E, Wefers B, Groeneweg L, Xiang X, et al. The FTD-like syndrome causing TREM2 T66M mutation impairs microglia function, brain perfusion, and glucose metabolism. *EMBO J* (2017) 36:1837–53. doi: 10.15252/embj.201796516
35. Korvatska O, Leverenz JB, Jayadev S, McMillan P, Kurtz I, Guo X, et al. R47H Variant of TREM2 Associated With Alzheimer Disease in a Large Late-Onset Family: Clinical, Genetic, and Neuropathological Study. *JAMA Neurol* (2015) 72:920–7. doi: 10.1001/jamaneurol.2015.0979

36. Sims R, van der Lee SJ, Naj AC, Bellenguez C, Badarinarayan N, Jakobsdottir J, et al. Rare coding variants in PLCG2, ABI3, and TREM2 implicate microglial-mediated innate immunity in Alzheimer's disease. *Nat Genet* (2017) 49:1373–84. doi: 10.1038/ng.3916
37. Deczkowska A, Keren-Shaul H, Weiner A, Colonna M, Schwartz M, Amit I. Disease-Associated Microglia: A Universal Immune Sensor of Neurodegeneration. *Cell* (2018) 173:1073–81. doi: 10.1016/j.cell.2018.05.003
38. Keren-Shaul H, Spinrad A, Weiner A, Matcovitch-Natan O, Dvir-Szternfeld R, Ulland TK, et al. A Unique Microglia Type Associated with Restricting Development of Alzheimer's Disease. *Cell* (2017) 169:1276–1290.e17. doi: 10.1016/j.cell.2017.05.018
39. Gratuze M, Leyns CE, Sauerbeck AD, St-Pierre MK, Xiong M, Kim N, et al. Impact of TREM2R47H variant on tau pathology-induced gliosis and neurodegeneration. *J Clin Invest* (2020) 130:4954–68. doi: 10.1172/JCI138179
40. Schlepckow K, Monroe KM, Kleinberger G, Cantuti-Castelvetri L, Parhizkar S, Xia D, et al. Enhancing protective microglial activities with a dual function TREM2 antibody to the stalk region. *EMBO Mol Med* (2020) 12:e11227. doi: 10.15252/emmm.201911227
41. Wang S, Mustafa M, Yuede CM, Salazar SV, Kong P, Long H, et al. Anti-human TREM2 induces microglia proliferation and reduces pathology in an Alzheimer's disease model. *J Exp Med* (2020) 217:9. doi: 10.1084/jem.20200785
42. Andreone BJ, Przybyla L, Llapashtica C, Rana A, Davis SS, van Lengerich B, et al. Alzheimer's-associated PLCγ2 is a signaling node required for both TREM2 function and the inflammatory response in human microglia. *Nat Neurosci* (2020) 23:927–38. doi: 10.1038/s41593-020-0650-6
43. Garcia-Reitboeck P, Phillips A, Piers TM, Villegas-Llerena C, Butler M, Mallach A, et al. Human Induced Pluripotent Stem Cell-Derived Microglia-Like Cells Harboring TREM2 Missense Mutations Show Specific Deficits in Phagocytosis. *Cell Rep* (2018) 24:2300–11. doi: 10.1016/j.celrep.2018.07.094
44. Nugent AA, Lin K, van Lengerich B, Lianoglou S, Przybyla L, Davis SS, et al. TREM2 Regulates Microglial Cholesterol Metabolism upon Chronic Phagocytic Challenge. *Neuron* (2020) 105:837–854.e9. doi: 10.1016/j.neuron.2019.12.007
45. Piers TM, Cosker K, Mallach A, Johnson GT, Guerreiro R, Hardy J, et al. A locked immunometabolic switch underlies TREM2 R47H loss of function in human iPSC-derived microglia. *FASEB J* (2020) 34:2436–50. doi: 10.1096/fj.201902447R
46. van Wilgenburg B, Browne C, Vowles J, Cowley SA. Efficient, long term production of monocyte-derived macrophages from human pluripotent stem cells under partly-defined and fully-defined conditions. *PloS One* (2013) 8: e71098. doi: 10.1371/journal.pone.0071098
47. Cusulin C, Wells I, Badillo S, Duran-Pacheco GC, Baumann K, Patsch C. Gamma secretase modulators and BACE inhibitors reduce Aβ production without altering gene expression in Alzheimer's disease iPSC-derived neurons and mice. *Mol Cell Neurosci* (2019) 100:103392. doi: 10.1016/j.mcn.2019.103392
48. Dobin A, Davis CA, Schlesinger F, Drenkow J, Zaleski C, Jha S, et al. STAR: ultrafast universal RNA-seq aligner. *Bioinf (Oxford England)* (2013) 29:15–21. doi: 10.1093/bioinformatics/bts635
49. Andrews S. FastQC: a quality control tool for high throughput sequence data. *Babraham Institute* (2010).
50. Ewels P, Magnusson M, Lundin S, Käller M. MultiQC: summarize analysis results for multiple tools and samples in a single report. *Bioinf (Oxford England)* (2016) 32:3047–8. doi: 10.1093/bioinformatics/btw354
51. Li H, Handsaker B, Wysoker A, Fennell T, Ruan J, Homer N, et al. The Sequence Alignment/Map format and SAMtools. Bioinformatics (Oxford. *England)* (2009) 25:2078–9. doi: 10.1093/bioinformatics/btp352
52. Mortazavi A, Williams BA, McCue K, Schaeffer L, Wold B. Mapping and quantifying mammalian transcriptomes by RNA-Seq. *Nat Methods* (2008) 5:621–8. doi: 10.1038/nmeth.1226
53. Metsalu T, Vilo J. ClustVis: a web tool for visualizing clustering of multivariate data using Principal Component Analysis and heatmap. *Nucleic Acids Res* (2015) 43:W566–70. doi: 10.1093/nar/gkv468
54. Friedman BA, Srinivasan K, Ayalon G, Meilandt WJ, Lin H, Huntley MA, et al. Diverse Brain Myeloid Expression Profiles Reveal Distinct Microglial Activation States and Aspects of Alzheimer's Disease Not Evident in Mouse Models. *Cell Rep* (2018) 22:832–47. doi: 10.1016/j.celrep.2017.12.066
55. Pomaznoy M, Ha B, Peters B. GOnet: a tool for interactive Gene Ontology analysis. *BMC Bioinf* (2018) 19:470. doi: 10.1186/s12859-018-2533-3
56. Muffat J, Li Y, Yuan B, Mitalipova M, Omer A, Corcoran S, et al. Efficient derivation of microglia-like cells from human pluripotent stem cells. *Nat Med* (2016) 22:1358–67. doi: 10.1038/nm.4189
57. Sala Frigerio C, Wolfs L, Fattorelli N, Thrupp N, Voytyuk I, Schmidt I, et al. The Major Risk Factors for Alzheimer's Disease: Age, Sex, and Genes Modulate the Microglia Response to Aβ Plaques. *Cell Rep* (2019) 27:1293–1306.e6. doi: 10.1016/j.celrep.2019.03.099
58. Srinivasan K, Friedman BA, Etxeberria A, Huntley MA, van der Brug MP, Foreman O, et al. Alzheimer's Patient Microglia Exhibit Enhanced Aging and Unique Transcriptional Activation. *Cell Rep* (2020) 31:107843. doi: 10.1016/j.celrep.2020.107843
59. Hamilton JA. GM-CSF-Dependent Inflammatory Pathways. *Front Immunol* (2019) 10:2055. doi: 10.3389/fimmu.2019.02055
60. Nimmerjahn A, Kirchhoff F, Helmchen F. Resting Microglial Cells Are Highly Dynamic Surveillants of Brain Parenchyma in Vivo. *Science* (2005) 308:1314–8. doi: 10.1126/science.1110647
61. Song D, Sulewski ME Jr., Wang C, Song J, Bhuyan R, Sterling J, et al. Complement C5a receptor knockout has diminished light-induced microglia/macrophage retinal migration. *Mol Vis* (2017) 23:210–8.
62. Gasque P, Singhrao SK, Neal JW, Gotze O, Morgan BP. Expression of the receptor for complement C5a (CD88) is up-regulated on reactive astrocytes, microglia, and endothelial cells in the inflamed human central nervous system. *Am J Pathol* (1997) 150:31–41.
63. Haynes SE, Hollopeter G, Yang D, Kurpius ME, Dailey W-B, Gan D, et al. The P2Y12 receptor regulates microglial activation by extracellular nucleotides. *Nat Neurosci* (2006) 9(12):1512–9. doi: 10.1038/nn1805
64. Honda S, Sasaki K, Ohsawa Y, Imai Y, Nakamura K, Inoue S, et al. Extracellular ATP or ADP induce chemotaxis of cultured microglia through Gi/o-coupled P2Y receptors. (2011). doi: 10.1523/JNEUROSCI.21-06-01975.2001
65. Light AR, Wu Y, Hughen RW, Guthrie PB. Purinergic receptors activating rapid intracellular Ca increases in microglia. *Neuron Glia Biol* (2006) 2 (2):125–38. doi: 10.1017/S1740925X05000323
66. Kleinberger G, Yamanishi Y, Suárez-Calvet M, Czirr E, Lohmann E, Cuyvers E, et al. TREM2 mutations implicated in neurodegeneration impair cell surface transport and phagocytosis. *Sci Trans Med* (2014) 6:243ra86. doi: 10.1126/scitranslmed.3009093
67. Yeh FL, Wang Y, Tom I, Gonzalez LC, Sheng M. TREM2 Binds to Apolipoproteins, Including APOE and CLU/APOJ, and Thereby Facilitates Uptake of Amyloid-Beta by Microglia. *Neuron* (2016) 91:328–40. doi: 10.1016/j.neuron.2016.06.015
68. Meilandt WJ, Ngu H, Gogineni A, Lalehzadeh G, Lee SH, Srinivasan K, et al. Trem2 Deletion Reduces Late-Stage Amyloid Plaque Accumulation, Elevates the Aβ42:Aβ40 Ratio, and Exacerbates Axonal Dystrophy and Dendritic Spine Loss in the PS2APP Alzheimer's Mouse Model. *J Neurosci Off J Soc Neurosci* (2020) 40:1956–74. doi: 10.1523/JNEUROSCI.1871-19.2019
69. Carrano A, Hoozemans JJ, van der Vies SM, van Horssen J, de Vries HE, Rozemuller AJ. Neuroinflammation and blood-brain barrier changes in capillary amyloid angiopathy. *Neurodegener Dis* (2012) 10:329–31. doi: 10.1159/000334916
70. Gosselin D, Skola D, Coufal NG, Holtman IR, Schlachetzki JCM, Sajti E, et al. An environment-dependent transcriptional network specifies human microglia identity. *Science* (2017) 356:6344. doi: 10.1126/science.aal3222
71. Haruwaka K, Ikegami A, Tachibana Y, Ohno N, Konishi H, Hashimoto A, et al. Dual microglia effects on blood brain barrier permeability induced by systemic inflammation. *Nat Commun* (2019) 10:5816. doi: 10.1038/s41467-019-13812-z
72. Marschallinger J, Iram T, Zardeneta M, Lee SE, Lehallier B, Haney MS, et al. Lipid-droplet-accumulating microglia represent a dysfunctional and proinflammatory state in the aging brain. *Nat Neurosci* (2020) 23:194–208. doi: 10.1038/s41593-019-0566-1
73. Zilkova M, Nolle A, Kovacech B, Kontsekova E, Weisova P, Filipcik P, et al. Humanized tau antibodies promote tau uptake by human microglia without any increase of inflammation. *Acta Neuropathol Commun* (2020) 8:74. doi: 10.1186/s40478-020-00948-z

74. Hammond TR, Dufort C, Dissing-Olesen L, Giera S, Young A, Wysoker A, et al. Single-Cell RNA Sequencing of Microglia throughout the Mouse Lifespan and in the Injured Brain Reveals Complex Cell-State Changes. *Immunity* (2019) 50:253–271.e6. doi: 10.1016/j.immuni.2018.11.004
75. Jung S, Aliberti J, Graemmel P, Sunshine MJ, Kreutzberg GW, Sher A, et al. Analysis of fractalkine receptor CX(3)CR1 function by targeted deletion and green fluorescent protein reporter gene insertion. *Mol Cell Biol* (2000) 20:4106–14. doi: 10.1128/MCB.20.11.4106-4114.2000
76. Jackson HM, Foley KE, O'Rourke R, Stearns TM, Fathalla D, Morgan BP, et al. A novel mouse model expressing human forms for complement receptors CR1 and CR2. *BMC Genet* (2020) 21:101. doi: 10.1186/s12863-020-00893-9
77. Ryan KJ, White CC, Patel K, Xu J, Olah M, Replogle JM, et al. A human microglia-like cellular model for assessing the effects of neurodegenerative disease gene variants. *Sci Trans Med* (2017) 9:421. doi: 10.1126/scitranslmed.aai7635
78. McQuade A, Coburn M, Tu CH, Hasselmann J, Davtyan H, Blurton-Jones M. Development and validation of a simplified method to generate human microglia from pluripotent stem cells. *Mol Neurodegeneration* (2018) 13:67. doi: 10.1186/s13024-018-0297-x
79. Douvaras P, Sun B, Wang M, Kruglikov I, Lallos G, Zimmer M, et al. Directed Differentiation of Human Pluripotent Stem Cells to Microglia. *Stem Cell Rep* (2017) 8:1516–24. doi: 10.1016/j.stemcr.2017.04.023
80. Xiang X, Piers TM, Wefers B, Zhu K, Mallach A, Brunner B, et al. The Trem2 R47H Alzheimer's risk variant impairs splicing and reduces Trem2 mRNA and protein in mice but not in humans. *Mol Neurodegeneration* (2018) 13:49. doi: 10.1186/s13024-018-0280-6
81. Brüll M, Spreng AS, Gutbier S, Loser D, Krebs A, Reich M, et al. Incorporation of stem cell-derived astrocytes into neuronal organoids to allow neuro-glial interactions in toxicological studies. *Altex* (2020) 37:409–28. doi: 10.14573/altex.1911111
82. Mazaheri F, Snaidero N, Kleinberger G, Madore C, Daria A, Werner G, et al. TREM2 deficiency impairs chemotaxis and microglial responses to neuronal injury. *EMBO Rep* (2017) 18:1186–98. doi: 10.15252/embr.201743922
83. Shi Y, Holtzman DM. Interplay between innate immunity and Alzheimer disease: APOE and TREM2 in the spotlight. *Nat Rev Immunol* (2018) 18:759–72. doi: 10.1038/s41577-018-0051-1
84. Krasemann S, Madore C, Cialic R, Baufeld C, Calcagno N, El Fatimy R, et al. The TREM2-APOE Pathway Drives the Transcriptional Phenotype of Dysfunctional Microglia in Neurodegenerative Diseases. *Immunity* (2017) 47:566–581 e9. doi: 10.1016/j.immuni.2017.08.008
85. Alepee N, Bahinski A, Daneshian M, De Wever B, Fritsche E, Goldberg A, et al. State-of-the-art of 3D cultures (organs-on-a-chip) in safety testing and pathophysiology. *ALTEX* (2014) 31:441–77. doi: 10.14573/altex.1406111

Conflict of Interest: During the course of this study, MR, IP, ND, CS, DR, RS, ME, JZ, CP, SG, and MB are or were full time employees or trainees at Roche and they may additionally hold Roche stock/stock options.

The remaining authors declare that the research was conducted in the absence of any commercial or financial relationships that could be construed as a potential conflict of interest.

Copyright © 2021 Reich, Paris, Ebeling, Dahm, Schweitzer, Reinhardt, Schmucki, Prasad, Köchl, Leist, Cowley, Zhang, Patsch, Gutbier and Britschgi. This is an open-access article distributed under the terms of the Creative Commons Attribution License (CC BY). The use, distribution or reproduction in other forums is permitted, provided the original author(s) and the copyright owner(s) are credited and that the original publication in this journal is cited, in accordance with accepted academic practice. No use, distribution or reproduction is permitted which does not comply with these terms.

Received: 2 August 2017 | Revised: 28 November 2017 | Accepted: 11 December 2017
DOI: 10.1002/glia.23287

GLIA
WILEY

RESEARCH ARTICLE

ProMoIJ: A new tool for automatic three-dimensional analysis of microglial process motility

Iñaki Paris[1] | Julie C. Savage[4,5] | Laura Escobar[1] | Oihane Abiega[1,2] | Steven Gagnon[4,5] | Chin-Wai Hui[4,5] | Marie-Ève Tremblay[4,5] | Amanda Sierra[1,2,3] | Jorge Valero[1,2]

[1]Achucarro Basque Center for Neuroscience, Science Park of the UPV/EHU, Leioa, Bizkaia, Spain
[2]Ikerbasque Basque Foundation for Science, Bilbao, Bizkaia, Spain
[3]University of the Basque Country, Leioa, Bizkaia, Spain
[4]Centre de recherche du CHU de Québec, Axe Neurosciences, Québec, Canada
[5]Département de médecine moléculaire, Université Laval, Québec, Canada

Correspondence
Jorge Valero, Achucarro Basque Center for Neuroscience, Scientific Park of the UPV/EHU, Sede Building 3rd floor, E-48940 Leioa, Bizkaia, Spain.
E-mail: jorge.valero@achucarro.org

Funding information
Basque Government, Grant Number: PI-2016-1-0011; Ikerbasque, Basque Foundation for Science, Grant Number: IIkerbasque start-up funds; Ministerio de Economía y Competitividad, Grant Number: BFU2015-66689-R, RYC-2013-12817; The Natural Sciences and Engineering Research Council of Canada NSERC, Grant Number: RGPIN-2014-05308.

Abstract

Microglia, the immune cells of the central nervous system, continuously survey the brain to detect alterations and maintain tissue homeostasis. The motility of microglial processes is indicative of their surveying capacity in normal and pathological conditions. The gold standard technique to study motility involves the use of two-photon microscopy to obtain time-lapse images from brain slices or the cortex of living animals. This technique generates four dimensionally-coded images which are analyzed manually using time-consuming, non-standardized protocols. Microglial process motility analysis is frequently performed using Z-stack projections with the consequent loss of three-dimensional (3D) information. To overcome these limitations, we developed ProMoIJ, a pack of ImageJ macros that perform automatic motility analysis of cellular processes in 3D. The main core of ProMoIJ is formed by two macros that assist the selection of processes, automatically reconstruct their 3D skeleton, and analyze their motility (process and tip velocity). Our results show that ProMoIJ presents several key advantages compared with conventional manual analysis: (1) reduces the time required for analysis, (2) is less sensitive to experimenter bias, and (3) is more robust to varying numbers of processes analyzed. In addition, we used ProMoIJ to demonstrate that commonly performed 2D analysis underestimates microglial process motility, to reveal that only cells adjacent to a laser injured area extend their processes toward the lesion site, and to demonstrate that systemic inflammation reduces microglial process motility. ProMoIJ is a novel, open-source, freely-available tool which standardizes and accelerates the time-consuming labor of 3D analysis of microglial process motility.

KEYWORDS
ImageJ Macro, life imaging, microglia, process motility, two-photon microscopy

1 | INTRODUCTION

Microglia, the resident immune cells of the central nervous system (CNS), are in charge of surveying the brain parenchyma and maintain tight homeostasis. Therefore, microglia have an important role in physiological conditions contributing to CNS angiogenesis (Arnold & Betsholtz, 2013), synaptic pruning, and phagocytosis of dead cells during development or newborn neurons in adult neurogenic niches (Sierra, Abiega, Shahraz, & Neumann, 2013; Wolf, Boddeke, & Kettenmann, 2017). In pathological conditions microglia remove dead cells, axonal fragments, myelin debris, tumor cells, invading microorganisms, and extracellular misfolded proteins (e.g., amyloid β deposits; Sierra et al., 2013; Wolf et al., 2017).

To accomplish their unique surveying function, microglia continuously protract and retract their processes while maintaining, in most cases, a static cell body (Nimmerjahn, Kirchhoff, & Helmchen, 2005). Indeed, it has been estimated that the constant movement of their processes allows microglia to screen the whole brain parenchyma in a few hours (Nimmerjahn et al., 2005). Since 2005, when Nimmerjahn and Davalos described the highly motile nature of microglia (Davalos et al., 2005; Nimmerjahn et al., 2005), many other groups have analyzed the motility of microglial processes to evaluate their function in

 © 2017 Wiley Periodicals, Inc.

physiological and pathological conditions. However, the analysis of microglial motility *in vivo* is not trivial. It requires the use of animal models that express a bright fluorescent protein in microglia for cell visualization and commonly involves the use of two-photon laser-scanning microscopy to obtain time-lapse images from brain slices or the brain of living animals. This technique generates a large amount of 4 dimensionally-coded images (XYZT) which need to be preprocessed to correct technical undesirable artifacts such as stage/focus three dimensional (3D) movements, photo-bleaching, electrical noise, and background signal. After pre-processing, images are analyzed using diverse time-consuming and non-standardized protocols which render non-comparable data. Although the analysis of time-lapse images to evaluate microglial processes motility is highly relevant to the understanding of microglial function, freely available tools to implement this analysis are lacking.

Different approaches have been developed to evaluate microglial processes motility, such as measurements of process length (Davalos et al., 2005; Nimmerjahn et al., 2005; Sipe et al., 2016), tip position (Kondo, Kohsaka, & Okabe, 2011; Batti et al., 2016; Fourgeaud et al., 2016), volume/area occupied by microglial processes (Davalos et al., 2005; Krabbe et al., 2013; Batti et al., 2016; Sipe et al., 2016), microglial volume, area, perimeter, number of branches per cell, or cell mass center (Damani et al., 2011; Fontainhas et al., 2011; Dissing-Olesen et al., 2014; Eyo, Miner, Weiner, & Dailey, 2016; Li, Du, Pei, Du, & Zhao, 2016; Sipe et al., 2016). The majority of the above-cited studies used 2D projections of time-lapse Z-stacks to simplify the analysis. However, this approach reduces the accuracy of the measurements obtained and disregards the intrinsic 3D nature of process motility.

Among the different parameters analyzed in previous studies, we focused on those that we consider the most direct measurements of process motility: process length (Davalos et al., 2005; Nimmerjahn et al., 2005; Kondo et al., 2011; Sipe et al., 2016) and tip position (Batti et al., 2016; Fourgeaud et al., 2016). Changes in process length are indicative of either protraction or retraction. In addition, tip position reflects lateral scanning movements or directionality toward injured regions, which are not accounted for when analyzing process length. Both parameters, i.e. changes in process length (process velocity) and in tip position (tip velocity), are thus complementary measurements to evaluate microglial process motility. In this study, we describe a reliable automatic tool to quantify these two main parameters in 3D. An earlier version of this tool was used to demonstrate reduced motility of microglial processes *in vivo* in a mouse model of mesial temporal lobe epilepsy (Abiega et al., 2016). We now introduce a freely available pack of macros (ProMoIJ: Process Motility in ImageJ) containing all macros required to perform image preprocessing and motility analysis based on the open source image analysis software Fiji, a distribution of the popular open-source software ImageJ focused on biological-image analysis (Schindelin et al., 2012). We also use ProMoIJ to demonstrate that 2D motility analysis underestimates microglial process motility, to reveal that only cells adjacent to a laser injured area extend their processes toward the lesion site, and to show that systemic administration of bacterial lipopolysaccharides (LPS), a model of sickness behavior, reduces microglial process motility *in vivo*. ProMoIJ performs batch processing of time-lapse images without manual intervention, thus reducing the analysis time and variability between researchers. Our validation experiments comparing microglial process motility estimated using ProMoIJ and manual protocols with the same set of processes demonstrate that ProMoIJ is a highly efficient tool for the systematic 3D analysis of microglial process motility both in health and disease.

2 | MATERIAL AND METHODS

2.1 | Animals

All experiments were performed in CX3CR1$^{GFP/+}$ mice, in which all microglia express the green fluorescent reporter (Jung et al., 2000). Three 2 month-old mice were used for macro testing and laser injury analysis, and seven 5 month-old mice were used to analyze the effects of systemic administration of LPS on microglial process motility. Four mice were intraperitoneally injected with saline, and three with LPS (1 mg/kg) 24 hr prior imaging to analyze the effects of systemic inflammation on microglial process motility. Mice were housed in 12:12 hr light cycle with *ad libitum* access to food and water. All procedures followed the Canadian Council on Animal Care guidelines and were approved by the Ethics Committees of the Animal Care Committee of Université Laval (protocol number 2013102–1).

2.2 | Two-photon imaging of the living cortex

Images obtained from a previously published study (Abiega et al., 2016) were used here to validate data obtained with ProMoIJ. In addition, a new set of images was acquired to analyze the effects of LPS administration on microglial process motility. Briefly, mice were anesthetized with isoflurane and their skull above the motor cortex exposed, cleaned, glued to a metal plate, and thinned to 20–30 mm thickness using a high-speed dental drill (Osada Inc) and a microsurgical blade. Drilling was interrupted periodically, and sterile saline was applied on the skull to prevent heat-induced damage. Next, the mice were placed under an Olympus two-photon microscope FV1000MPE equipped with a Ti:Sapphire laser (Mai Tai Deep See; Spectra Physics) tuned to 920 nm for transcranial imaging, and with a 25× water-immersion lens (1.05 N.A.; Olympus). Stacks of 41–44 Z slices taken every 1 μm were acquired in 1.58–1.57 min intervals during 14.22–15.8 min (10–11 time frames) with a 512 × 512 pixels XY resolution (0.497 μm of pixel width and height).

2.3 | Two-photon focal laser injury

Restricted injury was achieved by focusing a two-photon laser beam (3 microns) in the somatosensory area of the cortex for 8 s to create a small injury site around the focal point of the beam. The wavelength of the two-photon laser was set at 820 nm and the laser power was 50–70 mW at the sample. Images were acquired 90 s after laser injury induction.

2.4 | Macro writing

All macros were written in ImageJ1 macro language using the script editor of Fiji (Schindelin et al., 2012) and are freely available under the terms of the GNU General Public License version 3, as published by the Free Software Foundation (http://www.gnu.org/licenses). In addition, we wrote a step by step user's manual to guide non-expert researchers through the 3D analysis of process motility. Both ProMoIJ and the User's Manual can be downloaded from https://www.achucarro.org/downloads.

2.5 | Automatic process motility analysis with ProMoIJ

The automatic analysis of process motility was performed using a series of ImageJ macros that we combined into a package named ProMoIJ (Process Motility in ImageJ). ProMoIJ has been developed as a user-friendly, step-by-step protocol for the analysis of microglial motility by non-expert researchers. ProMoIJ includes macros for cell cropping (Macro 1), image preprocessing (Macro 2 and 3), process selection (Macro 4), automatic 3D reconstruction of the process skeleton, and motility analysis (process and tip velocity, Macro 5; Figure 1a–c). Each macro asks users to select the folders that contain the required files (i.e., time-lapse images files or process-selection files created with Macro 4), as well as the folders where the resulting images, selections, or data tables will be stored. In addition, macros ask users to specify different parameters (**Table** 1) necessary to transform or analyze the images. Importantly, ProMoIJ performs batch processing of the images (i.e., without manual intervention by the user), applying the same parameter values in all the images.

2.5.1 | Image size reduction (macro 1)

Large images (over 2 Gb size) may present problems during preprocessing due to the lack of available RAM memory. Therefore, we developed a macro (Macro 1: ProMoIJ_M1_Cropping) that allows reducing the number of image channels, Z-slices and/or time-frames, and cropping cells to generate smaller images for processing (Table 1, parameters M1.1–8).

2.5.2 | Pre-processing (macros 2 and 3)

Automated analysis of images was performed using two macros: Macro 2 (ProMoIJ_M2_Registration) and Macro 3 (ProMoIJ_M3_Image_corrections). Different ImageJ plugins were included in these macros to align 3D images across time frames (registration), correct photobleaching, reduce noise, and subtract background (Figure 1a).

Macro 2 performs batch registration of images using two ImageJ registration plugins: "MultistackReg v_1.45" (Brad Busse, http://bradbusse.net/downloads.html) to register stacks in 2D using "TurboReg" plugin (Thevenaz, Ruttimann, & Unser, 1998); and "Correct 3D drift" (Parslow, Cardona, & Bryson-Richardson, 2014), which corrects sample drifts in 3D. Images may be registered using either plugin or both (Table 1; parameters M2.1 and M2.2). Macro 2 allows selecting one of the following algorithms available from "MultisatckReg v_1.45" (Table 1; parameter M2.3): Translation, Rigid Body, Scaled rotation, and Affine. Appropriate registration is achieved when microglial soma remains almost static throughout the time-frames. Macro 2 includes an "Optimization mode" (Table 1; parameter M2.4) which allows visualization of registered images (more information about the "Optimization mode" is available in the User's manual).

Macro 3 performs batch photo-bleaching correction using the ImageJ plugin "CorrectBleach_V2.0.2" and applying its "Histogram Matching" method (Miura, Rueden, Hiner, Schindelin, & Rietdorf, 2014). In addition, Macro 3 uses a Difference of Gaussians filter to reduce noise and background. Gaussian filters smooth images by applying a Gaussian function, which combines the intensity of each pixel with the intensity of those pixels located within a determined radius around them. This radius is defined by the so-called "sigma value." The Difference of Gaussians filters is calculated as the difference between the images filtered with the minimum and the maximum sigma values. The minimum sigma value defines the grade of smoothness of the resulting image, whereas the maximum sigma value defines the amount of local intensity subtracted. Users should define their own optimal sigma values depending on the characteristics of their images (Table 1; parameters M3.1 and M3.2). Macro 3 includes an "Optimization mode" (Table 1; parameter M3.3) which allows visualization of images after correction (more information about the "Optimization mode" is available in the User's manual).

2.5.3 | Selection of processes (macro 4)

Microglial processes to be analyzed are manually selected and their orientation (base-to-tip) defined using ProMoIJ Macro 4 (ProMoIJ_M4_Process_selection). Macro 4 facilitates the selection of individual process by: (1) collapsing time-frame information into one single image (the maximum projection of all time frames) and (2) identifying the static regions of the cell from where the base of the process is defined. Static cellular regions are identified by highlighting in red the pixels that maintain an intensity value above a user-defined threshold level throughout the time frames (Table 1, parameter M4.1). This threshold level may be determined by activating the "Optimization mode" (Table 1, parameter M4.2) which allows image thresholding and visualization of static regions (more information about the "Optimization mode" is available in the User's manual). Then, the user is asked to select the processes of interest using the regions of interest (ROI) manager tool of Fiji. Selected process, that could be either primary or secondary branches, should be confined within the XYZT stack of images. In addition, the investigator must indicate the process orientation by drawing an arrow pointing from the constant basal region of the process to its tip (orientation vector). Finally, the macro saves all the selections and vectors for further analysis (Figure 1b).

2.5.4 | Process reconstruction and motility analysis (macro 5)

Motility analysis is performed by estimating process length and tip position in each time frame. ProMoIJ Macro 5 (ProMoIJ_M5_Motility_analysis) automatizes this analysis by reconstructing the 3D skeleton of the process. Once the 3D skeleton is reconstructed, the length and position of the skeleton tip in each time frame are analyzed to estimate

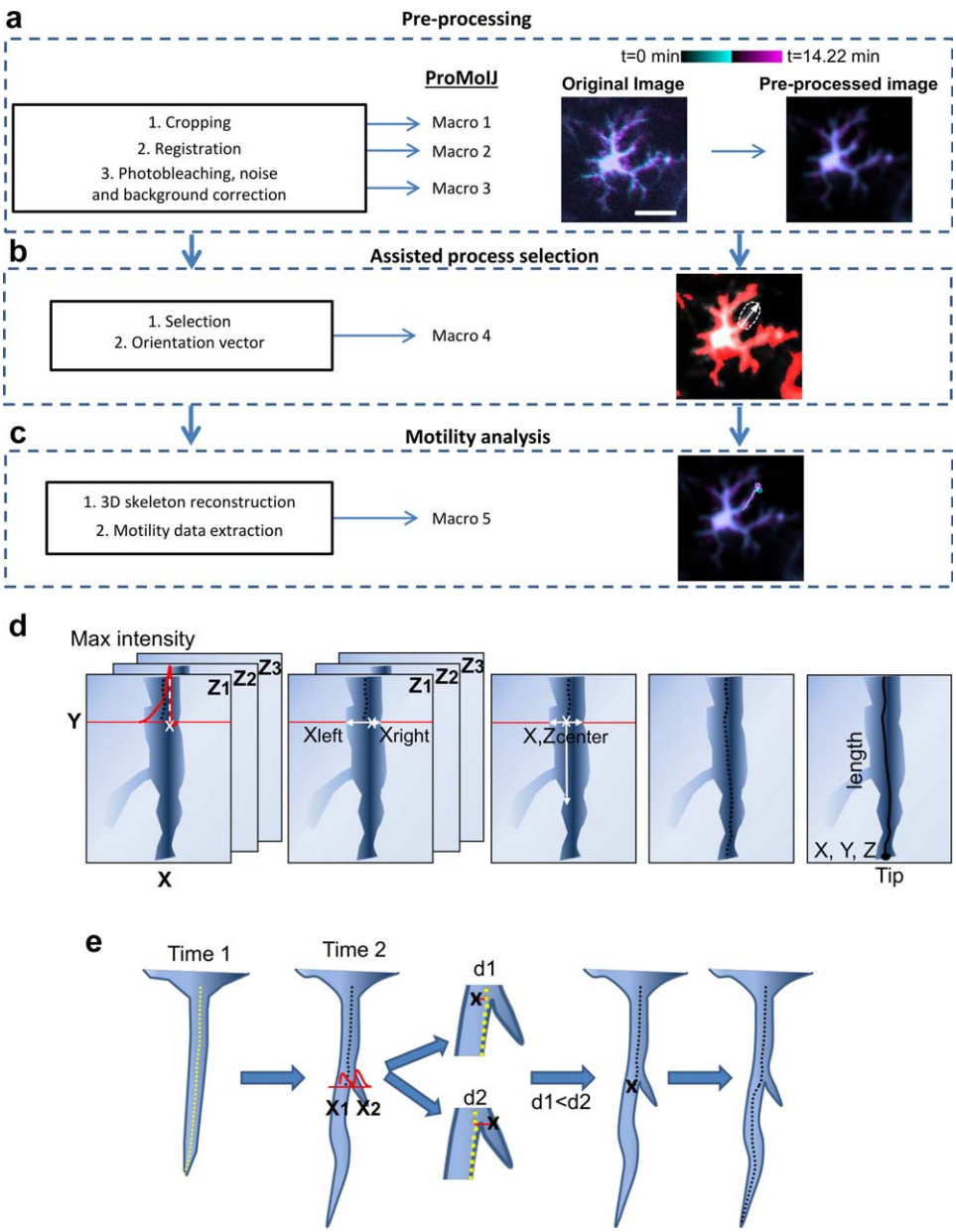

FIGURE 1 ProMoIJ work flow. (a) Image pre-processing is performed by Macro 1 for image cropping; Macro 2 for image registration; and Macro 3 for photobleaching, noise, and background corrections. Images on the right are representative projections (41 Z-slices = 41 μm) of 2-photon images of microglia at t0 (cyan) and 14.22 min (t10, magenta) in the mouse cortex showing a microglial cell before (left) and after (right) registration and corrections. Scale bar = 20 μm. (b) Assisted process selection is performed using Macro 4, which first highlights cell constant regions in red (right image) and then allows both manual selection of the process (white dotted line) and manual drawing of the orientation vector (white arrow). (c) Automated motility analysis is performed by Macro 5, which reconstructs the 3D skeleton of the selected process in all time frames and then extracts motility data. 3D skeletons are shown in the image as a line and tip positions as a filled circle (t0 = cyan and t10 = magenta). (d) 3D skeletons are reconstructed analyzing the intensity profiles of horizontal lines (red lines) and identifying the presence of processes and their borders in each Y position, based on the intensity of the profile maxima (red curve peak). Profile lines are analyzed in each Z-slice to obtain the X coordinates of the borders (Xleft and Xright) which are used to calculate the coordinates of the center of the process (X,Z center). Base-to-tip line profile analysis is performed and center coordinates smoothed and used to estimate the length of the process skeleton and the position of the tip (X, Y, Z). (e) A branching point is detected when more than one X central point (X1 and X2) is found. Macro 5 calculates the distances (d1 and d2) of both central points to the skeleton defined in the previous time frame (dotted yellow line). Then, the closest X central point is selected and 3D skeleton reconstruction continues [Color figure can be viewed at wileyonlinelibrary.com]

process velocity (changes in length, μm/min, including protraction and retraction) and tip velocity (changes in the position of the tip, μm/min; Figure 1c,d).

Macro 5 asks the user to define the value of several parameters that will be used to reconstruct the 3D skeleton of the processes and estimate motility (Table 1; parameters M5). First, the user must specify

TABLE 1 ProMoIJ parameters

	N°	Name	Possible values	Used value	Description
Macro 1 Cropping	M1.1	Crop cells	□/√	□	Activates cell cropping
	M1.2	Channel	1 – ∞	1	Channel used to analyze cells
	M1.3	Select Z-slices	□/√	□	Activates selection of Z-slices
	M1.4	First Z-slice	1 – ∞	N/A	Selects the first Z-slice to be used
	M1.5	Last Z-slice	1 – ∞	N/A	Selects the last Z-slice to be used
	M1.6	Select time frames	□/√	√	Activates selections of time frames
	M1.7	First time frame	1 – ∞	1	Selects the first time frame to be used
	M1.8	Last time frame	1 – ∞	10	Selects the last time frame to be used
Macro 2 Registration	M2.1	Apply 3D Drift Correction	None Before After Before & After MultistackReg	After	Activates 3D registration with the plugin "Correct 3D drift"
	M2.2	Apply MultistackReg	□/√	√	Activates registration with the plugin "MultistackReg"
	M2.3	Registration algorithm	Translation Rigid Body Affine Scaled Rotation	Rigid Body	Selects the algorithm used during registration
	M2.4	Optimization mode	□/√	□	Optimization and analysis
Macro 3 Image corrections	M3.1	Minimum sigma	1 – ∞	2	Image smoothing (higher values = smoother image)
	M3.2	Maximum sigma	1 – ∞	50	Local background subtraction, (lower values = more subtraction)
	M3.3	Optimization mode	□/√	□	Optimization and analysis
Macro 4 Process selection	M4.1	Threshold level	0 - ∞	100	Intensity threshold used to identify static regions (should be higher than the threshold used for analysis, M5.4)
	M4.2	Optimization mode	□/√	□	Optimization and analysis
Macro 5 Motility analysis	**M5.1[a]**	**Time interval**	**0 - ∞**	**1.58**	**Time interval between frames, in minutes**
	M5.2[a]	**3D Gaussian sigma**	**0 - ∞**	**1**	**3D smoothing (higher values = smoother image)**
	M5.3[a]	**Skeleton smoothing range**	**0 - ∞**	**2**	**Range (in pixels) for 3D skeleton smoothing, (higher values = smoother skeleton)**
	M5.4[a]	**Maxima threshold**	**0 - ∞**	**50**	**Intensity threshold used to identify a process**
	M5.5	Advanced menu	□/√	□	Advanced parameters (Supporting Information, Table S1)
	M5.6	Optimization mode	□/√	□	Optimization and parameters saving

[a]Relevant parameters for automatic analysis are highlighted in bold.

the time interval between consecutive time frames in minutes (Table 1; parameter M5.1). As will be demonstrated in this study, apart from time interval, only three parameters are critical for motility analysis and are included in the Main Menu (Table 1; parameters M5.2–4). The remaining parameters are set to default values that may be modified in the Advanced Parameters Menu, accessed by selecting the corresponding option in the Main Menu (Table 1, parameter M5.5). Optimization of parameters was performed by visualizing 3D skeleton reconstruction and modifying parameters when mismatches between the original process and the reconstructed 3D skeleton were found. Optimization may be accessed by selecting the "Optimization mode" in the Main Menu (Table 1; parameter M5.6, more information about the "Optimization mode" is available in the User's manual).

Macro 5 loads each batch of time-lapse images, as well as the process selections and orientation vectors associated with each image. For each selection (selected process) Macro 5 crops the process, clears all

pixels out of the selection, smooths the image using the filter "Gaussian Blur 3D" from Fiji, reorients the selected process in the Y axis following the direction of the orientation vector, and reconstructs the process from the basal constant region (the constant region of the process, included in the selection, that is farthest away from its tip).

To recreate the 3D skeleton, Macro 5 uses a strategy based on the identification of the process borders in each XZ plane along the *Y* axis. First, Macro 5 analyzes the intensity profiles of horizontal lines run from the top to the bottom of the image in each XZ plane. Intensity profiles are used to identify the presence of a process and its borders in each Y position based on the intensity of the profile maxima (above a user-defined threshold; Table 1, parameter M5.4). The process borders in each Z-slice are detected by consecutively checking the intensities of adjacent pixels flanking the profile maxima. A border is identified when: (1) a pixel intensity below a user-defined threshold is encountered (Table 1; parameter M5.4 or Supporting Information, Table S1, parameters M5.10 and M5.11) or (2) a concave inflexion with a determined amplitude (Supporting Information, Table S1, parameter M5.12) is found in regions that are close to splitting branches or adjacent processes. Profile lines are analyzed in each Z-slice and the X, Z coordinates of the borders are used to calculate the coordinates of the center of the process in each horizontal plane (XZ planes) using the following equations:

$$z_C = \frac{z_U + z_B}{2} \tag{1}$$

where z_C, z_U, and z_B are the Z coordinates of the center, the upper Z-slice, and the bottom Z-slice containing the process, respectively.

$$x_C = \frac{x_R + x_L}{2} \tag{2}$$

where x_C, x_R and x_L are the X coordinates of the center, the right border, and the left border of the process, respectively, in z_C. If z_C-slice is virtual (i.e., not an integer):

$$x_R = \frac{x_{R_{(z_C-0.5)}} + x_{R_{(z_C+0.5)}}}{2} \tag{4}$$

$$x_L = \frac{x_{L_{(z_C-0.5)}} + x_{L_{(z_C+0.5)}}}{2} \tag{5}$$

The reconstruction of the 3D process skeleton is made by connecting center points of adjacent XZ planes. Only center points belonging to the same process are connected. Thus, the coordinates of the borders corresponding to each center point are compared, and center points are connected if borders coordinates satisfy:

$$Z_{Y-1} - 1 \leq Z_Y \geq Z_{Y-1} + 1$$

and

$$XR_Y \geq XL_{Y-1} \text{ and } XL_Y \leq XR_{Y-1}$$

where Z_Y and Z_{Y-1} are Z coordinates in the current and previous (Y−1) Y positions, respectively; and XR_Y, XL_Y, XR_{Y-1} and XL_{Y-1} are the right and left border X coordinates in the current and previous Y positions.

Next, Macro 5 defines the last connected XZ plane as the one that corresponds to the process tip. Finally, the skeleton is smoothed using a Mean or Gaussian filter with a determined smoothing range (in pixels) defined by the user (Table 1; parameter M5.3 and Supporting Information, Table S1, parameter M5.20) to eliminate perturbations caused by small protrusions or noise in the borders of the processes.

The length of the 3D skeleton of the process is then calculated as the summation of the distances between each pair of center points located in consecutive XZ planes:

$$\text{length} = \sum_{i=y_0}^{y_{n-1}} \sqrt{(y_{i+1} - y_i)^2 + \left(x_{c_{y_{i+1}}} - x_{c_{y_i}}\right)^2 + \left(z_{c_{y_{i+1}}} - z_{c_{y_i}}\right)^2} \tag{5}$$

Where y_0 and y_n are the y coordinates of the first & last horizontal lines, respectively, containing the skeleton.

During the reconstruction of the 3D skeleton of the process two exceptions may occur:

(1) If more than one connected center point is detected, a branching point is identified. Macro 5 selects the branch that is closer to the skeleton defined in the previous time frame, if it exists (Figure 1e). If there is no skeleton in the previous time frame with coordinates similar to the current one, the macro will select the XZ central position that is closest to the skeleton that is being reconstructed.

(2) When no immediately adjacent center point is detected, the macro considers the existence of a gap in the process (i.e., lack of labeling in a portion of the process). Therefore, the macro searches for the process in the following Y positions until it reaches a distance in pixels either defined by default (2 pixels) or by the user in the advanced menu (Supporting Information, Table S1, parameter M5.17).

Macro 5 includes the possibility of activating a pre-detection step that improves the quality of the reconstruction and serves as a quality check. If the skeleton does not reach a certain percentage of the selection height (Supporting Information, Table S1, parameter M5.14), at least in one time frame, it is assumed that the reconstructed process is different from the one that was supposed to be analyzed and the reconstruction of the process is then aborted.

Finally, Macro 5 calculates process velocity as the absolute difference of process length between two consecutive time frames divided by the time interval, and tip velocity as the distance between the positions of the tip in two consecutive time frames divided by the time interval.

The following equation was used to calculate process velocity:

$$\text{process velocity} = \frac{\sqrt{(\text{length}_{f+1} - \text{length}_f)^2}}{t} \tag{6}$$

where f is time frame and t corresponds to the time interval between consecutive frames (1.58 min). Mean process velocity was used for analysis. Mean protraction and retraction of a process were calculated as the mean of process velocity from consecutive frames (*f* and *f* + 1) where the length of the process was increased or decreased, respectively. Net velocity of a process was calculated as the difference between its protraction and retraction.

Tip velocity was estimated as follows:

$$\text{tip velocity} = \frac{\sqrt{(X_{f+1} - X_f)^2 + (Y_{f+1} - Y_f)^2 + (Z_{f+1} - Z_f)^2}}{t} \tag{7}$$

where *t* corresponds to the time interval between consecutive frames (1.58 min), and X, Y and Z are the coordinates of the tip of

the process in the time frames f and $f + 1$. Mean tip velocity was used for analysis.

2.6 | Assisted manual process motility analysis

To compare ProMoIJ with conventional motility analysis methods, investigators measured the length of the selected processes and their tip position in each time frame manually. Process length was measured using the ImageJ plugin "Simple Neurite Tracer" (Longair, Baker, & Armstrong, 2011), which allows semi-automatic tracing of tube-like structures through 3D image stacks. However, "Simple Neurite Tracer" is not ready to analyze time-lapse images, and thus we developed an ImageJ macro (Macro 6, not included in ProMoIJ) that assisted the investigators in reconstructing the process over time. Macro 6 automatically imports the time-lapse images into Fiji and concatenates all the time frames into a single Z-stack, intercalating a white Z-slice between time frames to facilitate the identification of the limits between time frames. Then, Macro 6 crops the selected process using ROIs created with Macro 4, runs the ImageJ plugin "Simple Neurite Tracer", and allows manual tracing of the process in each time frame. Finally, Macro 6 calculates protraction, retraction, and process velocity using Equation 6.

To manually analyze process tip position, researchers used the ImageJ plugin "3D viewer" (Schmid, Schindelin, Cardona, Longair, & Heisenberg, 2010) and the point tool to obtain the 3D position (XYZ) of the tip in each frame. Tip velocity was calculated using Equation 7.

2.7 | Estimation of time required for analysis

The investigator used a computer equipped with an Intel Core i5–4590S 3GHz CPU processor, 8Gb of RAM, and Windows 7 Professional 64 bits and recorded time spent in analyzing 45 processes from three different time-lapse images using ProMoIJ or the assisted manual protocol.

2.8 | Analysis of data robustness

The variability of the data obtained was determined using the relative standard error (rse):

$$\text{rse} = \frac{\text{sem}}{\text{mean}} \times 100 \tag{8}$$

To estimate the minimum number of processes required to achieve an rse $\leq$15%, we generated random sets of process data of different sizes, ranging from 1 to 45 processes. We performed 10,000 data iterations and calculated the value of the rse per iteration. Then, we estimated the probability of obtaining a mean rse $\leq$15% for n processes:

$$\text{Probability}_n = \frac{\sum \text{iterations with rse} \leq 15\%}{\text{Total number of iterations}(10000)} \times 100\% \tag{9}$$

2.9 | Analysis of the response to laser injury

Nineteen time frames (28.44 min) were selected for analysis of microglial motility before (8 frames) and after (11 frames) laser injury induction. Microglial cells were divided in two groups: cells immediately adjacent to the injured area (maximum distance between cell soma and lesion center <60 μm), and cells distant from the injured area (minimum distance between cell soma and lesion center >60 μm). In addition, cell processes were divided into those directly oriented toward the injury site, and those positioned in the opposite region of the cell (Figure 7b). Then, process motility was obtained using ProMoIJ Macro 5. The relative distances of the tip of the processes to the center of the injured area were also calculated. First, we obtained the XYZ coordinates of the center of the injured region (X_i, Y_i, and Z_i) using the Point tool of ImageJ. Then, we used the XYZ position of the tips provided by ProMoIJ Macro 5 to calculate the absolute distance of the tips to the center of the injured area:

$$\text{Distance}_f = \sqrt{(X_f - X_i)^2 + (Y_f - Y_i)^2 + (Z_f - Z_i)^2} \tag{10}$$

Where Distance_f corresponds to the distance of the tip to the center of the lesioned area in the time frame f, and X_f, Y_f, and Z_f are the coordinates of the tip of the process in the frame f. The distances obtained for each frame were referred to the mean distance in the first five frames before laser injury induction (Mean Distance_0) to calculate relative distances:

$$\text{Relative distance}_f = \left(\frac{\text{Distance}_f}{\text{Mean Distance}_0} \times 100\right) - 100 \tag{11}$$

where Relative distance_f is the relative distance of the tip in the time frame f. This equation generates negative values when the distance to the center of the injured area decreases compared with the initial distance in time frame 0.

2.10 | Statistics

Experiments were analyzed using GraphPad Prism 5 (GraphPad Software, Inc, San Diego, CA) by Mann Whitney test or Wilcoxon signed-rank test to compare two groups of data, Friedman test to compare paired observations followed by the Dunn's Multiple comparison test, or two-way analysis of variance (ANOVA) for more than two groups of data, followed by Bonferroni *posthoc* analysis. Only $P < .05$ is reported to be significant. Box plot whiskers represent the 10th and 90th percentiles.

3 | RESULTS

Motility of microglial processes was evaluated by analyzing changes in their length (process velocity) and tip position (tip velocity). The analysis of process velocity in 3D requires reconstruction of their 3D skeleton through time, while the analysis of tip velocity requires tracking the position of the tip to estimate the mean distance covered per unit of time.

We have developed ProMoIJ to accelerate and systematize the analysis of microglial process motility. The analysis of process motility using time-lapse imaging requires several preprocessing steps aimed at correcting imaging artifacts. ProMoIJ facilitates the following preprocessing steps: image cropping (Macro 1), alignment (registration,

Macro 2), photobleaching correction (Macro 3), as well as noise and background subtraction (Macro 3; Figure 1a). The core of ProMoIJ is based on Macros 4 and 5, which allow the selection of individual microglial processes and the automated analysis of their motility (Figure 1b–c). The strategy followed is based on aligning each selected process along an orientation vector (base-to-tip) defined by the user. Once the process is oriented in the Y axis, profile intensity lines are run for each Y position to define the left and right borders of the process. The XZ geometric center of the process in each Y position is then calculated for each time point, thus defining the 3D skeleton of the process over time (Figure 1d). One of the main advantages of using ProMoIJ is that each macro facilitates and speeds up the analysis through batch processing (i.e., without manual intervention by the user), thus automatically opening and saving images, selections, and data tables.

3.1 | Pre-processing of images using ProMoIJ

A main problem with time-lapse imaging is sample drift, which may reflect translational movements (in *X* and *Y* axes) and rotations (at an angle) of the sample. Sample drift can be corrected using tools to align time-lapse images (registration). ProMoIJ Macro 2 runs "MultistackReg" (Thevenaz et al., 1998; Brad Busse) and "Correct 3D drift" (Parslow et al., 2014) ImageJ plugins to implement batch registration of the images. "MultistackReg" plugin contains several algorithms that allow Z-stacks registration. We tested two algorithms: "Translation", which aligns images correcting translational movements; and "Rigid Body", which aligns the images correcting for both translational and rotational movements. The registration was adequate when the soma of most cells in our images remained in the same position over time. "Rigid Body" algorithm produced the best results, and thus images registered with this algorithm were used for further processing. However, if the images evidence changes in sample size (shrinkage or expansion), users may also test the "Scaled rotation" or the "Affine" algorithms, which may correct even more complex morphological changes. In addition, we also found that the combination of both plugins "MultistackReg" and "Correct 3D drift" produced better results than using them alone, at least in our images. "Correct 3D drift" plugin allows corrections "in depth" (focal position). Therefore, we recommend registering the images using the algorithm "Rigid body" of "MultistackReg" plugin followed by "Correct 3D drift" as a first approach. This is the strategy that worked best in our hands when testing different types of images.

A second common problem in time-lapse imaging is photobleaching of fluorescent probes, which may be corrected using image processing tools that compensate intensity changes over time. ProMoIJ Macro 3 performs batch photo-bleaching correction using the ImageJ plugin "CorrectBleach_V2.0.2" and its "Histogram Matching" method (Miura et al., 2014), which homogenizes image intensity throughout time-frames by normalizing their histograms. In addition, this macro uses a "Difference of Gaussians filter" to reduce noise and background. Two parameters (Table 1; parameters M3.1 and M3.2) are defined for the "Difference of Gaussians filter": minimum sigma value (degree of image smoothing and noise elimination), and maximum sigma value (degree of background subtraction). It is important to consider that a large minimum sigma value, while it reduces noise, may also affect the resolution of the image thus decreasing the accuracy of further measurements. Moreover, utilizing large maximum sigma values better preserves the structures observed in the original image but subtracts less background. Thus, we recommend using the smaller minimum sigma value that adequately reduces image noise and the larger maximum sigma value that adequately reduces image background.

3.2 | Selection of processes using ProMoIJ

ProMoIJ Macro 4 assists the selection of processes to be analyzed. In addition, it allows defining the orientation vector used to align the process with the *Y* axis. A critical point is to define the static basal region of the process from where motility is to be calculated. To facilitate defining the constant basal region, Macro 4 collapses all Z-stacks through the time-lapse into one single image and highlights in red the pixels that maintain an intensity value above a user-defined threshold level throughout the time frames (Table 1; parameter M4.1). The threshold should be selected to only include pixels that clearly correspond to cellular elements. It is preferable to select a highly restrictive threshold than a permissive one, even if it excludes some cellular elements. The process is selected using the ROI manager tool of Fiji. The selection must include a part of the basal constant region of the process and any area occupied by the non-constant region of the process at any given time frame. Variations in the size of selected basal constant region are not expected to induce relevant changes in motility estimations, but it is recommended to select a small portion of the constant region to reduce the time of analysis. Finally, the orientation of the process is indicated by creating an arrow (orientation vector) pointing from the basal constant region to the tip of the process.

3.3 | Automatic analysis of microglial process motility using ProMoIJ

We evaluated motility of microglial processes by analyzing two main parameters: process velocity and tip velocity. ProMoIJ Macro 5 estimates process and tip velocity by reconstructing the process 3D skeleton. 3D reconstruction of the process skeleton is performed by analyzing the intensity profiles of horizontal lines and identifying the presence of processes and their borders in each Y position based on the intensity of the profile maxima (above a user-defined threshold; Table 1; parameter M5.4). Profile lines are analyzed in each Z-slice and the X and Z coordinates of the borders are used to calculate the coordinates of the center of the process in each horizontal plane (XZ planes; Figure 1d).

Macro 5 loads images and their corresponding process selections and orientation vectors. Then, to analyze motility, the macro reconstructs the skeleton of the same process over time by starting the reconstruction from the same constant region and selecting the branches, when they exist, that are closest to the previously reconstructed skeleton (Figure 1d,e).

During the development of ProMoIJ we occasionally observed that the reconstructed process was not the one we intented to analyze but a nearby, truncated one. Therefore, we added a pre-detection step in Macro 5 to force the detection of non-truncated processes and

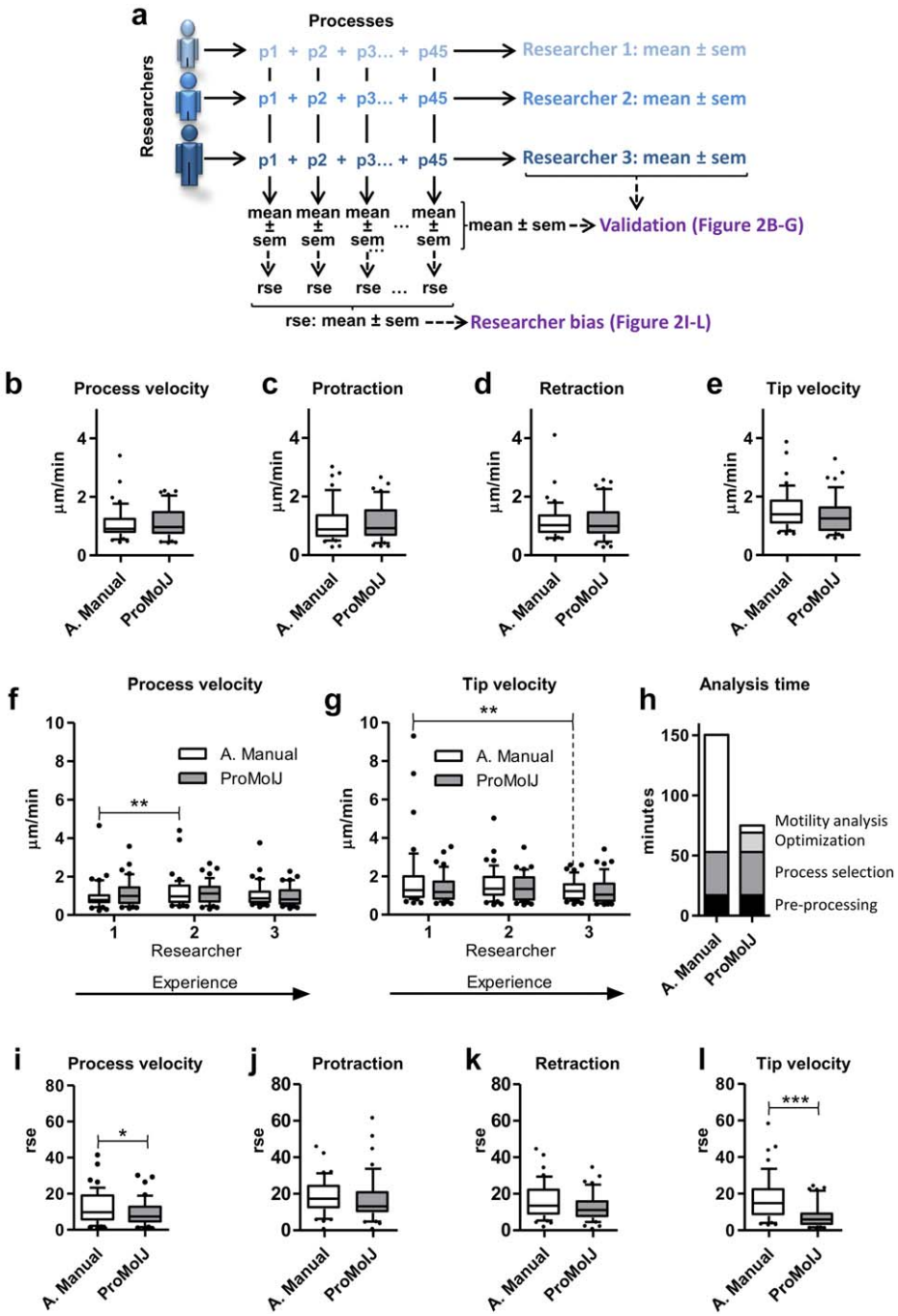

FIGURE 2 ProMoIJ validation. (a) Experimental design. The same 45 microglial processes were analyzed by three independent researchers with different levels of experience in the analysis of motility, from no-experience (1), with some experience (2), to highly-experienced (3) using ProMoIJ and the assisted manual protocol. (b–e) Mean motility data (process velocity [b], protraction [c], retraction [d], and tip velocity [e]) from the three researchers estimated with ProMoIJ or the assisted manual protocol. (f and g) Process (f) and tip velocity (g) data obtained with ProMoIJ and the assisted manual (A. manual) protocol by each researcher. ** indicates $P < .01$ by Bonferroni posthoc test (after two-way ANOVA was significant at $P < .05$ for researcher factor). (h) Time spent in data analysis (45 processes) by an experienced researcher using ProMoIJ or our assisted manual method. (i–l) Process velocity (i), protraction (j), retraction (k), and tip velocity (l) relative standard errors (rse) of combined data from the three researchers. * indicates $P < .05$ and *** indicates $P < .001$ by Wilcoxon signed rank test. Whiskers in box plots represent 10th and 90th percentiles, and the line in box plot represents 50th percentile [Color figure can be viewed at wileyonlinelibrary.com]

avoid their analysis. Macro 5 excludes from the analysis those process skeletons whose length does not reach a certain percentage of the length of the process selection at least in one time frame during the pre-detection step. This pre-detection step slows down the speed of the analysis and aborts skeleton reconstruction of some processes (when it is not able to reconstruct a skeleton that matches the length criteria), but we found it tremendously useful to improve the quality of the analysis.

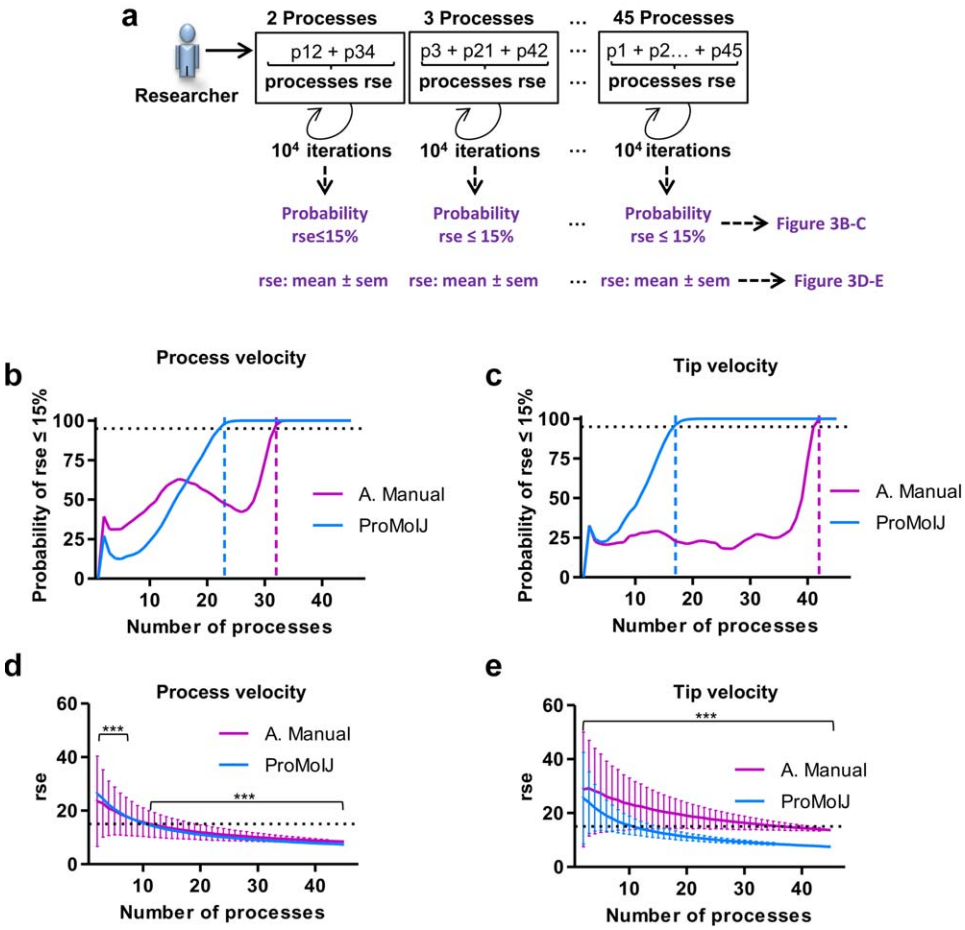

FIGURE 3 ProMoIJ robustness. (a) Experimental design. We generated random groups of process data (from the least experienced researcher) of different sizes, ranging from 1 to 45 processes. 10,000 data iterations were performed and the value of the relative standard error (rse) per iteration calculated. Then, we estimated the probability of obtaining an rse $\leq$ 15% when using ProMoIJ or assisted manual (A. manual) protocol. In addition, we calculated the mean rse of the iterations. (b and c) Lines show changes in the probability of obtaining a process velocity rse $\leq$ 15% (b), or tip velocity rse $\leq$ 15% (c) while the number of processes analyzed increases from 1 to 45. The horizontal black dotted lines represent 95% probability of obtaining an rse $\leq$ 15%. Vertical colored dotted lines represent the number of processes required to reach a probability >95%. (d and e) Lines show changes in mean process velocity rse (d), or mean tip velocity rse (e) while the number of processes analyzed increases. The dotted line indicates rse = 15%. Data in graphs are expressed as mean $\pm$ *SD*. *** indicates $P < .001$ by Bonferroni posthoc test for ProMoIJ vs A. Manual method (after two-way ANOVA was significant at $P < .0001$ for number of processes, method, and the interaction between the two factors) [Color figure can be viewed at wileyonlinelibrary.com]

In the following sections we validate ProMoIJ and then assess time required for analysis, sensitivity to experimenter bias, and robustness to the number of processes analyzed when using ProMoIJ or a manual method. Our manual method was assisted by Macros 2, 3, 4, and 6 (not included in ProMoIJ). Macro 6 loads and saves images, selections and data tables, and also prepares images for manual reconstruction of 3D skeletons with the ImageJ plugin "Simple Neurite tracer" (Longair et al., 2011). XYZ coordinates of process tips were obtained using the ImageJ plugin "3D viewer" (Schmid et al., 2010) and the "point" tool. Therefore, we named this protocol "assisted manual".

3.4 | ProMoIJ data validation

We validated ProMoIJ as a reliable tool to analyze microglial process motility through comparison with the assisted manual protocol. The same 45 microglial processes were analyzed by three independent researchers with different levels of experience in the analysis of motility, from non-experienced (1), with some experience (2), to highly-experienced (3) using both ProMoIJ and the assisted manual protocol. A schematic diagram of the different comparisons performed to validate ProMoIJ is shown in Figure 2a. First, we checked overall differences between assisted manual and ProMoIJ analysis using mean motility data from the three researchers. Overall, no significant differences were found in process velocity, protraction, retraction, and tip velocity when estimated with ProMoIJ or the assisted manual protocol (Figure 2b–e and Supporting Information, Table S2). In addition, motility data obtained with ProMoIJ and the assisted manual protocol by each researcher were not significantly different (Figure 2f,g and Supporting Information, Table S3), thus further validating ProMoIJ as a reliable tool to analyze microglial process motility.

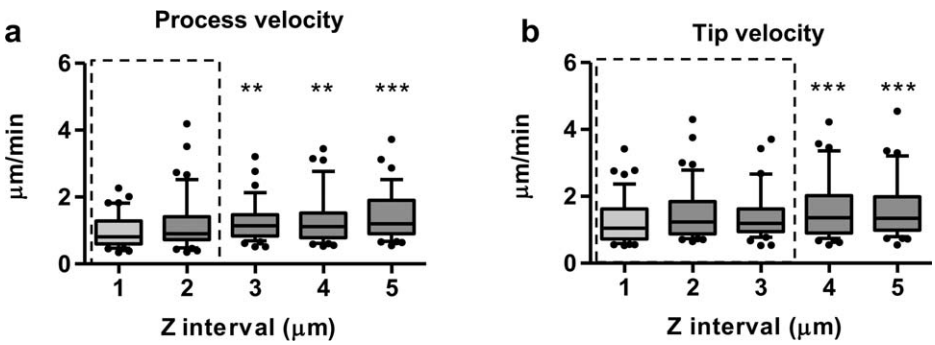

FIGURE 4 Relevance of Z-step size. (a and b) Comparison between data (process velocity [a] and tip velocity [b]) obtained from the same images using different Z-step intervals. The dotted box represents the interval of values that produces similar data to those obtained with a Z-slice interval of 1 µm. ** indicates $P < .01$, and *** $P < .0001$ by Dunn's multiple comparison test. Whiskers in box plots represent 10th and 90th percentiles, and the line in box plots represents 50th percentile

3.5 | Time required for analysis is greatly reduced by ProMoIJ

Manual analysis of microglial process motility is conventionally done in 2D by manually reconstructing the skeleton of the process in each time frame or by tracking the position of the tip, and it is therefore a time-consuming procedure. To compare the time spent in data analysis using our assisted manual method and ProMoIJ, an experienced researcher recorded the time required to measure motility from the same 45 processes (from three time-lapse images, each with five microglial cells; 41 Z-slices, and 10 time frames per image) using ProMoIJ or the assisted manual protocol. Both methods shared the same preprocessing and process selection steps, which required around 1 hr (53 min). When performing the assisted manual protocol, 97.5 min were spent performing the whole analysis (2.2 min per process). In contrast, only 22.0 min were required to perform the analysis when using ProMoIJ, of which 16.0 min were used to optimize ProMoIJ parameters and 6.0 min to perform the motility analysis itself (8.0 s per process). In summary, 2.5 hr were needed to obtain data with the assisted manual protocol, while ProMoIJ analysis required 1.25 hr (Figure 2h). It should be noted that without the assistance of Macros (Macros 2, 3, 4, and 6) image pre-processing would take considerably more time for manual analysis. Therefore, ProMoIJ greatly reduced the time required to obtain motility data, being twice as fast as the assisted manual protocol.

3.6 | ProMoIJ data are less sensitive to experimenter bias

One of the aims of this study was to develop a tool to homogenize motility analysis among different laboratories as to yield comparable and reproducible results. To test the effect of ProMoIJ on experimenter bias, we evaluated the variability between researchers by comparing the results they obtained individually when using ProMoIJ or the assisted manual protocol. We found that process and tip velocity data obtained by the least experienced researcher were significantly different from one of the other two researchers when using the assisted manual protocol (Figure 2f,g and Supporting Information, Table S3). In contrast, ProMoIJ reduced the between-researchers variability and no significant differences were found among any of the three researchers.

To further analyze the variability between researchers of data obtained with ProMoIJ and the assisted manual protocol, we compared the relative standard errors (rse) of combined data from the three researchers (Figure 2a). This analysis revealed that ProMoIJ significantly reduced the between-researchers variability in process and tip velocity analysis (Figure 2i–l and Supporting Information, Table S4). Therefore, motility data obtained with ProMoIJ are less sensitive to experimenter bias than data obtained using the assisted manual protocol.

3.7 | ProMoIJ analysis variability is robust to changes in the number of processes analyzed

Data variability observed in our experiments is a combination of researcher bias, biological variability, and methodological variability (e.g., acquisition and processing artifacts). The impact of these sources of variation may be minimized by increasing the number of processes analyzed. We thus evaluated motility data robustness to the number of processes analyzed when using ProMoIJ or the assisted manual protocol, with data from the least experienced researcher. We established as robustness criterion to reach a 95% probability of obtaining an rse $\leq$15%, and calculated the minimum number of processes to be analyzed in order to achieve this criterion. We generated 45 sets of data, each with 10,000 groups of 1 to 45 processes, and calculated in each of these sets the percentage of groups with an rse $\leq$15%. This percentage represents the probability of obtaining an rse $\leq$15% for each set of "*n*" processes (Figure 3a).

Our analysis indicates that data obtained with ProMoIJ are more homogeneous than data obtained with the assisted manual protocol (Figures 2i,l and 3b,c). Increasing the number of processes analyzed increased the probability of obtaining an rse $\leq$15% following a regular, sigmoidal pattern when using ProMoIJ (Figure 3b,c). In contrast, in the data obtained with the assisted manual protocol, the probability of reaching an rse $\leq$15% for both process and tip velocity fluctuated when increasing the number of processes. Furthermore, we calculated how many processes should be analyzed to reach the robustness criterion: 32 and 42 processes for process and tip velocity, respectively,

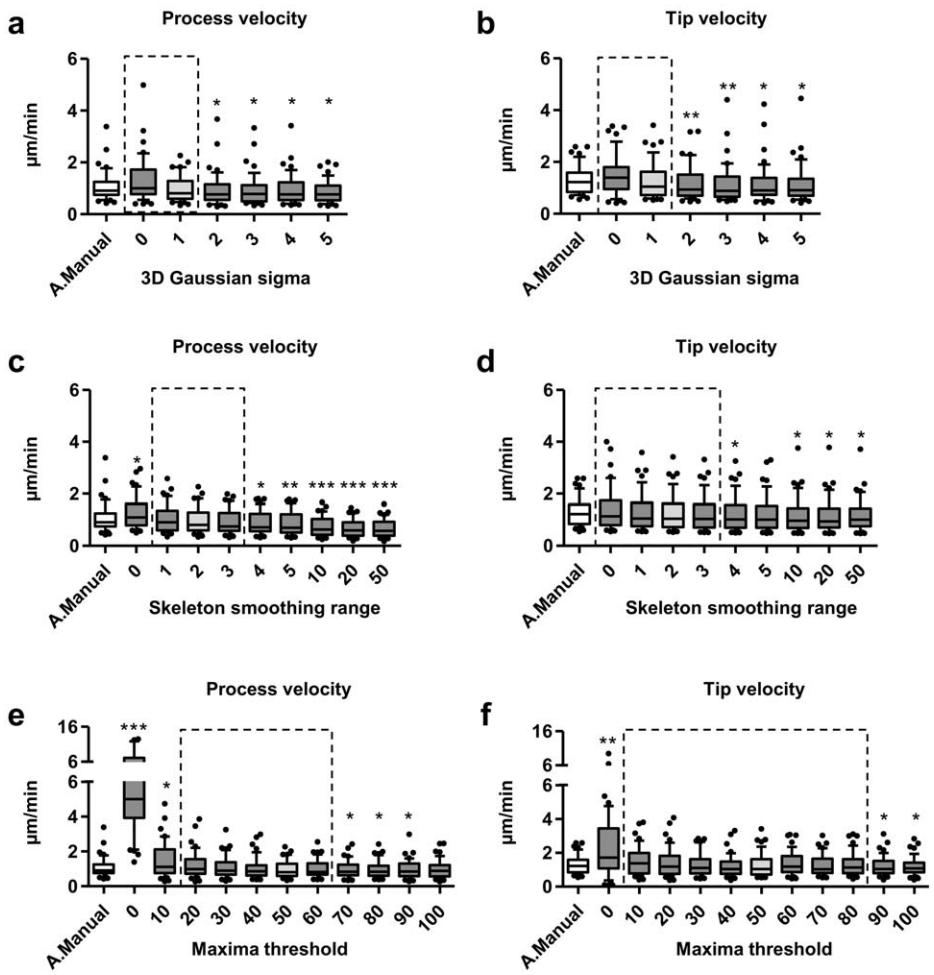

FIGURE 5 ProMoIJ parameters relevance. (a–f) Comparison between process (a, c, and e) and tip velocity (b, d, and f) data obtained with ProMoIJ and the assisted manual (A. manual) method when a ProMoIJ parameter (3D gaussian sigma [a and b], skeleton smoothing range [c and d], and maxima threshold [e and f]) was systematically varied while maintaining the remaining parameters in their optimized values. White box plots correspond to data obtained with the A. manual protocol and light gray box plot to data obtained with ProMoIJ using the optimal value. The dotted box represents the interval of values that produce similar data to those obtained with the A. Manual protocol. * indicates $P < .05$ and *** indicates $P < .001$ by Wilcoxon signed rank test for ProMoIJ vs A. Manual method. Whiskers in box plots represent 10th and 90th percentiles, and the line in box plot represents 50th percentile

were necessary when using the assisted manual protocol, while only 23 and 17 processes were required when using ProMoIJ (dotted lines in Figure 3b,c).

We finally analyzed the average rse for the 10,000 iterations calculated. As expected, the variability of process and tip velocity decreased when more processes were analyzed (Figure 3d,e). In addition, the rse of both process and tip velocity obtained with ProMoIJ were significantly lower when compared with the rse of data obtained with the assisted manual protocol (Figure 3d,e). Therefore, compared with the assisted manual protocol, ProMoIJ analysis requires a reduced number of processes to produce robust and representative data.

3.8 | Relevance of Z-step size to estimate process motility

One of the key parameters that must be selected during image acquisition is the Z-step size, which ranged from 0.5 to 3 μm in previous studies (Davalos et al., 2005; Nimmerjahn et al., 2005; Damani et al., 2011; Kondo et al., 2011; Krabbe et al., 2013; Dissing-Olesen et al., 2014; Gyoneva et al., 2014; Batti et al., 2016; Eyo et al., 2016; Fourgeaud et al., 2016; Li et al., 2016; Sipe et al., 2016). ProMoIJ can use any size of Z-step interval to estimate process motility. Large Z-step intervals reduce the time required to acquire Z-stacks, but in turn they reduce the image axial resolution. Therefore, the size of the Z-step interval may have a significant effect on process motility estimation in 3D. To evaluate the influence of the Z-step size on process motility estimations we processed the same images with increased Z-step size by reducing the number of Z slices at fixed intervals. Increasing the Z slice interval by 2 μm (from 1 to 3 μm) significantly altered process velocity estimations (Figure 4a,b and Supporting Information, Table S5). Thus, ProMoIJ analysis overestimates process motility when the Z-step interval is increased. This effect may be related to the loss of axial resolution resulting from the increased Z-step interval, leading to higher variability in 3D skeleton reconstructions and length estimations. Thus,

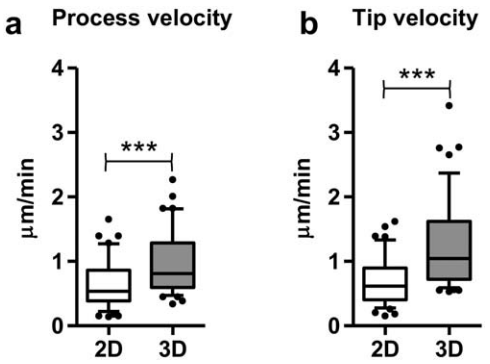

FIGURE 6 3D versus 2D motility analysis. (a and b) Comparison between data (process velocity [a] and tip velocity [b]) obtained from the same images preserving 3D information or using their maximum projection of Z-stacks (2D analysis). *** indicates $P < .001$ by Wilcoxon signed rank test. Whiskers in box plots represent 10th and 90th percentiles, and the line in box plots represents 50th percentile

the size of the Z-step is a relevant factor to take into account when capturing images, and when comparing data from different experiments.

3.9 | Influence of ProMoIJ parameters in motility estimations

ProMoIJ Macro 5 utilizes 20 parameters that may be defined by the user to optimize the reconstruction of processes skeleton. All these parameters are summarized in Table 1 (parameters M5.1–6) and Supporting Information, Table S1 (parameters M5.7–20). From those parameters, the time interval (Table 1; M5.1) is inherent to capturing the time-lapse images, thus precluding the need for optimization during analysis. For the remaining parameters, deciding which of them should be optimized may be an arduous process. Therefore, we statistically determined the parameters which had a relevant influence on the final motility estimations. We systematically varied each parameter while maintaining the others in their optimized values (settings and process selection from the most experienced researcher) and obtained motility data. To test which combination was optimal, we compared different sets of data produced with ProMoIJ with the data obtained using the assisted manual protocol (Figure 5). It is important to note that the optimization of these parameters by users should be performed by visual inspection of the reconstructed 3D skeleton (Macro 5 "Optimization mode"), rather than by comparison between ProMoIJ and the assisted manual protocol. Most of the parameters analyzed did not induce significant deviation between the data obtained with ProMoIJ versus the assisted manual protocol (data not shown). However, we identified three parameters (sigma value of the 3D Gaussian filter, the range of skeleton smoothing, and the threshold of the maxima, Table 1, parameters M5.2–4) that showed a relevant effect on final data (Figure 5).

Importantly, parameters related to smoothing filters produced the largest impact on final data. The sigma value of the 3D Gaussian filter (Table 1, parameter M5.2) was decisive for obtaining accurate process

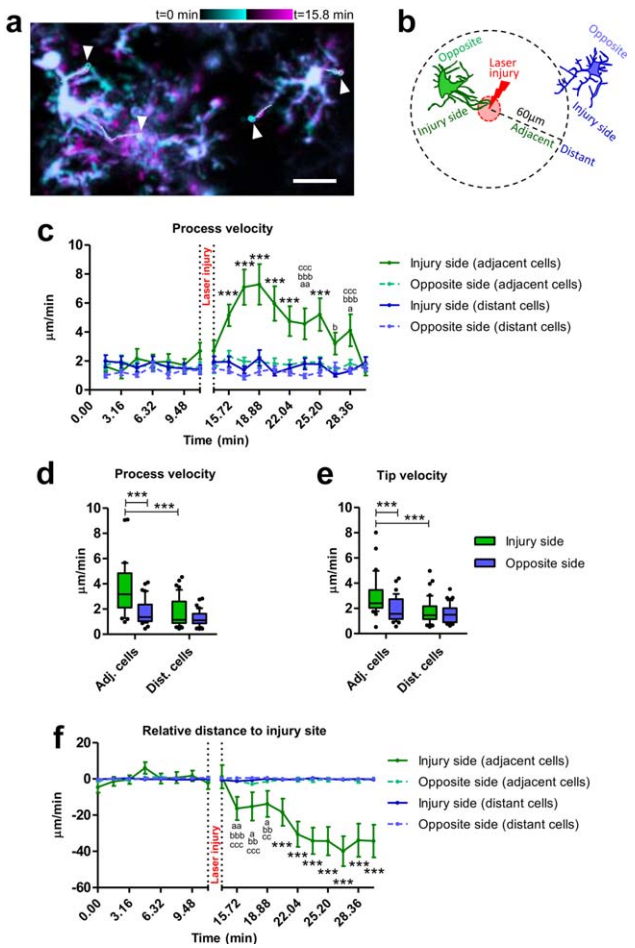

FIGURE 7 Microglial process motility analysis after laser-induced injury. (a) Representative projections (41 Z-slices = 41 µm) of 2-photon images of microglial cells at t0 (cyan) and 15.8 min (t11, magenta) in the mouse cortex injured with a laser beam. Scale bar = 20 µm. Arrowheads point to reconstructed skeletons. (b) Representative scheme of the image showed in (a). (c) Comparison between process velocities (mean ± *SEM*) obtained from processes of adjacent and distant microglial cells, and oriented toward the injury side or situated in the opposite region of the cell. (d and e) Comparison between motility data (process velocity [d] and tip velocity [e]) obtained from processes of adjacent and distant microglial cells, and oriented toward the lesion or situated in the opposite region of the cell. (f) Comparison between relative distances to the center of the laser-injured region (mean ± *SEM*) obtained from processes of adjacent and distant microglial cells, and oriented toward the injury side or situated in the opposite region of the cell. Negative relative distances indicate shorter distances to the center of the injured region. In (c) and (f) *, a, b and c represent significance respect other groups, opposite processes from adjacent cells, injury oriented processes from distant cells, and opposite processes form distant cells, respectively. One symbol is used for $P < .05$, two symbols for $P < .01$, and three symbols for $P < .001$ by Bonferroni posthoc test after two-way repeated measures ANOVA. The vertical dotted lines separate the data from the images obtained before and after the induction of laser lesions. In (d) and (e) *** indicates $P < .001$ by Bonferroni test. Whiskers in box plots represent 10th and 90th percentiles, and the line in box plots represents 50th percentile [Color figure can be viewed at wileyonlinelibrary.com]

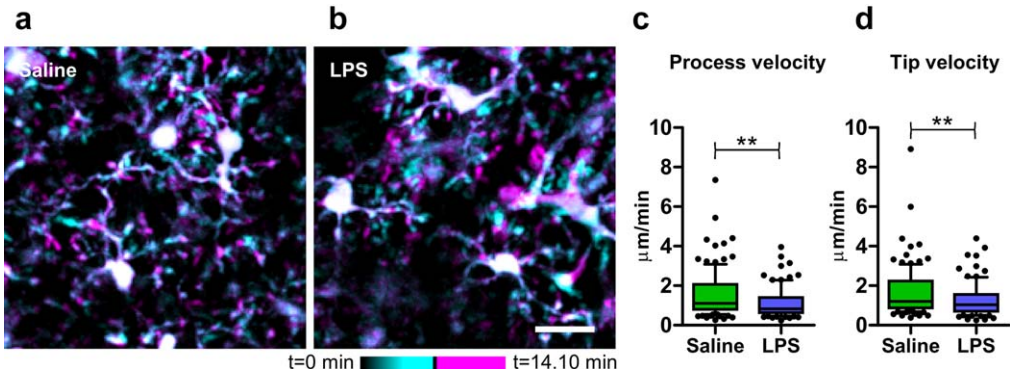

FIGURE 8 LPS effects on microglial process motility. (a) Representative projections (44 Z-slices = 44 μm) of 2-photon images of microglial cells at t0 (cyan) and t10 (14.10 min, magenta) in the cortex of mice systemically treated with saline (left) or LPS (right) 24 hr before imaging. (b and c) Comparison between data (process velocity [b] and tip velocity [c]) obtained from saline and LPS treated mice. ** indicates $P < .01$ by Mann-Whitney test. Whiskers in box plots represent 10th and 90th percentiles, and the line in box plots represents 50th percentile [Color figure can be viewed at wileyonlinelibrary.com]

and tip velocity data (Figure 5a,b), as small variations in this parameter significantly deviated the data obtained with ProMoIJ from data obtained with the assisted manual protocol. In addition, the skeleton smoothing range (Table 1; parameter M5.3) was also important to obtain accurate process and tip velocity data (Figure 5c,d). Finally, the threshold of the maxima (Table 1; parameter M5.4), a parameter that defines the intensity threshold for the analysis, admitted a wide range of values without inducing significant deviations in process and tip velocity data obtained with PromoIJ from data obtained with the assisted manual protocol (Figure 5e,f). Thus, ProMoIJ analysis is relatively robust to variations in image intensity but sensitive to image smoothing.

Summarizing, ProMoIJ motility estimations strongly depend on the adequate selection of smoothing filter parameters. Thus, the use of the optimization step included in the main menu of Macro 5 (Table 1; parameter M5.6) is recommended to select the optimal smoothing parameters for the analysis.

3.10 | Data obtained from 2D projections underestimate motility

Several studies have analyzed microglial motility using two-dimensional projections of Z-stacks of images to simplify the analysis (Davalos et al., 2005; Nimmerjahn et al., 2005; Kondo et al., 2011; Fourgeaud et al., 2016; Sipe et al., 2016). Therefore, we evaluated differences in motility estimations (obtained with ProMoIJ) when analyzing the same images preserving their 3D information or using their maximum projection of Z-stacks (2D analysis). Our analysis revealed, as expected, that the lack of 3D information leads to a significant underestimation of process motility (Figure 6a,b).

3.11 | Only cells adjacent to a laser-injured area extended their processes toward the lesion site

Focal laser injury has been widely used to test the capacity of microglial cell processes to respond to a lesion (Davalos et al., 2005; Nimmerjahn et al., 2005; Damani et al., 2011; Krabbe et al., 2013; Dissing-Olesen et al., 2014; Gyoneva et al., 2014; Fourgeaud et al., 2016; Sipe et al., 2016). We used ProMoIJ Macros to analyze directional process motility toward a focal lesion induced with a laser beam in the cortex. We differentiated between microglial cells immediately adjacent to the injured area, and microglial cells distant from the injured area. In addition, we distinguished between processes directly oriented toward the injury site, and processes positioned in the opposite region of the cell (Figure 7a,b). We detected a significant increase in process velocity after laser injury induction only in processes oriented toward the injured region of cells adjacent to the lesion (Figure 7c). In addition, mean process velocity and tip velocity were significantly increased only in processes oriented toward the lesion from adjacent cells (Figure 7d,e). Interestingly, oriented processes from adjacent cells also showed increased retraction (Supporting Information, Table S7), although their net process velocity was significantly increased (Supporting Information, Table S7), indicating an overall extension toward the injured area. No significant changes were detected either in opposite processes from adjacent cells or in the process from distant cells (Figure 7c–e and Supporting Information, Table S7).

To further analyze the extension of processes to the lesion, we estimated the relative distance of the processes tip to the center of the injured region. Again, only oriented processes from adjacent cells significantly decreased their distance to the center of the lesion (Figure 7f). Our data reveal that only cells adjacent to the injured area extended their processes toward the lesion site, and that only the processes that emerge from the region of the cell oriented toward the injured region increased their motility and approached the injury site.

3.12 | Systemic administration of LPS reduces microglial process motility

Systemic inflammation is known to trigger neuroinflammation, affecting the behavior of microglial cells (Sierra, Gottfried-Blackmore, McEwen, & Bulloch, 2007). We analyzed the effect of a systemic inflammatory challenge, induced by intraperitoneal administration of LPS (1 mg/kg),

on microglial process motility 24 hr after its induction, when microglial expression of pro-inflammatory cytokines is largely resolved (Sierra et al., 2007). Our data showed that process motility was significantly reduced by LPS administration (Figure 8 and Supporting Information, Table S8), indicating that systemic inflammation reduces microglial process motility in the cortex.

4 | DISCUSSION

We have developed a new tool, ProMoIJ, which allows automatic analysis of microglial process motility in 3D. Data obtained with ProMoIJ protocol were validated by comparing them with data obtained with an assisted manual protocol. Our results revealed that ProMoIJ analysis of process motility is faster, less sensitive to experimenter bias, and produces more robust data than manual analysis. We also show here that commonly used 2D projections (maximum projection) of 3D acquired images significantly underestimate microglial processes motility. In addition, we analyzed the extension of microglial processes toward a focal laser injury revealing that only cells adjacent to the injured area sent their processes toward the lesion site, and observed that 24 hr after intraperitoneal administration of LPS microglial process motility is reduced *in vivo* in the cortex.

ProMoIJ is a freely available and user-friendly tool to facilitate the quantification of microglial process and tip velocity in 3D. Many different, non-comparable protocols have been used to extract microglial process motility information from live-imaging experiments (Davalos et al., 2005; Nimmerjahn et al., 2005; Damani et al., 2011; Fontainhas et al., 2011; Kondo et al., 2011; Krabbe et al., 2013; Dissing-Olesen et al., 2014; Batti et al., 2016; Eyo et al., 2016; Fourgeaud et al., 2016; Li et al., 2016; Sipe et al., 2016). To analyze microglial process motility we selected two direct measurements of motility that provide full and complementary information: changes in processes length (process velocity) and tip position (tip velocity) over time. Manual extraction of these data from 3D time-lapse images is time consuming and tedious, often prompting the use of 2D projections of original images (Davalos et al., 2005; Nimmerjahn et al., 2005; Kondo et al., 2011; Fourgeaud et al., 2016; Sipe et al., 2016). Hence, we developed ProMoIJ for naïve and expert researchers as a step-by-step guided tool to analyze 3D process motility.

The protocol implemented by ProMoIJ consists of 5 steps: Macro (1) Image cropping; Macro (2) image registration; Macro (3) photobleaching, noise and background correction; Macro (4) process selection; and Macro (5) automated 3D motility analysis (Figure 1). Although we mainly focused on process and tip velocity (including protraction and retraction), other three biologically relevant parameters were extracted from data obtained with ProMoIJ: protraction-retraction velocity, net change in process length per time unit, and tip directionality. In physiological conditions protraction and retraction of processes are counterbalanced hence preventing net changes in process length (Figure 2c,d and Supporting Information, Table S2; Nimmerjahn et al., 2005). However, this balance is disrupted after laser injury leading to a net growth of processes toward the lesion (Figure 7 and Supporting Information, Table S7). In addition, tip directionality may be tracked and analyzed using tip position data, providing information about the influence of attractants or repellents. Importantly, ProMoIJ saves XZY coordinates of process tip in each time frame, thus offering the possibility of evaluating the directionality of tip movements toward a specific region of the image in 3D (e.g., lesioned regions or dendritic spines). Therefore, using tip XZY coordinates provided by ProMoIJ we showed here that in early time points (≈15 min) only processes facing the laser injury site from adjacent cells (<60 mm) increased their motility and extended toward the lesion (Figure 7 and Supporting Information, Table S7). In addition, previous reports suggest that at later time points (30 min), processes situated in the part of the cell opposite to the lesion retract, while processes from distant microglial cells also changed their motility after laser injury, becoming polarized toward the lesioned region (Lee, Liang, Fariss, & Wong, 2008; Davalos et al., 2005; Nimmerjahn et al., 2005).

ProMoIJ protocol was validated through comparison with the assisted manual protocol. Our validation demonstrated that both ProMoIJ and the assisted manual protocols produce similar microglial process motility data (Figure 2b–e and Supporting Information, Table S2). Due to the lack of *in vivo* 3D microglial process motility analysis, we were unable to compare our data with previous publications. However, several studies have analyzed 2D microglial process motility in uninjured brains obtaining mean process velocity values ranging from 0.58 to 1.47 μm/min (Nimmerjahn et al., 2005; Sipe et al., 2016) and 2D tip velocity data with mean values around 0.81 μm/min (Kondo et al., 2011; Fourgeaud et al., 2016). Our 2D results pooling together primary and secondary order processes (process velocity: 0.66 ± 0.06 μm/min, tip velocity: 0.71 ± 0.05 μm/min, Supporting Information, Table S6) are in the same range of those obtained by others, although image resolution and time intervals were different (Nimmerjahn et al., 2005; Kondo et al., 2011; Fourgeaud et al., 2016; Sipe et al., 2016). Importantly, our results indicate that 2D motility analysis greatly underestimates process motility and that microglial processes movements are faster than previously thought (Figure 6a and Supporting Information, Table S6).

One main benefit of using ProMoIJ is that it prevents bias related to the investigator. Indeed, we observed that using the assisted manual protocol the least experienced researcher obtained statistically different motility data compared with the other two researchers. Importantly, data obtained with ProMoIJ protocol were similar between researchers and showed lower between-researchers variability than data obtained with the assisted manual protocol (Figure 2f,g,i–l and Supporting Information, Table S3 and S4). Hence, our analyses indicate the ProMoIJ will contribute to homogenize motility analysis among different laboratories rendering comparable results.

Another advantage of ProMoIJ is that the motility analysis is more robust to variations in the number of processes analyzed compared with the assisted manual protocol. During manual analysis it is expected that, depending on the investigator, crucial decisions (i.e., selection of the starting basal point, process central points, final tip

position, branch selection and gap inclusion) may be less consistent between time frames and processes, thus introducing extra sources of variability. Increasing the number of processes analyzed may buffer the impact of this extra variability on motility estimations. Indeed, data precision obtained with both ProMoIJ and assisted motility protocol in validation tests seemed acceptable when analyzing 45 processes, as indicated by their relative standard error (rse $\leq$10%, Figure 3d,e). However, ProMoIJ analysis requires a lower number of processes to produce representative data (rse $\leq$15%) than the assisted manual protocol (Figure 3b,c), indicating that data obtained with ProMoIJ are, as expected, more robust.

The third asset of ProMoIJ is that it reduces the time required to analyze microglial process motility. ProMoIJ performs batch processing of time-lapse images, without manual intervention after selection of folders and parameters, thus reducing the analysis time and allowing for consistent pre-processing settings in the whole experiment. In addition, we show here that ProMoIJ analysis of microglial process motility (Macro 5) is twice as fast as the assisted manual protocol (Macro 6; Figure 2h). However, because we used batch processing to assist our manual analysis, these results likely underestimate the time required for analysis with more conventional manual protocols, and thus ProMoIJ's impact on the acceleration of motility analysis might be underestimated here. In addition, our data indicate that ProMoIJ reduces the number of processes needed to obtain a robust estimation of microglial process motility, further contributing to saving imaging and analysis time.

A limitation of ProMoIJ is that users may optimize 3D skeleton reconstructions by re-defining up to 20 parameters. Although the possibility of varying parameters converts ProMoIJ into a flexible tool, it may also render the process of optimization tedious. To overcome this limitation we identified three parameters which had a significant influence on final motility estimations (Figure 5) and simplified the optimization establishing default values for the remaining parameters. However, default values of these remaining parameters may be changed by activating the "Advanced Menu" option in the main menu (Table 1, M5.5). Image acquisition, processing, and analysis related factors affect the comparability of motility results obtained by different laboratories. One critical parameter previously identified is the time sampling interval, and it was recommended to use short time intervals (30–45 s) to obtain accurate data (Nimmerjahn et al., 2005). Another critical parameter is the Z-step interval as it significantly affects the process motility estimations (Figure 4 and Supporting Information, Table S5). Nonetheless, the spatiotemporal resolution of our images (0.497 μm/pixel, 1 μm of Z-step interval and 1.57–1.58 min/frame) was sufficient to detect differences between control and experimental conditions both in LPS-induced neuroinflamamtion (**Figure** 8 and Supporting Information, Table S8) and in a model of mesial temporal lobe epilepsy (Abiega et al., 2016). Another critical issue is whether image resolution is decreased by image preprocessing, particularly when using smoothing filters, which combine 2D pixels or 3D information. Indeed, we show here that optimization of smoothing-related parameters is crucial to obtain adequate estimations of microglial process motility (Figure 5). We observed that the use of these filters, although sometimes necessary, should be limited to the minimum (between values 1 and 2) in order to eliminate noise and background without affecting the accuracy of the analysis.

ProMoIJ presents two other limitations that should be considered: (1) ProMoIJ use is limited to the analysis of non-hollow structures because 3D skeleton reconstruction is based on the use of maximum intensities and the search of connected pixels and (2) ProMoIJ is not able to reconstruct twisted structures as it assumes that microglial processes are oriented in one main direction along their entire length. These limitations may be solved in the future, as ProMoIJ is open source (downloadable from https://www.achucarro.org/downloads) and thus amendable for further functionality upgrades. However, in its current version, the possibility of varying up to 20 parameters in ProMoIJ allows fine tuning of process motility analysis and extends the use of ProMoIJ for other applications. Therefore, ProMoIJ may be used by a wide range of scientists interested in analyzing the motility of non-hollow and non-twisted tubular structures such as, in addition to microglial processes, filaments, dendrites, dendritic spines, growth cone filopodia, cilia, plant roots, growing stalactites, etc.

Microglia continuously survey the brain parenchyma to detect alterations and maintain tissue homeostasis. Importantly, microglial process motility has been shown to be reduced in aged mice (Damani et al., 2011), as well as mouse models of Alzheimer's disease (Krabbe et al., 2013; Gyoneva, Swanger, Zhang, Weinshenker, & Traynelis, 2016) and epilepsy (Abiega et al., 2016). In addition, using ProMoIJ we described here a decrease in microglial process motility in cortex 24 hr after the induction of a systemic inflammation mediated by intraperitoneal administration of LPS, when microglial expression of pro-inflammatory cytokines is largely resolved (Sierra et al., 2007) but morphological changes are still evident (Kondo et al., 2011). Previous studies provided controversial results regarding LPS effects on microglial motility 48 hrs after challenge, reporting either increased microglial process motility (2 mg/kg of LPS, 48 hr, Gyoneva et al., 2014) or no changes (0.5 mg/kg of LPS, 48 hr, Kondo et al., 2011). Indeed, our data shows a very small effect (0.25-fold reduction) of LPS on microglial motility, which is likely to be missed when analyzed manually. Inflammation is known to be exacerbated in most neurodegenerative diseases and therefore further experiments will be crucial in determining the relationship between microglial release of pro-inflammatory mediators and process motility.

In summary, understanding the mechanisms that contribute to the reduction of microglial process motility might lead to the development of therapies aimed to restore brain homeostasis through the recovery of microglial physiological functions. Therefore, the analysis of microglial process motility, as a measurement of microglial surveillance capacity, is highly relevant in the context of aging and neurodegenerative diseases. To the best of our knowledge, ProMoIJ is the first freely available tool that standardizes and accelerates 3D microglial process motility analysis, a measure directly linked to microglial function in health and disease.

ACKNOWLEDGMENT

This work was supported by grants from the Spanish Ministry of Economy and Competitiveness with FEDER funds to A. S. (RYC-2013–12817), A. S. and J. V. (BFU2015–66689-R), from the Basque Government to A. S. (PI-2016-1-0011), the Natural Sciences and Engineering Research Council of Canada (NSERC; RGPIN-2014–05308) to M. -E. T., and Ikerbasque start-up funds to J. V. I. P. was supported by a Jesus de Gangoiti Barrera Foundation Fellowship, J. V. by an Ikerbasque Research Fellow grant, and J. C. S by a Postdoctoral Fellowship from Fonds de la recherche du Québec – Santé (FRQS). We are grateful to Steve Lacroix at CRCHU de Québec-Université Laval for the use of his two-photon microscope.

ORCID

Marie-Ève Tremblay http://orcid.org/0000-0003-2863-9626
Amanda Sierra http://orcid.org/0000-0001-8415-096X
Jorge Valero http://orcid.org/0000-0001-6072-3313

REFERENCES

Abiega, O., Beccari, S., Diaz-Aparicio, I., Nadjar, A., Layé, S., Leyrolle, Q., . . . Sierra, A. (2016). Neuronal hyperactivity disturbs ATP microgradients, impairs microglial motility, and reduces phagocytic receptor expression triggering apoptosis/microglial phagocytosis uncoupling. *PLOS Biology*, *14*, e1002466. https://doi.org/10.1371/journal.pbio.1002466

Arnold, T., & Betsholtz, C. (2013). The importance of microglia in the development of the vasculature in the central nervous system. *Vascular Cell*, *5*, 4. https://doi.org/10.1186/2045-824X-5-4

Batti, L., Sundukova, M., Murana, E., Pimpinella, S., De Castro Reis, F., Pagani, F., . . . Heppenstall, P. A. (2016). TMEM16F regulates spinal microglial function in neuropathic pain states. *Cell Reports*, *15*, 2608–2615. https://doi.org/10.1016/j.celrep.2016.05.039

Damani, M. R., Zhao, L., Fontainhas, A. M., Amaral, J., Fariss, R. N., & Wong, W. T. (2011). Age-related alterations in the dynamic behavior of microglia. *Aging Cell*, *10*, 263–276. https://doi.org/10.1111/j.1474-9726.2010.00660.x

Davalos, D., Grutzendler, J., Yang, G., Kim, J. V., Zuo, Y., Jung, S., . . . Gan, W.-B. (2005). ATP mediates rapid microglial response to local brain injury in vivo. *Nature Neuroscience*, *8*, 752–758. https://doi.org/10.1038/nn1472

Dissing-Olesen, L., LeDue, J. M., Rungta, R. L., Hefendehl, J. K., Choi, H. B., & MacVicar, B. A. (2014). Activation of neuronal NMDA receptors triggers transient ATP-mediated microglial process outgrowth. *Journal of Neuroscience*, *34*, 10511–10527. https://doi.org/10.1523/JNEUROSCI.0405-14.2014

Eyo, U. B., Miner, S. A., Weiner, J. A., & Dailey, M. E. (2016). Developmental changes in microglial mobilization are independent of apoptosis in the neonatal mouse hippocampus. *Brain, Behavior, and Immunity*, *55*, 49–59. https://doi.org/10.1016/j.bbi.2015.11.009

Fontainhas, A. M., Wang, M., Liang, K. J., Chen, S., Mettu, P., Damani, M., . . . Wong, W. T. (2011). Microglial morphology and dynamic behavior is regulated by ionotropic glutamatergic and GABAergic neurotransmission. *PLoS ONE*, *6*, e15973. https://doi.org/10.1371/journal.pone.0015973

Fourgeaud, L., Través, P. G., Tufail, Y., Leal-Bailey, H., Lew, E. D., Burrola, P. G., . . . Lemke, G. (2016). TAM receptors regulate multiple features of microglial physiology. *Nature*, *532*, 240–244. https://doi.org/10.1038/nature17630

Gyoneva, S., Davalos, D., Biswas, D., Swanger, S. A., Garnier-Amblard, E., Loth, F., . . . Traynelis, S. F. (2014). Systemic inflammation regulates microglial responses to tissue damage in vivo. *Glia*, *62*, 1345–1360. https://doi.org/10.1002/glia.22686

Gyoneva, S., Swanger, S. A., Zhang, J., Weinshenker, D., & Traynelis, S. F. (2016). Altered motility of plaque-associated microglia in a model of Alzheimer's disease. *Neuroscience*, *330*, 410–420. https://doi.org/10.1016/j.neuroscience.2016.05.061.

Jung, S., Aliberti, J., Graemmel, P., Sunshine, M. J., Kreutzberg, G. W., Sher, A., & Littman, D. R. (2000). Analysis of fractalkine receptor CX3CR1 function by targeted deletion and green fluorescent protein reporter gene insertion. *Molecular and Cellular Biology*, *20*, 4106–4114. https://doi.org/10.1128/MCB.20.11.4106-4114.2000

Kondo, S., Kohsaka, S., & Okabe, S. (2011). Long-term changes of spine dynamics and microglia after transient peripheral immune response triggered by LPS in vivo. *Molecular Brain*, *4*, 27. https://doi.org/10.1186/1756-6606-4-27

Krabbe, G., Halle, A., Matyash, V., Rinnenthal, J. L., Eom, G. D., Bernhardt, U., . . . Heppner, F. L. (2013). Functional impairment of microglia coincides with β-amyloid deposition in mice with Alzheimer-like pathology. *PLOS One*, *8*, e60921. https://doi.org/10.1371/journal.pone.0060921

Lee, J. E., Liang, K. J., Fariss, R. N., & Wong, W. T. (2008). Ex vivo dynamic imaging of retinal microglia using time-lapse confocal microscopy. *Investigative Ophthalmology & Visual Science*, *49*, 4169–4176. https://doi.org/10.1167/iovs.08-2076.

Li, Y., Du, X., Pei, G., Du, J., & Zhao, J. (2016). β-Arrestin1 regulates the morphology and dynamics of microglia in zebrafish *in vivo*. *European Journal of Neuroscience*, *43*, 131–138. https://doi.org/10.1111/ejn.13065

Longair, M. H., Baker, D. A., & Armstrong, J. D. (2011). Simple neurite tracer: Open source software for reconstruction, visualization and analysis of neuronal processes. *Bioinformatics*, *27*, 2453–2454. https://doi.org/10.1093/bioinformatics/btr390

Miura, K., Rueden, C., Hiner, M., Schindelin, J., & Rietdorf, J. (2014). ImageJ Plugin CorrectBleach V2.0.2. Zenodo [Internet]. Available from: https://zenodo.org/record/30769

Nimmerjahn, A., Kirchhoff, F., & Helmchen, F. (2005). Resting microglial cells are highly dynamic surveillants of brain parenchyma in vivo. *Science*, *308*, 1314–1318. https://doi.org/10.1126/science.1110647

Parslow, A., Cardona, A., & Bryson-Richardson, R. J. (2014). Sample drift correction following 4D confocal time-lapse imaging. *Journal of Visualized Experiments*, e51086. https://doi.org/10.3791/51086

Schindelin, J., Arganda-Carreras, I., Frise, E., Kaynig, V., Longair, M., Pietzsch, T., . . . Cardona, A. (2012). Fiji: An open-source platform for biological-image analysis. *Nature Methods*, *9*, 676–682. https://doi.org/10.1038/nmeth.2019

Schmid, B., Schindelin, J., Cardona, A., Longair, M., & Heisenberg, M. (2010). A high-level 3D visualization API for Java and ImageJ. *BMC Bioinformatics*, *11*, 274. https://doi.org/10.1186/1471-2105-11-274

Sierra, A., Abiega, O., Shahraz, A., & Neumann, H. (2013). Janus-faced microglia: Beneficial and detrimental consequences of microglial phagocytosis. *Frontiers in Cell Neuroscience*, *7*, 6. https://doi.org/10.3389/fncel.2013.00006

Sierra, A., Gottfried-Blackmore, A. C., McEwen, B. S., & Bulloch, K. (2007). Microglia derived from aging mice exhibit an altered inflammatory profile. *Glia*, *55*, 412–424. https://doi.org/10.1002/glia.20468

Sipe, G. O., Lowery, R. L., Tremblay, M.-È., Kelly, E. A., Lamantia, C. E., & Majewska, A. K. (2016). Microglial P2Y12 is necessary for synaptic plasticity in mouse visual cortex. *Nature Communications*, *7*, 10905. https://doi.org/10.1038/ncomms10905

Thevenaz, P., Ruttimann, U. E., & Unser, M. (1998). A pyramid approach to subpixel registration based on intensity. *IEEE Transactions on Image Process*, *7*, 27–41. https://doi.org/10.1109/83.650848

Wolf, S. A., Boddeke, H. W. G. M., & Kettenmann, H. (2017). Microglia in physiology and disease. *Annual Review of Physiology*, *79*, 619–643. https://doi.org/10.1146/annurev-physiol-022516-034406

SUPPORTING INFORMATION

Additional Supporting Information may be found online in the supporting information tab for this article.

How to cite this article: Paris I, Savage JC, Escobar L, et al. ProMolJ: A new tool for automatic three-dimensional analysis of microglial process motility. *Glia*. 2017;00:1–18. https://doi.org/10.1002/glia.23287

Development/Plasticity/Repair

Microglia Actively Remodel Adult Hippocampal Neurogenesis through the Phagocytosis Secretome

Irune Diaz-Aparicio,[1,2] Iñaki Paris,[1,2] Virginia Sierra-Torre,[1,2] Ainhoa Plaza-Zabala,[1] Noelia Rodríguez-Iglesias,[1,2] Mar Márquez-Ropero,[1,2] Sol Beccari,[1,2] Paloma Huguet,[1,2] Oihane Abiega,[1,2] Elena Alberdi,[1,2] Carlos Matute,[1,2] Irantzu Bernales,[2] Angela Schulz,[3] Lilla Otrokocsi,[4] Beata Sperlagh,[4] Kaisa E. Happonen,[5,6] Greg Lemke,[5,6] Mirjana Maletic-Savatic,[7,8] Jorge Valero,[1,2,9] and Amanda Sierra[1,2,9]

[1]Achucarro Basque Center for Neuroscience, Leioa, Bizkaia 48940, Spain, [2]University of the Basque Country UPV/EHU, Leioa, Bizkaia 48940, Spain, [3]Rudolf-Schönheimer-Institute of Biochemistry, Medical Faculty, University Leipzig 04109, Germany, [4]Laboratory of Molecular Pharmacology, Institute of Experimental Medicine, Hungarian Academy of Sciences, Budapest H-1083, Hungary, [5]Molecular Neurobiology Laboratory, [6]Immunobiology and Microbial Pathogenesis Laboratory, Salk Institute for Biological Studies, La Jolla, California 92037, [7]Jan and Dan Duncan Neurological Research Institute at Texas Children's Hospital, Houston, Texas 77030, [8]Department of Pediatrics and Neuroscience, Program in Developmental Biology, Baylor College of Medicine, Houston, Texas 77030, and [9]Ikerbasque Foundation, Bilbao, Bizkaia 48013, Spain

During adult hippocampal neurogenesis, most newborn cells undergo apoptosis and are rapidly phagocytosed by resident microglia to prevent the spillover of intracellular contents. Here, we propose that phagocytosis is not merely passive corpse removal but has an active role in maintaining neurogenesis. First, we found that neurogenesis was disrupted in male and female mice chronically deficient for two phagocytosis pathways: the purinergic receptor P2Y12, and the tyrosine kinases of the TAM family Mer tyrosine kinase (MerTK)/Axl. In contrast, neurogenesis was transiently increased in mice in which MerTK expression was conditionally downregulated. Next, we performed a transcriptomic analysis of the changes induced by phagocytosis in microglia *in vitro* and identified genes involved in metabolism, chromatin remodeling, and neurogenesis-related functions. Finally, we discovered that the secretome of phagocytic microglia limits the production of new neurons both *in vivo* and *in vitro*. Our data suggest that microglia act as a sensor of local cell death, modulating the balance between proliferation and survival in the neurogenic niche through the phagocytosis secretome, thereby supporting the long-term maintenance of adult hippocampal neurogenesis.

Key words: **adult neurogenesis; MerTK/Axl; microglia; P2Y12; phagocytosis; secretome**

Significance Statement

Microglia are the brain professional phagocytes and, in the adult hippocampal neurogenic niche, they remove newborn cells naturally undergoing apoptosis. Here we show that phagocytosis of apoptotic cells triggers a coordinated transcriptional program that alters their secretome, limiting neurogenesis both *in vivo* and *in vitro*. In addition, chronic phagocytosis disruption in mice deficient for receptors P2Y12 and MerTK/Axl reduces adult hippocampal neurogenesis. In contrast, inducible MerTK downregulation transiently increases neurogenesis, suggesting that microglial phagocytosis provides a negative feedback loop that is necessary for the long-term maintenance of adult hippocampal neurogenesis. Therefore, we speculate that the effects of promoting engulfment/degradation of cell debris may go beyond merely removing corpses to actively promoting regeneration in development, aging, and neurodegenerative diseases.

Introduction

Neurogenesis, or the formation of new neurons, is a complex process that extends throughout adulthood in specific regions of the mammalian brain. Here we focus on the subgranular zone of the hippocampus, whose radial neural stem cells (rNSCs) generate newborn granule cells in rodents (Ehninger and Kemp-

Received May 2, 2019; revised Dec. 12, 2019; accepted Dec. 13, 2019.

Author contributions: I.D.-A., I.P., J.V., and A. Sierra designed research; I.D.-A., I.P., V.S.-T., A.P.-Z., N.R.-I., M.M.-R., S.B., P.H., O.A., E.A., I.B., L.O., K.E.H., J.V., and A. Sierra performed research; I.D.-A., I.P., I.B., J.V., and A. Sierra analyzed data; C.M., B.S., G.L., and A. Sierra contributed unpublished reagents/analytic tools; I.D.-A., I.P., V.S.-T., A.P.-Z., N.R.-I., M.M.-R., S.B., A. Schulz, L.O., B.S., K.E.H., G.L., M.M.-S., J.V., and A. Sierra wrote the paper.

This work was supported by grants from the Spanish Ministry of Economy and Competitiveness (http://www.mineco.gob.es) with FEDER funds to A.S. (BFU2012-32089 and RYC-2013-12817) to A.S. and J.V. (BFU2015-66689); a Leonardo Award from the BBVA Foundation to A.S. (IN16_BBM_BAS_0260); a Basque Government Department of Education project to A.S. (PI_2016_1_0011; http://www.euskadi.eus/basque-government/department-education/); Ikerbasque start-up funds to J.V.; a Hungarian Research and Development Fund Grant (K116654) to B.S.; a Hungarian Brain Research Program Grant (2017-1.2.1-NKP-2017-00002) to B.S.; a National Institutes of Health Grant (AG060748) to G.L. In addition, I.D.-A., N.R.-I., and M.M.-R. are recipients of pre-doctoral fellowships from the University of the Basque Country EHU/UPV (http://www.ehu.eus/en/en-home); I.P. is a recipient of a Gangoiti Foundation Fellowship; S.B. is recipients of pre-doctoral fellowship from the Spanish Ministry of Economy

ermann, 2008) and humans (Moreno-Jimenez et al., 2019). Nowadays, newly generated neurons are strongly suggested to contribute to hippocampus-dependent learning and memory, among other functions (Deng et al., 2010). Multiple endogenous factors regulate the proliferation, survival, differentiation, and integration of the new neurons in the adult hippocampus. In the cellular niche, one key element is microglia, the resident macrophages of the nervous system that coordinate the brain inflammatory response. The detrimental effect of neuroinflammation on neurogenesis is well described, and is mediated by inflammatory cytokines such as interleukin (IL)-1β, tumor necrosis factor α (TNFα), and IL-6 (Ekdahl et al., 2003; Monje et al., 2003).

Microglia also beneficially affect neurogenesis, as they are capable of producing factors that modulate proliferation or survival of different cells within the neuronal lineage. *In vitro* studies demonstrate that cultured microglia promote differentiation of precursor cells (Aarum et al., 2003), whereas microglia-conditioned media enhances neuroblast production and neuronal survival (Morgan et al., 2004; Walton et al., 2006). Furthermore, microglia were suggested to inhibit the proliferation of hippocampal rNSCs, as their number inversely correlates with adult hippocampal neurogenesis (Gebara et al., 2013). Recently, experiments using diphtheria toxin-induced ablation of microglia propose that microglia are essential for neuroblast survival (Kreisel et al., 2019) but the mechanisms underlying the regulation of hippocampal neurogenesis by microglia are still unexplored both *in vitro* and especially *in vivo* (Sierra et al., 2014).

Here, we focus on another major role of microglia in the adult hippocampal neurogenic niche: the removal of apoptotic newborn cells through phagocytosis (Sierra et al., 2010). The majority of hippocampal newborn cells undergo apoptosis in the first few days of cells' life through adulthood (Beccari et al., 2017) and are immediately recognized and degraded by "unchallenged" microglia (Sierra et al., 2010). Microglia are the brain professional phagocytes compared with other cell types (Sierra et al., 2013) and prevent the release of toxic intracellular contents (Nagata et al., 2010), and thus, this process is essential to avoid alterations of the surrounding tissue.

In this study, we propose that microglial phagocytosis does not conclude with the physical elimination of apoptotic cells, but is followed by a coordinated transcriptional program that triggers the production of neurogenic modulatory factors, which directly contribute to the maintenance and correct regulation of the adult hippocampal neurogenic cascade. We have used constitutive and inducible knock-out (KO) mice to abolish two phagocytosis-related receptors: the purinergic receptor P2Y12 and the Mer tyrosine kinase (MerTK) of the TAM (Tyro, Axl, and Mer) family. We discovered that chronic phagocytosis deficiency disrupts neurogenesis but acute phagocytosis impairment only transiently increases neurogenesis. In addition, using a combined *in vitro* and *in vivo* based experimental strategy, we found that the secretome of phagocytic microglia limits the production of new neurons to maintain the homeostasis of the adult hippocampal neurogenic niche.

and Competitiveness; V.S.-T. and O.A. are recipients of pre-doctoral fellowship from the Basque Government; and A.P.-Z. is the recipient of a Juan de la Cierva postdoctoral fellowship from the Spanish Ministry of Economy and Competitiveness. The funders had no role in study design, data collection and analysis, decision to publish, or preparation of the manuscript; UPV/EHU SGIker technical and human support is gratefully acknowledged. We thank Victor Sánchez Zafra for technical support, and Isabel Fariñas, María Domercq, and Ismael Galve-Roperh for thoughtful discussion of the data.

The authors declare no competing financial interests.

Correspondence should be addressed to Amanda Sierra at amanda.sierra@achucarro.org or Jorge Valero at jorge.valero@achucarro.org.

https://doi.org/10.1523/JNEUROSCI.0993-19.2019

Copyright © 2020 Diaz-Aparicio et al.

This is an open-access article distributed under the terms of the Creative Commons Attribution License Creative Commons Attribution 4.0 International, which permits unrestricted use, distribution and reproduction in any medium provided that the original work is properly attributed.

Materials and Methods

Mice. All experiments were performed in fms-EGFP (MacGreen) mice, except where indicated, in which all microglia express the fluorescent reporter (Sasmono et al., 2003; Sierra et al., 2007). KO mice were provided by Beata Sperlagh, Institute of Experimental Medicine (P2Y12 KO) and Greg Lemke, Salk Institute (MerTK/Axl KO). Microglial-specific, inducible MerTK/Axl mice were generated using $Cx3cr1^{CreER}$ (Parkhurst et al., 2013) and $Mertk^{fl/fl}$ (Fourgeaud et al., 2016), described previously. To induce deletion of the $Mertk^{fl/fl}$ allele in $Cx3cr1^{CreER/+}Mertk^{fl/fl}$ mice, two doses of tamoxifen dissolved in corn oil (75 mg/kg) or corresponding volume of corn oil alone (control mice) were administered intraperitoneally at postnatal days (P)21 and P23. All mice used were in a C57BL/6 background. Mice were housed in 12 h light/dark cycle with *ad libitum* access to food and water. Mice received a single dose of 5-bromo-2′-deoxyuridine (BrdU; 100–150 mg/kg) at P28. At 24 h or 28 d after BrdU injection, mice were anesthetized with a mixture of ketamine and xylazine (100 mg/kg and 10 mg/kg, respectively), perfused with 20 U/ml heparin in PBS followed by 4% PFA in PBS. Brains were collected, immersion fixed for 4 h in 4% PFA in PBS, and stored in 30% sucrose, 30% ethylene glycol at −20°C until analysis. All procedures followed the European Directive 2010/63/EU and NIH guidelines, and were approved by the Ethics Committees of the University of the Basque Country EHU/UPV (Leioa, Spain; CEBA/205/2011, CEBA/206/2011, CEIAB/82/2011, CEIAB/105/2012).

SH-SY5Y cell line. SH-SY5Y (American Type Culture Collection), a human neuroblastoma cell line derived from the bone marrow of 4-year-old female was used for phagocytic assay experiments. SH-SY5Y cells were grown as an adherent culture in non-coated culture flasks covered with 10–15 ml of medium. The medium consisted of DMEM (Invitrogen), supplemented with 10% fetal bovine serum (FBS) and 1% antibiotic/antimycotic (all from Invitrogen). When confluency was reached, cells were trypsinized and re-plated at 1:4.

BV2 cell line. BV2 (Interlab Cell Line Collection San Martino-Instituto Scientifico Tumori-Instituto Nazionale per la Ricerca sul Cancro), a cell line derived from raf/myc-immortalized murine neonatal microglia was used to obtain LPS-induced conditioned media. BV2 cells were grown as an adherent culture in non-coated culture flasks covered with 10–15 ml of medium. The medium consisted of DMEM (Invitrogen), supplemented with 10% FBS and 1% antibiotic/antimycotic (all from Invitrogen). When confluency was reached, cells were trypsinized and replated at 1:4.

Primary microglia cultures. Primary microglia cultures were performed as previously described (Abiega et al., 2016; Beccari et al., 2018). P0–P1 fms-EGFP mice pup brains were extracted and the meninges were peeled off. The olfactory bulb and cerebellum were discarded and the rest of the brain was then mechanically homogenized by careful pipetting and enzymatically digested with papain (20 U/ml; Sigma-Aldrich), a cysteine protease enzyme, and DNase (150 U/μl; Invitrogen) for 15 min at 37°C. The resulting cell suspension was then filtered through a 40 μm nylon cell strainer (Fisher) and transferred to a 50 ml Falcon tube quenched by 5 ml of 20% FBS (Invitrogen) in HBSS. Afterward, the cell suspension was centrifuged at 200 × *g* for 5 min, the pellet was resuspended in 1 ml DMEM (Invitrogen) supplemented with 10% FBS and 1% antibiotic/antimycotic (Invitrogen), and seeded in T75 poly-L-lysine-coated (15 μl/ml; Sigma-Aldrich) culture flasks at a density of two brains per flask. Medium was changed the day after and then every 3–4 d, always enriched with granulocyte-macrophage colony stimulating factor (5 ng/ml GM-CSF; Sigma-Aldrich), which promotes microglial proliferation. After confluence (at 37°C, 5% CO_2 for ~14 d), microglia cells were harvested by shaking at 100–150 rpm, 37°C, 4 h. Isolated cells were counted and plated at a density of 80,000 cells/well on poly-L-lysine-coated glass coverslips in 24-well plates for immunofluorescence purposes or 1,000,000 cell/dish on coated Petri dishes for real-time quantitative PCR (qPCR). Microglia were allowed to settle for at least 24 h before any experiment.

NPC culture. Neurosphere cultures were performed as previously described (Babu et al., 2011) with some modifications. Briefly, P0–P1 fms-EGFP pups were decapitated and the brains extracted and placed in cold HBSS. The homogenization process was performed as detailed in the Primary microglia cultures section, except that no FBS was used in any step to avoid undesired neurosphere adhesion and differentiation. Afterward, the cell suspension was centrifuged at 200 × *g* for 5 min, the pellet was resuspended in 1 ml DMEM/F12 with GlutaMAX (Invitrogen) supplemented with 1% penicillin/streptomycin, 1% B27, EGF (12.5 ng/ml), FGF-2 (5 ng/ml; Xapelli et al., 2013). Cells were plated on uncoated Petri dishes (P60); each brain was plated in four Petri dishes with supplemented DMEM/F12. After 6 d, neurospheres were then disaggregated into a single-cell suspension of neuroprogenitor cells (NPCs) using NeuroCult chemical dissociation kit following the manufacturer's instructions and each Petri dish was plated in two 6-multiwell plates. To maintain replicability through the experiments, neurospheres were frozen until their use at −80°C in 15% DMSO after the first passage.

In vitro *phagocytosis assay.* The protocol was detailed previously (Beccari et al., 2018). In brief, microglia were allowed to rest and settle for at least 24 h before phagocytosis experiments. Phagocytosis experiments were performed in DMEM +10% FBS to ensure the presence of complement molecules, which are related to microglial phagocytosis *in vivo* (Diaz-Aparicio and Sierra, 2019) and whose presence determines the immunomodulatory outcome of phagocytosis (Fraser et al., 2010). Primary microglia cells were fed for different time points with SH-SY5Y. The cell line was previously labeled with the membrane marker CM-DiI (5 μM; 10 min at 37°C, 15 min at 4°C; Invitrogen) and treated with staurosporine (STP; 3 μM, 4 h; Sigma-Aldrich) to induce apoptosis. Only the floating dead-cell fraction was collected from the supernatant and added to the primary microglia cultures in a proportion of ~1:1. Apoptotic cells were visualized and quantified by trypan blue in a Neubauer chamber. Because cell membrane integrity is still maintained in early induced apoptotic cells, cells not labeled with trypan blue were considered apoptotic. The media of naive and phagocytic (24 h) microglia was immediately stored at −80°C until its use as conditioned media for NPCs.

In some experiments, control and phagocytic microglia were treated with LPS. Three different LPS paradigms were used. In the low LPS concentration paradigm, media was removed and fresh medium with 150 ng/ml LPS or vehicle (PBS) was added for 18 h to primary microglia (Fraser et al., 2010). In the high LPS concentration paradigm, medium was removed and fresh medium with 1 μg/ml LPS or vehicle (PBS) was added for 24 h to primary or BV2 cells (Monje et al., 2003). To control for LPS presence in the phagocytic media, a third paradigm was performed in which primary microglia was treated with 1 μg/ml LPS or vehicle (PBS) for 6 h, then media was changed into fresh media for another 18 h. All supernatants were collected and stored at −80°C until its use as conditioned media for NPCs, and all of them were filter-sterilized before adding to the NPC culture.

NPC proliferation and differentiation. Neurospheres of Passage 1 were thawed and expanded for 1 week before the experiment in proliferative conditions (2 passages were performed in total).The day of the experiment Passage 3 neurospheres were dissociated into NPCs, cells were counted and plated at a 80,000 cells/well density on poly-L-lysine-coated glass coverslips in 24-well plates in supplemented (Penicillin/streptomycin, B27, EGF, and FGF2) DMEM/F12. NPCs were allowed to proliferate for 48 h (Babu et al., 2011) and then washed with PBS before treatment with conditioned media (CM) from control or phagocytic (24 h) microglia. For the experimental group, DMEM was also added as a control because it is the media in which microglia were grown. NPCs were then fixed with 4% PFA for 10 min at 3 d, and 5 d of differentiation. For multipotency experiments, NPCs treated for 3 d with CM (control, 24 h phagocytosis or DMEM) were transferred back to DMEM/F12 (without trophic factors) medium and were allowed to differentiate for 5 and 9 d. For late survival and differentiation assay, after the 48 h of proliferation, NPCs were allowed to differentiate in DMEM/F12 (no trophic factors) for 10 d and then were treated with CM from control or phagocytic (24 h) microglia or DMEM for another 3 and 5 d.

Calcium imaging. Intracellular calcium imaging experiments were performed as described previously (Alberdi et al., 2013). CM-treated NPCs were incubated and loaded with 5 μM Fura-2 AM (Invitrogen) for 30 min at 37°C and then washed in HBSS containing 20 mM HEPES, pH 7.4, 10 mM glucose, and 2 mM $CaCl_2$ for 10 min at room temperature. The perfusion chamber was assembled on the platform of an inverted epifluorescence microscope (Zeiss Axiovert 35) equipped with a 150-W xenon lamp Polychrome IV (TILL Photonics) and a Plan Neofluar 40× oil-immersion objective (Zeiss). NPCs were treated with 50 mM KCl, 10 μM AMPA, 1 mM ATP, and 100 μM histamine, sequentially. Cells were allowed to recover their baseline before adding the next compound. Cells were visualized with a digital black/white CCD camera (ORCA; Hamamatsu Photonics). Intracellular calcium signaling responses were calculated as the proportion of different cell phenotypes responding to the different stimuli. The baseline was calculated as the mean of the first 60 s of recording for each cell. Only peaks that increase or decrease three times the SEM of the baseline were considered as a significant response.

FACS sorting. Microglia cells were isolated from brains as described previously (Sierra et al., 2007; Abiega et al., 2016). The corresponding tissues from fms-EGFP mice were dissected and placed in enzymatic solution (in mM: 116 NaCl, 5.4 KCl, 26 $NaHCO_3$, 1 NaH_2PO_4, 1.5 $CaCl_2$, 1 $MgSO_4$, 0.5 EDTA, 25 glucose, 1 L-cysteine) with papain (20 U/ml) and DNase I (150 U/μl; Invitrogen) for digestion at 37°C for 15 min. The homogenization process was also helped by careful pipetting. After homogenization, tissue clogs were removed by filtering the cell suspension through a 40 μm nylon strainer to a 50 ml Falcon tube quenched by 5 ml of 20% FBS in HBSS. For further enrichment of microglia, myelin was removed by using Percoll gradients. For this purpose, cells were centrifuged at 200 × *g* for 5 min and resuspended in a 20% solution of isotonic percoll (SIP; 20% in HBSS), obtained from a previous stock of SIP (9 parts Percoll per 1 part PBS 10×). Then, each sample was layered with HBSS poured very slowly by fire-polished pipettes. Afterward, gradients were centrifuged for 20 min at 200 × *g* with minimum acceleration and no brake so the interphase was not disrupted. Then the interphase was removed, cells were washed in HBSS by centrifuging at 200 × *g* for 5 min and pellet was resuspended in 500 μl of sorting buffer (25 mM HEPES, 5 mM EDTA, 1% BSA, in HBSS). Microglia cell sorting was performed by FACS Jazz (BD Biosciences), in which the population of green fluorescent cells was selected, collected in Lysis Buffer (Qiagen) containing 0.7% β-mercaptoethanol and stored at −80°C until processing.

Administration of microglia CM in vivo. CM from control and phagocytic (Ph24h) microglia was administrated via osmotic pumps for 6-d to 2-month-old fms-EGFP mice. Briefly, osmotic pump (flow rate 1 μl/h; Model 2001, Alzet) and infusion catheter tubes (Alzet) were filled with the conditioned media (200 μl) and connected. Pumps were incubated overnight at 37°C in PBS before the surgery. Mice were anesthetized with ketamine/xylazine (10/1 mg/kg) and received a single dose of the analgesic buprenorphine (1 mg/kg) subcutaneously. The infusion cannulae were inserted at anteroposterior: −1.7 mm, laterolateral: −1.6 mm, and dorsoventral: −1.9 mm from bregma. The injection site did not reach nor damage the DG in any of the mice included in the study. Afterward, a surface of dental cement was created from the cannulae to the screw to avoid any unwanted removal of the cannulae. Osmotic pumps were inserted inside the skin of the mice. After 6 d, mice were intraperitoneally injected with BrdU (150 mg/kg, single injection), and transcardially perfused 2 h later to assess proliferation. For differentiation experiments, CM-containing osmotic pumps were inserted for 6-d to 2-month-old fms-EGFP mice. Pumps were removed at 6 d and afterward, a single intraperitoneal injection of BrdU (150 mg/kg) was administered, and mice were killed 28 d later.

Gene expression arrays. Gene arrays analysis was performed following the recommendations of the MIAME (Minimum Information About a Microarray Experiment) consortium (Brazma et al., 2001). Cell samples from control, Ph3h, and Ph24h microglia ($n = 3$ independent experiments) were lysed and kept at −80°C until processing. Total RNA was isolated using PureLink RNA Mini kit (Ambion), following the manufacturer's instructions. RNA amount was quantified in a UV/VIS NanoDrop 1000 spectrophotometer (ThermoFisher Scientific), and its integrity was analyzed with Lab-chip technology in an Agilent 2100 Bio-

analyzer in combination with Agilent RNA 6000 Nano Chips. Eukaryote Total RNA Nano Assay was used as type of test. In all samples, RIN > 9.3, and 28S/18S > 1.3 values were obtained. Sample labeling, hybridization, and scanning gene expression profiling were performed at the Gene Expression Unit of Genomics Core Facility of the University of the Basque Country UPV/EHU.

One-color microarray-based gene expression analysis was performed following the One-Color (p/n5190–2305) protocol from Agilent Technologies (Low Input Quick Amp Labeling kit) for the labeling of the samples. First, 50 ng of total RNA were retrotranscribed with the AffinityScript Reverse enzyme Transcriptase (AffinityScript RT), a thermostable modified enzyme derived from Moloney murine leukemia virus retrotranscriptase, using promoter-coupled T7 Oligo dT primers. The double-stranded cDNA synthesized by AffinityScript RT was transcribed *in vitro* by the T7 RNA pol in the presence of Cy3-CTP to generate labeled and amplified cRNA. The labeled samples were purified with columns of RNeasy Mini kit (Qiagen). Subsequently the labeled samples were quantified in the NanoDrop ND-1000 to determine the performance of the specific activity of the fluorochromes after labeling. All the hybridized samples met the following minimum requirements: yield > 0.825 μg per reaction and cyanine 3-specific activity > 6 pmol/μg.

For the hybridization, 600 ng of labeled cRNA were fragmented and cohybridized to SurePrint G3 Mouse GE 8X60K Microarray Design ID: 028005. Each array/slide contained 8 identical subarrays of >60,000 60-mer oligonucleotides of high resolution and performance. It contained probes for 55,681 sequences or transcripts (biological features or non-control features). Several of these biological probes were replicated 10 times for the calculations and quality control measurements (QCMetrics) of the microarrays. It also contained probes for internal positive controls (spike-ins), which were added to the RNA sample before labeling and were used for evaluation and verification of the microarray processing. Manual washing method was performed following Agilent's recommendations to prevent ozone-related problems.

Slides were scanned on a G2565CA Microarray DNA Scanner from Agilent Technologies with a resolution of 3 μm and a Tiff image size of 20bit, using the Scan software v8.5.1 with default settings (Scan profile Agilent, G3_GX_1color). The scanned TIFF images were processed and the fluorescence of the probes quantified using Agilent Feature Extraction software 10.7.3.1. Feature Extraction protocol for data extraction: GE1_107_Sep09; Design File: 28005_D_F_20140728. Software extracts information of the raw fluorescence signal (mean signal) for the fluorochrome or channel (Cy3: green channel) from the spot containing the probes (positive and negative controls and no controls or biological feature) and the background, obtained from the negative controls (which contains sequences for which no hybridization is expected, nonspecific binding indicators).

Default parameters (Agilent Feature Extraction software 10.7.3.1) for one-color gene expression microarrays were used for flagging of non-uniform features, population outliers for replicated probes, and features with no significant intensities in Cy3 channel. Agilent Feature Extraction raw data were processed with software GeneSpring GX 13.0 (Agilent Technologies). Probes not present in any sample were filtered out. A list of the filtered 36,665 probes was used in the statistical analysis.

Tissue or cultured cells RNA isolation and retrotranscription. The corresponding tissue (P8 hippocampi for positive PCR controls) was rapidly isolated immediately under tribromoethanol overdose, and stored at −80°C. Tissue was disrupted with a roto-stator homogenizer with Lysis Buffer (Qiagen) containing 0.7% β-mercaptoethanol and stored at −80°C until processed. Cultured cells (>500,000 cells) were lysed and stored at −80°C until processed. Total RNA was isolated using Qiagen RNeasy Mini Kit (Qiagen), following the manufacturer's instructions, including a DNase treatment step to eliminate genomic DNA residues. RNA was quantified in a NanoDrop 2000, and 1.5 μg were retrotranscribed using random hexamers (Invitrogen) and Superscript III Reverse Transcriptase kit (Invitrogen), following the manufacturer's instructions in a Veriti Thermal Cycler (Applied Biosystems).

FACS-sorted cells RNA isolation and retrotranscription. RNA from FACS-sorted microglia (<500,000 cells) was isolated by RNeasy Plus micro kit (Qiagen) according to the manufacturer's instructions, and the RNA was retrotranscribed using an iScript Advanced cDNA Synthesis Kit (Bio-Rad) following the manufacturer's instructions in a Veriti Thermal Cycler (Applied Biosystems).

Real-time qPCR. Real-time qPCR was performed following MIQE guidelines (Minimal Information for Publication of Quantitative Real Time Experiments; Bustin, 2010). Three replica of 1.5 μl of a 1:3 dilution of cDNA were amplified using Power SYBR Green (Bio-Rad) for tissue or cell culture experiments or SsoFast EvaGreen Supermix (Bio-Rad) for FACS-sorted microglia experiments in a CFX96 Touch Real-Time PCR Detection System (Bio-Rad). The amplification protocol for both enzymes was 3 min 95°C, and 40 cycles of 10 s at 95°C, 30 s at 60°C.

Primers. Primers were designed to amplify exon–exon junctions using PrimerBlast (NIH) to avoid amplification of contaminating genomic DNA, and their specificity was assessed using melting curves and electrophoresis in 2% agarose gels. Primer sequences are listed in Table 1. For each set of primers, the amplification efficiency was calculated using the software LinRegPCR (Ramakers et al., 2003) or standard curve of 1:2 consecutive dilutions, and was used to calculate the relative amount using the following formula:

$$\Delta\Delta Ct = \frac{(1 + \text{eff} \cdot \text{target gene})^{(Ct\ sample - Ct\ control)}}{(1 + \text{eff} \cdot \text{reference gene})^{(Ct\ sample - Ct\ control)}}.$$

Up to three independent reference genes were compared: L27A, which encodes a ribosomal protein of the 60S subunit (Sierra et al., 2007); OAZ-1, which encodes ornithine decarboxylase antizyme, a rate-limiting enzyme in the biosynthesis of polyamines and recently validated as reference gene in rat and human (Kwon et al., 2009); and HPRT, which encodes hypoxanthine guanine phosphoribosyl transferase (van de Moosdijk and van Amerongen, 2016). The expression of L27A, OAZ-1, and HPRT remained constant independently of time and treatments, validating their use as reference genes. In all experiments, the pattern of mRNA expression was similar using the assigned couple of reference genes, and in each experiment the reference gene that rendered lower intragroup variability was used for statistical analysis.

Immunofluorescence. Six series of 50-μm-thick coronal sections of mouse brains were cut using a Leica VT 1200S vibrating blade microtome (Leica Microsystems). Fluorescent immunostaining was performed following standard procedures (Sierra et al., 2010; Beccari et al., 2018). Free-floating vibratome sections were blocked in permeabilization solution (0.3% Triton X-100, 0.5% BSA in PBS; all from Sigma-Aldrich) for 3 h at room temperature (RT), and then incubated overnight with the primary antibodies diluted in the permeabilization solution at 4°C. For BrdU labeling an antigen retrieval procedure was performed by incubating in 2 M HCl for 30 min at 37°C and then washing with 0.1 M sodium tetraborate for 10 min at RT before the blockade of the sections. After overnight incubation with primary antibodies, brain sections were thoroughly washed with 0.3% Triton in PBS. Next, the sections were incubated with fluorochrome-conjugated secondary antibodies and DAPI (5 mg/ml; Sigma-Aldrich) diluted in the permeabilization solution for 3 h at RT. After washing with PBS, the sections were mounted on glass slides with Dako Cytomation Fluorescent Mounting Medium.

Primary microglial cultures were fixed for 10 min in 4% PFA and then transferred to PBS. Fluorescent immunostaining was performed following standard procedures (Abiega et al., 2016; Beccari et al., 2018). Coverslips with primary microglial cultures were blocked in 0.1% Triton X-100, 0.5% BSA in PBS for 30 min at RT. The cells were then incubated with primary antibodies in permeabilization solution (0.2% Triton X-100, 0.5% BSA in PBS) for 1 h at RT, rinsed in PBS and incubated in the secondary antibodies containing DAPI (5 mg/ml) in the permeabilization solution for 1 h at RT. After washing with PBS, primary cultures were mounted on glass slides with Dako Cytomation Fluorescent Mounting Medium.

For fluorouridine labeling, SH-SY5Y were treated with 2 mM 5′-fluorouridine (Sigma-Aldrich) for 30 min. Afterward, cells were fixed in 4% PFA with 0.5% Triton X-100. The immunofluorescence was performed as described with primary microglial cultures and anti-BrdU primary antibody was used to detect fluorouridine.

Table 1. qPCR primer sequences

	Gene	Gene Bank	Amplicon size	Sequence 5′-3′
Reference genes	OAZ1	NM_008753	51	Fwd AGCGAGAGTTCTAGGGTTGCC Rev CCCCGGACCCAGGTTACTAC
	L27A	BC086939	101	Fwd TGTTGGAGGTGCCTGTGTTCT Rev CATGCAGACAAGGAAGGATGC
	HPRT	NM_013556.2	150	Fwd ACAGGCCAGACTTTGTTGGA Rev ACTTGCGCTCATCTTAGGCT
Phagocytosis receptors	P2Y12	NM_027571	88	Fwd GCAGAACCAGGACCATGGAT Rev CTGACGCACAGGGTGCTG
	MerTK	NM_008587.1	131	Fwd AAGGTCCCCGTCTGTCCTAA Rev GCGGGGAGGGGATTACTTTG
	Axl	NM_009465.4	86	Fwd GTTGGTGTCTGGAGGATGGG Rev TGTGTGTCCTTATGGGCTGC
Peptides and hormones	VGF	NM_001039385.1	74	Fwd CACCGGCTGTCTCTGGC Rev AAGGAAGCAGAAGAGGACGG
	Cartpt	NM_013732.7	106	Fwd GCGCTATGTTGCAGATCGAAG Rev GCGTCACACATGGGGACTTG
	FGF2	NM_008006.2	113	Fwd CGGCTGCTGGCTTCTAAGTG Rev AGTGCCACATACCAACTGGAG
Trophic factors	VEGFA	NM_001025250.3	88	Fwd GGCCTCCGAAACCATGAACT Rev CTGGGACCACTTGGCATGG
	PDGFα	NM_008808.3	94	Fwd TACCCCGGGAGTTGATCGAG Rev TCAGCCCCTACGGAGTCTATC
	IGF-1	NM_010512.4 NM_184052.3 NM_001111274.1 NM_001111275.1 NM_001111276.1	122	Fwd TTACTTCAACAAGCCCACAGG Rev GTGGGGCACAGTACATCTCC
	EGF	NM_010113.3	136	Fwd GGACTGAGTTGCCCTGACTC Rev CAATATGCATGCACACGCCA
	GDNF	NM_010275.2	145	Fwd CGCTGACCAGTGACTCCAA Rev TGCCGATTCCTCTCTCTTCG
Matrix protein	Mmp3	NM_010809.2	88	Fwd ACCCAGTCTACAAGTCCTCCA Rev GGAGTTCCATAGAGGGACTGA
Surface ligands	Jag1	NM_013822.5	119	Fwd TTCAGGGCGATCTTGCATCA Rev CACACCAGACCTTGGAGCAG
	Dll4	NM_019454.3	113	Fwd GGTTACACAGTGAGAAGCCAGA Rev GGCAATCACACACTCGTTCC
Cytokines	Csf3	NM_009971.1	70	Fwd GCAGCCCAGATCACCCAGAAT Rev TGCAGGGCCATTAGCTTCAT
	IL1β	NM_000576.2	72	Fwd AGATGAAGTGCTCCTTCCAGG Rev GGTCGGAGATTCGTAGCTGG
	IL6	NM_000600.3	107	Fwd GAAAGCAGCAAAGAGGCACTG Rev TTCACCAGGCAAGTCTCCTCAT
	TNFα	NM_000594.3	142	Fwd TGCACTTTGGAGTGATCGGC Rev GCTTGAGGGTTTGCTACAACA
	TGFβ	NM_000660.5	112	Fwd TCCTGGCGATACCTCAGCAA Rev CAATTTCCCCTCCACGGCTC

List of primers used to amplify reference genes, phagocytosis receptors, peptides and hormones, trophic factors, matrix protein, surface ligands, and cytokines. The gene name, Gene Bank accession number, amplicon size, and sequence are listed.

NPC cultures were fixed for 10 min in 4% PFA and then transferred to PBS. Coverslips containing the cells were blocked in blocking solution (0.5% Triton X-100, 3% BSA in PBS) for 1 h at RT, and then incubated overnight with the primary antibodies diluted in the permeabilization solution (0.2% Triton X-100, 3% BSA in PBS) at 4°C. After overnight incubation, coverslips were allowed to warm at RT and were thoroughly rinsed in PBS. Next, the coverslips were incubated with fluorochrome-conjugated secondary antibodies and DAPI (5 mg/ml; Sigma-Aldrich) diluted in the permeabilization solution for 2 h at RT. After washing with PBS, the coverslips were mounted on glass slides with Dako Cytomation Fluorescent Mounting Medium.

Western blot. CM-treated NPCs were directly lysed in RIPA buffer containing protease and phosphatase inhibitor cocktail (100×; ThermoFisher Scientific). Cells were sonicated for 5 s and then centrifuged (10,000 × *g*, 10 min). Solubilized protein was quantified in triplicates by BCA Assay Kit (ThermoFisher Scientific) at 590 nm using a microplate reader (Synergy HT, BioTek). Ten to 15 μg of protein (denatured with β-mercaptoethanol) were loaded onto Tris-glycine gradient polyacrylamide gels (8–16%; ThermoFisher Scientific) and run at 120 V for 90 min. Protein samples were then blotted to nitrocellulose membranes (0.45 μm pore size; ThermoFisher Scientific) at 220 mA for 2 h. Transfer efficiency was verified by Ponceau S (Sigma-Aldrich) staining. For immunoblotting, membranes were rinsed in Tris-Buffered Saline containing 0.1% Tween 20 (TBS-T; Sigma-Aldrich) and then blocked for 1 h in TBS-T containing 5% powder milk. Membranes were afterward incubated with rabbit primary antibodies for REST (1:500; EMD, Millipore), and phosphorylated Smad 1/5/9 (1:500; Cell Signaling Technology), and mouse primary antibodies for Smad 1 (1:500; Santa Cruz Biotechnology), Ascl1 (1:500; BD Biosciences), and β-actin (1:5000; Sigma-Aldrich), in TBS-T containing 4% BSA overnight (4°C, shaker). Next day, membranes were rinsed and incubated with horseradish peroxidase-conjugated anti-rabbit (1:5000) and anti-mouse (1:5000) secondary antibodies (Cell Signaling Technology) in TBS-T containing 5% powder

Table 2. Statistics for Figures 1 and 2

Figure	Parameter	Groups	Statistical test	Statistic	p
1*B*	Ph index	WT vs P2Y12 KO (1 m + 1 d)	Unpaired *t* test	$t_{(6)} = 13.5$	$p < 0.001$
	Ph capacity		Unpaired *t* test	$t_{(6)} = 5.08$	$p = 0.002$
	Apoptosis		Unpaired *t* test	$t_{(6)} = 1.17$	$p = 0.287$
	Microglia		Unpaired *t* test	$t_{(6)} = -0.05$	$p = 0.964$
1*C*	Ph index	WT vs MerTK/Axl KO (1 m)	Unpaired *t* test	$t_{(4)} = -3.97$	$p < 0.001$
	Ph capacity		Unpaired *t* test	$t_{(4)} = 2.90$	$p = 0.044$
	Apoptosis		Unpaired *t* test	$t_{(4)} = -3.97$	$p = 0.017$
	Microglia		Unpaired *t* test	$t_{(4)} = 0.98$	$p = 0.382$
1*E*	Neuroblasts	WT vs P2Y12 KO (1 m + 1 d)	Unpaired *t* test	$t_{(6)} = 10.83$	$p < 0.001$
	Proliferating Neuroblasts		Unpaired *t* test	$t_{(6)} = 3.51$	$p = 0.013$
1*F*	Neuroblasts	WT vs MerTK/Axl KO (1 m)	Unpaired *t* test	$t_{(4)} = 2.97$	$p = 0.041$
	Proliferating Neuroblasts		Unpaired *t* test	$t_{(4)} = 0.38$	$p = 0.723$
2*B*	Newborn cells	WT vs P2Y12 KO (1 m + 4 w)	Unpaired *t* test	$t_{(8)} = 2.72$	$p = 0.026$
	Newborn neurons		Unpaired *t* test	$t_{(8)} = 2.68$	$p = 0.028$
2*C*	Ph index	WT vs P2Y12 KO (1 m + 4 w)	Unpaired *t* test	$t_{(6)} = 7.45$	$p < 0.001$
	Ph capacity		Unpaired *t* test	$t_{(6)} = 9.93$	$p < 0.001$
	Apoptosis		Unpaired *t* test	$t_{(6)} = 1.17$	$p = 0.287$
	Microglia		Unpaired *t* test	$t_{(6)} = -0.05$	$p = 0.964$
2*E*	Ph index	WT vs P2Y12 KO (7 m)	Unpaired *t* test	$t_{(8)} = 4.21$	$p = 0.003$
	Apoptosis		Unpaired *t* test	$t_{(8)} = -0.18$	$p = 0.863$
	Microglia		Unpaired *t* test	$t_{(8)} = -0.95$	$p = 0.375$
2*G*	Neuroblasts		Unpaired *t* test	$t_{(8)} = 3.14$	$p = 0.014$
2*I*	P2Y12	GFP+ vs GFP−	Unpaired *t* test	$t_{(4)} = 552{,}3$	$p < 0.001$
	MerTK		Unpaired *t* test	$t_{(4)} = 14.91$	$p < 0.001$
	Axl		Unpaired *t* test	$t_{(4)} = 1.82$	$p = 0.144$

Table 3. Statistics for Figure 3

Figure	Parameter	Groups	Statistical test	Statistic	p value
3*E*	Ph index	Control vs iKO (1 m + 1 d)	Unpaired *t* test	$t_{(4)} = 18.40$	$p < 0.001$
	Ph capacity		Unpaired *t* test	$t_{(4)} = 3.40$	$p = 0.027$
	Apoptosis		Unpaired *t* test	$t_{(4)} = -2.17$	$p = 0.096$
	Microglia		Unpaired *t* test	$t_{(4)} = 1.17$	$p = 0.308$
3*F*	Ph index	Control vs iKO (1 m + 4 w)	Unpaired *t* test	$t_{(5)} = 19.56$	$p < 0.001$
	Ph capacity		Unpaired *t* test	$t_{(5)} = 4.53$	$p = 0.006$
	Apoptosis		Unpaired *t* test	$t_{(5)} = -2.40$	$p = 0.062$
	Microglia		Unpaired *t* test	$t_{(5)} = 1.33$	$p = 0.240$
3*H*	Proliferating cells	Control vs iKO (1 m + 1 d)	Unpaired *t* test	$t_{(4)} = -3.79$	$p = 0.019$
	Proliferating neuroblasts		Unpaired *t* test	$t_{(4)} = -3.30$	$p = 0.030$
3*I*	Neuroblasts	Control vs iKO (1 m + 1 d)	Unpaired *t* test	$t_{(4)} = -0.54$	$p = 0.616$
3*K*	Newborn cells	Control vs iKO (1 m + 4 w)	Unpaired *t* test	$t_{(8)} = 1.77$	$p = 0.114$
	Newborn neurons		Unpaired *t* test	$t_{(8)} = 0.63$	$p = 0.547$
3*L*	$BrdU^+$ yield	Control vs iKO (1 m + 4 w)	Unpaired *t* test	$t_{(8)} = 5.95$	$p < 0.001$

milk. After rinsing membranes, protein was visualized by enhanced chemiluminescence using Supersignal West Femto Maximum Sensitivity Substrate (ThermoFisher Scientific) in a ChemiDoc imaging system (Bio-Rad). Band intensity was quantified using the Gel Analyzer method of Fiji software. Phospho-Smad 1/5/9 levels were normalized to total levels of Smad 1. β-actin was used as loading control.

Image analysis. All fluorescence immunostaining images were collected using an Olympus FluoView or a Leica SP8 laser-scanning microscope using a 40× oil-immersion objective and a *z*-step of 0.7 μm. All images were imported into Adobe Photoshop 7.0 in Tiff format. Brightness, contrast, and background were adjusted equally for the entire image using the "brightness and contrast" and "levels" controls from the "image/adjustment" set of options without any further modification. For tissue sections, two to three 20-μm-thick *z*-stacks of the sections containing the septal hippocampus from one vibratome series was analyzed (usually 6 slices, spanning from −1 to −2.5 mm in the AP axes, from bregma), to avoid variability due to the differential regulation of neurogenesis in the septal and temporal regions of the hippocampus. For primary cultures, over 4–5 *z*-stacks were obtained per coverslip.

Phagocytosis analysis in vivo *and* in vitro. The analysis of phagocytosis *in vivo* was performed as described in a series containing the six most septal sections (Abiega et al., 2016; Beccari et al., 2018). Apoptotic cells were defined based on their nuclear morphology after DAPI staining as cells in which the chromatin structure (euchromatin and heterochromatin) was lost and appeared condensed and/or fragmented (pyknosis/karyorrhexis). Phagocytosis was defined as the formation of an enclosed, three-dimensional pouch of microglial processes surrounding an apoptotic cell. In tissue sections, the number of apoptotic cells, phagocytosed cells, BrdU+ cells, and microglia were estimated using unbiased stereology in the volume of the DG contained in the *z*-stack (determined by multiplying the thickness of the stack by the area of the DG at the center of the stack using ImageJ, Fiji). To obtain the absolute numbers, this density value was then multiplied by the volume of the septal hippocampus (spanning from −1 to −2.5 mm in the AP axes, from bregma; ~6 slices in each of the 6 series), which was calculated using Fiji from a Zeiss Axiovert epifluorescent microscope images collected at 20×. *In vitro*, the percentage of phagocytic microglia was defined as cells with pouches containing apoptotic SH-SY5Y nuclei and/or CM-DiI particles (Beccari et al., 2018).

Neurogenesis analysis in vivo *and* in vitro. The analysis of neurogenesis *in vivo* was performed as described previously (Encinas and Enikolopov, 2008; Abiega et al., 2016; Beccari et al., 2018). Six sections from one series

Table 4. Statistics for Figure 8

Figure	Parameter	Groups	Statistical test	Statistic	p
8C	VGF (log10)	C vs Ph3 h vs Ph24 h	One-way ANOVA	$F_{(2,9)} = 527.4$	$p < 0.001$
	Cartpt (log10)		One-way ANOVA	$F_{(2,8)} = 19.37$	$p < 0.001$
	FGF2		One-way ANOVA	$F_{(2,9)} = 5.55$	$p = 0.027$
	VEGF (log10)		One-way ANOVA	$F_{(2,9)} = 89.23$	$p < 0.001$
	PDGFa (log10)		One-way ANOVA	$F_{(2,9)} = 5.57$	$p = 0.027$
	IGF1 (log10)		One-way ANOVA	$F_{(2,9)} = 153.2$	$p < 0.001$
	EGF (log10)		One-way ANOVA	$F_{(2,9)} = 4.99$	$p = 0.035$
	GDNF (log10)		One-way ANOVA	$F_{(2,9)} = 128.8$	$p < 0.001$
	Mmp3 (log10)		One-way ANOVA	$F_{(2,9)} = 147.9$	$p < 0.001$
	Jag1		One-way ANOVA	$F_{(2,9)} = 15.26$	$p = 0.001$
	Csf3 (log10)		One-way ANOVA	$F_{(2,9)} = 242.7$	$p < 0.001$
	IL-1β (log10)		One-way ANOVA	$F_{(2,9)} = 86.82$	$p < 0.001$
	IL-6		Kruskal–Wallis	$H_{(2)} = 0.20$	$p = 0.011$
	TNFα (log10)		One-way ANOVA	$F_{(2,9)} = 25.50$	$p < 0.001$
	TFGβ (log10)		One-way ANOVA	$F_{(2,9)} = 29.04$	$p < 0.001$

Table 5. Statistics for Figure 9

Figure	Parameter	Groups	Statistical test	Statistic	p
9C	Proliferation	MicroC vs MicroPh vs DMEM	One-way ANOVA	$F_{(2,6)} = 14.94$	$p = 0.005$
9D	Proliferation	Treatment × cell types	Two-way ANOVA	$F_{\text{treat} \times \text{cell}(4,18)} = 16.99$	$p < 0.001$
				$F_{\text{treat}(2,18)} = 0.00$	$p = 1$
				$F_{\text{cell}(2,18)} = 34.60$	$p < 0.001$
	Proliferation MicroC			$F_{(2,6)} = 8.43$	$p = 0.018$
	Proliferation MicroPH			$F_{(2,6)} = 35.90$	$p < 0.001$
	Proliferation MicroDMEM	GFAP only vs nestin $^+$ vs unlabelled	One-way ANOVA	$F_{(2,6)} = 46.23$	$p < 0.001$
9F	Differentiation	Treatment × cell types × time	Three-way ANOVA	$F_{\text{treat} \times \text{cell} \times \text{time}(6,48)} = 0.245$	$p = 0.959$
				$F_{\text{treat} \times \text{cell}(6,48)} = 138.69$	$p < 0.001$
				$F_{\text{treat} \times \text{time}(2,48)} = 0.14$	$p = 0.870$
				$F_{\text{cell} \times \text{time}(2,48)} = 1.26$	$p = 0.300$
				$F_{\text{treat}(2,48)} = 4.77$	$p = 0.013$
				$F_{\text{cell}(3,48)} = 194.79$	$p < 0.001$
				$F_{\text{time}(1,48)} = 0.44$	$p = 0.510$
	Bipolar		One-way ANOVA	3 d $F_{(2,8)} = 336.60$	$p < 0.001$
				5 d $F_{(2,8)} = 70.58$	$p < 0.001$
	Stellate		One-way ANOVA	3 d $F_{(2,8)} = 35.29$	$p < 0.001$
				5 d $F_{(2,8)} = 29.17$	$p < 0.001$
	Early ramified		One-way ANOVA	3 d $F_{(2,8)} = 3.06$	$p = 0.121$
				5 d $F_{(2,8)} = 0.86$	$p = 0.471$
	Late ramified		One-way ANOVA	3 d $F_{(2,8)} = 2.18$	$p = 0.194$
		MicroC vs MicroPh vs DMEM		5 d $F_{(2,8)} = 1.54$	$p = 0.288$
9H	Dead and live cells	Treatment × life × time	Three-way ANOVA	$F_{\text{treat} \times \text{life} \times \text{time}(2,24)} = 0.589$	$p = 0.563$
				$F_{\text{treat} \times \text{life}(2,24)} = 37.22$	$p < 0.001$
				$F_{\text{treat} \times \text{time}(2,24)} = 4.54$	$p = 0.021$
				$F_{\text{life} \times \text{time}(1,24)} = 1.92$	$p = 0.179$
				$F_{\text{treat}(2,24)} = 20.24$	$p < 0.001$
				$F_{\text{life}(1,24)} = 128.33$	$p < 0.001$
				$F_{\text{time}(1,24)} = 0.15$	$p = 0.702$
			One-way ANOVA	3 d $F_{(2,8)} = 8.93$	$p = 0.016$
	Live			5 d $F_{(2,8)} = 24.86$	$p = 0.001$
				3 d $F_{(2,8)} = 16.85$	$p = 0.003$
	Dead	MicroC vs MicroPh vs DMEM	One-way ANOVA	5 d $F_{(2,8)} = 1.54$	$p = 0.306$

containing the septal hippocampus were analyzed in all experiments except in mice injected with microglia CM, in which only the three tissue sections closest to the injection site were analyzed. Proliferation was assessed by BrdU$^+$ cell quantification; neural stem cells were identified by the expression of the markers Nestin and glial fibrillary acidic protein (GFAP) and their radial morphology for cell quantification; neuroblast were assessed by doublecortin (DCX)$^+$ cell quantification and morphology to classify them in AB, CD, or EF neuroblasts (Plümpe et al., 2006); neurons were assessed by NeuN$^+$ cell quantification. The proliferation of either of these populations was assessed by their mentioned staining combined with BrdU. Numbers of cells were estimated using unbiased stereology in the volume of the DG of the *z*-stack, which was determined by multiplying the thickness of the *z*-stack (12 μm) by the area of the DG at the center of the stack using the software ImageJ (Fiji). *In vitro*, the effect of microglia-derived conditioned media on neuroprogenitor cells was analyzed considering both their morphology and the expression of cell-specific markers. Percentages of the different morphologies present in the population were obtained as well as the percentages of the different cell markers (nestin, GFAP, DCX, S100β) per morphology.

Statistical analysis. SigmaPlot (Systat Software) was used for statistical analysis. Data were tested for normality and homoscedasticity. When the data did not comply with these assumptions, a logarithmic transformation was performed and the data were analyzed using parametric tests. In the case of IL-6 mRNA expression, normality was not achieved with the

Table 6. Functional analysis of the phagocytic microglia transcriptome reveals changes in apoptosis

Gene symbol	FC Ph3h	FC Ph24 h	Location	Effect on apoptosis
PRDX1	1,1	2	Autologous	Anti-apoptotic
SIRT1	2	1,6	Autologous	Anti-apoptotic
SMO	1	3,6	Autologous	Anti-apoptotic
SOD2	1,2	2	Autologous	Anti-apoptotic
SPHK1	4,4	1,6	Autologous	Anti-apoptotic
UBE2B	1,4	1,5	Autologous	Anti-apoptotic
XRCC5	2,1	3,8	Autologous	Anti-apoptotic
PRNP	1,8	1,3	Auto/Hetero	Anti-apoptotic
TGM2	5,5	4,5	Auto/Hetero	Anti-apoptotic
CNTF	1,5	2,6	Heterologous	Anti-apoptotic
FGF2	4,2	3,7	Heterologous	Anti-apoptotic
FGF8	1,7	1,6	Heterologous	Anti-apoptotic
VEGFA	4,5	1,8	Heterologous	Anti-apoptotic
RARG	1,3	3	Autologous	Pleiotropic
IL6	18,7	15,8	Heterologous	Pleiotropic
BAD	1,8	2,2	Autologous	Proapoptotic
FAS	1,5	1,5	Autologous	Proapoptotic
FOXO3	21	38	Autologous	Proapoptotic
GAS1	2,7	3	Autologous	Proapoptotic
NLRP3	12	19	Autologous	Proapoptotic
PPP2CB	1,5	1,6	Autologous	Proapoptotic
PTEN	1,1	1,6	Autologous	Proapoptotic
RHOA	1	1,7	Autologous	Proapoptotic
SCRIB	1,9	2,4	Autologous	Proapoptotic
STK3	1	1,5	Autologous	Proapoptotic
TFPT	2,4	3	Autologous	Proapoptotic
GAL	1,2	1,8	Heterologous	Proapoptotic
IL1β	8,9	30,7	Heterologous	Proapoptotic

Classification of the genes related to cell death obtained from DAVID analysis. The genes were classified according to their FC, to the effects on microglia (autologous), or on the surrounding cells (heterologous) and to the positive or negative effect on apoptosis.

logarithmic transformation and the data were analyzed using a Kruskal–Wallis ranks test, followed by Tukey test as a *post hoc*. In the rest of the cases, two-sample experiments were analyzed by Student's t test and more than two-sample experiments by ANOVA. In two-way and three-way ANOVA, when interactions between factors were found, the analysis of the relevant variable was split into several one-way ANOVAs and Holm–Sidak method was used as a *post hoc*. The transformation used (if any), the test used, the comparison performed, the value of the statistical and the p values are shown in Tables 2–5 and 7–9. Only $p < 0.05$ is reported to be significant. Data are shown as mean ± SEM.

Statistical analysis of gene expression arrays. To analyze the differential expression between naive ($t = 0$) and phagocytic ($t = 3$ h and $t = 24$ h) microglia groups over time the statistical analysis the maSigPro package of R/Bioconductor was used (R v3.0.3, Bioconductor release v2.13, maSigPro v1.34.1; Conesa et al., 2006). This method is based on a general regression approximation for the modeling and adjustment of the parameters required according to the type of analysis. The parameter "Time" is considered as a continuous variable, and creates a regression model of the gene response. The analysis was performed in three steps. First, genes that exhibited changes in expression over time were selected based on a p-corrected Benjamini–Hochberg (FDR) value. Next, for each of the genes that presented a significant change in their expression over time a regression was applied to determine their model ($R^2 > 0.7$) to identify patterns or models of change based on time variables, obtaining 20,800 probes. Finally, the probes were selected according to their fit to the regression model. Next, the number of genes with a very high differential pattern was reduced by applying a more restrictive criterion ($R^2 > 0.9$), obtaining 13,146. The $R^2 > 0.7$ list was used for the identification of neurogenesis related genes and the $R^2 > 0.9$ list was used for the study of transcriptional profile of phagocytic microglia.

DAVID. The database for annotation, visualization, and integrated discovery (DAVID; https://david.ncifcrf.gov/) v6.8 provides a comprehensive set of functional annotation tools to understand biological meaning behind large list of genes. DAVID was used to generate a gene-GO term enrichment analysis that identified enriched biological themes and to highlight the most relevant GO terms associated with the array gene list. The array gene list of $R^2 > 0.9$ was used for this gene profile analysis. The analysis of each expression pattern was performed separately and only terms with an adjusted p value (Benjamini–Hochberg) > 0.05 were considered significant.

ClueGO. ClueGO was used to generate protein pathways and to constitute the network of pathways based on the Gene Ontology and KEGG database (Bindea et al., 2013). ClueGO is a plugin of Cytoscape (http://www.cytoscape.org/) that visualizes the non-redundant biological terms for large clusters of genes in a functionally grouped network. A ClueGO network is created with κ statistics and reflects the relationships between the terms based on the similarity of their associated genes (Mlecnik et al., 2018). Gene ontology (GO) analysis of mouse array data were performed with ClueGO v1.4 (Bindea et al., 2013) using the following parameters: enrichment/depletion two-sided hypergeometric statistical test; correction method: Benjamini–Hochberg; GO term range levels: 3–8; minimal number of genes for term selection: 10; minimal percentage of genes for term selection: 10%; κ-score threshold: 0.8; general term selection method: smallest p value; group method: κ; minimal number of subgroups included in a group: 3; minimal percentage of shared genes between subgroups: 50%.

Results

Chronic impairment of microglial phagocytosis reduces adult hippocampal neurogenesis

To examine the impact of microglial phagocytosis on adult hippocampal neurogenesis *in vivo*, we focused on two signaling pathways involved on phagocytosis: P2Y12 (purinergic receptor type Y12), which mediates chemotaxis toward the "find-me" signal ADP (Haynes et al., 2006); and the TAM family tyrosine kinases MerTK and Axl, which bind to phosphatidylserine adapter/bridging molecules: growth arrest specific factor 6 and protein S (Elliott et al., 2009; Fourgeaud et al., 2016). We used two transgenic mouse models in which these proteins are constitutively knocked out (P2Y12 KO and MerTK/Axl KO). We decided to study the impact of phagocytosis in young mice (1 month old), as neurogenesis and apoptosis of newborn cells and subsequent phagocytosis by microglia rapidly declines with age (Sierra et al., 2010; Beccari et al., 2017). Apoptotic cells were defined as pyknotic/karyorrhectic nuclei labeled with the DNA dye DAPI, which we have previously characterized to express other apoptosis markers such as activated caspase 3 and fractin (Sierra et al., 2010). First, we assessed phagocytosis in the hippocampus of the two KO models by quantifying the Ph index (the percentage of apoptotic cells engulfed by microglia), which is ~90% in physiological conditions (Abiega et al., 2016), and found significantly lower Ph index in the two KO models (74.8 ± 0.9% for P2Y12, 61.5 ± 1.6% for MerTK/Axl; Fig. 1*A–C*). In addition, the microglial Ph capacity (weighted average of the number of pouches containing apoptotic cells per microglia, i.e., the average number of phagocytic pouches per microglia) was significantly reduced in both KO models (Fig. 1*A–C*). Nonetheless, we found no changes in the number of microglia and the phagocytosis reduction was small, possibly because of compensatory mechanisms resulting from the chronic depletion, and we only detected the expected increase of apoptotic cells in MerTK/Axl KO mice (Fig. 1*A–C*), possibly indicating not a complete dysfunction but a slowdown of phagocytosis.

Next, we examined hippocampal neurogenesis in these phagocytosis impaired KO models and observed that the two showed a significant decrease in the population of neuroblasts and immature neurons, labeled with DCX, compared to wild-

Table 7. Statistics for Figure 10

10*F*	Dead and live cells (log10)	Treatment × life × time	Three-way ANOVA	$F_{\text{treat} \times \text{life} \times \text{time}(4,18)} = 0.595$	$p = 0.671$
				$F_{\text{treat} \times \text{life}(4,18)} = 4.656$	$p < 0.009$
				$F_{\text{treat} \times \text{time}(2,18)} = 0.265$	$p = 0.770$
				$F_{\text{life} \times \text{time}(2,18)} = 1.481$	$p = 0.254$
				$F_{\text{treat}(2,18)} = 0.544$	$p = 0.590$
				$F_{\text{life}(2,18)} = 50.494$	$p < 0.001$
				$F_{\text{time}(1,18)} = 0.695$	$p = 0.415$
	Live	MicroC vs MicroPh vs DMEM	One-way ANOVA	5 d (log10) $F_{(2,6)} = 8.774$	$p = 0.017$
				9 d $F_{(2,6)} = 14.103$	$p = 0.005$
	Dead		One-way ANOVA	5 d $F_{(2,6)} = 1.476$	$p = 0.301$
				9 d $F_{(2,6)} = 8.563$	$p = 0.017$
10*G*	Bipolar	MicroC vs MicroPh vs DMEM	Kruskal Wallis	5 d $H_{(2)} = 7.624$	$p = 0.071$
				9 d $H_{(2)} = 7.624$	$p = 0.071$
	Stellate		Kruskal Wallis	5 d $H_{(2)} = 5.956$	$p = 0.025$
	One-way ANOVA			9 d $F_{(2,6)} = 15.331$	$p = 0.004$
	Early ramified		One-way ANOVA	5 d $F_{(2,6)} = 1.469$	$p = 0.303$
	Kruskal Wallis			9 d $H_{(2)} = 2.000$	$p = 0.829$
				5 d $F_{(2,6)} = 7.249$	$p = 0.025$
	Late ramified		One-way ANOVA	9 d $F_{(2,6)} = 1.880$	$p = 0.232$

Table 8. Statistics for Figures 11–13

Figure	Parameter	Groups	Statistical test	Statistic	*p* value
11*F*	REST	MicroC vs MicroPh vs DMEM	One-way ANOVA	$F_{(3,11)} = 0.688$	$p = 0.594$
	Ascl		One-way ANOVA	$F_{(3,11)} = 3.53$	$p = 0.068$
	pSMAD/SMAD		One-way ANOVA	$F_{(3,11)} = 27.30$	$p < 0.001$
12*C*	Differentiation	Treatment × cell types × time	Three-way ANOVA	$F_{\text{treat} \times \text{cell} \times \text{time}(2,24)} = 0.24$	$p = 0.787$
				$F_{\text{treat} \times \text{cell}(2,24)} = 0.46$	$p = 0.636$
				$F_{\text{treat} \times \text{time}(2,24)} = 0.156$	$p = 0.856$
				$F_{\text{cell} \times \text{time}(1,24)} = 1.052$	$p = 0.315$
				$F_{\text{treat}(2,24)} = 6.42$	$p = 0.006$
				$F_{\text{cell}(1,24)} = 1235.66$	$p < 0.001$
				$F_{\text{time}(1,24)} = 0.361$	$p = 0.554$
12*D*	CSF3 (log10)	MicroC vs MicroPH vs LPS vs MicroPH + LPS	One-way ANOVA	$F_{(3,12)} = 44.56$	$p < 0.001$
	IL-1β (log10)		One-way ANOVA	$F_{(3,12)} = 19.44$	$p < 0.001$
	IL-6		Kruskal–Wallis	$H_{(3)} = 11.43$	$p = 0.010$
	TNFα (log10)		One-way ANOVA	$F_{(3,12)} = 52.539$	$p < 0.001$
	TGFβ (log10)		One-way ANOVA	$F_{(3,12)} = 3.57$	$p = 0.047$
13*B*	Dead and live cells	Treatment × life × time	Three-way ANOVA	$F_{\text{treat} \times \text{life} \times \text{time}(2,24)} = 0.512$	$p = 0.606$
				$F_{\text{treat} \times \text{life}(2,24)} = 4.79$	$p = 0.018$
				$F_{\text{treat} \times \text{time}(2,24)} = 0.14$	$p = 0.872$
				$F_{\text{life} \times \text{time}(1,24)} = 0.90$	$p = 0.757$
				$F_{\text{treat}(2,24)} = 1.33$	$p = 0.283$
				$F_{\text{life}(1,24)} = 309.10$	$p < 0.001$
				$F_{\text{time}(1,24)} = 0.01$	$p = 0.912$

type (WT) controls. In addition, we assessed proliferation by quantifying the number of dividing cells using either BrdU, an analog of thymidine that gets incorporated into the DNA during S phase of dividing cells (mice were injected with 150 mg/kg and killed 24 h later); or the proliferation marker Ki67$^+$ (Scholzen and Gerdes, 2000). P2Y12 KO mice had a decrease in both neuroblasts (reduction of 31.7 ± 2.7%) and neuroblast proliferation (reduction of 39.3 ± 9.8%), and MerTK/Axl KO mice showed a reduction in neuroblasts (reduction of 26.2 ± 9.4%) compared to WT mice (Fig. 1*D*–*F*). We further studied the formation of newborn neurons using BrdU pulse-and-chase in the most robust model, the P2Y12 KO. Four weeks after the BrdU injection, when the mice were 2 months old, both total BrdU$^+$ cells and newborn neurons (NeuN$^+$/BrdU$^+$) were reduced in P2Y12 KO mice compared to WT mice (reduction of 24.6 ± 9.7%; Fig. 2*A*,*B*), in parallel to a decrease in phagocytosis (Ph index and Ph capacity) and no changes in apoptosis nor microglia (Fig. 2*C*). The defect in neurogenesis was maintained later in life, because at 7 months, P2Y12 KO mice still showed a significant reduction in phagocytosis (Ph index) without alterations in apoptosis nor microglia (Fig. 2*D*,*E*), in parallel to a reduction in neuroblasts compared to WT mice (Fig. 2*F*,*G*).

To confirm the specificity of these results, we analyzed the expression of P2Y12, MerTK, and Axl in FACS-sorted cells from 1-month-old fms-EGFP mice, in which microglia is labeled with EGFP. We found that, P2Y12 and MerTK, but not Axl, were highly expressed in microglia compared with other cells of the hippocampal parenchyma (Fig. 2*H*,*I*), suggesting that the disruption of neurogenesis in the KO models might be attributable to the lack of these receptors in microglia. These receptors regulate multiple features of microglial physiology (Elliott et al., 2009; Fourgeaud et al., 2016). In addition, constitutive MerTK/Axl KO mice show autoimmune diseases (Rothlin and Lemke, 2010), as both MerTK and Axl are highly expressed in peripheral macrophages (http://rstats.immgen.org/Skyline/skyline.html). In addition, in the brain Axl is also expressed in astrocytes (http://

Table 9. Statistics for Figure 14

Figure	Parameter	Groups	Statistical test	Statistic	p
14*C*	$BrdU_{2\,h}$ (log10)	MicroC vs MicroPh	Unpaired *t* test	$t_{(18)} = -0.003$	$p = 0.998$
14*D*	Apoptosis	MicroC vs MicroPh	Unpaired *t* test	$t_{(12)} = -0.867$	$p = 0.403$
14*F*	Stem cells	MicroC vs MicroPh	Unpaired *t* test	$t_{(18)} = 0.42$	$p = 0.677$
14*G*	Stem cell proliferation	MicroC vs MicroPh	Unpaired *t* test	$t_{(18)} = 1.97$	$p = 0.065$
14*I*	Neuroblasts (total)	MicroC vs MicroPh	Unpaired *t* test	$t_{(12)} = 0.02$	$p = 0.984$
	AB		Unpaired *t* test	$t_{(12)} = -0.18$	$p = 0.862$
	CD		Unpaired *t* test	$t_{(12)} = -0.42$	$p = 0.679$
	EF		Unpaired *t* test	$t_{(12)} = 0.293$	$p = 0.774$
14*J*	BrdU neuroblasts (log10)	MicroC vs MicroPh	Unpaired *t* test	$t_{(12)} = -0.47$	$p = 0.650$
14*M*	$BrdU_{4w}$ (log10)	MicroC vs MicroPh	Unpaired *t* test	$t_{(17)} = 2.41$	$p = 0.031$
14*N*	Apoptosis	MicroC vs MicroPh	Unpaired *t* test	$t_{(11)} = 0.12$	$p = 0.908$
14*P*	Neuroblasts	Treatment × distance	Two-way $ANOVA_{rep}$	$F_{treat \times dist(1,11)} = 0.20$	$p = 0.664$
				$F_{dist(1,11)} = 0.852$	$p = 0.376$
				$F_{treat(1,11)} = 14.19$	$p = 0.003$
14*R*	Neuroblasts (total)	MicroC vs MicroPh	Unpaired *t* test	$t_{(18)} = 3.38$	$p = 0.003$
	AB		Unpaired *t* test	$t_{(18)} = 1.80$	$p = 0.099$
	CD		Unpaired *t* test	$t_{(18)} = 2.09$	$p = 0.035$
	EF		Unpaired *t* test	$t_{(18)} = 4.62$	$p < 0.001$
14*S*	New neurons	MicroC vs MicroPh	Unpaired *t* test	$t_{(17)} = 2.28$	$p = 0.036$

www.brainrnaseq.org/). Nonetheless, P2Y12 is largely specific to microglia (http://www.brainrnaseq.org/) and P2Y12 KO mice show an impairment of microglial phagocytosis and concomitant decrease in neurogenesis up to 7 months. Thus, the similar phagocytosis impairment and neurogenesis reduction in the two KO models suggests that an intact microglial phagocytosis is necessary for the long-term maintenance of hippocampal neurogenesis.

Acute microglial phagocytosis impairment transiently increases adult hippocampal neurogenesis

We then studied the effect of acute phagocytosis blockage on neurogenesis using an inducible MerTK KO model (generated by crossing *Mertk*$^{fl/fl}$ to *Cx3cr1*$^{CreER/+}$ mice; Fourgeaud et al., 2016). Mice received tamoxifen (two 75 mg/kg i.p. injections) or vehicle (corn oil) at P21 and P23 to induce microglial-specific Cre-mediated depletion of *Mertk*, and one injection of BrdU at P28 to label dividing cells. Phagocytosis and neurogenesis were analyzed at 1 d and 4 weeks after BrdU administration (i.e., when mice were 1 and 2 months old, respectively; Fig. 3*A*,*B*). Phagocytosis was strongly reduced in the inducible KO mice injected with tamoxifen (iKO) compared to control mice injected with vehicle, as shown by the Ph index (73.0 ± 3.7% and 72.9 ± 2.6% reduction at 1 d and 4 weeks, respectively) and the Ph capacity (54.5 ± 3.1% and 65.6 ± 11.0% reduction at 1 d and 4 weeks, respectively), together with an accumulation of apoptotic cells (Fig. 3*C*–*F*). iKO mice showed no significant changes in the number of microglia but a trend toward increased apoptotic cells compared to control mice (Fig. 3*E*,*F*). Concomitantly, 1 d after the BrdU injection the number of proliferating $BrdU^+$ cells and the number of DCX^+, $BrdU^+$, proliferating neuroblasts increased (51.8 ± 10.2% and 55.4 ± 12.2% increase, respectively), whereas there was no change in the total number of neuroblasts in MerTK iKO compared to control mice injected with oil (Fig. 3*G*–*I*). However, at 4 weeks after BrdU injection there were no significant changes in the total number of newborn cells nor newborn neurons ($BrdU^+$, $NeuN^+$; Fig. 3*J*,*K*). Thus, the excess of BrdU cells formed at 1 d were lost at 4 weeks, and indeed the net yield of newborn cells, calculated as a ratio of the cells at 4 weeks over the cells at 1 d, was significantly lower in iKO compared to control mice (43.1 ± 4.5% reduction; Fig. 3*L*).

This transient increase in neurogenesis in the MerTK iKO model (Fig. 3) is in apparent disagreement with the reduction of neurogenesis in the constitutive P2Y12 and MerTK/Axl KO models (Figs. 1, 2). It is important to note that in the iKO model, phagocytosis is acutely and strongly impaired in the adult hippocampus, whereas in the constitutive KO models the effect on phagocytosis is low, chronic and from embryonic development. In addition, other differences could explain the contrast between the models, including targeting peripheral immune cells in MerTK/Axl KO mice, but not in the P2Y12 KO mice or the MerTK iKO mice; or the fact that iKO mice were generated in a heterozygous CX3CR1 background, which reduces basal neurogenesis (Rogers et al., 2011). Importantly, the administration of tamoxifen, used to activate the Cre recombinase, does not affect neurogenesis (Rotheneichner et al., 2017). Nonetheless, the data from the three models altogether suggests that microglial phagocytosis participates in the regulation of adult hippocampal neurogenesis.

Phagocytosis of apoptotic cells triggers the expression of neurogenic modulatory factors by microglia *in vitro*

To study the mechanism by which microglial phagocytosis regulates neurogenesis, we developed a xenogenic *in vitro* model of phagocytosis of apoptotic cells (Beccari et al., 2018), in which mouse primary microglia were fed for different lengths of time (1–24 h) with a human neuronal line (SH-SY5Y), previously labeled with CM-DiI and treated with STP (4 h, 3 μM) to induce apoptosis (Fig. 4*A*,*B*). In this model, pooled telencephalic microglia were used in the cultures, disregarding possible specific effects of hippocampal microglia. When fed with apoptotic human cells, microglia were phagocytic as early as 1 h (30.2 ± 5.8%), a percentage that kept increasing until 24 h (83.8 ± 3.6%; Fig. 4*C*). We then performed a mouse-specific genome-wide transcriptomic analysis using gene expression mouse-specific arrays to compare naive versus phagocytic microglia.

Hence, we compared the genome-wide transcriptome naive versus phagocytic microglia (3 and 24 h) using gene expression arrays. Hierarchical clustering and principal component analysis (PCA) of the transcriptome of control, Ph3h and Ph24h microglia showed strong differences in the clustering of the expression profile of three groups (Fig. 4*D*,*E*). To analyze which particular

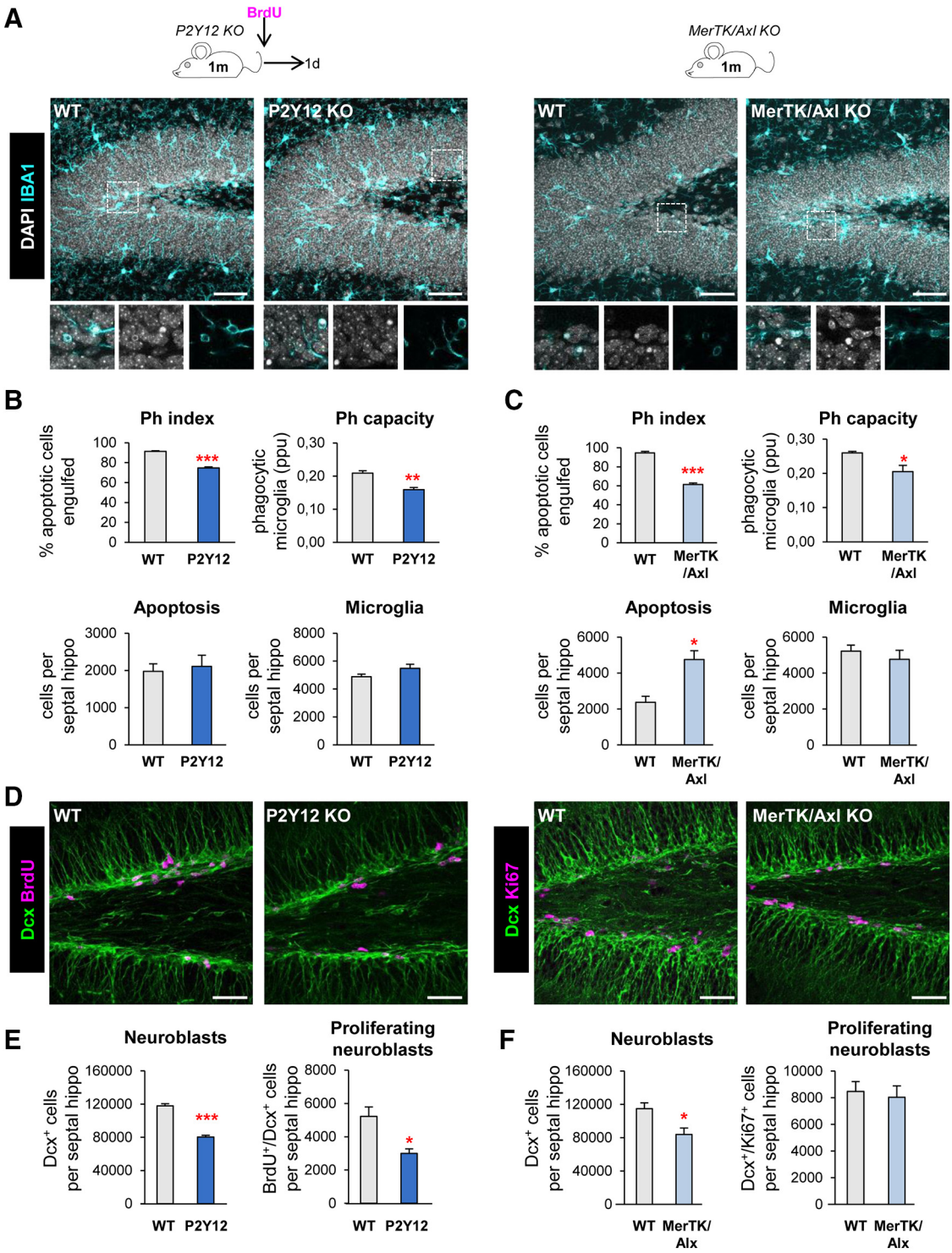

Figure 1. Chronic microglial phagocytosis impairment reduces adult hippocampal neurogenesis. ***A***, Representative maximum projection of confocal *z*-stack of P2Y12 and MerTK/Axl KO mice immunofluorescence in the mouse hippocampal DG at 1 month (1 m). Microglia were labeled with Iba1 (cyan) and apoptotic nuclei were detected by pyknosis/karyorrhexis (white, DAPI). ***B***, ***C***, Percentage of apoptotic cells engulfed (Ph index), weighted average of the percentage of microglia with phagocytic pouches (Ph capacity), apoptotic cells and microglia per septal hippocampus in P2Y12 KO mice (***B***) and MerTK/Axl KO mice (***C***). ***D***, Representative confocal *z*-stack of P2Y12 and MerTK/Axl KO mice immunofluorescence in the mouse hippocampal DG at 1 m. Neuroblasts were labeled with DCX (green) and proliferation was labeled with either BrdU (150 mg/kg, 24 h) or Ki67 (magenta). ***E***, Neuroblast and neuroblast proliferation in 1-month-old P2Y12 KO mice. ***F***, Neuroblast and neuroblast proliferation in 1-month-old MerTK/Axl KO mice. Scale bars: ***A***, ***D***, 50 μm (inserts, 10 μm); ***A***, left, $z = 20$ μm; ***A***, right, $z = 17$ μm; ***D***, left, $z = 7$ μm; ***D***, right, $z = 10$ μm. $N =$ 3–4 mice (***B***, ***C***, ***E***, ***F***). Error bars represent mean ± SEM. *$p < 0.05$, **$p < 0.01$, ***$p < 0.001$ by Student's *t* test. Only significant effects are shown. Values of statistics used are shown in Table 2.

genes were different among the three experimental groups, we searched for array probes with significant changes over time using a *p*-corrected Benjamini–Hochberg value and a polynomial regression model to identify time patterns (Conesa et al., 2006). We obtained 10,000 significantly regulated probes with a restrictive criterion of $R^2 > 0.9$ and a fold-change (FC) > 1.5 or < -1.5, eventually obtaining 6585 genes that presented significant changes over time (Fig. 4*F*).

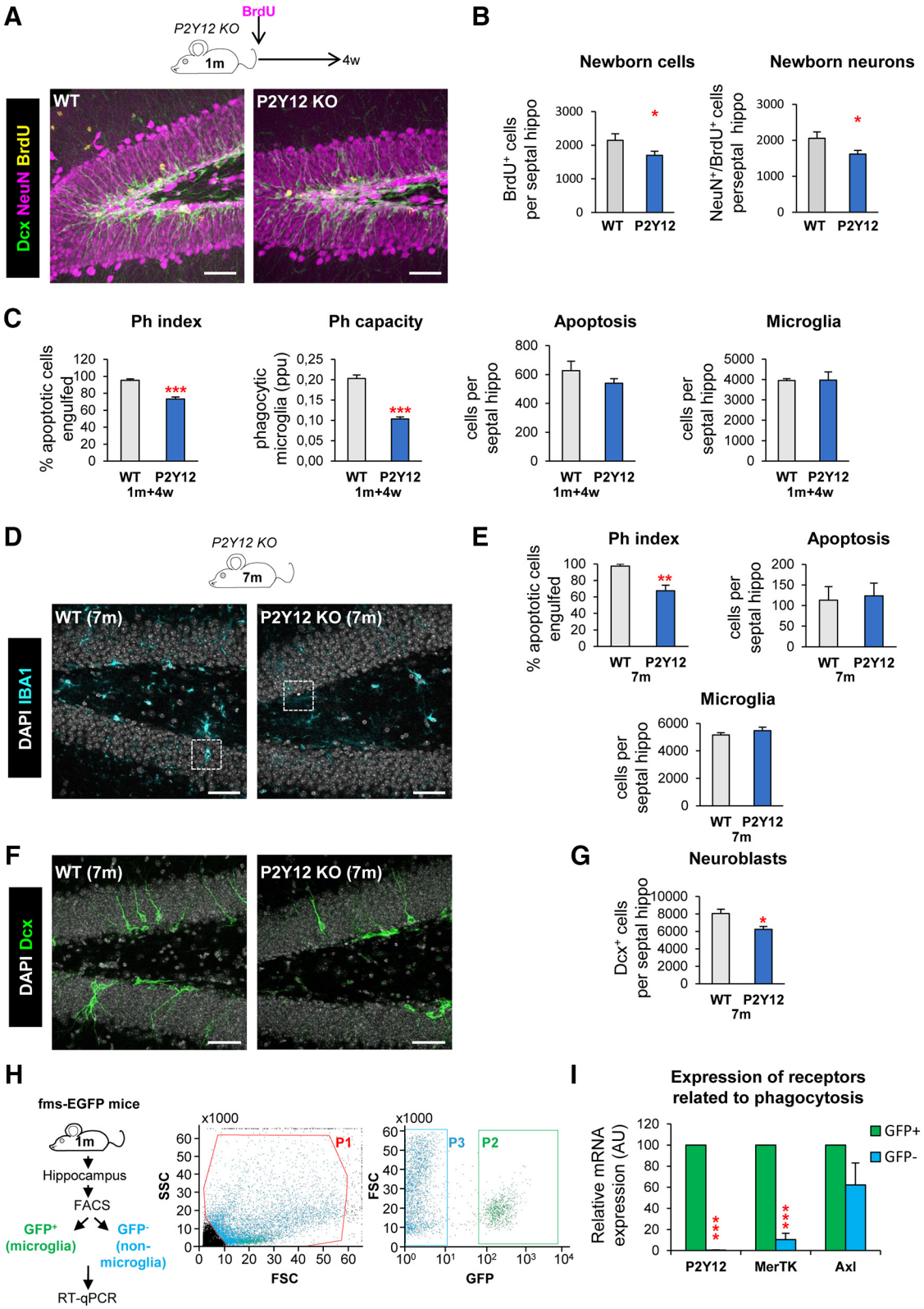

Figure 2. Chronic microglial phagocytosis impairment reduces adult hippocampal neurogenesis in the long term. ***A***, Representative confocal *z*-stack of P2Y12 KO mice immunofluorescence in the mouse hippocampal DG at 2 months. Neuroblasts were labeled with DCX (green), neurons were labeled with NeuN (magenta) and proliferation was labeled with BrdU (yellow; 4 weeks after BrdU injection). ***B***, New cells and new neurons (NeuN $^{+}$, BrdU $^{+}$) in 2-month-old P2Y12 KO mice, 4 weeks after the BrdU injection. ***C***, Percentage of apoptotic cells engulfed (Ph index), weighted average of the percentage of microglia with phagocytic pouches (Ph capacity), apoptotic cells and microglia per septal hippocampus in P2Y12 KO mice 4 weeks after BrdU injection (2m). ***D***, Representative maximum projection of confocal *z*-stack of P2Y12 KO mice immunofluorescence in the mouse hippocampal DG at 7 months (7 m). Microglia were labeled with Iba1 (cyan) and apoptotic nuclei were detected by pyknosis/karyorrhexis (white, DAPI). ***E***, Percentage of apoptotic cells engulfed (Ph index), number of apoptotic cells and microglia per septal hippocampus in 7-month-old P2Y12 KO mice. ***F***, Representative confocal *z*-stack of P2Y12 KO mice immunofluorescence in the mouse hippocampal DG at 7 months. Neuroblasts were labeled with DCX (green). ***G***, Number of neuroblasts per septal hippocampus in 7-month-old P2Y12 KO mice. ***H***, Experimental design used to isolate microglia (GFP $^{+}$) versus non-microglial cells (GFP $^{-}$) from 1-month-old fms-EGFP mice using flow cytometry. First, debris was excluded using the P1 gate in FSC versus SSC (left). Next, gates for GFP $^{+}$ microglia cells (P2) (*Figure legend continues.*)

We classified these genes according to four main expression patterns (Fig. 4*G*): UP (upregulation both at 3 and 24 h), DOWN (downregulation in both time points), transient UP (upregulation at 3 h and downregulation at 24 h), and transient DOWN (downregulation at 3 h and upregulation at 24 h). Genes in the UP expression pattern showed the largest average FC changes among all patterns, some of them even reaching 8000 FC at 24 h. The rest of the patterns had on average more modest changes.

Next, we performed a functional analysis of the phagocytic microglia transcriptome using the ClueGO network (Fig. 5) and DAVID (Fig. 6*A*). These analyses revealed a number of functional biological pathways associated with each of the four main expression patterns of phagocytic microglia including downregulation in pathways related to DNA and chromosomes and upregulation of different functions associated with metabolism and chromatin remodeling. Interestingly, different studies suggesting metabolic changes in phagocytes upon the uptake of apoptotic cells have recently emerged (Morioka et al., 2018). Importantly, for many upregulated genes, ClueGO revealed specific terms like "generation of neurons", "neuron differentiation" or "neuron development" that were grouped under the term "neurogenesis" and had a direct interrelation with "neuron projection development" group.

We then focused on the identity of the neurogenesis-related genes using the following strategy (Fig. 6*B*). To identify phagocytosis-related potential regulators of neurogenesis, we used MANGO (The Mammalian Adult Neurogenesis Gene Ontology), a database of 259 genes already described to be involved in the regulation of adult hippocampal neurogenesis (Overall et al., 2012). Of the MANGO genes, 213 were found significantly regulated in our arrays. We then filtered those MANGO genes by disregarding those encoding for autologous proteins (i.e., acting on the same cell, such as transcription factors) and focusing on those encoding heterologous proteins (i.e., acting on neighbor cells, such as secreted molecules). We first applied this criterion to MANGO, and found 26 heterologous genes that had been previously identified to regulate adult hippocampal neurogenesis. To further extend the list of heterologous genes outside MANGO that could be potential regulators of neurogenesis, we looked into the filtered gene array list ($R^2 > 0.9$ and $-1.5 > \mathrm{FC} > 1.5$), searched the GO terms associated with each MANGO heterologous gene, and selected those terms that could be related to different steps of the neurogenic process (proliferation, differentiation, migration, chemotaxis, survival, and development). MANGO heterologous genes encompassed 57 different neurogenesis-related GO terms, such as growth factor activity (GO: 0008083), nervous system development (GO:0007399), learning (GO:0007612), memory (GO:0007613), cell proliferation (GO: 0008283), cell differentiation (GO:0030154), and neuron development (GO:0048666).

We then searched for heterologous genes belonging to each of these 57 categories in our arrays, using a less-restrictive list of 20,800 probes ($R^2 > 0.7$, no screening of FC). We finally obtained 224 genes with differential expression between naive and phagocytic microglia, which were heterologous and whose function had been previously involved in neurogenesis (based on the GO terms). The 224 candidate genes were classified according to their main regulatory expression patterns: 94 UP, 73 DOWN, 28 transient-UP, and 29 transient-DOWN genes (Fig. 6*B*). In the four regulation patterns, the majority of the genes were categorized as trophic factors (between 23 and 29% in all regulatory patterns; Fig. 7*A*,*B*). We also found cytokines, chemokines, peptides, and hormones as the main gene types of the candidates. Despite the fact that trophic factors were the largest percentage in each regulation pattern, they showed a similar and rather low mean FC compared to the other categories. Only the upregulated peptides and hormones revealed a large mean of 800 FC at both 3 and 24 h of phagocytosis. These data suggest that peptides and hormones were the most likely molecules to perform modulatory functions in the neurogenic niche by phagocytic microglia.

To disregard the possible detection of residual mRNA from the (human) apoptotic cells, we checked the sequence of the 60,000 array probes against the human transcriptome by BLAST. We found that 96% of the probes had low homology to the human transcriptome (MegaBlast homology $< 5\%$). In addition, we analyzed the RNA integrity in apoptotic cells using a bioanalyzer, and found that whereas naive and phagocytic (24 h) microglia had the expected 18S and 28S rRNAs profile, apoptotic SH-SY5Y cells (24 h) showed a smear typical of RNA degradation (Fig. 8*A*). Finally, we analyzed whether apoptotic cells could synthesize new mRNA using 5′-fluorouridine (FU; a uridine analog that integrates at transcription sites; Fig. 8*B*). Apoptotic SH-SY5Y, unlike live cells, did not exhibit nuclear FU labeling, evidencing that they were not transcriptionally active. Altogether, the RNA profiling and analysis of transcription in apoptotic cells strongly suggests that although the gene arrays used could virtually detect up to 4% of mRNAs from human apoptotic cells, their lack of residual RNA would result solely in the detection of microglial-specific transcriptional changes after phagocytosis.

Finally, we validated the mRNA expression of the candidates in naive and phagocytic microglia by real-time qPCR. We selected a subset of genes for validation based both on their high FC in the array and/or the well known neurogenesis modulatory potential described in the literature. We found that the expression pattern of the selected candidates determined by real-time qPCR was largely in agreement with that obtained in the arrays. Among the genes with the largest mRNA expression were the neuropeptide VGF, the matrix metalloprotease 3, and the cytokine colony stimulating factor 3 (Fig. 8*C*), reinforcing the notion that phagocytosis promotes the production of neurogenic modulators by microglia.

The secretome from phagocytic and naive microglia drives neuroprogenitor cells toward different fates *in vitro*

Of the 224 heterologous candidates, 83.5% belonged to the secretome, suggesting an important role of the phagocytic microglial secretome on the modulation of neurogenesis. We thus directly tested the effect of the phagocytic microglial secretome on neurogenesis *in vitro*. To model neurogenesis, we used a monolayer of NPC cultures derived from disaggregated neurospheres, obtained from whole P0–P1 brains and allowed them to proliferate 48 h in DMEM/F12 with trophic factors EGF/FGF2 (Babu et al., 2011). We first performed a neurogenesis differentiation assay in which NPCs were allowed to differentiate during a time course (1–5 d) in the presence of conditioned media from control [naive

←

(*Figure legend continued.*) and GFP$^-$ non-microglial cells (P3) were defined based on the distribution of the fms-EGFP$^+$ cells in EGFP versus FSC (right). ***I***, Expression of P2Y12, MerTK, and Axl in microglia (GFP$^+$) versus non-microglial cells (GFP$^-$) by real-time qPCR in FACS-sorted cells from fms-EGFP mice hippocampi. OAZ1 (ornithine decarboxylase antizyme 1) was selected as a reference gene. Scale bars: ***A***, ***D***, ***F***, 50 μm; ***A***, $z = 20$ μm; ***D***, ***F***, $z = 17.5$ μm. $N =$ 5 mice (***A***). $N = 4–6$ mice (***E***, ***G***), $N = 3$ independent experiments (***H***; each from 8 pooled hippocampi), $^*p < 0.05$, $^{**}p < 0.01$, $^{***}p < 0.001$ by Student's *t* test. Values of statistics used are shown in Table 2.

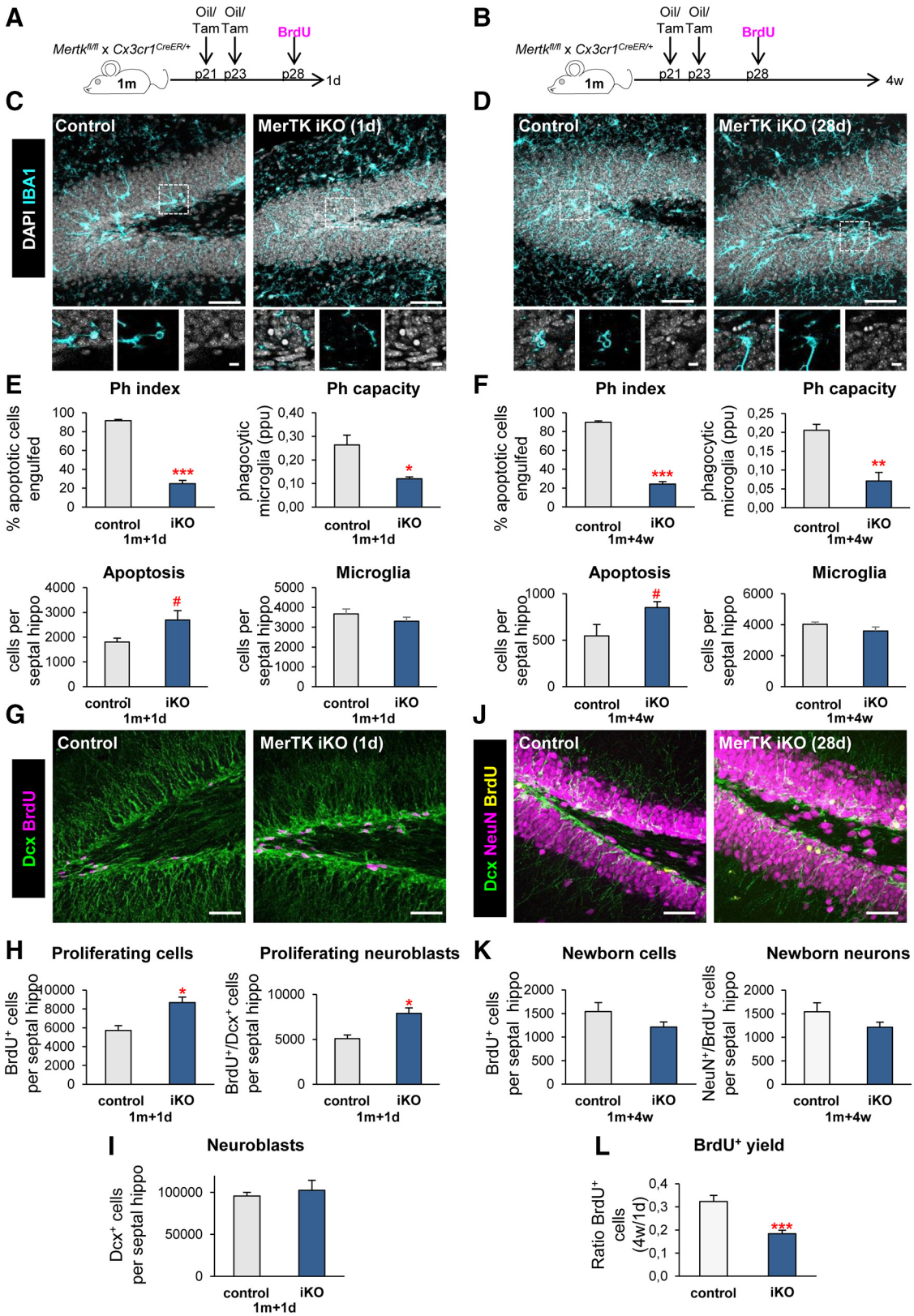

Figure 3. Acute microglial phagocytosis impairment transiently increases adult hippocampal neurogenesis. ***A***, ***B***, Experimental design in microglial-specific MerTK inducible KO mice, generated by crossing *Mertk*$^{fl/fl}$ and *Cx3cr1*^{CreER} mice treated with tamoxifen (iKO) or corn oil (control) at P21 and P23 and injected with BrdU at p28 (100 mg/kg). Mice were killed at 1 d (***A***) or 4 weeks (***B***) after the BrdU injection. ***C***, ***D***, Representative maximum projection of confocal *z*-stack of MerTK iKO mice immunofluorescence in the mouse hippocampal DG at 1 d (***C***) and 4 weeks (***D***). Microglia were labeled with Iba1 (cyan) and apoptotic nuclei were detected by pyknosis/karyorrhexis (white, DAPI). ***E***, ***F***, Percentage of apoptotic cells engulfed (Ph index), weighted average of the percentage of microglia with phagocytic pouches (Ph capacity), apoptotic cells and microglia per septal hippocampus in MerTK iKO mice at 1 d (***E***) and 4 weeks (***F***). ***G***, Representative confocal *z*-stack of MerTK iKO mice immunofluorescence in the mouse hippocampal DG at 1 d. Neuroblasts were labeled with DCX (green) and proliferation was detected with BrdU (magenta). ***H***, Newborn cells (BrdU^{+}) and newborn neuroblasts (DCX^{+}, BrdU^{+}) in MerTK iKO mice at 1 d post-BrdU. ***I***, Neuroblasts (DCX^{+}) in MerTK iKO mice at 1 d post-BrdU. ***J***, Representative confocal *z*-stack of MerTK iKO mice immunofluorescence in the mouse hippocampal DG at 4 weeks post-BrdU. Neuroblasts were labeled with DCX (green), neurons were labeled with NeuN (magenta) (*Figure legend continues.*)

microglia (CM microC)] and phagocytic [24 h phagocytic microglia (CM microPH)] microglia (Fig. 9*A*). DMEM was used as an internal control, because microglia were cultured in this media. After 1 d of differentiation, cultures in CM microPH maintained higher levels of proliferation than CM microC as observed by a higher proportion of cells labeled with the proliferation marker Ki67$^+$ (Fig. 9*B*,*C*). Most of the proliferating cells in microPH cultures expressed nestin, a marker of progenitor cells, stem cells, and reactive astrocytes (Encinas and Sierra, 2012; Lopez-Atalaya et al., 2018; Fig. 9*D*). We then followed the progeny of those populations at 3 and 5 d and labeled them with cell identity markers: nestin, GFAP, a marker of astrocytes (Encinas and Sierra, 2012) and DCX, a marker of neuroblasts (Brown et al., 2003; Fig. 9*E*). We found that CM microC treatment mainly produced GFAP^{high}, nestin$^{+/-}$, stellate cells both at 3 and 5 d, as well as a small percentage of DCX ramified cells. In contrast, in CM microPH cultures the majority of the cells were nestin^{high}, GFAP$^+$, with a bipolar morphology (Fig. 9*F*,*G*). Cell death (apoptosis) was observed in all conditions, as has been noted before in this type of cultures upon growth factor withdrawal-induced differentiation (Babu et al., 2011). However, higher rates of apoptosis were found in NPCs cultured in CM microPH, which resulted in a lower cell density (Fig. 9*H*). Importantly, the majority (57%) of cell death-related upregulated heterologous genes were anti-apoptotic (Table 6), suggesting that the phagocytic microglia secretome did not directly induce NPCs apoptosis. Together, the above results (Fig. 9) results indicate that naive microglia led to the production of stellate cells, resembling astrocytes in culture, and a small proportion of ramified DCX$^+$-expressing cells, corresponding to an immature stage of the neuronal lineage. In contrast, phagocytic microglia drove NPCs toward a unique bipolar cell type, expressing nestin and GFAP but never DCX, which is characteristic of both astrocytes and undifferentiated progenitor cells (Encinas and Sierra, 2012).

The secretome from phagocytic microglia drives neuroprogenitor cells toward an astrocytic phenotype *in vitro*

To precisely identify bipolar cells produced by CM microPH, we performed several studies to characterize their phenotype: labeling with the mature astrocytic marker (S100β; Raponi et al., 2007), a multipotency assay, response to stimuli by calcium imaging, and Western blot analysis of neural and astrocyte-committed transcription factors.

First, we tested whether bipolar cells could be mature astrocytes and stained the CM-treated cultures with S100β, a marker of mature astrocytes (Raponi et al., 2007; Fig. 10*A*). In CM microC few stellate cells were S100β^+ and exhibited rather dim labeling, suggesting that they were still immature astrocytes (Fig. 10*B*,*C*). In addition, in CM microC cultures, we observed a small percentage of cells that did not express GFAP, expressed high levels of S100β and had several branched processes, that may possibly be oligodendrocytes (Hachem et al., 2005). On the other hand, in CM microPH cultures the majority of both bipolar and stellate cells had a very dim S100β staining and oligodendrocyte-like cells were not found. Therefore, the faint S100β expression in bipolar cells triggered by conditioned media from phagocytic microglia suggested that they could be immature astrocytes.

Second, we analyzed the multipotency of bipolar cells. After 3 d of differentiation into stellate, ramified, and bipolar cells in CM microC and microPH, we switched the culture media to DMEM/F12 culture media (the regular media to grow neurospheres) without trophic factors and allowed cells to differentiate for another 5–9 d (Fig. 10*D*–*G*). We found that after 5–9 d in DMEM/F12, cells derived from microPH CM had lower rates of cell death than cultures derived from microC and DMEM treatments, calculated as a ratio over the number of cells at 3 d in each culture (Fig. 10*F*). We then analyzed the multipotency of the cultures by calculating the ratio of change of each cell type after DMEM/F12. CM microC-derived cultures presented similar ratios of stellate cells and ramified cells after 5–9 d in DMEM/F12 (Fig. 10*G*). In contrast, cultures derived from microPH CM had a strong increase in the ratio of differentiation into stellate cells while neuroblasts were not found (Fig. 10*G*). These data strongly suggest that bipolar cells produced after treatment with the phagocytic microglia secretome were unlikely to be prototypical neuroprogenitors because they only gave rise to astrocytes but not to neuron-committed cells.

Third, we used calcium responses to different cell-specific stimuli to characterize bipolar cells triggered by microPH medium. We used Fura-2 AM, a cell permeant calcium indicator: KCl, which triggers an intracellular Ca^{+2} response in excitable cells (De Melo Reis et al., 2011); AMPA, which depolarizes neurons expressing the corresponding glutamate receptors (Bloodgood and Sabatini, 2008); ATP, which activates purinergic receptors in astrocytes and neurons (De Melo Reis et al., 2011); histamine, which triggers intracellular Ca^{+2} response in immature cells through histamine receptor, highly expressed on immature/stem cells and embryonic stem cells (Eiriz et al., 2011); and NMDA (Fig. 11*A*–*D*). We examined the calcium response to these stimuli of bipolar and stellate cells, as well as freshly dissociated NPCs as control. We found that 69% of the freshly dissociated NPCs depolarized in response to ATP and histamine, and became hyperpolarized in response to KCl. The majority of stellate cells depolarized in response to KCl, AMPA, and ATP, and the majority of ramified cells responded to all stimuli except NMDA, most likely because they were still immature neuroblasts. On the other hand, in CM microPH-treated cultures, the majority of bipolar cells highly depolarized when incubated with ATP and hyperpolarized when incubated with KCl (Fig. 11*C*,*D*). These data show that bipolar cells have similar features as both NPCs and astrocytes, suggesting an intermediate phenotype.

Finally, we performed Western blot analysis of NPCs as well as CM microC and CM microPH cultures of different fate-committing transcription factors: REST (RE1 silencing transcription factor 1), a repressor of neuronal genes that is highly expressed in astrocytes (Kohyama et al., 2010); Ascl (ASC1-like protein), which is related to neuronal fate commitment (Liu et al., 2015); and SMAD1, which is highly phosphorylated in differentiating astrocytes (Kohyama et al., 2010). In the CM-treated NPC cultures, we found no differences for REST and Ascl, but the pSMAD/SMAD ratio was significantly increased in CM microPH-treated cells compared to CM microC (Fig. 11*E*,*F*), suggesting that CM microPH bipolar cells were committed to the astrocytic lineage. All together, these *in vitro* data demonstrate that at the cellular level, the microglial phagocytosis secretome

←

(*Figure legend continued.*) and proliferation was labeled with BrdU (yellow). ***K***, Newborn cells (BrdU$^+$) and newborn neurons (NeuN$^+$, BrdU$^+$) in MerTK iKO mice at 4 weeks post-BrdU. ***L***, BrdU+ yield was calculated as a ratio of the BrdU$^+$ cells at 4 weeks over the average BrdU$^+$ cells of each group at 1 d after injection. Scale bars: ***C***, ***D***, ***G***, ***J***, 50 μm (insets, 10 μm); ***C***, ***D***, $z = 16.1$ μm; ***G***, $z = 7$ mm; ***J***, $z = 23.1$ μm. $N = 3$ mice (***E***, ***H***, ***I***), $N = 4-6$ mice (***F***, ***K***, ***L***). Error bars represent mean ± SEM. #$p = 0.096$ (***E***), #$p = 0.062$ (***F***), *$p < 0.05$, **$p < 0.01$, ***$p < 0.001$ by Student's *t* test. Only significant effects are shown. Values of statistics used are shown in Table 3.

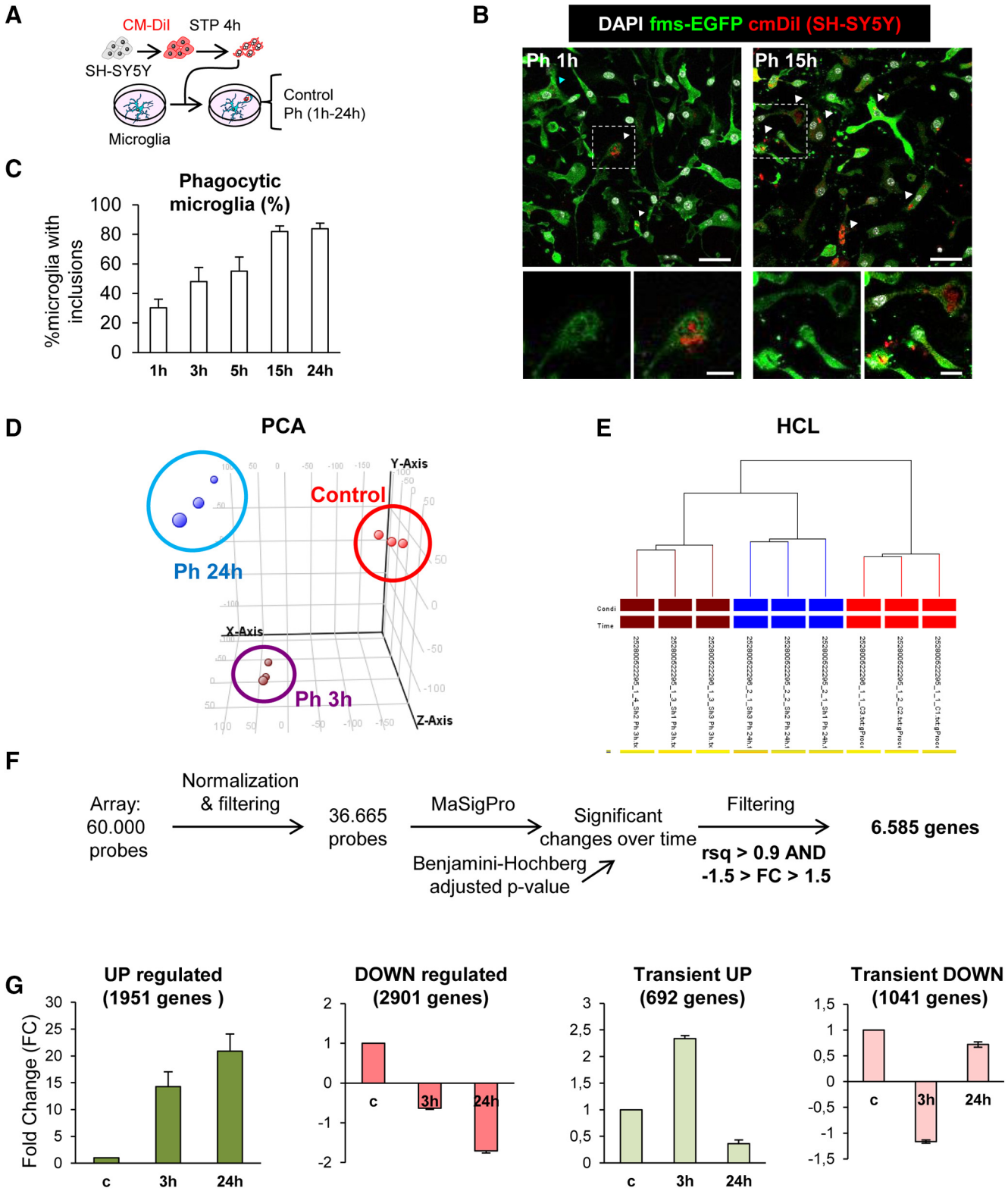

Figure 4. Phagocytosis assay with a human neural cell line (SH-SY5Y). ***A***, Experimental design of the phagocytosis assay. ***B***, Representative confocal microscopy images of primary microglia (GFP; green) fed with SH-SY5Y, which were previously labeled with CM-DiI (red) and treated with STP (4 h, 3 μM) for the induction of apoptosis (pyknosis/karyorrhexis; DAPI, white). Arrowheads, phagocytosed apoptotic SH-SY5Y cells. ***C***, Percentage of microglia with CM-DiI and/or DAPI inclusions along a time course. Only fully closed pouches with particles within were identified as phagocytosis. ***D***, PCA of the different replica of the samples: Control microglia, Ph3h, and Ph24h. ***E***, Hierarchical clustering (HCL) of the different replica of the samples control microglia (blue), Ph3h (brown), and Ph24h (red). ***F***, Representation of the strategy followed to screen genes from the gene array. ***G***, FC mean of the genes classified under the UP, DOWN, transient UP, and transient DOWN regulation patterns. Scale bars: ***B***, 30 μm (inserts, 10 μm). $N = 3$ independent experiments (***C***–***G***).

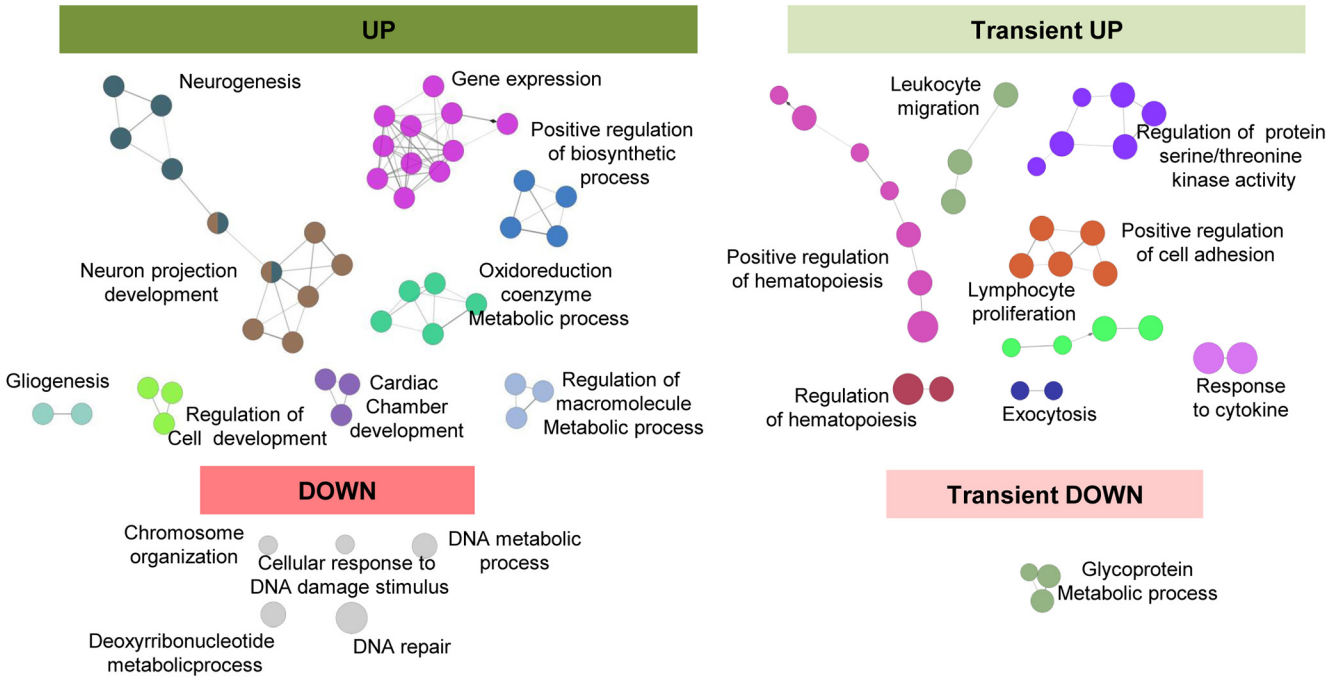

Figure 5. Functional analysis of phagocytic microglia using ClueGO. Charts show the interactions among the significantly different functions for the four main expression patterns. Biological functions are visualized as colored nodes linked to related groups based on their κ score level. The node size reflects the enrichment significance of the term and functionally related groups are linked. Non-grouped terms are shown in gray.

promotes the inhibition of neural-committed cells and resulted in the differentiation of NPCs into astrocytes.

Cytokines are unlikely to drive the bipolar phenotype triggered by phagocytic microglia conditioned media

We next focused on characterizing the nature of the phagocytosis secretome. As observed in the arrays (Figs. 7, 8), phagocytic microglia expressed the mRNA of several cytokines, such as Csf3, IL-1β, IL-6, TNF-α, or TGF-β among others. In addition to phagocytosis, these molecules are also released by microglia upon inflammatory stimuli and some have already been reported to impair neurogenesis (Ekdahl et al., 2003; Monje et al., 2003). To directly compare cytokine expression induced by phagocytosis and by a classical inflammatory stimulus such as LPSs (bacterial lipopolysaccharides) we treated NPCs with the CM of primary microglia that had been pretreated with LPSs (1 μg/ml; Monje et al., 2003) for 6 h to trigger the inflammatory response, and then changed to fresh media for another 18 h to ensure that the CM would not contain any leftover LPSs (Fig. 12*A*). We found that NPC cultures treated with LPSs or CM microLPS produced a majority of stellate cells and a small proportion of ramified cells, although there were no differences between the two treatments in terms of cell-type proportion and numbers (Fig. 12*B*,*C*). CM microLPS treatments did not trigger bipolar cells, strongly suggesting that cytokines were unrelated to the effect of the phagocytosis secretome on NPCs.

Unexpectedly, neither LPSs nor CM microLPS reduced the number of neuroblasts compared to CM microC (Fig. 12*B*,*C*). These were surprising results because proinflammatory cytokines are well documented to exert detrimental consequences for neurogenesis (Ekdahl et al., 2003; Monje et al., 2003). To disregard that this discrepancy resulted from different LPS concentration or exposure time compared with prior publications, we performed a series of LPS-based experiments in which we used first, a lower LPS dosage (150 ng/ml for 18 h; Fraser et al., 2010) that produced a very similar cytokine expression as phagocytosis in microglia (Fig. 12*D*–*F*); second, the exact LPS dosage and time (1 μg/ml, 24 h) described by Monje et al. (2003), where they found a reduction in DCX^+ cells after CM microLPS treatment (Fig. 12*G*,*H*); and third, the paradigm described by Monje et al. (2003), who used the BV2 cell line instead of primary microglia (Fig. 12*I*,*J*), although they used hippocampal NPC cultures derived from adult rats. None of the LPS or CM LPS treatments gave rise to bipolar cells, strongly suggesting that cytokines are highly unlikely to drive the bipolar phenotype triggered by the phagocytic microglia secretome.

The phagocytosis secretome reduces neuronal differentiation

We next characterized the effect of the CMs at later stages of neurogenesis using a late survival/differentiation assay in which NPCs were allowed to differentiate for 10 d into neuroblasts and astrocytes using DMEM/F12 without trophic factors. At this stage ($t = 0$), the cultures exhibited a high percentage of cell death (65.8 ± 2.4%) and the majority of the cells had a stellate morphology. These differentiated cultures were then treated for 3 and 5 d with CM microC and microPH as well as DMEM for positive control (Fig. 13*A*,*B*). Importantly, treatment with microPH did not result in higher levels of apoptosis than microC or DMEM (Fig. 13*B*). Cultures treated with CM microC presented a vast majority of stellate cells and few ramified cells. In contrast, CM microPH-treated cultures showed no DCX^+ cells, a small percentage of stellate cells and a majority of stellate cells with a more mature morphology (more complex ramifications; Fig. 13*C*,*D*). Nonetheless, the gene array data did not support a direct induction of astrogenesis. The functions "gliogenesis" and "glial cell differentiation" were significantly upregulated in the ClueGo analysis (Fig. 5), but the majority of the genes found under those categories were autologous, and therefore, their overexpression would only modulate the microglial cells expressing them. As the astrocytic lineage is the default differentiation mode of neural

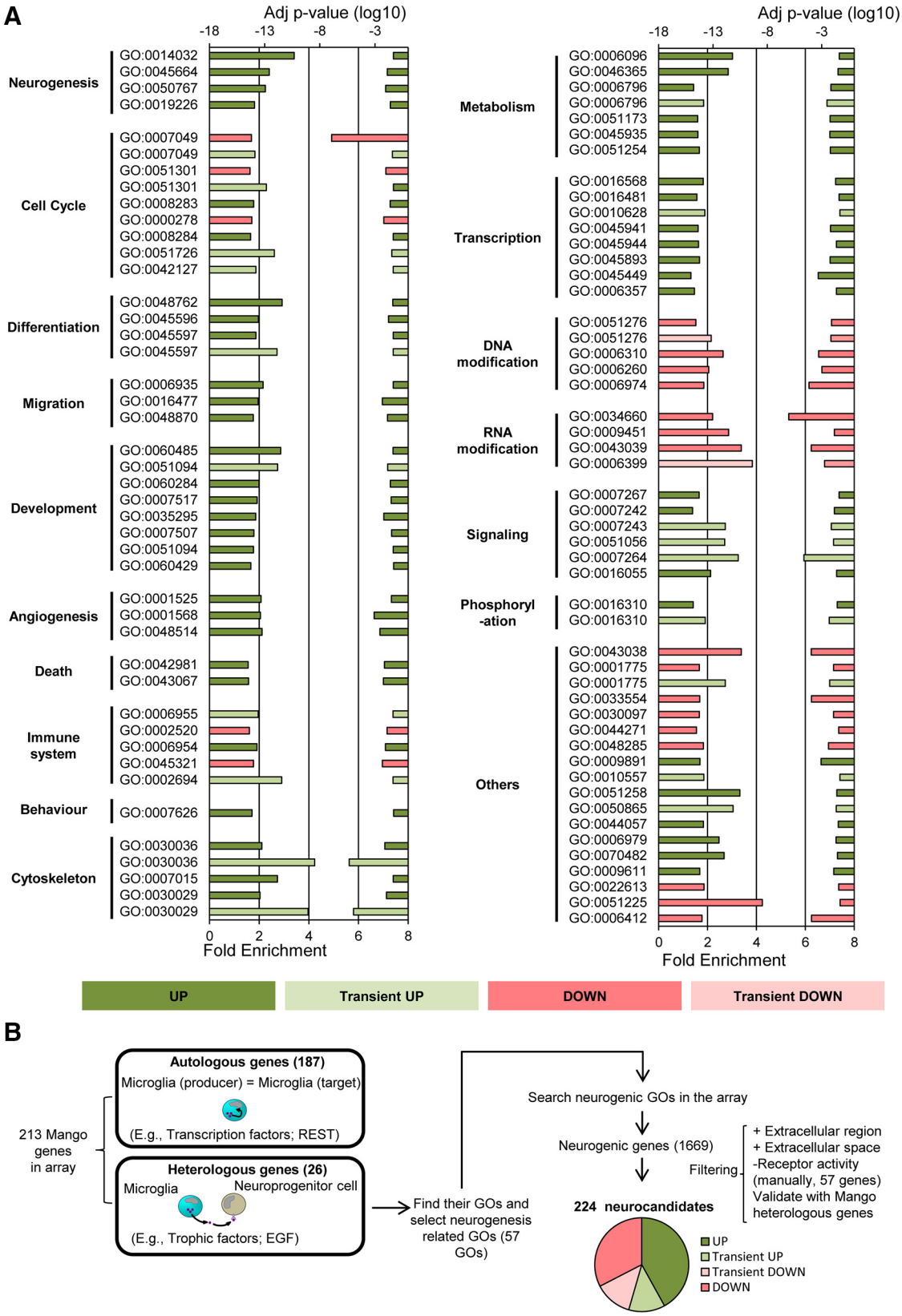

Figure 6. Functional analysis of phagocytic microglia using DAVID and MANGO. ***A***, Functional analysis of phagocytic microglia using DAVID software. Left axis represents the fold enrichment of each biological function and right axis represents the adjusted *p* value of each GO term. Key for the GO terms: GO:0014032, neural crest cell development; GO:0045664, regulation of neuron differentiation; GO:0050767, regulation of neurogenesis; GO:0019226, transmission of nerve impulse; GO:0007049, cell cycle; GO:0051301, cell division; GO:0008283, cell proliferation; GO:0000278, mitotic cell cycle; GO:0008284, positive regulation of cell proliferation; GO:0051726, regulation of cell cycle; GO:0042127, regulation of cell proliferation; GO:0048762, mesenchymal cell differentiation; GO:0045596, negative regulation of cell differentiation; GO:0045597, positive regulation of cell differentiation; GO:0006935, chemotaxis; GO:0016477, cell migration; GO:0048870, cell motility; GO:0060485, mesenchyme development; GO:0051094, positive regulation of developmental process; GO:0060284, regulation of cell development; GO:0007517, muscle organ development; GO:0035295, tube development; GO:0007507, heart development; GO:0051094, positive regulation of developmental process; GO:0060429, epithelium (*Figure legend continues.*)

stem cells (Bonaguidi et al., 2011; Encinas et al., 2011), these data suggest that the phagocytosis secretome inhibited neuronal differentiation, indirectly promoting astrocyte differentiation.

Neurogenic modulatory factors secreted by phagocytic microglia *in vitro* alter neurogenesis *in vivo*

To then confirm the neurogenic modulatory role of the phagocytosis secretome on adult hippocampal neurogenesis *in vivo*, we injected CM microC and microPH into the hippocampus of 2-month-old fms-EGFP mice for 6 d using osmotic minipumps. After this period, BrdU was administered to track proliferating cells and mice were killed 2 h later (Fig. 14*A*).

We observed no differences in the density of total $BrdU^+$ proliferative cells in CM microPH treated mice compared to CM microC treatment (Fig. 14*B*,*C*). Importantly, CM microPH did not induce apoptosis *in vivo* (Fig. 14*D*). In addition, there was a trend toward decreased density of proliferating $BrdU^+$ rNSCs in mice treated with CM microPH compared to CM microC ($p = 0.0649$; Fig. 14*E*–*G*). Moreover, the density of DCX^+ neuroblasts, the proportion of the different neuroblast subpopulations (AB, CD, and EF), and neuroblast proliferation did not differ between CM microC and microPH (Fig. 14*H*–*J*).

Because we observed a declining trend for rNSCs in the presence of CM microPH after 6 d, we hypothesized that the induced alterations would accumulate over time. Therefore, we performed a long-term experiment in which mice were treated with CM microC and microPH through osmotic minipumps for 6 d, followed by BrdU administration, and killed 28 d later to allow differentiation of the labeled cells (Fig. 14*K*). The density of $BrdU^+$ cells in mice treated with CM microPH showed a significant decrease compared to CM microC (Fig. 14*L*,*M*). Importantly, CM microPH did not induce apoptosis *in vivo* (Fig. 14*N*). We then quantified neuroblasts and newborn neurons ($NeuN^+$, $BrdU^+$; Fig. 14*O*–*S*). In all experiments in Figure 14, because the conditioned media diffused over the 6 d infusion period, we found a stronger effect closer to the injection site (Fig. 14*P*). Thus, for this set of experiments, only the three tissue slices of the sectioning series most proximal to the injection site were quantified. We found a significant reduction in the intermediate (CD) and most mature (EF) neuroblast subpopulations in mice treated with CM microPH compared to CM microC (Fig. 14*R*). Finally, the density of newborn neurons was also reduced in CM microPH compared to CM microC (Fig. 14*S*). In summary, we found a trend toward fewer proliferative stem cells at 2 h after BrdU, and reduced number of mature neuroblasts and newborn neurons after 28 d, suggesting that the acute (24 h) phagocytic microglia secretome limits neurogenesis via the reduction in the production of neuronal-committed cells.

Discussion

In this paper, we provide evidence that microglia modulate adult hippocampal neurogenesis through the secretome associated with phagocytosis of apoptotic newborn cells, based on the following major findings. First, adult hippocampal neurogenesis was reduced in two KO models with chronic microglial phagocytosis impairment. Second, neurogenesis was transiently increased in an acute model of phagocytosis impairment. Third, transcriptomic analysis *in vitro* revealed that phagocytosis triggered an expression change in a panoply of neurogenesis-related genes in microglia, strongly suggesting a coordinated neurogenic modulatory program that encompasses up to 224 heterologous genes previously shown to modulate neurogenesis, including peptides, trophic factors, matrix metalloproteases, and cytokines. Fourth, the secretome of phagocytic microglia drove NPCs differentiation toward a bipolar phenotype of astrocytic lineage *in vitro*, characterized by high expression of astrocytic markers such as nestin, GFAP and S100β; calcium responses to ATP and other stimuli; and high levels of phosphorylation of SMAD. Finally, the secretome of phagocytic microglia reduced the most mature neuroblast subpopulation at 28 d *in vivo*. Hence, we present evidence that microglial phagocytosis is a pivotal mechanism for the maintenance of homeostasis in the adult neurogenic cascade.

Microglia control the long-term homeostasis of the adult hippocampal neurogenic cascade

The accurate homeostasis of stem cell niches is crucial for their long-term maintenance, as disruption of the equilibrium between quiescence and proliferation leads to early exhaustion (Santos et al., 2018). In the adult hippocampal neurogenic niche, the mechanisms described to maintain homeostasis rely on the quiescence of rNSCs (Encinas et al., 2011), a feature that prevents an early exhaustion of the niche (Sierra et al., 2015). Herein we focus on the unexplored role of resident immune cells, microglia, which engulf newborn cells that undergo apoptosis (Sierra et al., 2010). Immune cells are increasingly recognized to participate in stem cell niches, and macrophages have been recently

←

(*Figure legend continued.*) development; GO:0001525, angiogenesis; GO:0001568, blood vessel development; GO:0048514, blood vessel morphogenesis; GO:0042981, regulation of apoptosis; GO:0043067, regulation of programmed cell death; GO:0006955, immune response; GO:0002520, immune system development; GO:0006954, inflammatory response; GO:0045321, leukocyte activation; GO:0002694, regulation of leukocyte activation; GO:0007626, locomotory behavior; GO:0030036, actin cytoskeleton organization; GO:0007015, actin filament organization; GO:0030029, actin filament-based process; GO:0006096, glycolysis; GO:0046365, monosaccharide catabolic process; GO:0006796, phosphate metabolic process; GO:0006796, phosphate metabolic process; GO:0051173, positive regulation of nitrogen compound metabolic process; GO:0045935, positive regulation of nucleobase, nucleoside, nucleotide and nucleic acid metabolic process; GO:0051254, positive regulation of RNA metabolic process; GO:0016568, chromatin modification; GO:0016481, negative regulation of transcription; GO:0010628, positive regulation of gene expression; GO:0045941, positive regulation of transcription; GO:0045944, positive regulation of transcription from RNA polymerase II promoter; GO:0045893, positive regulation of transcription, DNA-dependent; GO:0045449, regulation of transcription; GO:0006357, regulation of transcription from RNA polymerase II promoter; GO:0051276, chromosome organization; GO:0006310, DNA recombination; GO:0006260, DNA replication; GO:0006974, response to DNA damage stimulus; GO:0034660, ncRNA metabolic process; GO:0009451, RNA modification; GO:0043039, tRNA aminoacylation; GO:0006399 tRNA metabolic process; GO:0007267, cell–cell signaling; GO:0007242, intracellular signaling cascade; GO:0007243, protein kinase cascade; GO:0051056, regulation of small GTPase-mediated signal transduction; GO:0007264, small GTPase-mediated signal transduction; GO:0016055, Wnt receptor signaling pathway; GO:0016310, phosphorylation; GO:0043038, amino acid activation; GO:0001775, cell activation; GO:0033554, cellular response to stress; GO:0030097, hemopoiesis; GO:0044271, nitrogen compound biosynthetic process; GO:0048285, organelle fission; GO:0009891, positive regulation of biosynthetic process; GO:0010557, positive regulation of macromolecule biosynthetic process; GO:0051258, protein polymerization; GO:0050865, regulation of cell activation; GO:0044057, regulation of system process; GO:0006979, response to oxidative stress; GO:0070482, response to oxygen levels; GO:0009611, response to wounding; GO:0022613, ribonucleoprotein complex biogenesis; GO:0051225, spindle assembly; GO:0006412, translation. Left axis represents the fold enrichment of each biological function and right axis represents the adjusted *p* value of each GO term. Only statistically significant changes are shown. ***B***, Diagram depicting the strategy followed to search for potential modulators of neurogenesis produced by phagocytic microglia in the arrays. The filtering started by differentiating the heterologous and autologous genes in the MANGO database. Then, GO terms related to neurogenesis were selected for the heterologous MANGO genes. Afterward, the molecules that presented the neurogenic GO terms were searched in the array. Finally, the candidate genes were filtered only to select those that appeared extracellularly (heterologous genes), and genes with receptor activity were manually discarded.

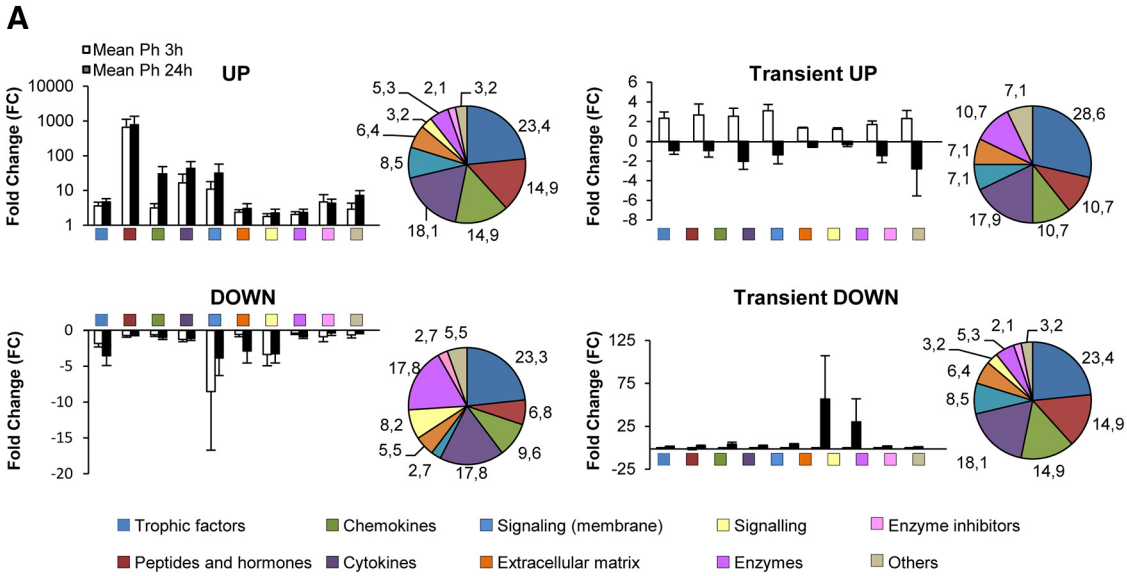

B

Trophic factors (51genes)

Gene Symbol	FC Ph3h	FC Ph24h
Prl3c1	7,7	25,3
Ereg	5,4	16,0
Areg	22,6	5,9
Inha	1,0	5,6
Artn	1,0	5,1
Bmp1	4,7	5,0
Fgf23	3,8	4,4
Nrtn	2,5	3,7
Fgf2	4,2	3,7
Prl2a1	1,0	3,6
Ins1	1,9	2,6
Vegfa	6,0	2,6
Ins2	1,8	2,5
Inhba	2,3	2,3
Prl3d1	1,7	2,3
Fgf14	3,4	2,2
Cntf	1,5	2,2
Gal	1,2	1,9
Fgf8	1,8	1,7
Flt3l	1,0	1,5
Fbrs	1,3	1,2
Fgf18	1,3	1,2
Gdf15	1,5	-1,1
Tgfb1	1,3	-1,1
Nenf	1,1	-1,2
Hbegf	6,1	-1,2
Pdgfa	1,5	-2,2
Tgfb3	3,9	-2,2
Pdgfb	1,7	-2,3
Cyr61	1,8	-4,3
Nrg4	-1,2	2,2
Nodal	-1,2	1,7
Lefty2	-1,8	1,4
Gpi1	-1,3	1,2
Hdgf	-1,3	-1,1
Prl3a1	-3,3	-1,2
Gdf9	-2,2	-1,3
Vegfb	-1,8	-1,3
Pdgfc	-1,9	-1,4
Egfl7	-2,6	-1,7
Grn	-1,4	-1,7
Fgf9	-2,5	-2,3
Lefty1	-1,2	-2,6
Bmp2	-1,1	-2,7
Cdnf	-3,5	-3,5
Nov	-2,7	-4,6
Grem1	-3,8	-4,7
Igf1	-1,4	-5,5
Gdf3	-2,5	-7,3
Vegfc	-4,7	-9,3
Ctgf	-10,0	-24,7

Peptides & Hormones (26 genes)

Gene Symbol	FC Ph3h	FC Ph24h
Vgf	5968,2	7966,9
Scg2	2931,9	2685,4
Amh	372,1	276,4
Cartpt	19,3	34,0
Nmb	9,9	19,0
Edn2	4,0	7,6
Npy	1,1	5,3
Sct	2,3	3,9
Retn	4,1	3,8
Fndc5	8,6	3,5
Cort	2,1	3,3
Nts	1,3	2,3
Npff	1,7	1,5
Rln3	1,6	1,4
Calca	2,0	-1,0
Gnrh1	4,9	-1,6
Prok2	1,2	-3,2
Adm	-1,8	4,7
Gcg	-1,1	1,5
Stc2	-5,3	1,5
Nppa	-1,2	1,0
Pomc	-1,8	-1,2
Insl6	-2,3	-1,4
Edn1	-2,2	-1,6
Hgf	-1,0	-1,7
Gnl3	-1,2	-2,1

Chemokines (30 genes)

Gene Symbol	FC Ph3h	FC Ph24h
Cxcl3	6,2	250,1
Cxcl1	14,5	104,9
Cxcl2	8,8	37,5
Ccl5	1,3	5,8
Pf4	1,2	4,5
Ccl6	1,1	3,8
Ccl9	2,0	3,3
Ppbp	1,2	3,1
Cxcl11	1,9	2,0
Ccl2	1,1	1,8
Ccl25	1,1	1,4
Cmtm3	1,0	1,2
Ybx1	1,3	1,1
Ccl7	1,3	1,1
Ccl12	2,0	-1,4
Cxcl10	4,1	-3,6
Cx3cl1	1,5	-4,1
Cxcl5	-1,2	16,6
Ccl3	-3,3	1,8
Cmtm4	-1,7	1,5
Cmtm7	-1,2	1,5
Cklf	-1,1	1,3
Cmtm2a	-1,2	1,2
Ccl4	-1,4	-1,1
Cmtm8	-1,8	-1,3
Ccl8	-1,2	-1,7
Ccl27a	-2,1	-1,9
Cxcl14	-1,0	-2,2
Cxcl12	-2,7	-2,6
Cmtm5	-1,1	-3,1

Cytokines (39 genes)

Gene Symbol	FC Ph3h	FC Ph24h
Csf3	10,1	344,2
Ptn	223,9	255,1
Il1f6	2,5	64,2
Il1b	8,9	30,8
Il6	1,2	18,7
Il1a	2,1	6,0
Osm	8,1	3,0
Lif	3,2	2,9
Il19	2,8	2,7
Tnfsf13b	1,1	2,7
Clcf1	3,5	2,2
Il27	1,4	1,6
Mdk	1,2	1,6
C3	1,3	1,6
Il24	1,9	1,4
Il1rn	5,4	1,3
Il18	1,6	1,2
Ebi3	1,6	-1,2
Ifnb1	3,5	-1,3
Ltb	3,4	-1,7
Tnfsf14	5,1	-1,7
Il10	2,1	-6,0
Il1f9	-2,5	3,8
Tnfsf9	-1,7	2,5
Nampt	-1,3	2,0
Mif	-2,2	1,0
Tnf	-1,9	-1,0
Il15	-1,6	-1,1
Twsg1	-1,2	-1,5
Aimp1	-1,2	-1,6
Lta	-1,8	-1,6
Metrn	-1,2	-1,8
Kitl	-2,9	-2,0
Ctf1	-3,1	-2,0
Il16	-2,2	-2,0
Il4	-2,4	-2,1
Tnfsf15	-3,2	-2,7
Csf1	-1,3	-2,9
Tnfsf10	-5,3	-5,2

Enzymes (23 genes)

Gene Symbol	FC Ph3h	FC Ph24h
Lipg	1,7	3,8
Aldh3a1	1,1	3,7
Enpp2	2,8	1,5
Ihh	3,1	1,4
Furin	1,3	1,3
Alox5	2,1	-1,6
Zcchc11	1,0	-1,9
Plau	2,1	-3,9
Prdx1	-1,2	2,1
Pla2g7	-2,1	1,5
Ppt1	-1,1	-1,0
Uspl1	-1,1	-1,0
Entpd5	-3,2	-1,2
Arsa	-1,2	-1,2
Casp1	-1,1	-1,4
Utp11l	-1,1	-1,5
Ctsh	-1,4	-1,5
Ang	-1,3	-1,9
Cela1	-1,4	-2,1
Pycard	-1,2	-2,2
Ang4	-1,4	-2,8
Htra1	-1,2	-3,2
Ang3	-1,4	-3,6

Signaling molecules (12 genes)

Gene Symbol	FC Ph3h	FC Ph24h
Wnt1	2,5	3,5
S100a13	1,5	1,7
Lgals3	1,3	1,5
S100a8	-1,0	83,7
S100a9	-1,2	6,0
Hmgb2	-1,2	1,0
Agrp	-7,5	-1,0
Tulp3	-1,9	-1,3
Angpt2	-1,9	-2,3
S100b	-1,9	-5,9
Angptl3	-2,3	-6,4
Angptl6	-10,7	-8,7

Others (9 genes)

Gene Symbol	FC Ph3h	FC Ph24h
Dmkn	1,2	11,3
Hilpda	5,8	8,0
Hrg	1,6	2,2
Pecam1	1,5	-1,0
Uts2b	3,1	-6,6
Copa	-1,2	-1,5
Atxn10	-1,2	-1,5
Aggf1	-1,3	-1,2
Ngrn	-2,9	-1,5

Extracellular Matrix (15 genes)

Gene Symbol	FC Ph3h	FC Ph24h
Thbs1	2,8	8,3
Lamc1	2,1	3,0
Lamb2	1,7	2,6
Mmp9	4,2	2,1
Nog	1,6	1,2
Tnfaip6	2,0	1,0
Adam17	1,4	-1,1
Sepp1	1,1	-1,5
Mmp3	-1,0	157,9
Mmp10	-1,6	10,8
Ecm1	-1,1	1,4
Lepre1	-2,5	-1,6
Spp1	-1,2	-2,4
Gas6	-1,4	-2,5
Mgp	-1,2	-8,9

Membrane-bound Signaling molecules (13 genes)

Gene Symbol	FC Ph3h	FC Ph24h
Dll4	61,3	215,9
Sema3b	8,1	8,9
Cd70	2,8	8,4
Sema3f	4,8	7,5
Sema3a	3,1	4,7
Jag1	3,3	2,7
Sdc1	1,5	2,0
Dll3	1,6	1,7
B4galt1	1,3	-1,6
Anxa1	1,4	-1,6
Sema3c	-1,4	4,6
Sema4d	-1,3	-2,4
Efna1	-17,7	-7,3

Enzymes inhibitors (6 genes)

Gene Symbol	FC Ph3h	FC Ph24h
Camp	1,8	5,5
Serpinf2	7,5	3,0
Serpine1	-1,8	1,2
Timp2	-1,3	1,1
Cst3	-1,2	-1,0
Spink2	-2,6	-1,7

FC < 2	FC < -2
FC 2-4	FC -2-4
FC > 4	FC > -4

Figure 7. Phagocytosis-related candidates include trophic factors and peptides and hormones. ***A***, Classification of the 224 potential modulators of neurogenesis. "Trophic factor" was the category with the highest percentage of genes in every regulatory pattern, however, the category "Peptides and hormones" included genes with the highest FC changes in the UP regulation pattern. ***B***, The 224 candidates classified by their identity and FC.

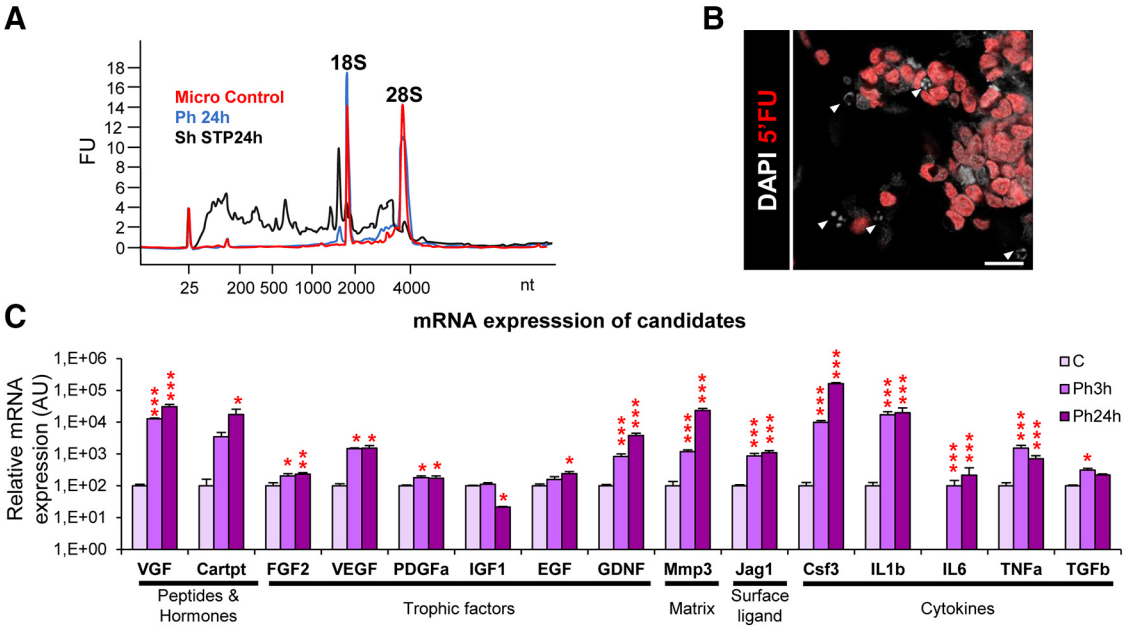

Figure 8. Validation of transcriptional changes induced by phagocytosis. ***A***, Electropherogram obtained by a bioanalyzer comparing the RNA profile (nt, nucleotides) of control and phagocytic microglia as well as apoptotic SH-SY5Y (treated with 3 μM STP for 24 h). ***B***, Representative confocal images of FU $^+$ active transcription sites of SH-SY5Y cells treated with STP (3 μM, 4 h) for apoptosis induction. Nuclei were labeled with DAPI (white), cell death was detected by pyknosis/karyorrhexis (white, DAPI; arrowheads), and transcription sites were detected by FU (red). ***C***, mRNA expression levels of the candidates selected for validation by real-time qPCR. $N = 4$ independent experiments. HPRT was selected as a reference gene. Scale bar, 20 μm. $N = 4$ independent experiments (***F***). Error bars represent mean ± SEM. *$p < 0.05$, **$p < 0.01$, ***$p < 0.001$ by Holm–Sidak *post hoc* test of (after one-way ANOVA was significant at $p < 0.05$). Only significant effects are shown. Values of statistics used are shown in Table 4.

shown to promote erythroblast production in the bone marrow (Chow et al., 2013), and to be required for ductal morphogenesis in the mammary gland (Chakrabarti et al., 2018). We found that chronic disruption of microglial phagocytosis impairs neurogenesis using two constitutive KO mice models for receptors P2Y12, and MerTK/Axl, which participate in different stages of phagocytosis (Scott et al., 2001; Elliott et al., 2009). Nonetheless, it is important to note that these receptors regulate multiple features of microglial physiology, and that MerTK and Axl are also expressed in peripheral macrophages (Rothlin and Lemke, 2010). In addition, microglial phagocytosis impairment leads to the accumulation of non-removed apoptotic cells, which may also affect neurogenesis directly through the release of toxic intracellular contents. However, the similar reduction in adult neurogenesis in the two models strongly supports the key role of microglial phagocytosis.

In contrast to the effect of constitutive phagocytosis impairment, acute phagocytosis impairment by inducible depletion of MerTK resulted in a transient increase in early neuroblasts that was compensated at later time points. Several effects may explain the differences between the constitutive MerTK/Axl KO and the inducible MerTK KO mice (i.e., double KO vs single KO; body-wide in all TAM-expressing cells vs microglial-specific; and knock out from embryonic development vs only in selected cells in the adult). Nonetheless, the transient increase in early neuroblasts after acute impairment of phagocytosis in the iKO MerTK model, together with the chronic reduction of neurogenesis in the P2Y12 and MertK/Axl constitutive KO models, and the reduction in neurogenesis in mice treated with the phagocytic microglia conditioned media, suggest that the microglial phagocytosis of newborn cells participates in a feedback loop that maintains the homeostasis of adult hippocampal neurogenesis (Fig. 15).

Microglia regulates neurogenesis through the phagocytosis secretome

We found that phagocytosis of apoptotic cells induced a neurogenic modulatory phenotype in microglia that was mostly related to their secretome, as the majority of the modulatory genes encoded secreted proteins, including neuropeptides such as VGF, and growth factors such as VEGF and FGF2, some of which have already been described to participate in the microglial regulation of neurogenesis (Kreisel et al., 2019). In addition, the microglial secretome may contain metabolites, miRNAs and extracellular vesicles, which may also alter neurogenesis (Rodríguez-Iglesias et al., 2019). When administered *in vivo*, the acute secretome of phagocytic microglia inhibited hippocampal neurogenesis, as it had an early tendency to decrease rNSCs proliferation that was later followed by a reduction in mature neuroblasts. The effect was similar on isolated NPCs, as we found a decreased production of neuroblasts. However, this effect was unlikely related to an active promotion of apoptosis, which was not detected *in vivo*. In agreement, the *in vitro* transcriptomic analysis did not reveal significant increases in heterologous proapoptotic genes, and cell death was not observed in the late survival/differentiation assays. Nonetheless, many early NPCs did die upon culture with the early phagocytic microglia conditioned media, an effect that may be attributed to the lack of key survival factors, possibly metabolites consumed by phagocytic microglia. Apoptosis is common in these early cultures and has been linked to the stress associated with differentiation upon growth factor withdrawal (Babu et al., 2011). Overall, these results suggest that the secretome of phagocytic microglia modulates neurogenesis by acting not on the survival but on the differentiation of neural-committed cells.

The reduced neuronal differentiation induced by the secretome of phagocytic microglia was unlikely related to an enhance-

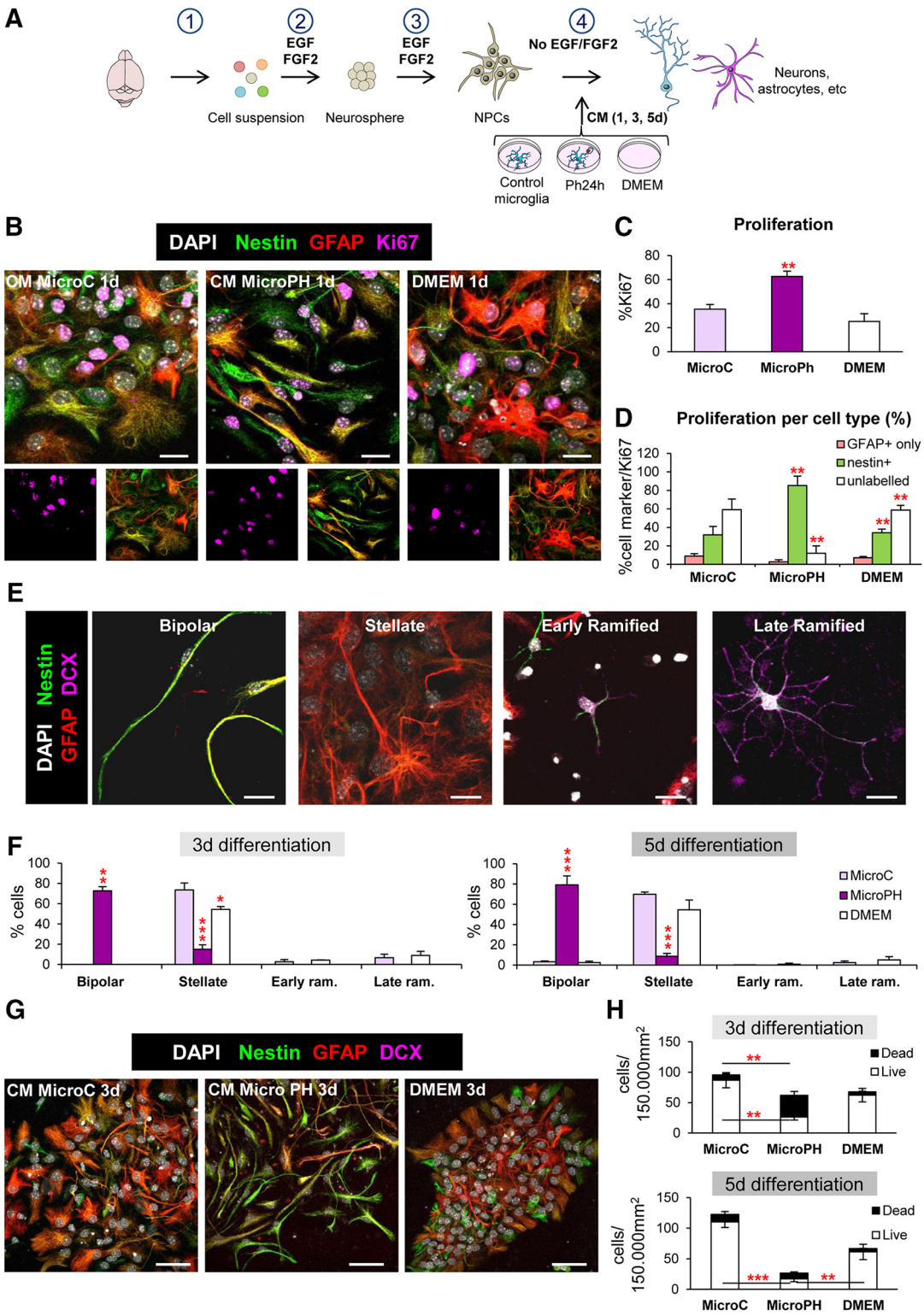

Figure 9. Effect of phagocytic microglia secreted factors on neurogenesis *in vitro*. ***A***, Experimental design of the *in vitro* neurogenesis assay: (1) brain disaggregation; (2) neurosphere proliferation; (3) dissociation, plating, and proliferation of NPCs for 48 h; (4) differentiation in the presence of conditioned media (CM) from control microglia (microC) or 24 h phagocytic microglia (microPh). ***B***, Representative confocal microscopy images of NPCs treated with CM microC or microPH after 1 d. DMEM was used as control. ***C***, Percentage of cells labeled with Ki67 over total cells labeled with DAPI. ***D***, Percentage of different cell markers over total Ki67 population: nestin$^+$ (with or without GFAP), GFAP only, or unlabeled. ***E***, Representative confocal microscopy images of the different morphologies observed in the neurogenesis assay images. ***F***, Percentage of the different cell types found after 3 and 5 d treatment with CM microC or microPH. Early/late ram refers to early/late ramified cells. ***G***, Representative confocal microscopy images of NPCs treated with CM microC or microPH after 3 d. ***H***, Density of live and dead cells (determined by pyknosis/karyorrhexis) after CM treatment for 3 and 5 d. Scale bars: ***B***, 50 μm; ***E***, 9 μm; ***B***, $z = 11.9$ μm; ***G***, $z = 20$ μm. $N = 3$ independent experiments (***C***, ***D***, ***F***, ***H***). Error bars represent mean $\pm$ SEM. Two-way ANOVA (treatment $\times$ cell types, ***D***) and three-way ANOVA (treatment $\times$ cell types $\times$ time, ***F***; and treatment $\times$ life $\times$ time, ***H***) showed interactions between the different factors and thus the data were split into several one-way ANOVAs. *$p < 0.05$, **$p < 0.01$, ***$p < 0.001$ by Holm–Sidak *post hoc* test versus MicroC group (after one-way ANOVA was significant at $p < 0.05$). Values of statistics used are shown in Table 5.

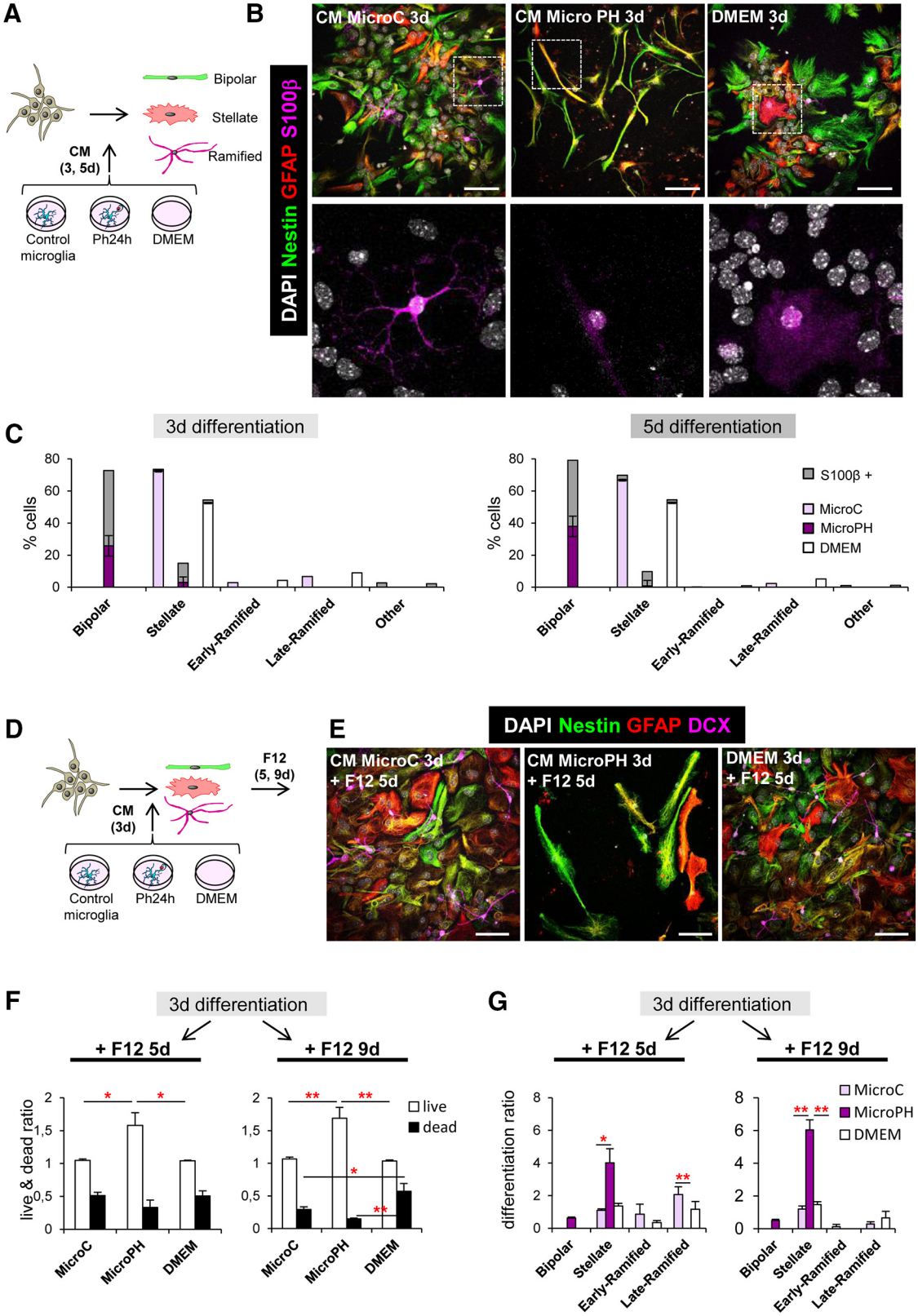

Figure 10. Characterization of CM cell types by S100β and multipotency assays. ***A***, Experimental design of the *in vitro* neurogenesis assay for S100β staining. ***B***, Representative confocal microscopy images of NPCs treated with CM microC or microPH. DMEM was used as control. ***C***, Percentage of expression of S100β in the different cell types found after 3 and 5 d treatment with CM microC or microPH. The category "Other" refers to cells with strong S100β expression, no GFAP and a ramified morphology suggest that they may be oligodendrocytes (Hachem et al., 2005). ***D***, Experimental design of the *in vitro* multipotency assay. ***E***, Representative confocal microscopy images of NPCs treated with CM microC, microPH or DMEM followed by 5 d of DMEM/F12. ***F***, Ratio of live/dead cell density over the cells at 3 d after each treatment. ***G***, Differentiation ratio of each phenotype after 3 d treatment with CM microC or microPH followed by 5 or 9 d DMEM/F12. Scale bars: ***B***, ***E***, 20 μm (inserts in ***B***, 10 μm); ***B***, ***F***, $z = 9$ μm. $N = 3$ independent experiments (***C***, ***F***, ***G***). Error bars represent mean $\pm$ SEM. *$p < 0.05$, **$p < 0.01$. Values of statistics used are shown in Table 7.

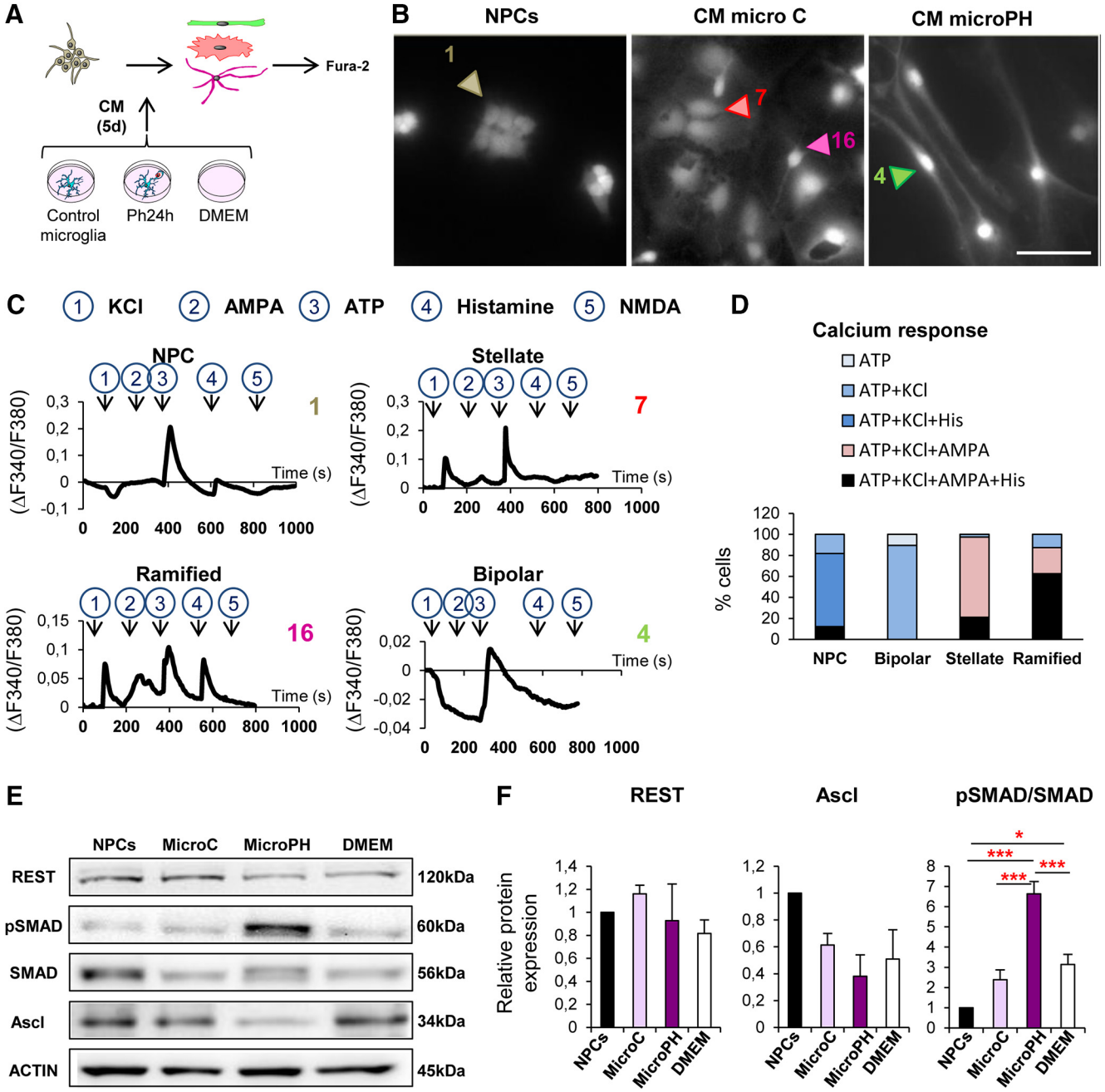

Figure 11. Characterization of CM cell types by calcium imaging and late survival/differentiation assays. ***A***, Experimental design of the *in vitro* calcium imaging assay. NPCs were treated with CM microC or microPH for 5 d and the resulting stellate, ramified and bipolar cells were incubated and loaded with Fura-2 AM and afterward, cells were challenged with KCl, AMPA, ATP, histamine, and NMDA to measure their Ca^{+2} response. ***B***, Representative epifluorescence microscopy images of neuroprogenitors treated with CM microC or microPH for 5 d. Freshly dissociated NPCs were used as control. ***C***, Calcium responses to consecutive stimuli (KCl, AMPA, ATP, histamine, NMDA) determined as a ratio of Fura2 fluorescence of cells shown in ***B***. ***D***, Percentage of cell phenotypes responding to each stimulus (38 stellate cells, 8 ramified cells, 19 bipolar cells, and 33 NPCs; pooled from $N = 2$ independent experiments). The baseline was calculated as the mean of the first 60 s of recording for each cell. Only peaks that increase or decrease three times the SEM of the baseline were considered as a positive response. ***E***, Representative blots showing relative levels of REST, Ascl, phospho-SMAD1/5/9, and SMAD1 in NPCs treated with CM microC or microPH for 3 d. ***F***, Quantification of the relative expression of REST, Ascl and the ratio phospho-SMAD/total-SMAD in NPCs treated with CM microC or microPH for 3 d. β-actin was used as a loading control. Scale bar, 20 μm. $N = 2$ independent experiments (***D***, pooled cells), $N = 3$ independent experiments (***F***). Error bars represent mean ± SEM. *$p < 0.05$, ***$p < 0.001$ by Holm–Sidak *post hoc* test (after one-way ANOVA was significant at $p < 0.05$). Values of statistics used are shown in Table 8.

ment of gliogenesis. *In vivo* no changes in the production of newborn astrocytes were observed in the neurogenic cascade, although on isolated NPCs the phagocytic microglial secretome gave rise to astrocyte-committed cells with a bipolar phenotype, reminiscent of radial glia (Encinas and Enikolopov, 2008). These cells presented several astrocytic features, including the expression of GFAP and S100β (Raponi et al., 2007; Encinas and Enikolopov, 2008); intracellular calcium response to ATP (De Melo Reis et al., 2011) and high phosphorylation of SMAD, which interacts with TGFβ to give rise to astrocytes/radial glia (Stipursky and Gomes, 2007). Nonetheless, our transcriptional assay did not show heterologous 'gliogenic' genes in phagocytic microglia, suggesting that rather than actively promoting astrogenesis, the acute phagocytosis secretome indirectly promote the default astrocytic lineage (Miller and Gauthier, 2007) by restricting the neuronal lineage.

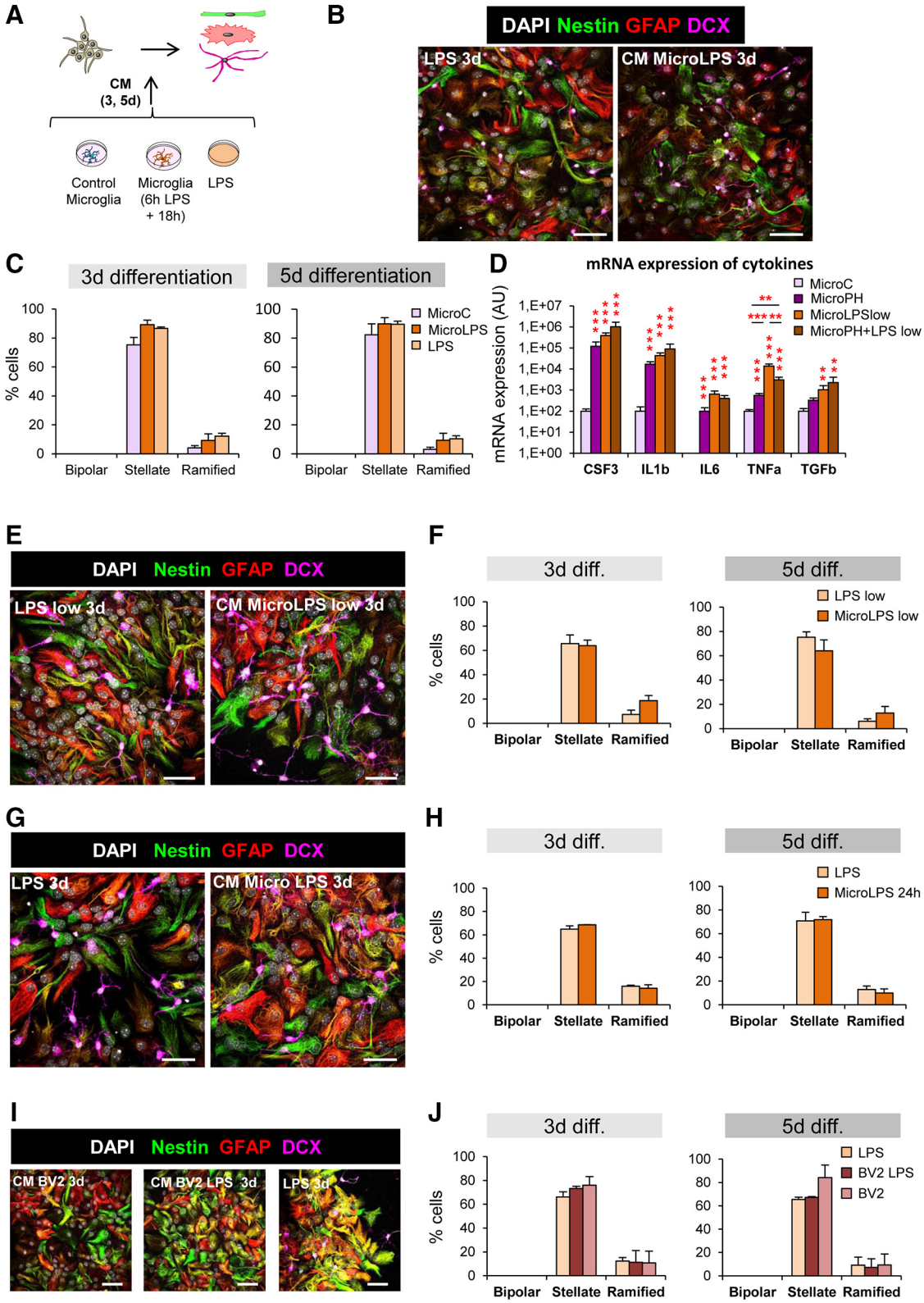

Figure 12. Effect of CM microLPS on neurogenesis *in vitro*. ***A***, Experimental design of the *in vitro* neurogenesis assay. ***B***, Representative confocal microscopy images of neuroprogenitors treated with CM MicroC, CM MicroLPS 6 h + 18 h (1 μg/ml) or LPS alone (1 μg/ml; 24 h). ***C***, Percentage of cell types found after 3 or 5 d treatment with CM MicroC, CM MicroLPS (6 h + 18 h), LPS. The group "bipolar cells" is included for visualization purposes, but as this cell type was not found with any of the treatments, it was not included in the statistical analysis. Three-way ANOVA (treatment × life × time) showed interactions between the different factors and thus the data were split into several one-way ANOVAs, which showed no significant effect of the treatment. ***D***, mRNA expression levels of selected cytokines by real-time qPCR in control microglia (microC), 24 h phagocytic microglia (microPH), as well as control and phagocytic microglia treated with LPS (150 ng/ml, 18 h). HPRT was selected as a reference gene. ***E***, Representative confocal microscopy images of NPCs treated with CM from LPS treated microglia or LPS alone (low concentration: 150 ng/ml; 18 h). ***F***, Quantification of the different cell types found after 3 or 5 d treatment with CM from LPS treated microglia or LPS. ***G***, Representative confocal microscopy images of NPCs treated with CM MicroLPS or LPS (1 μg/ml; 24 h). ***H***, Quantification of the different cell types found after 3 or 5 d treatment with CM MicroLPS or LPS (high concentration: 1 μg/ml; 24 h). ***I***, Representative confocal microscopy images of neuroprogenitors treated with CM BV2, CM BV2 LPS high or LPS high (1 μg/ml; 24 h). ***J***, Quantification of the different cell types found after 3 or 5 d (*Figure legend continues.*)

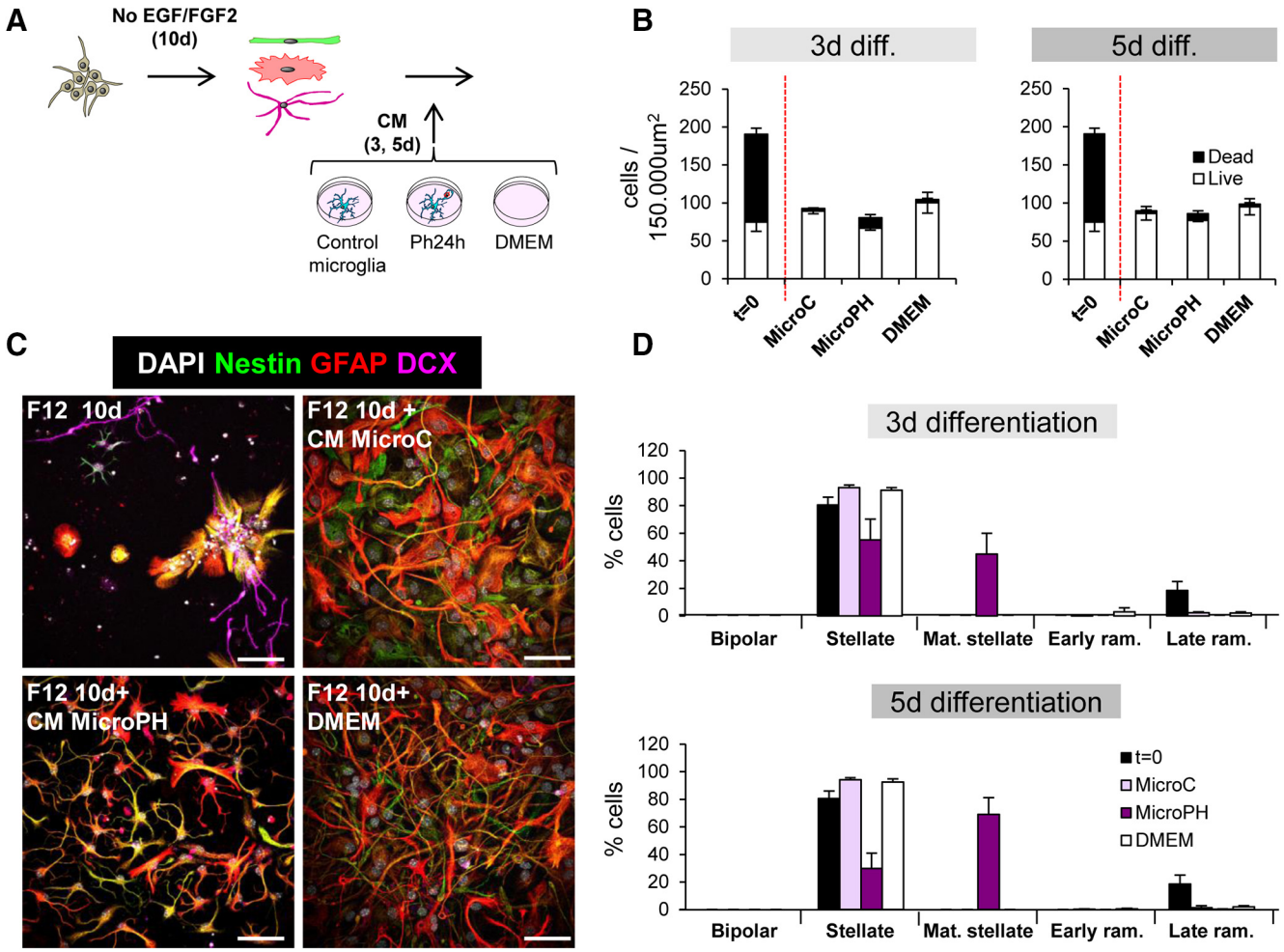

Figure 13. Effect of phagocytic microglia secreted factors on late neurogenesis *in vitro*. ***A***, Experimental design of the *in vitro* late survival and differentiation assay. ***B***, Density of live and dead cells found after 10 d of DMEM/F12 followed by 3–5 d of CM microC or microPH and DMEM. The number of cells before adding the CM ($t = 0$) is shown as a control. ***C***, Representative confocal microscopy images of NPCs treated for 10d with DMEM/F12 followed by 3–5 d of CM microC, microPH, or DMEM. Top, Left, DMEM/F12 treatment of 10 d, before adding any CM. ***D***, Percentage of cell types found after 10 d of DMEM/F12 followed by 3–5 d of CM microC or microPH and DMEM. The number of cells before adding the CM ($t = 0$) is shown as a control. Mat stellate designates stellate cells with mature (more branched) morphology, and early/late ram designates early/late ramified cells. Scale bars: 20 μm, $z = 6.3$ μm. $N = 3$ independent experiments (***B***, ***D***). Three-way ANOVA (treatment × life × time, ***F***) showed interactions between the different factors and thus the data were split into several one-way ANOVAs, which showed no significant effect of the treatment. Data in ***D*** could not be normalized because some cell categories were only present in particular treatments (i.e., the mature stellate phenotype only occurred in MicroPH groups). Error bars represent mean ± SEM. Values of statistics used are shown in Table 8.

Cytokines are unrelated to the effect of phagocytosis secretome on neurogenesis

Several cytokines were also expressed by phagocytic microglia, such as IL-1β, IL-6, and TNFα, which have been reported to decrease survival of neuroprogenitors *in vitro* (IL-1β, TNFα) and *in vivo* (IL-6; Breton and Mao-Draayer, 2011), inhibiting adult neurogenesis. This cytokine expression profile of phagocytic microglia holds some parallelism to the proinflammatory profile triggered upon inflammation, a process that impairs neurogenesis (Ekdahl et al., 2003; Monje et al., 2003). However, in our hands the inflammatory microglia secretome did not trigger a reduction in the survival of NPCs. Furthermore, we found that treatment with neither LPS nor the secretome of LPS-stimulated microglia reduced the production of neuroblasts *in vitro*, suggesting that inflammation is not as detrimental for neurogenesis as previously stated (Ekdahl et al., 2003; Monje et al., 2003) and that cytokines were not responsible for the effects of phagocytic microglial secretome on neural-committed cells. In addition, the neurogenic modulatory program initiated by phagocytosis encompassed genes involved in matrix remodeling (matrix metalloproteases) and membrane ligands (Jag1, ligand for Notch receptor), suggesting that the observed direct contact between microglia and rNSCs/neuroblasts (Sierra et al., 2010) may also participate in shaping the neurogenic niche through participating in the local control of neuroblast differentiation, survival and synaptic integration (Rodríguez-Iglesias et al., 2019).

Phagocytosis reprograms microglia

Finally, we here show that phagocytosis is not simply a terminal process designed to eliminate debris. In fact, in peripheral macrophages engulfment and degradation result in epigenetic, metabolic and functional reprogramming, a process named 'trained immunity' (Bekkering et al., 2018). Similarly, we here show that

←

(*Figure legend continued.*) treatment with CM BV2, CM BV2 LPS, or LPS. Scale bars: ***B***, ***E***, ***G***, ***I***, 20 μm, $z = 6.3$ μm. $N = 3$ independent experiments (***C***), $N = 4$ independent experiments (***D***), $N = 2$ independent experiments (***F***, ***H***, ***J***). Error bars represent mean ± SEM. $^{**}p < 0.01$, $^{***}p < 0.001$ by Holm–Sidak *post hoc* test (after one-way ANOVA was significant at $p < 0.05$). Only significant effects are shown. Values of statistics used are shown in Table 8.

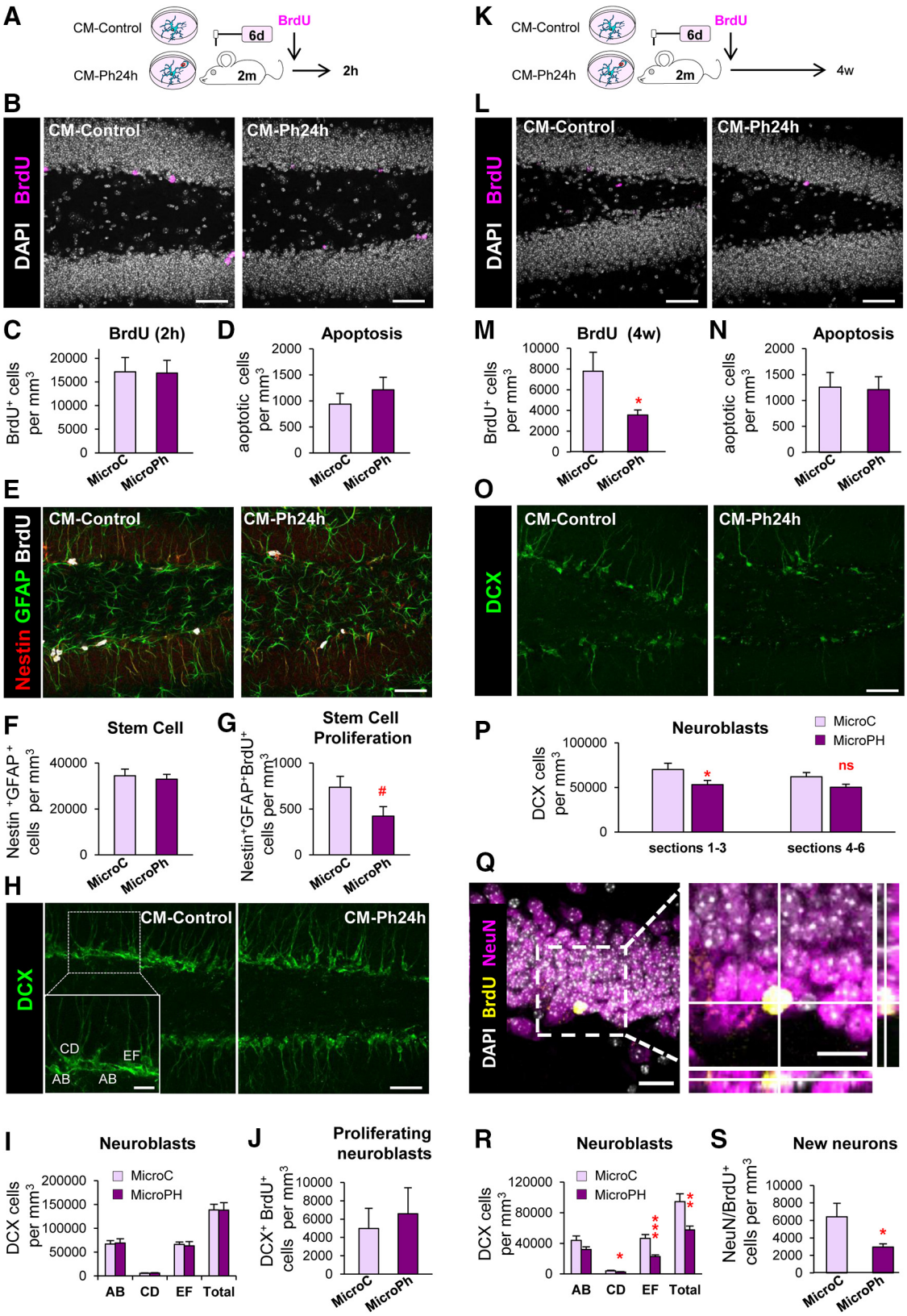

Figure 14. Acute and long-term effects of phagocytic microglia secreted molecules on neurogenesis *in vivo*. ***A***, Experimental design used for the administration of CM microC or microPH by osmotic pumps to 2-month-old fms-EGFP mice. ***B***, Representative confocal images of cell proliferation after the CM treatments for 6 d. Cell nuclei were labeled with DAPI (white) and BrdU was used as a proliferative marker (magenta). ***C***, BrdU $^{+}$ cell density after CM microC or microPH treatment. ***D***, Apoptotic cell density after CM microC or microPH treatment. ***E***, Representative confocal images of stem cells labeled with nestin (red) and GFAP (green). ***F***, Stem cell density after CM microC or microPH treatment. ***G***, Proliferating stem cell (nestin $^{+}$, GFAP $^{+}$, BrdU $^{+}$) density after CM microC or microPH treatment. ***H***, Representative confocal images of neuroblast cell populations AB, CD, EF, and total neuroblasts. Neuroblast cells are labeled with DCX (green). ***I***, Density of neuroblast types AB, CD, and EF. ***J***, Proliferating neuroblasts (BrdU $^{+}$, DCX $^{+}$) density after treatment with CM microC or microPH. ***K***, Experimental design used for the administration of CM microC or microPH by osmotic pumps to 2-month-old fms-EGFP mice. ***L***, Representative confocal images of BrdU $^{+}$ cells in the dentate gyrus. ***M***, BrdU $^{+}$ cell density after CM microC or (*Figure legend continues.*)

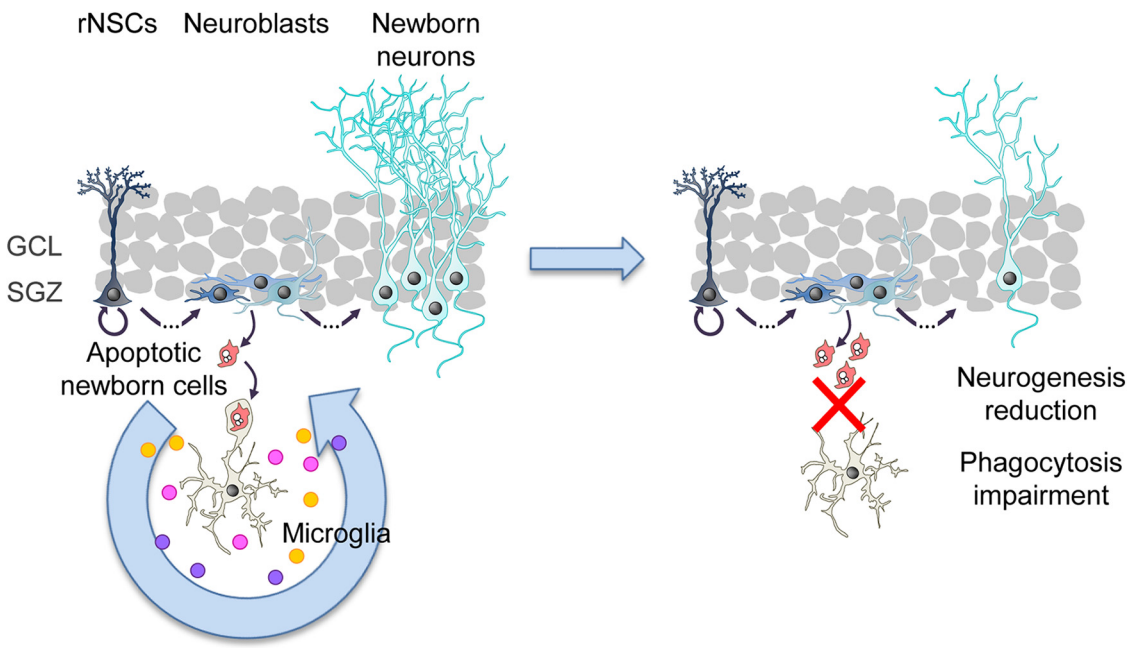

Figure 15. Microglia provides a feedback loop that controls neurogenesis through the phagocytosis-secretome.

in microglia phagocytosis of apoptotic cells triggers a coordinated transcriptional program that involves key chromatin remodeling and metabolic genes, suggesting a long-term reprogramming that may affect multiple microglial functions, from spine surveillance to inflammation. Whether these changes are triggered by the recognition of find-me and "eat-me" surface receptors, or by downstream steps in the phagocytic process of apoptotic cells, remains to be determined. Apoptosis is a widespread phenomenon in neurodegenerative diseases (Abiega et al., 2016) and we speculate that phagocytosis of cell debris and the subsequent alteration of the secretome, as well as other potential functions, may be a key to understanding how microglia impacts surrounding surviving neurons. Similarly, during aging (Pluvinage et al., 2019) or in diseases in which microglial phagocytosis is impaired, such as epilepsy (Abiega et al., 2016), the beneficial effects of promoting engulfment/degradation of cell debris may go beyond merely removing corpses to actively promote regeneration.

In summary, in this paper, we provide strong evidence that phagocytic microglia are a central mechanism to control the homeostasis of the adult hippocampal neurogenic cascade by acutely providing a negative feedback loop via their secretome. This 'brake' is necessary for the long-term maintenance of the neurogenic cascade, since neurogenesis is transiently increased when phagocytosis is acutely blocked, but is disrupted when microglial phagocytosis is chronically impaired, as observed in genetically deficient mice for P2Y12 and MerTK/Axl. Importantly, the link between the proliferation of newborn cells and apoptosis was already suggested to be necessary for the correct learning and memory of the adult brain (Dupret et al., 2007), and our data here points toward microglial phagocytosis of apoptotic cells as the connecting mechanism. As apoptosis is closely related to neural stem cell proliferation, our data suggest that microglial phagocytosis may also shape other developmental and adult neurogenesis sites, such as the SVZ (Cunningham et al., 2013). In addition, phagocytosis of newborn cells has also been recently shown to play a role in sculpting sex differences in the developing amygdala (VanRyzin et al., 2019). While previous work has suggested a largely detrimental effect of microglia on hippocampal neurogenesis (Valero et al., 2016), our data are in agreement with recent evidences supporting the essential role of macrophages and other immune cells in remodeling stem cells niches (Naik et al., 2018).

←

(*Figure legend continued.*) microPH treatment. ***N***, Apoptotic cell density after CM microC or microPH treatment. ***O***, Representative confocal images of neuroblasts labeled with DCX (green). ***P***, Density of total number of neuroblasts in Sections 1–3 closest to the injection site, and 4–6 further away. ***Q***, Representative confocal images of a newborn neuron labeled with BrdU (yellow) and NeuN (magenta). ***R***, Density of neuroblast types AB, CD, EF, and total neuroblasts. ***S***, New neurons ($NeuN^+$, $BrdU^+$) density after CM microC or microPH treatment. Scale bars: ***B***, ***L***, ***E***, ***O***, ***H***, 50 μm (insert in ***H***, 20 μm); ***Q***, 20 μm (insert, 10 μm); ***B***, ***L***, ***E***, ***O***, ***H***, $z = 12$ μm; ***Q***, $z = 6$ μm. $N = 7$–10 mice (***B***–***J***), $N = 5$–11 mice (***L***–***S***). Error bars represent mean ± SEM. #$p = 0.0649$, *$p < 0.05$, **$p < 0.01$, ***$p < 0.001$ by Student's *t* test. Values of statistics used are shown in Table 9. ns, not significant.

References

Aarum J, Sandberg K, Haeberlein SL, Persson MA (2003) Migration and differentiation of neural precursor cells can be directed by microglia. Proc Natl Acad Sci U S A 100:15983–15988.

Abiega O, Beccari S, Diaz-Aparicio I, Nadjar A, Layé S, Leyrolle Q, Gómez-Nicola D, Domercq M, Pérez-Samartín A, Sánchez-Zafra V, Paris I, Valero J, Savage JC, Hui CW, Tremblay MÈ, Deudero JJ, Brewster AL, Anderson AE, Zaldumbide L, Galbarriatu L, et al. (2016) Neuronal hyperactivity disturbs ATP microgradients, impairs microglial motility, and reduces phagocytic receptor expression triggering apoptosis/microglial phagocytosis uncoupling. PLoS Biol 14:e1002466.

Alberdi E, Wyssenbach A, Alberdi M, Sánchez-Gómez MV, Cavaliere F, Rodríguez JJ, Verkhratsky A, Matute C (2013) Ca^{2+}-dependent endoplasmic reticulum stress correlates with astrogliosis in oligomeric amyloid beta-treated astrocytes and in a model of Alzheimer's disease. Aging Cell 12:292–302.

Babu H, Claasen JH, Kannan S, Rünker AE, Palmer T, Kempermann G (2011) A protocol for isolation and enriched monolayer cultivation of neural precursor cells from mouse dentate gyrus. Front Neurosci 5:89.

Beccari S, Valero J, Maletic-Savatic M, Sierra A (2017) A simulation model of neuroprogenitor proliferation dynamics predicts age-related loss of hippocampal neurogenesis but not astrogenesis. Sci Rep 7:16528.

Beccari S, Diaz-Aparicio I, Sierra A (2018) Quantifying microglial phagocytosis of apoptotic cells in the brain in health and disease. Curr Protoc Immunol 122:e49.

Bekkering S, Arts RJW, Novakovic B, Kourtzelis I, van der Heijden CD, Li Y, Popa CD, Ter Horst R, van Tuijl J, Netea-Maier RT, van de Veerdonk FL, Chavakis T, Joosten LAB, van der Meer JWM, Stunnenberg H, Riksen NP, Netea MG (2018) Metabolic induction of trained immunity through the mevalonate pathway. Cell 172:135–146.e9.

Bindea G, Galon J, Mlecnik B (2013) CluePedia cytoscape plugin: pathway insights using integrated experimental and in silico data. Bioinformatics 29:661–663.

Bloodgood BL, Sabatini BL (2008) Regulation of synaptic signalling by postsynaptic, non-glutamate receptor ion channels. J Physiol 586:1475–1480.

Bonaguidi MA, Wheeler MA, Shapiro JS, Stadel RP, Sun GJ, Ming GL, Song H (2011) *In vivo* clonal analysis reveals self-renewing and multipotent adult neural stem cell characteristics. Cell 145:1142–1155.

Brazma A, Hingamp P, Quackenbush J, Sherlock G, Spellman P, Stoeckert C, Aach J, Ansorge W, Ball CA, Causton HC, Gaasterland T, Glenisson P, Holstege FC, Kim IF, Markowitz V, Matese JC, Parkinson H, Robinson A, Sarkans U, Schulze-Kremer S, et al. (2001) Minimum information about a microarray experiment (MIAME)-toward standards for microarray data. Nat Genet 29:365–371.

Breton J, Mao-Draayer Y (2011) Impact of cytokines on neural stem/progenitor cell fate. J Neurol Neurophysiol. S4.

Brown JP, Couillard-Després S, Cooper-Kuhn CM, Winkler J, Aigner L, Kuhn HG (2003) Transient expression of doublecortin during adult neurogenesis. J Comp Neurol 467:1–10.

Bustin SA (2010) Why the need for qPCR publication guidelines? The case for MIQE. Methods 50:217–226.

Chakrabarti R, Celià-Terrassa T, Kumar S, Hang X, Wei Y, Choudhury A, Hwang J, Peng J, Nixon B, Grady JJ, DeCoste C, Gao J, van Es JH, Li MO, Aifantis I, Clevers H, Kang Y (2018) Notch ligand Dll1 mediates cross-talk between mammary stem cells and the macrophageal niche. Science 360:eaan4153.

Chow A, Huggins M, Ahmed J, Hashimoto D, Lucas D, Kunisaki Y, Pinho S, Leboeuf M, Noizat C, van Rooijen N, Tanaka M, Zhao ZJ, Bergman A, Merad M, Frenette PS (2013) CD169(+) macrophages provide a niche promoting erythropoiesis under homeostasis and stress. Nat Med 19: 429–436.

Conesa A, Nueda MJ, Ferrer A, Talón M (2006) maSigPro: a method to identify significantly differential expression profiles in time-course microarray experiments. Bioinformatics 22:1096–1102.

Cunningham CL, Martínez-Cerdeño V, Noctor SC (2013) Microglia regulate the number of neural precursor cells in the developing cerebral cortex. J Neurosci 33:4216–4233.

De Melo Reis RA, Schitine CS, Köfalvi A, Grade S, Cortes L, Gardino PF, Malva JO, de Mello FG (2011) Functional identification of cell phenotypes differentiating from mice retinal neurospheres using single cell calcium imaging. Cell Mol Neurobiol 31:835–846.

Deng W, Aimone JB, Gage FH (2010) New neurons and new memories: how does adult hippocampal neurogenesis affect learning and memory? Nat Rev Neurosci 11:339–350.

Diaz-Aparicio I, Sierra A (2019) C1q is related to microglial phagocytosis in the hippocampus in physiological conditions. Science Matters.

Dupret D, Fabre A, Döbrössy MD, Panatier A, Rodríguez JJ, Lamarque S, Lemaire V, Oliet SH, Piazza PV, Abrous DN (2007) Spatial learning depends on both the addition and removal of new hippocampal neurons. PLoS Biol 5:e214.

Ehninger D, Kempermann G (2008) Neurogenesis in the adult hippocampus. Cell Tissue Res 331:243–250.

Eiriz MF, Grade S, Rosa A, Xapelli S, Bernardino L, Agasse F, Malva JO (2011) Functional evaluation of neural stem cell differentiation by single cell calcium imaging. Curr Stem Cell Res Ther 6:288–296.

Ekdahl CT, Claasen JH, Bonde S, Kokaia Z, Lindvall O (2003) Inflammation is detrimental for neurogenesis in adult brain. Proc Natl Acad Sci U S A 100:13632–13637.

Elliott MR, Chekeni FB, Trampont PC, Lazarowski ER, Kadl A, Walk SF, Park D, Woodson RI, Ostankovich M, Sharma P, Lysiak JJ, Harden TK, Leitinger N, Ravichandran KS (2009) Nucleotides released by apoptotic cells act as a find-me signal to promote phagocytic clearance. Nature 461:282–286.

Encinas JM, Enikolopov G (2008) Identifying and quantitating neural stem and progenitor cells in the adult brain. Methods Cell Biol 85:243–272.

Encinas JM, Sierra A (2012) Neural stem cell deforestation as the main force driving the age-related decline in adult hippocampal neurogenesis. Behav Brain Res 227:433–439.

Encinas JM, Michurina TV, Peunova N, Park JH, Tordo J, Peterson DA, Fishell G, Koulakov A, Enikolopov G (2011) Division-coupled astrocytic differentiation and age-related depletion of neural stem cells in the adult hippocampus. Cell Stem Cell 8:566–579.

Fourgeaud L, Través PG, Tufail Y, Leal-Bailey H, Lew ED, Burrola PG, Callaway P, Zagórska A, Rothlin CV, Nimmerjahn A, Lemke G (2016) TAM receptors regulate multiple features of microglial physiology. Nature 532:240–244.

Fraser DA, Pisalyaput K, Tenner AJ (2010) C1q enhances microglial clearance of apoptotic neurons and neuronal blebs, and modulates subsequent inflammatory cytokine production. J Neurochem 112:733–743.

Gebara E, Sultan S, Kocher-Braissant J, Toni N (2013) Adult hippocampal neurogenesis inversely correlates with microglia in conditions of voluntary running and aging. Front Neurosci 7:145.

Hachem S, Aguirre A, Vives V, Marks A, Gallo V, Legraverend C (2005) Spatial and temporal expression of S100B in cells of oligodendrocyte lineage. Glia 51:81–97.

Haynes SE, Hollopeter G, Yang G, Kurpius D, Dailey ME, Gan WB, Julius D (2006) The P2Y12 receptor regulates microglial activation by extracellular nucleotides. Nat Neurosci 9:1512–1519.

Kohyama J, Sanosaka T, Tokunaga A, Takatsuka E, Tsujimura K, Okano H, Nakashima K (2010) BMP-induced REST regulates the establishment and maintenance of astrocytic identity. J Cell Biol 189:159–170.

Kreisel T, Wolf B, Keshet E, Licht T (2019) Unique role for dentate gyrus microglia in neuroblast survival and in VEGF-induced activation. Glia 67:594–618.

Kwon MJ, Oh E, Lee S, Roh MR, Kim SE, Lee Y, Choi YL, In YH, Park T, Koh SS, Shin YK (2009) Identification of novel reference genes using multiplatform expression data and their validation for quantitative gene expression analysis. PLoS One 4:e6162.

Liu Y, Miao Q, Yuan J, Han S, Zhang P, Li S, Rao Z, Zhao W, Ye Q, Geng J, Zhang X, Cheng L (2015) Ascl1 converts dorsal midbrain astrocytes into functional neurons *in vivo*. J Neurosci 35:9336–9355.

Lopez-Atalaya JP, Askew KE, Sierra A, Gomez-Nicola D (2018) Development and maintenance of the brain's immune toolkit: microglia and non-parenchymal brain macrophages. Dev Neurobiol 78:561–579.

Miller FD, Gauthier AS (2007) Timing is everything: making neurons versus glia in the developing cortex. Neuron 54:357–369.

Mlecnik B, Galon J, Bindea G (2018) Comprehensive functional analysis of large lists of genes and proteins. J Proteomics 171:2–10.

Monje ML, Toda H, Palmer TD (2003) Inflammatory blockade restores adult hippocampal neurogenesis. Science 302:1760–1765.

Moreno-Jiménez EP, Flor-García M, Terreros-Roncal J, Rábano A, Cafini F, Pallas-Bazarra N, Ávila J, Llorens-Martín M (2019) Adult hippocampal neurogenesis is abundant in neurologically healthy subjects and drops sharply in patients with Alzheimer's disease. Nat Med 25:554–560.

Morgan SC, Taylor DL, Pocock JM (2004) Microglia release activators of neuronal proliferation mediated by activation of mitogen-activated protein kinase, phosphatidylinositol-3-kinase/Akt and delta-notch signalling cascades. J Neurochem 90:89–101.

Morioka S, Perry JSA, Raymond MH, Medina CB, Zhu Y, Zhao L, Serbulea V, Onengut-Gumuscu S, Leitinger N, Kucenas S, Rathmell JC, Makowski L, Ravichandran KS (2018) Efferocytosis induces a novel SLC program to promote glucose uptake and lactate release. Nature 563:714–718.

Nagata S, Hanayama R, Kawane K (2010) Autoimmunity and the clearance of dead cells. Cell 140:619–630.

Naik S, Larsen SB, Cowley CJ, Fuchs E (2018) Two to tango: dialog between immunity and stem cells in health and disease. Cell 175:908–920.

Overall RW, Paszkowski-Rogacz M, Kempermann G (2012) The mammalian adult neurogenesis gene ontology (MANGO) provides a structural framework for published information on genes regulating adult hippocampal neurogenesis. PLoS One 7:e48527.

Parkhurst CN, Yang G, Ninan I, Savas JN, Yates JR 3rd, Lafaille JJ, Hempstead BL, Littman DR, Gan WB (2013) Microglia promote learning-dependent synapse formation through brain-derived neurotrophic factor. Cell 155:1596–1609.

Plümpe T, Ehninger D, Steiner B, Klempin F, Jessberger S, Brandt M, Römer B, Rodriguez GR, Kronenberg G, Kempermann G (2006) Variability of doublecortin-associated dendrite maturation in adult hippocampal neu-

rogenesis is independent of the regulation of precursor cell proliferation. BMC Neurosci 7:77.

Pluvinage JV, Haney MS, Smith BAH, Sun J, Iram T, Bonanno L, Li L, Lee DP, Morgens DW, Yang AC, Shuken SR, Gate D, Scott M, Khatri P, Luo J, Bertozzi CR, Bassik MC, Wyss-Coray T (2019) CD22 blockade restores homeostatic microglial phagocytosis in ageing brains. Nature 568:187–192.

Ramakers C, Ruijter JM, Deprez RH, Moorman AF (2003) Assumption-free analysis of quantitative real-time polymerase chain reaction (PCR) data. Neurosci Lett 339:62–66.

Raponi E, Agenes F, Delphin C, Assard N, Baudier J, Legraverend C, Deloulme JC (2007) S100B expression defines a state in which GFAP-expressing cells lose their neural stem cell potential and acquire a more mature developmental stage. Glia 55:165–177.

Rodríguez-Iglesias N, Sierra A, Valero J (2019) Rewiring of memory circuits: connecting adult newborn neurons with the help of microglia. Front Cell Dev Biol 7:24.

Rogers JT, Morganti JM, Bachstetter AD, Hudson CE, Peters MM, Grimmig BA, Weeber EJ, Bickford PC, Gemma C (2011) CX3CR1 deficiency leads to impairment of hippocampal cognitive function and synaptic plasticity. J Neurosci 31:16241–16250.

Rotheneichner P, Romanelli P, Bieler L, Pagitsch S, Zaunmair P, Kreutzer C, Konig R, König R, Marschallinger J, Aigner L, Couillard-Després S (2017) Tamoxifen activation of cre-recombinase has no persisting effects on adult neurogenesis or learning and anxiety. Front Neurosci 11:27.

Rothlin CV, Lemke G (2010) TAM receptor signaling and autoimmune disease. Curr Opin Immunol 22:740–746.

Santos AJM, Lo YH, Mah AT, Kuo CJ (2018) The intestinal stem cell niche: homeostasis and adaptations. Trends Cell Biol 28:1062–1078.

Sasmono RT, Oceandy D, Pollard JW, Tong W, Pavli P, Wainwright BJ, Ostrowski MC, Himes SR, Hume DA (2003) A macrophage colony-stimulating factor receptor-green fluorescent protein transgene is expressed throughout the mononuclear phagocyte system of the mouse. Blood 101:1155–1163.

Scholzen T, Gerdes J (2000) The ki-67 protein: from the known and the unknown. J Cell Physiol 182:311–322.

Scott RS, McMahon EJ, Pop SM, Reap EA, Caricchio R, Cohen PL, Earp HS, Matsushima GK (2001) Phagocytosis and clearance of apoptotic cells is mediated by MER. Nature 411:207–211.

Sierra A, Gottfried-Blackmore AC, McEwen BS, Bulloch K (2007) Microglia derived from aging mice exhibit an altered inflammatory profile. Glia 55:412–424.

Sierra A, Encinas JM, Deudero JJ, Chancey JH, Enikolopov G, Overstreet-Wadiche LS, Tsirka SE, Maletic-Savatic M (2010) Microglia shape adult hippocampal neurogenesis through apoptosis-coupled phagocytosis. Cell Stem Cell 7:483–495.

Sierra A, Abiega O, Shahraz A, Neumann H (2013) Janus-faced microglia: beneficial and detrimental consequences of microglial phagocytosis. Front Cell Neurosci 7:6.

Sierra A, Beccari S, Diaz-Aparicio I, Encinas JM, Comeau S, Tremblay MÈ (2014) Surveillance, phagocytosis, and inflammation: how never-resting microglia influence adult hippocampal neurogenesis. Neural Plast 2014:610343.

Sierra A, Martín-Suárez S, Valcárcel-Martin R, Pascual-Brazo J, Aelvoet SA, Abiega O, Deudero JJ, Brewster AL, Bernales I, Anderson AE, Baekelandt V, Maletić-Savatić M, Encinas JM (2015) Neuronal hyperactivity accelerates depletion of neural stem cells and impairs hippocampal neurogenesis. Cell Stem Cell 16:488–503.

Stipursky J, Gomes FC (2007) TGF-beta1/SMAD signaling induces astrocyte fate commitment *in vitro*: implications for radial glia development. Glia 55:1023–1033.

Valero J, Paris I, Sierra A (2016) Lifestyle shapes the dialogue between environment, microglia, and adult neurogenesis. ACS Chem Neurosci 7:442–453.

van de Moosdijk AA, van Amerongen R (2016) Identification of reliable reference genes for qRT-PCR studies of the developing mouse mammary gland. Sci Rep 6:35595.

VanRyzin JW, Marquardt AE, Argue KJ, Vecchiarelli HA, Ashton SE, Arambula SE, Hill MN, McCarthy MM (2019) Microglial phagocytosis of newborn cells is induced by endocannabinoids and sculpts sex differences in juvenile rat social play. Neuron 102:435–449.e6.

Walton NM, Sutter BM, Laywell ED, Levkoff LH, Kearns SM, Marshall GP 2nd, Scheffler B, Steindler DA (2006) Microglia instruct subventricular zone neurogenesis. Glia 54:815–825.

Xapelli S, Agasse F, Sardà-Arroyo L, Bernardino L, Santos T, Ribeiro FF, Valero J, Bragança J, Schitine C, de Melo Reis RA, Sebastião AM, Malva JO (2013) Activation of type 1 cannabinoid receptor (CB1R) promotes neurogenesis in murine subventricular zone cell cultures. PLoS One 8:e63529.